For Ari and Oni

Supervisor:
Prof. Dr. ir. Piet Seuntjens
Flemish Institute for Technological Research, Environmental Modeling Unit
Ghent University, Department of Soil Management

Co-supervisors:
Dr. ir. Ingeborg Joris
Flemish Institute for Technological Research, Environmental Modeling Unit
Prof. Dr. Okke Batelaan
Flinders University, School of the Environment

Faculty of Bioscience Engineering
Dean: Prof. Dr. ir. Guido Van Huylenbroeck
Ghent University
Rector: Prof. Dr. Anne De Paepe

Water Flow and Contaminant Transformation in the Hyporheic Zone of Lowland Rivers

Uwe Schneidewind

Thesis submitted in fulfillment of the requirements for the degree of Doctor (PhD) in Bioscience Engineering

Waterstroming en Transformatie van Contaminanten in de Hyporheische Zone van Laaglandrivieren

This work should be cited as:

Schneidewind, U. (2016): Water Flow and Contaminant Transformation in the Hyporheic Zone of Lowland Rivers. PhD thesis, 234 pp, Ghent University, Ghent.

ISBN: 978-90-5989-864-6

Acknowledgements

This PhD thesis would not have been possible without the support of numerous people. First and foremost I would like to thank my supervisors Piet Seuntjens and Ingeborg Joris for acquiring funding within the EU Marie Curie program, for putting up with me, for letting me pursue mostly my own research ideas, for giving me feedback and support whenever needed and for gently pushing me into the right direction whenever I was on the verge of bearing away. Thank you also Piet, for providing some extra funding from Ghent University (UGent).

My co-supervisor Okke Batelaan I would like to thank especially for helping me with the start of my scientific career in Belgium, for the many insightful talks about what it means to work in academia and for the provision of some funding for conference visits.

As a participant of the EU Marie Curie ITN ADVOCATE I would like to thank the EU tax payers for providing three years of funding and of course all my colleagues and the associated partners for the good times and all the work and efforts that made the ITN truly a great experience. Steve Thornton, Gabriella Kakonyi, Jenny Chambers, Mario Schirmer and Ruth Garcia: a special thanks again for a great organization! Alistair Beames, thanks for making me laugh so many times and for "suffering" through everything with me.

I would like to thank the co-authors on all my publications for their efforts and invaluable feedback. Especially, I would like to acknowledge Pieter Jan Haest and Siavash Atashgahi, (back then with VITO), with whom I worked together on modeling the degradation of chlorinated ethenes in microcosms. I learned a lot about the positive and more difficult aspects of modeling and how important a good collaboration is. To Kelly Hamonts and Winnie Dejonghe (VITO) a specially thanks for sharing some of their data. Furthermore, I would like to extend my appreciation to Christian Anibas, Matthijs van Berkel and Gerd Vandersteen from the Vrije University of Brussel (VUB), who worked together with me on modeling groundwater-surface water exchange fluxes from streambed temperature measurements. Thanks for the fruitful collaboration that amounted to two very nice publications, and hopefully more to come. To Gerd and Matthijs a special thanks for explaining the mathematics behind modeling in the frequency domain and to being especially patient with me when it came to MATLAB. Christian, a special thanks goes to you for your help during the many hours of field work at and in the Slootbeek and for all the discussions on streambed temperatures and other relevant and not-so-relevant stuff.

From UFZ I would like to acknowledge Christian Schmidt, for his provision of a lot of field equipment and for the fruitful collaboration on some aspects of temperature modeling.

From VITO I would like to thank all the people that were involved in the acquisition and organization of the ADVOCATE project. Additionally, I would like to thank Jan Bronders, and Nele De Smet for making my visits to VITO a pleasant time. Danny Wilczek I would like to thank for his support during some of the field work and for helping me improve my Dutch while we shared a carpool.

From UGent I would like acknowledge my colleague Ellen Van De Vijver for her help with the many aspects of geostatistics. Additional thanks goes to her as well as to Jan De Pue and Meizam Rezaei for the good times there.

From the University of Sheffield I would like to thank Steve Thornton for providing some data and for receiving me during my secondment. Thanks also to Richard Gill, Petra Hedbavna, Lukasz Cieslak and the others for a great time.

From VUB I would like to say thanks to Elga Salvadore, Boud Verbeiren, Jiri Nossent, Jef Dams, Eva Ampe, Anja Cosemans, Juliette Dujardin and all the others there for making my visits pleasant and my lunch breaks never boring.

I am deeply grateful to my family for all their support, be it moral or otherwise. The most debt of gratitude I owe to Ona, my wonderful wife, partner and friend, who started on this journey together with me and who shared with me all facets of being a PhD student. Thanks for always being there for me!

Würselen, January 2016

Uwe Schneidewind

Table of Contents

List of Figures

List of Tables

List of Acronyms and Symbols

ATSDR	Agency for Toxic Substances and Disease Registry
CAH	chlorinated aliphatic hydrocarbon
CE	chlorinated ethene
DCE	dichloroethene
DNA	deoxyribonucleic acid
DNAPL	dense non-aqueous phase liquid
DOC	dissolved organic carbon
EF	exchange flux
GPR	ground penetrating radar
GSEF	groundwater-surface water exchange flux
GW-SW	groundwater-surface water
HEF	hyporheic exchange flux
HZ	hyporheic zone
LP	local polynomial method
ML, MLE	maximum-likelihood estimator
NAC	natural attenuation capacity
ODE	ordinary differential equation
PCE	tetrachloroethene
PCR	polymerase chain reaction
PDE	partial differential equation
REV	representative elementary volume
RMSE	root-mean-square error
RSD	relative standard deviation or absolute coefficient of variation
TCE	trichloroethene
USEPA	United States Environmental Protection Agency
VC	vinylchloride
VEF	vertical exchange flux
VHG	vertical hydraulic gradient
cdf	cumulative distribution function
pdf	probability density function
A	channel cross-section or area [L^2]
A_T	magnitude of the amplitude of the temperature variations
A_r	amplitude ratio
B	saturated streambed thickness [L]
C	dimensionless shape factor [-]

C, C_b, C_w, C_g	contaminant concentrations: general, in solid, aqueous, gas phases [ML^{-3}]
C_D	damping factor used in slug test type curve matching [-]
C_i	electron donor concentration [NL^{-3}]
C_i	species-dependent concentration [NL^{-3}]
Cr	Courant number [-]
COV	covariance
CV	coefficient of variation [-]
D	dispersion coefficient [L^2T]
D_H	flow depth [L]
D_T	thermal dispersion coefficient or diffusivity [$L^2\ T^{-1}$]
D_w	moisture diffusivity [L^2T]
$E(\omega)$	additive circular-complex normal noise in a temperature signal
E_{NS}	Nash-Sutcliffe efficiency criterion
F	statistical sample, number of frequency lines used
Fi	Fisher information matrix
$G(\omega), G_{LP}(\omega)$	frequency response functions
H	Henry's constant (vapor phase) [-]
I_i	species-dependent inhibition constant [NL^{-3}]
$J,\ J^h$	analytical Jacobian matrix and Hermitian transpose
K, K_h, K_r, K_v	hydraulic conductivity, horizontal, radial, vertical [LT^{-1}]
K_{bg}	soil-gas partition coefficient [L^3M^{-1}]
K_d	soil-water partition coefficient [L^3M^{-1}]
$K_{s,d}$	electron donor half-velocity (saturation) constant [NL^{-3}]
$K_{s,i}$	species-dependent half-velocity constant [NL^{-3}]
L	characteristic length [L], distance between filter screens or filter screen/streambed top in VHG calculation [L]
L_E, L_{ML}, V_E, V_{ML}	expected and actual values in the cost function analysis
L_e	effective water column length [L] in a piezometer
$L_{ML}(\theta)$	likelihood cost function
P	oscillation period of the temperature signal
Pe	grid Péclet number [-]
Pe_T	thermal Péclet number [-]
Q	discharge [L^3T^{-1}]
Q_L	flow rate in the HZ [L^3T^{-1}]
R	retardation factor [-]
R_T	thermal retardation factor [-]
R_{a_k}, R_{b_k}	ranks
Re	Reynolds number [-]
Re	real number
R_e	effective radius parameter after Bower and Rice (1976)

RP	reaction and mass transfer processes
S_s	specific storage [-]
$T, T_u,\ T_l, T_z$	temperature: general, at upper, lower boundary, at depth z [Θ]
$Tr(\omega)$	transient parts of a temperature signal
$U(\omega), U_{ST}(\omega)$	input spectra in temperature modeling
U	coefficient of uniformity [-]
V_0	representative elementary volume [L^3]
$V_{g,} V_{aq}$	volumes of the gaseous, aqueous phase [L^3]
$V_{ML}(\theta, \omega_k)$	log-likelihood cost function
$X,\ X_{obs,} X_{mod}$	microbial concentrations [cells L^{-3}]
Y_i	species-dependent specific yield [cells N^{-1}]
$Y(\omega), Z(\omega)$	output spectra in temperature modeling
a	realizations, anisotropy ratio
a_{max}	maximum
a_{min}	minimum
b	cell decay rate [T^{-1}], screen length of a well or piezometer [L]
c	specific heat capacity [$L^2MT^{-2}\Theta^{-1}$]
$c_{1,} c_{2,} c_{3,} c_{4,}$	Boolean parameters [-]
$d, d_x, d_{10}, d_{20}, d_{60}$	grain diameters of the sediment [L]
e	Euler number
e_{ML}	complex-valued residual least-squares error
f(n)	porosity function
g	acceleration due to gravity [LT^{-2}]
h	hydraulic head [L], elevation [L]
i	hydraulic gradient [-]; imaginary unit
k	intrinsic permeability [L^2]
l	lag distance
log K_{ow}	octanol water partition coefficient
m	arithmetic mean
m_0, m_f	channel friction slopes [-]
n	porosity [-], number of free parameters
n_e	effective porosity [-]
$n(l)$	number of pairs for variogram
p	pressure [$ML^{-1}T^{-2}$]
q_D, q_T	specific discharge, Darcy flux, exchange flux [LT^{-1}]
q_z	exchange flux in the vertical direction [LT^{-1}]
r_a	range
r_c	effective radius of a well casing [L]
r_i	species-dependent reaction rate [$NL^{-3}T^{-1}$]
r_P	Pearson's linear correlation coefficient

r_R	Spearman's rank correlation coefficient
$r_{w,we}$	radius of a well or piezometer [-]
r_X	net bacterial growth rate [cells $T^{-1}L^{-3}$]
s	source/sink term [LT^{-1}]
s_r, s_s	sinks and sources [L^2T^{-1}]
t	time [T]
t_d	dimensionless time
t_R	residence time [T]
u	stream velocity [LT^{-1}]
u_{rx}, u_{sx}	velocity of sinks and sources [LT^{-1}]
v	average linear velocity of water or fluid [LT^{-1}]
v_c	average contaminant transport velocity [LT^{-1}]
v_T	thermal front velocity [LT^{-1}]
x	direction [L]
y	sample standard deviation
z	elevation head [L] or depth [L]
Θ, Θ_{meas}	temperature in the frequency domain
α	anisotropy ratio [-]
α, β, γ	parameters introduced in the heat transport equation (3-17)
$\gamma(l)$	semi-variogram
θ	volumetric water content [-], parameter vector
ϑ	kinematic viscosity [L^2T]
κ	bulk or effective thermal conductivity [$ML\,T^{-3}\,\Theta^{-1}$]
κ_s	thermal conductivity of solids [$ML\,T^{-3}\,\Theta^{-1}$]
κ_w	thermal conductivity of water [$ML\,T^{-3}\,\Theta^{-1}$]
λ_i	rate coefficient (constant) of species *i* [different units]
μ_e, μ	(effective) dynamic viscosity [$ML^{-1}T^{-1}$]
ρ	density [ML^{-3}]
ρ_b	bulk density of sediment [ML^{-3}]
ρ_w	density of water [ML^{-3}]
ρc	volumetric heat capacities of the water-sediment mixture [$ML^{-1}\,T^{-2}\Theta^{-1}$]
$\rho_s c_s$	volumetric heat capacity of solids [$ML^{-1}\,T^{-2}\Theta^{-1}$]
$\rho_w c_w$	volumetric heat capacities of water [$ML^{-1}\,T^{-2}\Theta^{-1}$]
$\sigma_{G_{LP}}, \sigma_{D_T}, \sigma_{\hat{q}_z}, \sigma_e$	standard deviations
τ	tortuosity [-]
ϕ	phase
ψ	thermal dispersivity [L]
ω	angular frequency

Nederlandse Samenvatting

Tijdens de afgelopen twee decennia is er een toenemend aantal wetenschappelijke studies verschenen waarin de fysische en biochemische processen in de grondwater-oppervlakte water interfase bestudeerd werden. Deze interfase wordt ook hyporheische zone genoemd en is de verzadigde grenszone tussen aquifer en oppervlakte water in een gekoppeld grondwater-opervlakte water systeem. De hyporheische zone ontleent haar kenmerken aan de actieve vermenging van grondwater en oppervlaktewater, biedt een habitat voor interstitiële organismen, een wortelzone voor bepaalde waterplanten en een paaigebied voor vissen. Hydrologische kenmerken bepalen op hun beurt de uitwisseling van koolstof, voedingsstoffen en energie tussen grond- en oppervlaktewater. Bovendien kan de HZ fungeren als een zone van natuurlijke afbraak van verschillende types verontreiniging. De hyporheische zone is dynamisch in ruimte en tijd en parameters die waterstroming alsook transport en transformatie van contaminatie beschrijven, zijn onderhevig aan aanzienlijke heterogeniteit en onzekerheid.

In deze thesis worden drie belangrijke parameters onderzocht, die cruciaal zijn voor vele van de fysische en biochemische processen in de hyporheische zone van laaglandrivieren; (i) afbraakcoëfficiënten, die de biologische afbraak van stoffen en het natuurlijk afbraakpotentieel bepalen, (ii) fluxen tussen grondwater, rivierbed en rivier, en (iii) de hydraulische geleidbaarheid van het rivierbed.

(i) De sequentiële reductieve dechlorinatie van trichlooretheen (TCE) en haar dochterproducten 1,2 dichlooretheen (cis-DCE) en vinylchloride (VC) in de aanwezigheid van *Dehalococcoides mccartyi* werd onderzocht op basis van sedimentstalen genomen uit het rivierbed en de aquifer van het Zenne studiegebied ten noorden van Brussel, België. Dit gebied is zwaar verontreinigd met gechloreerde alifatische koolwaterstoffen. De dechlorering werd onderzocht door het modelleren van eerste orde, Michaelis-Menten en Monod kinetiek met gegevens uit eerder uitgevoerde microcosmos experimenten. Voor het modelleren van de kinetische reacties werd AMALGAM gebruikt, een multi-objectief evolutionair algoritme voor parameterschatting dat met verschillende optimalisatiealgoritmes tegelijk werkt. Resultaten van de modellering toonden aan dat geen van de verschillende kinetische modellen de gehele microcosmos experimenten kon benaderen. Eerste orde en Michaelis-Menten modellen konden het best de dechlorering aan het einde van ieder microcosmos experiment benaderen, terwijl het Monod model de dechlorering aan het begin van ieder experiment het best kon weergeven, waar zich een wachttijd had voorgedaan. De relatie tussen *Dehalococcoides mccartyi* aantal en de geoptimaliseerde parameters toonde een grote onzekerheid en het opnemen van donor beperking in de modellen verbeterde de simulaties niet. De resultaten duiden aan dat niet alle limiterende factoren waren opgenomen in de stofafbraakcoëfficiënten van de verschillende kinetische modellen.

(ii) Grondwater-oppervlakte water interactie in de Slootbeek, een kleine zijarm van de Aa, een rivier in België werd onderzocht door het kwantificeren van verticale fluxen over het

rivierbed met behulp van warmte als tracer. Temperatuur-tijdreeksen werden verzameld op verschillende locaties in het rivierbed en dienden als input voor de LPML en LPMLE3 methoden, die worden gebruikt voor de schatting van de fluxen, en de thermische diffusiviteiten. Beide methodes werden hier voor het eerst toegepast voor gebruik in de hydrologie en berekenen 1D waterstroming en warmtetransport in het frequentiedomein. Terwijl de LPML methode het rivierbed beschouwd als een onderdeel van een homogene semi-oneindige halfruimte, kan met de LPMLE3 methode het rivierbed gedefinieerd worden als bestaande uit eindige subdomeinen, wat voordelig kan zijn in de kwantificering van fluxen in een meer heterogeen rivierbed. Beide methodes kunnen gebruik maken van meer spectrale informatie tijdens parameterschatting dan klassieke analysemethoden die alleen het dag-nacht (diel) signaal gebruiken. Periodieke, niet-periodieke en fout (error) signaalinformatie bevat in een temperatuur-tijdreeks worden geïsoleerd middels een lokale polynomiale methode, terwijl een maximum likelihood afschatter wordt gebruikt voor parameterschatting. Beide methoden kunnen ook informatie leveren over parameteronzekerheid alsmede informatie over modelkwaliteit. Eerst werden beide methoden uitgetest op synthetische data om hun gedrag onder gecontroleerde omstandigheden te bestuderen. Daarna werden temperatuurgegevens uit de Slootbeek gebruikt als input voor de parameterschatting. De kwantificering van fluxen voor verschillende periodes (winter, lente, zomer, op korte termijn, op lange termijn) op verschillende locaties van het rivierbed leverde gedetailleerde informatie op over de ruimtelijke en tijdelijke variabiliteit van fluxen voor de onderzochte riviersectie. Met de resultaten in combinatie met aanvullende informatie over de verticale hydraulische gradiënten, alsook waterpeilen in de aquifer en de rivier kon de lokale waterstroming in detail worden bestudeerd en tijdens een deel van de observatieperiode werd het bestaan van een flow-through systeem aangetoond.

(iii) De variabiliteit van de hydraulische geleidbaarheid van het rivierbed werd onderzocht voor een kleine riviersectie van de River Tern, UK. Eerder verzamelde en gezeefde bodemstalen van twaalf locaties in het rivierbed werden geclassificeerd en de hydraulische geleidbaarheid werd berekend voor elke bodemkernsectie met behulp van vier empirische standaard modellen (Beyer, Hazen, Kozeny-Köhler en USBR). Bij alle twaalf locaties werd de hydraulische geleidbaarheid ook bepaald op drie dieptes door analyse van data van eerder uitgevoerde falling head slug experimenten met een semi-analytische oplossing (Springer-Gelhar zoals geïmplementeerd in AQTESOLV). Ook werden variaties in anisotropie en rivierbeddikte bekeken. Met methodes uit de beschrijvende statistiek kon informatie over parameterdistributie en correlatie worden bekomen. Ook werd vastgesteld dat ondankshet vrij grote aantal aan waarden van hydraulische geleidbaarheid, meer geavanceerde geostatistische technieken zoals variogramanalyse niet konden worden toegepast om de ruimtelijke verdeling van de hydraulische geleidbaarheid van het rivierbed te beschrijven. In het algemeen vallen de hier bekomen resultaten van rivierbed hydraulische geleidbaarheden binnen het bereik bepaald in eerdere studies gedaan in gelijkaardige riviermilieus.

English Summary

Over the last two decades many scientific studies have been devoted to improve our understanding of the physical and biochemical processes occurring at the groundwater-surface water interface, also called the hyporheic zone. This zone is the saturated region connecting groundwater and surface water bodies in coupled groundwater-surface water systems. It derives its characteristics from the active mixing of groundwater and surface water, provides a habitat for interstitial organisms, a rooting zone for certain aquatic plants and a spawning ground for fish. Hydrological conditions determine the exchange of carbon, nutrients and energy between groundwater and surface water. Additionally, the HZ can act as a zone of natural attenuation for a variety of contaminants. The hyporheic zone is dynamic in space and time and parameters characterizing water flow and contaminant transformation processes are subject to considerable heterogeneity and uncertainty.

In this thesis, three key parameters are investigated that define many physical and biochemical processes in the hyporheic zone of lowland rivers; (i) rate coefficients determining biodegradation and the natural attenuation potential, (ii) exchange fluxes between groundwater, streambed and stream, and (iii) streambed hydraulic conductivities.

(i) The sequential reductive dechlorination of trichloroethene (TCE) and its daughter products 1,2 dichloroethene (cis-DCE) and vinylchloride (VC) in the presence of *Dehalococcoides mccartyi* was studied on streambed and aquifer sediment samples taken from the Zenne field site north of Brussels, Belgium that is heavily polluted with chlorinated aliphatic hydrocarbons. The dechlorination reaction was investigated by modeling First order, Michaelis-Menten and Monod kinetics using data from previously conducted microcosm experiments, in which dechlorination had been stimulated by adding various additional carbon sources as electron donors. For modeling the complex kinetic reactions a multi-objective evolutionary algorithm called AMALGAM was used for parameter estimation that employs several optimization algorithms simultaneously. Modeling results indicated that none of the discerned kinetics could approximate the entire microcosm experiments. First order and Michaelis-Menten kinetics could best approximate dechlorination towards the end of each microcosm test, while Monod kinetics could best approximate dechlorination at the beginning of each experiment where a lag time was present. The relation between *Dehalococcoides mccartyi* numbers and the optimized dechlorination parameters showed a large uncertainty and not even the inclusion of donor limitation would significantly improve the simulations. Results suggest that not all limiting factors had been included in the degradation rate coefficients of the different kinetics.

(ii) Groundwater-surface water interaction at the Slootbeek, a small sidearm of the River Aa in Belgium was studied by quantifying vertical exchange fluxes across the streambed using heat as a tracer. Temperature-time series were collected at several locations in the streambed and served as input to the LPML and LPMLE3 methods used for the estimation of fluxes, and

thermal diffusivities. Both methods were newly adapted to the field of hydrology and solve for 1D water flow and heat transport in the frequency domain. However, while the LPML method assumes the streambed to be part of a homogeneous semi-infinite halfspace, the LPMLE3 method allows for the definition of finite streambed subdomains and as such for the quantification of fluxes under more heterogeneous streambed conditions. Both methods can make use of more spectral information during parameter estimation than classical analytical methods that use only the diel signal. To separate periodic, non-periodic and error information contained in a temperature-time series a local polynomial method is applied, while a maximum likelihood estimator is utilized for parameter estimation. Both methods can also provide information on parameter uncertainty by using the covariance matrix as well as information regarding model quality through a cost function analysis. First, both methods were tested on synthetic data to study their behavior under controlled conditions. Afterwards, temperature data from the Slootbeek was used as input to quantify fluxes and thermal diffusivities. The quantification of fluxes for periods of different time length (winter, spring, summer, short-term, long-term) at several locations of the streambed provided detailed information on the spatial and temporal variability of fluxes for the investigated stream section. With the results as well as additional information on vertical hydraulic gradients, stream stage, and groundwater levels the local flow regime could be studied in detail and the existence of a flow-through system for parts of the observation period was uncovered.

(iii) The variability in streambed hydraulic conductivity was investigated for a small stream section of the River Tern, UK. Previously collected and sieved core samples from twelve locations in the streambed were classified and hydraulic conductivity for each core section was determined using four standard empirical models (Beyer, Hazen, Kozeny-Köhler and USBR). At all twelve locations, streambed hydraulic conductivity was also directly determined at three depths by analyzing data from previously conducted falling head slug tests with a semi-analytical solution (Springer-Gelhar as implemented in AQTESOLV) and by considering variations in anisotropy and streambed thickness. By means of descriptive statistics, information regarding parameter distribution and correlation could be delineated. It was also found that despite a relatively large sample size more advanced geostatistical techniques such as variogram analysis to delineate the spatial distribution of streambed hydraulic conductivity could not be applied. In general, results fall within the range of streambed hydraulic conductivities determined in previous studies for similar stream environments.

1 Introduction

This chapter is in part based on the following works:

1 **Schneidewind, U.** (2013): Contaminant transport and attenuation in the hyporheic zone of streams. *State of science report for ADVOCATE project. Grant agreement no. 265063.* 83 pages.

2 **Schneidewind, U.**, Joris, I. (2013): Modeling contaminant transport and attenuation in the hyporheic zone of streams – model guidance document. *Deliverable for ADVOCATE project. Grant agreement no. 265063.* 43 pages.

3 **Schneidewind, U**., Anibas, C., Joris, I., Seuntjens, P. (2015): Delineating Groundwater-Surface Water Interaction. *ADVOCATE Bulletin AB9, 9 pages, doi: 10.13140 /RG.2.1.2730.6405.*

In many countries the release of contaminants into surface water and groundwater bodies has deteriorated water quality as well as the functionality of aquatic and connected terrestrial ecosystems to an extent that statutory limits set in regulatory legislation such as the European Water Framework Directive (2000/60/EC) [*EU*, 2000] are difficult to meet. Without proper mitigation measures including concepts of sustainability and integrated water resource management, this deterioration will likely increase as population growth and intensified economic activities will put growing pressure on water as a resource [*UNESCO*, 2009]. To address these issues, researchers have started to consider connected surface water and groundwater bodies as coupled systems and over the last three decades an increasing number of studies [see *Krause et al.*, 2009a for a discussion] have been devoted to the understanding and characterization of the groundwater surface water interface, also called the hyporheic zone (HZ).

The delineation of groundwater-surface water (GW-SW) interaction has become an important aspect in the study of coupled groundwater-surface water systems. Interaction between aquifers and surface water compartments can be of (i) hydrological, (ii) geochemical or (iii) biological nature as extensively discussed in *Buss et al.* [2009 and references therein]. Reliable information regarding this interaction is essential in the study of the transport and fate of contaminants [*Conant*, 2004; *Gandy et al.*, 2007; *Lewandowski et al.*, 2011b; *Dujardin et al.*, 2014] and nutrients [*Krause et al.*, 2009b; *Smith et al.*, 2009; *Bardini et al.*, 2013; *Bartsch et al.*, 2014], for sustainable river management and restoration [*Woessner*, 2000; *Bukaveckas*, 2007; *Andersen and Acworth*, 2009; *Daniluk et al.*, 2013; *Käser et al.*, 2013] or for the determination of ecosystem characteristics [*Findlay*, 1995; *Allen et al.*, 2010; *Crossman et al.*, 2013] to delineate ecosystem services. Many processes in the HZ are

characterized by their variability in time and space [e.g. *Findlay*, 1995; *Brunke and Gonser*, 1997; *Fleckenstein et al.*, 2006]. They occur at different scales [*Poole et al.*, 2008; *Kikuchi et al.*, 2012] and are often subject to geologic heterogeneity [e.g. *Cardenas et al.*, 2004; *Fleckenstein et al.*, 2006; *Schmidt et al.*, 2006]. As such, the parameters quantifying these processes as well as the models used for their quantification are subject to uncertainty.

This first chapter conceptualizes the hyporheic zone (HZ, section 1.1) and shortly delineates predominant water flow and contaminant transport processes (sections 1.2 to 1.4) with a special focus on exchange flux, streambed hydraulic conductivity and natural attenuation. It then discusses options of mapping and monitoring hyporheic zone processes (section 1.5), specifically considering heat as a tracer. Afterwards, section 1.6 on modeling hyporheic zone processes shortly classifies model types, lists model codes and discusses some modeling applications. Section 1.7 discusses various types of uncertainty as a key aspect to flow and transport in the HZ. Section 1.8 focuses on spatial heterogeneity, while the remaining sections define the research question, major objectives, introduce the study areas and provide a further outline of the subsequent chapters.

1.1 The Hyporheic Zone Concept

1.1.1 Definition

The term hyporheic was used in the scientific literature early on by *Orghidan* [1959], who named the transition zone between streams and groundwater the ‘hyporheic biotope’. Until today, a single accepted definition of the term ‘hyporheic zone’ does not exist; rather do definitions reflect approaches and individual research questions addressed in various scientific disciplines like ecology, hydrology or hydrogeology. A detailed discussion regarding different definitions of the term ‘hyporheic zone’, can be found in *White* [1993], *Brunke and Gonser* [1997], *Smith* [2005] and *Boulton et al.* [2010]. This work adopts a rather broad and integrative definition from *Krause et al.* [2009a, page 2103] based on the 2008 European Geosciences Union (EGU) General Assembly session HS7.4:

“The hyporheic zone is the saturated transition zone between surface water and groundwater bodies that derives its specific physical and biogeochemical characteristics from active mixing of surface and groundwater to provide a habitat and refugia for obligate and facultative species”

The hyporheic zone (HZ) provides various ecological goods and services, which are summarized by *Buss et al.* [2009] and include the provision of a habitat for interstitial organisms, a rooting zone for certain aquatic plants and a spawning ground for fish. Hydrological conditions determine the exchange of carbon, nutrients and energy between groundwater and surface water. Additionally, the HZ can act as a zone of natural attenuation for a variety of pollutants. In a recent paper *Lewandowski et al.* [2015] revisited the terminology and discussed differences for streams, lakes and marine systems. This thesis only looks at the HZ between lowland streams and their connected aquifers.

1.1.2 Conceptualization

The conceptualization of the hyporheic zone used in literature varies with the scientific discipline. *Smith* [2005] distinguishes among conceptual HZ models used in **(i)** ecology, **(ii)** hydrology and **(iii)** hydrogeology as most of the current research articles on the HZ are presented within these three disciplines.

(i) In ecology the HZ is considered a dynamic ecotone between aquifer and stream [*Boulton et al.*, 1998; *Hancock et al.*, 2005; *Boulton et al.*, 2010], that can be found below the streambed succeeding the benthic zone, i.e. the lowest region of a stream including the top of the streambed [*Brunke and Gonser*, 1997]. The HZ extends into the adjacent stream banks (Figure 1.1) and shows characteristics of both, groundwater and surface water systems. Compared to the stream it demonstrates a deficit in dissolved oxygen and is described by low biodiversity and species density as well as slow biochemical processes [*Gibert et al.*, 1994].

(ii) In hydrogeology the HZ is often considered to be part of the aquifer as it contains mostly saturated sediments with interstitial spaces where considerable mixing of stream water and groundwater occurs under fully saturated conditions. Compared to the aquifer the HZ is rich in dissolved oxygen, organic carbon and biodiversity.

(iii) In hydrology the HZ is often considered an extension of the stream channel as streambed topography and morphology are mostly influenced by stream flow characteristics [*Smith*, 2005].

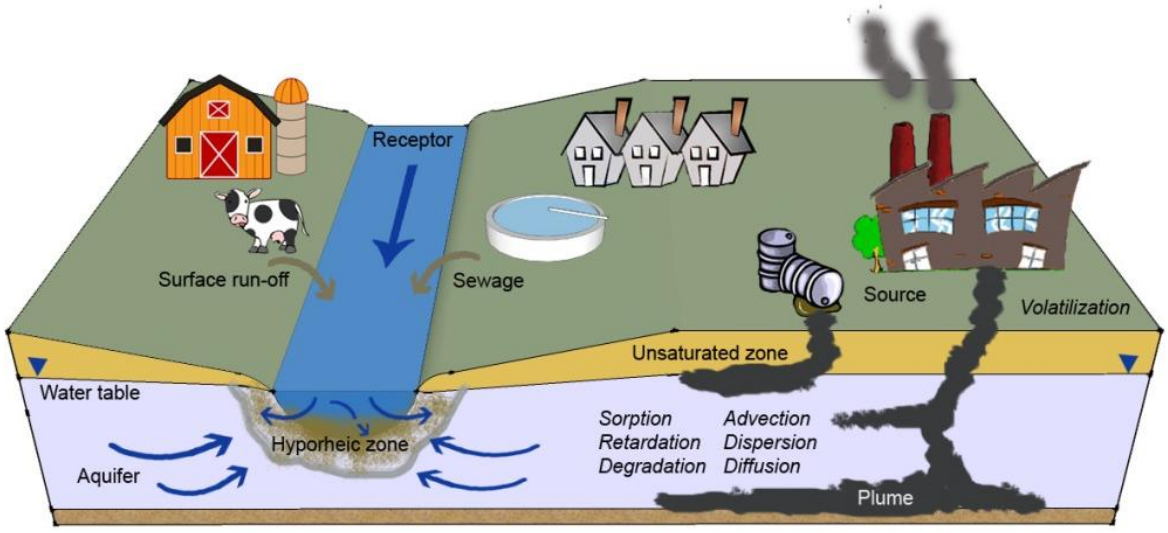

Figure 1.1: The hyporheic zone as the interface between a stream and its connected aquifer, where active mixing of surface water and groundwater occurs. Source: *own*.

Most of the early hyporheic zone research was conducted by scientists interested in the structure and functioning of riverine ecosystems [e.g. *Orghidan*, 1959; *Schwoerbel*, 1961; *Stanford and Gaufin*, 1974] and fish spawning [*Pollard*, 1955]. Consequently, various theoretical concepts were developed to relate the distribution of biota to (a) biogeochemical and hydrological gradients (e.g. river continuum concept [*Vannote et al.*, 1980] or hyporheic

corridor concept [*Stanford and Ward*, 1993]), to (b) the state of disturbance or deviation from equilibrium conditions (e.g. flood pulse concept [*Junk et al.*, 1989]) and to (c) different scales (e.g. catchment hierarchy concept [*Frissell et al.*, 1986]). These and additional concepts are in detail reviewed by *Ward et al.* [2002]. All of these concepts have in common that they assume nature as deterministic and spatially homogeneous on a small scale and none but the hyporheic corridor concept take a four-dimensional perspective (space and time). Recently, also the aspect of hydrological, biochemical and ecosystem connectivity has become of increased interest, as it is now by most researchers accepted that aquifer, hyporheic zone and surface water body form a connected system in a non-equilibrated state with various interactions taking place [*Boulton et al.*, 2010].

1.2 Water Flow in the Hyporheic Zone

1.2.1 General Characteristics

The HZ comprises a mix of stream water and groundwater. This mix is defined by the aquifer-stream connectivity. Similar to flow in aquifers [*Toth*, 1963], flow in the HZ has been envisioned along flow paths. As hyporheic flow paths originating from the stream and groundwater flow paths originating from the aquifer cross in the HZ, water and solutes are mixed and biogeochemical reactions can be stimulated. This often leads to multi-scale hyporheic flow and transport.

Boano et al. [2014] discuss general characteristics of water flow in the HZ and distinguish between five main flow mechanisms: **(i)** laminar flow defined by hydrostatic and hydrodynamic components of the hydraulic head, **(ii)** turbulent flow, **(iii)** flow induced by waves and tides, **(iv)** flow induced by biological processes and **(v)** flow induced by buoyant forces.

(i) Mostly, HZ flow is simply induced by differences in pressure head within the streambed or between stream, streambed and aquifer. Pressure heads can be hydrostatic or hydrodynamic [*Boano et al.*, 2014]. Whereas the former represents differences in the elevation of the overlying water column the latter is induced by stream flow over bedforms (i.e. periodic topographical features such as dunes and ripples) or around in-stream features, such as boulders, rocks or wood, during which a momentum transfer occurs. Depending on the pressure head differences, flow can occur from the stream to the aquifer (losing stream or infiltrating conditions), from the aquifer to the stream (gaining stream or exfiltrating conditions), horizontally parallel to the streambed or lateral to the streambed as so-called flow-through, as can be seen in Figure 1.2 [*Winter et al.*, 1998; *Woessner*, 2000]. If the groundwater level is sufficiently low, the stream can become effectively disconnected from the aquifer. An unsaturated zone will form underneath the streambed and the infiltration rate of stream water into the streambed and the unsaturated zone above the aquifer will eventually become constant representing the highest possible losing conditions. *Brunner et al.* [2009] revisited the conceptualization of a disconnected stream and developed and tested a method to assess the exact status of disconnection.

In general, most lowland streams in Central and Western Europe show alternating losing and gaining patterns at different spatial and temporal scales.

(ii) Turbulent flow in the HZ may occur in coarse-grained streambeds due to turbulence in the overlying water column. This turbulence is usually of low frequency and causes pressure fluctuations that penetrate into the uppermost part of the HZ. This can lead to non-linear effects that increase the flow resistance [*Barr*, 2001; *Packman et al.*, 2004; *Higashino and Stefan*, 2011].

(iii) In the stream environment, wave-induced and tidal flow mainly plays a role in coastal streams, or estuaries [*Higashino and Stefan*, 2011; *Boano et al.*, 2014]. Surface waves in streams, e.g. during flood events can also influence hyporheic flow [*Banzhaf and Scheytt*, 2009]. As streambed geomorphologic features are often subdued during flood events hyporheic flow due to hydrodynamic pressure head changes can increase with increasing stream velocity [*Boano et al.*, 2007]. Flood events can also lead to a temporary change in bedforms, in a way that hyporheic flow is increased [*Harvey et al.*, 2012].

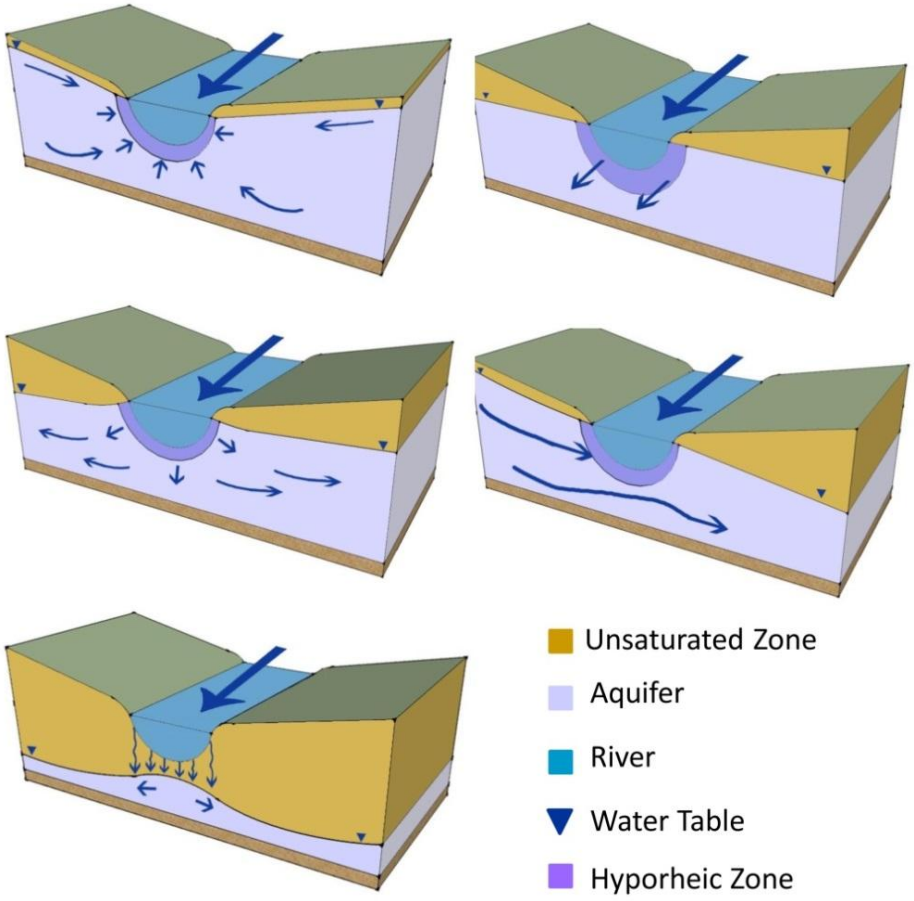

Figure 1.2: Stream-aquifer connections. Source: Modified after *Winter et al.* [1998] and *Woessner* [2000]. Top left: Gaining stream. Middle left: losing stream. Bottom left: Temporarily disconnected losing stream. Top right: Parallel flow. Bottom right: Flow-through.

(iv) HZ flow can be induced or influenced by a variety of biological activities. Plant roots, benthic organisms or certain fish reorganize the streambed sediment and create preferential

flow paths [*Jones and Mulholland*, 2000; *Tonina and Buffington*, 2009] while vertebrates like beavers can change stream channel characteristics [*Fanelli and Lautz*, 2008]. Additionally, the transpiration of in-stream or riparian vegetation can cause cyclic HZ flow patterns with more flow during the day or warmer periods and less flow during the night or colder periods [*Jones and Mulholland*, 2000; *Wondzell et al.*, 2010]. Microbial biofilms on sediments have been shown to increase the retention of water and suspended particles in the HZ and change the uptake behavior of organic molecules [*Battin et al.*, 2003].

(v) In slow flowing or standing waters buoyancy can induce free convection due to gradients in temperature or solute concentration [*Jin et al.*, 2011; *Boano et al.*, 2014].

1.2.2 Mathematical Description of Flow

Three-dimensional surface water flow in streams is commonly described by some form of the Navier-Stokes equation

$$\frac{\partial u}{\partial t} + u \cdot \nabla u = -\frac{\nabla p}{\rho_w} + \vartheta \nabla^2 u \tag{1-1}$$

where ρ_w [ML^{-3}] is the density of water, p [$ML^{-1}T^{-2}$] is the pressure, u [LT^{-1}] is the stream velocity, ϑ [L^2T] is the kinematic viscosity and t [T] is the time.

In case only one- or two-dimensional surface water flow is considered, a form of the de Saint-Venant equation is usually applied, the 1D case of which can be written as [*Yen and Tsai*, 2001]

$$\frac{\partial A}{\partial t} + \frac{\partial Q}{\partial x} = s_r - s_s \tag{1-2}$$

$$c_1 \frac{\partial Q}{gA\partial t} + c_2 \left\{ \frac{\partial}{gA\partial x}\left(\frac{Q^2}{A}\right) + \frac{1}{gA}\left[u_{rx}s_r - u_{sx}s_s - (s_r - s_s)\frac{Q}{A}\right]\right\} + c_3 \frac{\partial D_H}{\partial x} - c_4(m_0 - m_f) = 0 \tag{1-3}$$

where Q [L^3T^{-1}] is the flow discharge in the channel, A [L^2] is the channel cross-section, D_H [L] is the flow depth, s_r and s_s [L^2T^{-1}] are channel sinks and sources in terms of volume per unit length per unit time, m_0 and m_f [-] are channel friction slopes, g [LT^{-2}] is the acceleration due to gravity, u_{rx} and u_{sx} [LT^{-1}] are velocity components of sinks and sources in the *x*-direction [L], i.e. the direction along the channel and c_1 through c_4 [-] are so-called Boolean parameters. Depending on their value these Boolean parameters allow for Eq. (1-3) to be rewritten as the kinematic wave equation (c_1 to c_3 = 0, c_4 = 1), the diffusion wave equation ($c_{1,2}$ = 0, $c_{3,4}$ = 1), the gravity wave equation (c_1 to c_3 = 1, c_4 = 0) or the dynamic wave equation (c_1 to c_4 = 1), which are also further discussed by *Furman* [2008].

Flow through the streambed can be considered as flow through a porous medium. Laminar flow can then be represented by the linear parabolic aquifer equation Eq. (1-4) or the non-linear Richards equation Eq. (1-5) that takes into account unsaturated flow and hysteretic effects, i.e. a dependence on past states of the system under consideration.

$$S_s \frac{\partial h}{\partial t} = \nabla \cdot (K \nabla h) + s \tag{1-4}$$

$$\frac{\partial \theta}{\partial t} = \nabla \cdot [D_w(\theta) \cdot \nabla \theta] + \nabla \cdot [K(\theta) \cdot \nabla z] \tag{1-5}$$

Here, s is the source/sink term [LT^{-1}], K [LT^{-1}] is the hydraulic conductivity, h [L] is the hydraulic head, z [L] is the elevation, S_s [-] is the specific storage, θ [-] represents the volumetric water content and D_w [L^2T] is the moisture diffusivity. The basis for both equations is formed by Darcy's law [*Darcy*, 1856], which can be considered a reduced averaged Navier-Stokes equation [*Bear and Cheng*, 2010]. It is written as

$$q_D = \frac{Q_L}{A} = -Ki \tag{1-6}$$

Here q_D [LT^{-1}] is the specific discharge or Darcy flux with Q_L [L^3T^{-1}] as the flow rate of water in the hyporheic zone crossing area A [L^2] and i [-] is the hydraulic gradient. Eq. (1-6) can be extended by the Brinkmann term to account for interface flow between a porous medium and a free water phase as shown by *Bear and Cheng* [2010] (eq. 4.3.7, page 149) then reading

$$q_D + \mu_e \frac{k}{\mu} \nabla^2 q_D = -Ki \tag{1-7}$$

where μ is the dynamic viscosity [$ML^{-1}T^{-1}$] and k [L^2] is the intrinsic permeability (see a discussion in *Nield* [2000]). The effective dynamic viscosity μ_e [$ML^{-1}T^{-1}$] is defined as $\mu_e = \frac{\mu}{\tau n}$ with n [-] as the porosity and τ [-] as the tortuosity.

Darcy's Law is only applicable in saturated sediments and for laminar flow conditions. Non-Darcian flow in saturated sediments may occur under more turbulent conditions (and higher velocities), for example in coarse grained environments, in point bar and riffle structures, near artificial hydraulic structures or in filter beds. Whether flow is laminar or turbulent is defined by the Reynolds number Re, with the transition between both flow types commonly occurring at Re = 2000 in pipes, open channels or conduits. However, in porous media Darcy's law is considered strictly valid only for Re < 1-10 [*Fetter*, 2001; *Bear and Cheng*, 2010]. In a modeling study *Higashino and Stefan* [2011] found that pressure differences caused by turbulent flow become only significant if $K > 10$ cm s^{-1}.

In sandy streambeds that are covered by bedforms q_D can depend to a large part on the hydrodynamic pressure head at these bedforms. Here q_D can be assessed by using the wave number of the bedform and information from the sinusoidal head distribution at the streambed surface [*Packman and Salehin*, 2003]. *Boano et al.* [2010] quantify the exchange flux using an analytical first-order model that considers variations in streambed topography, stream sinuosity and meander wave number.

The hydraulic conductivity K depends on the properties of the subsurface sediment as well as on the properties of the fluid flowing through the HZ, i.e. usually water. It can be represented by (see Bear and Cheng [2010], page 118/119)

$$K = k\frac{\rho_w g}{\mu} \tag{1-8}$$

Here, K depends on the density of water ρ_w [ML^{-3}] and the dynamic viscosity μ [$ML^{-1}T^{-1}$], both in turn depending on the local temperature. The average linear flow velocity of water in the HZ v [LT^{-1}] can then be described as

$$v = \frac{q_D}{n_e} \tag{1-9}$$

where n_e [-] is the effective porosity. Connections between the variables above as well as other forms of the equations presented here that include e.g. turbulent or multi-phase (variable density) flow or flow in macropores can be found in many textbooks on hydrology/hydrogeology [e.g. *Freeze and Cherry*, 1979; *Fetter*, 2001; *Bear and Cheng*, 2010].

1.2.3 Exchange Flux

One essential parameter describing GW-SW interaction, flow and transport in the HZ is the Darcy flux or specific discharge q_D, i.e.flow per unit area. The value of q_D usually forms an upper limit to the exchange of dissolved non-reactive contaminants between streams and aquifers. Additionally, it influences the availability of oxygen and promotes more aerobic or anaerobic conditions. The flux between the stream, streambed and aquifer compartments is called exchange flux (EF) and contains two components (a) hyporheic exchange flux (HEF) and (b) groundwater-surface water exchange flux (GSEF) [*Hannah et al.*, 2009]. HEF is stream water entering the HZ upstream and leaving it at some point downstream, It is mostly caused by hydrodynamic pressure head changes and turbulent flow (chapter 1.2.1). GSEF is aquifer water entering the stream or vice versa and as such being the net gain or loss of the stream. EF and net flux only equal if solely vertical flow occurred in the HZ, which rarely is the case [*Buss et al.*, 2009].

However, distinguishing between HEF and GSEF is difficult and for practical reasons in most studies both are lumped together. Direction, magnitude and variability of EFs determine the

transport of energy, water, solutes and suspended matter, define sorption and degradation processes, chemical reaction rates, microbial growth and influence the HZ ecosystem [*Jones and Mulholland*, 2000]. EF can vary due to natural and anthropogenic factors (Figure 1.3); in space from the millimeter to the kilometer scale [*Elliott and Brooks*, 1997a; *Tonina and Buffington*, 2007; *Poole et al.*, 2008; *Boano et al.*, 2014] and in time from seconds to years [*Stanford and Ward*, 1988; *Harvey and Wagner*, 2000; *Boano et al.*, 2006]. Many of these factors are also variable in space and time.

Water flow in the HZ is a multi-scale problem and commonly three distinct scales are studied: **(i)** the catchment scale, **(ii)** the reach scale and **(iii)** the sediment scale.

(i) At the catchment scale, one can often find downwelling conditions in the upper stream reaches due to unsaturated subsurface conditions resulting in losing or disconnected streams that are often perched or ephemeral. In mid-reaches groundwater contribution to stream flow (baseflow) increases and streams are mostly gaining and perennial. In lower reaches hydraulic gradients are often small and more parallel flow occurs resulting in less net exchange flux. However, this flow behavior strongly depends on local topography. Stream flow and bedform are influenced by catchment scale runoff and drainage processes determining sediment and organic matter load as well as basin-channel connectivity.

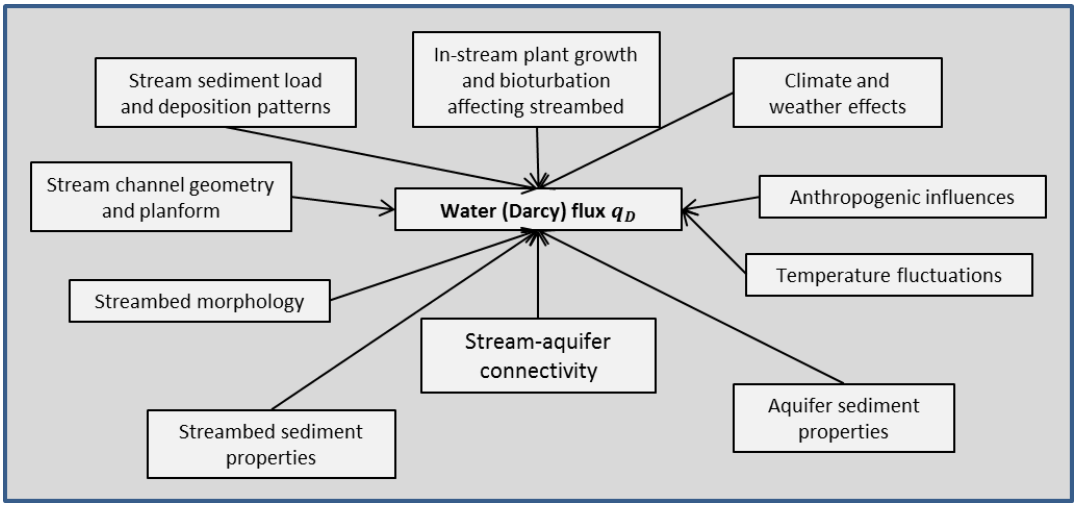

Figure 1.3: Factors influencing exchange flow (flux) in and across the hyporheic zone. Source: *own.*

In general, stream sediment depositional patterns lead to an accumulation of more coarse-grained sediments like pebbles and gravel in the upper reaches while in the lower reaches the sediment bed structure is mostly defined by fine sands, silts and higher organic matter content. These depositional patterns are mainly caused by changes in the longitudinal hydraulic gradient, that decreases downstream as well as by channel geometry and planform [*Buss et al.*, 2009].

(ii) At the reach scale (from 1 m to several 10 m) flow conditions vary depending on stream width to depth ratio, wetted perimeter, streambed sediment structure, channel planform, streambed morphology as well as local characteristics of the connected aquifer and

hydrostatic pressure conditions [*Buss et al.*, 2009]. Flow conditions are more effluent, when the stream width to depth ratio becomes smaller or when streams follow an increasingly meandering or sinuous path. Regional and local climatic conditions may influence reach-scale flow patterns, e.g. through the occurrence of heavy rainfall, which can cause local inundation and subsequent recharge of the surrounding floodplain sediments leading to changes in hydraulic head differences between aquifer and stream. Streambed sediment structure (that also acts on the sediment scale) defines hydraulic conductivity and the behavior of local flow paths [*Ellis et al.*, 2007]. EFs can also be caused by stream bank structures (bars) reaching into the channel and changing local hydrostatic pressure conditions. Streambed morphology influences exchange flows and discharge patterns mainly by pool-riffle sequences [*Tonina and Buffington*, 2007]. At local elevation highs in the streambed, water tends to flow downwards (downwelling zones), passing through the streambed sediments and exiting at local elevation lows (upwelling zones).

(iii) At the sediment scale (<1 m), flow patterns are mainly defined by sediment physical properties. Grain size, shape and packing directly influence permeability and hydraulic conductivity, leading to the formation of preferential pathways. Given a sufficient pore throat width, a larger sediment surface area to volume ratio could increase microbial growth, which in turn leads to a reduction in local porosity and hydraulic conductivity as biofilm and gas produced may decrease pore space [*Buss et al.*, 2005]. Flow patterns at sediment and reach scale can also be influenced by small-scale geomorphologic features (bedforms) such as dunes, ripples or simply by objects acting as obstacles like wood, pebbles, litter or anthropogenic features that change the hydrodynamic pressure head components. The size of bedforms is closely related to stream size and flow rates [*Boano et al.*, 2014].

Minor factors influencing exchange flow at sediment and reach scales include daily and seasonal temperature variations, which directly affect fluid density, viscosity and thus the hydraulic conductivity of the HZ. An increase in water temperature from e.g. 10 °C to 12 °C would lead to a decrease in kinematic viscosity by 6 % and a slight increase in hydraulic conductivity and flux. This effect would presumably however only be of importance in shallow streams exposed to strong daily or seasonal temperature fluctuations, where the streambed would also be strongly heated by direct radiation from the sun.

Stream sediment load can play a crucial role as sediments can be deposited on top of the streambed by gravitational settling (depending on grain size and flocculation capability) and thus alter streambed morphology. Non-settable particles (colloids) can enter the streambed by turbulent flow and by advection. This process is called colmation [*Brunke and Gonser*, 1997], and can induce clogging of the HZ by reducing the available pore space [*Sear et al.*, 2008]. Clogging can also be caused by the precipitation of oxidized metals [see *Boano et al.*, 2014 for a review]. Sediment deposition can also be affected by vegetation growth, which often varies seasonally. In areas with dense vegetation, flow velocities are reduced and finer sediments can settle forming local low permeability areas with increased organic matter content. Flow patterns can be influenced by bioturbation, i.e. the destruction or alteration of natural sediment structures by aquatic plants rooting in the streambed as well as by animals.

Changing water volumes and flow velocities as well as increased turbulent flow in the stream channel on the other hand can cause bedforms to move leading to the erosion of the colmated layer and thereby also changing local permeability patterns.

Climate can influence EFs via changing pressure heads in aquifers and stream stages. The HZ can change in its size with wet and dry seasons [*Harvey et al.*, 1996]. Snowmelt or evapotranspiration changes in in-stream and riparian vegetation can also impact hyporheic flow [*Wondzell et al.*, 2010].

Anthropogenic influences include stream channel engineering procedures and landuse. A canalization of a stream leads to a loss in connectivity with the aquifer and to changes in stream velocity, sediment load, sedimentation processes and finally hydraulic properties. Landuse procedures influence recharge and drainage patterns, sediment and contaminant load in the stream and the connected aquifer, and as such sedimentation processes and hydraulic properties.

1.2.4 Streambed Hydraulic Conductivity

In unconsolidated porous media hydraulic conductivity can be considered as a primary control on subsurface flow and transport of non-sorbing solutes [*Dagan*, 1986, 1989; *Koltermann and Gorelick*, 1996]. Variations in *K* directly affect other parameters such as exchange flux (flow paths), velocity and dispersion behavior of solutes. This holds true for aquifers as well as for the hyporheic zone. As shown in Eq. (1-8) and Figure 1.4, streambed hydraulic conductivity depends on properties of **(i)** the fluid (e.g. density and viscosity), and **(ii)** the sediment/matrix (e.g. grain size, porosity). Both in turn are influenced by different factors (e.g. temperature) or processes (e.g. microbial activity in the streambed) that act on different spatial and temporal scales and are also often interconnected. Streambed sediments are formed by (very) slow-acting geological processes like tectonics, diagenesis, deposition and deformation that define the sediment matrix as well as by more rapidly acting sedimentological processes related to hydrological activity (streamflow, stream-aquifer interaction), such as colmation, erosion and bioturbation that exert a bigger influence especially on the upper part of the streambed.

Exchange flow and streambed *K* are directly related and most of the factors determining EFs (Figure 1.3) described in the previous section do so by altering streambed *K*. In general, EFs potentially increase with increasing streambed hydraulic conductivity. On the other hand, increasing anisotropy in *K* can lead to a decrease in EFs as flow paths might be skewed away from the streambed. *Zlotnik et al.* [2011] investigated the role of anisotropy in streambed *K* at different scales by looking at the flushing intensity at different depths and showed that an increase in *K* with depth leads to a weaker influence of the local flow system on hyporheic flow. Streambed *K* has also been found to influence the composition and distribution of interstitial fauna [*Boulton et al.*, 1998; *Hancock et al.*, 2005; *Claret and Boulton*, 2009; *Boulton et al.*, 2010] and can be associated with long-term changes in riparian vegetation [*Webb and Leake*, 2006].

Values of streambed *K* can vary over several orders of magnitude for different stream environments (Table 5.1) and also depend on the method of assessment (discussed in detail in chapter 1.5). In a meta study, *Calver* [2001] reported *K* ranges from 8.64×10^{-5} to 8.64×10^{2} md^{-1} found in previous field and modeling studies. She highlighted that *K* ranges obtained from modeling studies are generally smaller than from field/lab studies, presumably due to spatial averaging in models. In many hydrogeological studies *K* is assumed to be log-normally distributed although no physical reason behind this assumption has been found so far [*de Marsily et al.*, 2005]. *Genereux et al.* [2008] reviewed previous studies on streambed *K* and concluded that it can indeed be log-normally distributed but they also found other studies where *K* followed normal or bi-modal distribution.

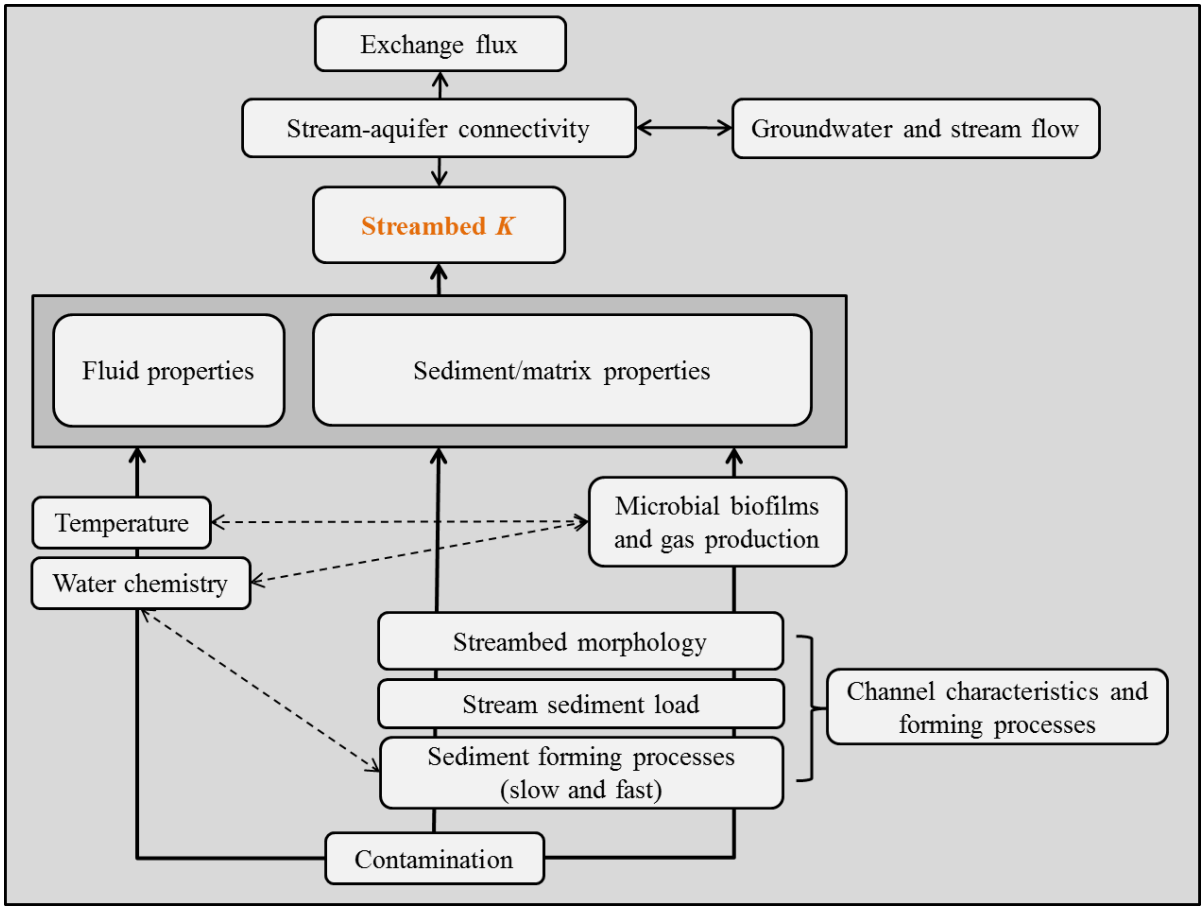

Figure 1.4: Parameters and Processes defining streambed hydraulic conductivity. Source: *own*.

1.3 Transport and Attenuation of Contaminants in the Hyporheic Zone

1.3.1 Natural Attenuation Processes

The attenuation of contaminants occurs under natural conditions by a variety of natural attenuation (NA) processes (Figure 1.5). In general, NA is defined as the degradation/removal of contaminants by various physical, chemical or biological processes that act in-situ and

without human intervention. During NA a reduction of contaminant mass, contaminant flux, concentration, volume, toxicity or mobility is aspired to meet certain remediation criteria that are defined by legislation [*Wiedemeier et al.*, 1998]. Whether natural attenuation may be applied as the sole remediation option at a contaminated site or only in combination with other remediation technique depends on a country's legislation. Either way, its effectiveness has to be properly demonstrated by designing a site-specific monitoring program showing (1) significant reduction in contaminant mass, flux or concentration, (2) a sufficient availability of nutrients and other compounds so that NA processes will continue and (3) microbial activity through which the contaminant is degraded [*Mulligan and Yong*, 2004]. This concept is called the 'three lines of evidence.'

NA processes can act destructively (i.e. transforming a contaminant) or non-destructively on a contaminant, depending on its physico-chemical characteristics as well as environmental conditions. Destructive processes include biodegradation and (photo)chemical (abiotic) transformation. Non-destructive processes include diffusion, dispersion, volatilization, and sorption [*Wiedemeier et al.*, 1998; *Khan et al.*, 2004; *Gandy et al.*, 2007]. Other processes such as radioactive decay, stabilization or solidification commonly do not play a role in the hyporheic zone.

Diffusion results from density and concentration gradients, while hydromechanical dispersion is caused by a variability in v due to differences in pore size, increased frictional forces at grain surfaces and tortuous flow paths due to differences in grain shape and packing [see e.g. *Bear and Cheng*, 2010]. Both processes are often combined under the term hydrodynamic dispersion. Both processes eventually lead to a dilution of dissolved contaminants, i.e. the reduction of contaminant concentration by mixing of waters polluted to different degrees. The term sorption includes adsorption and absorption processes. During adsorption, contaminants (often inorganic) adsorb to the outside of the surface of the soil grains. During absorption, contaminants (mostly hydrophobic organic) are absorbed within the organic coatings of the sediment. Desorption is the detachment and remobilization of the sorbed contaminants. Sorption depends mostly on physicochemical characteristics of the respective contaminant, natural flow conditions, pore water chemistry and properties of the sediment grains. An increase in clay (increased negative charge) and organic matter content for example increases the HZ sediment sorption capacity as shown by *Younger et al.* [1993] in studies on the River Thames. The change of surface properties due to sorption also leads to alterations in the deposition of fine particles/colloids [*Ren and Packman*, 2004b, a, 2005]. Sorption processes in the HZ have mostly been studied for heavy metals [see *Boano et al.*, 2014 for a review].

Sorption also influences the rate of contaminant volatilization, diffusion and leaching as well as biotic and abiotic transformation processes [*Alexander*, 1994]. During volatilization contaminants migrate from the liquid to the gas phase and are evaporated. Abiotic transformation processes include hydrolysis and other nucleophilic substitution and elimination reactions, redox reactions, direct and indirect photolysis. These processes are described in detail by *Schwarzenbach et al.* [2003]. Biotic transformation or biodegradation takes place when naturally occurring microorganisms (bacteria, viruses, fungi, algae and

protozoa) mediate contaminant break-down. Biodegradation can occur in the presence of oxygen (aerobic) and without oxygen (anaerobic). Its extent depends on contaminant chemistry (concentration, molecular structure, distribution), environmental conditions (e.g. temperature, the mixing behavior of water in the HZ defining the residence time; the availability of fine sediment), as well as characteristics (e.g. predominant metabolism) and abundance of the respective microorganism [*Riser-Roberts*, 1998]. Environmental conditions influence the availability of substrate (e.g. organic carbon), external electron donors or acceptors such as oxygen, sulfate, nitrate and others, and define whether biodegradation occurs aerobic or anaerobic. Microbial community structure is thus influenced by environmental conditions as well as contaminant chemistry and the growth of most microorganisms is strongly limited with substrate availability. In general, contaminants are degraded by microorganisms by two ways:

a. The contaminant is used by the microorganism as the primary food source (substrate) depending on its metabolism. The energy produced in such a reaction is used by the microorganism for growth.
b. The contaminant is degraded by means of enzymes that are produced by the microorganism during degradation of the primary substrate (co-metabolism) and cannot serve as the sole source of energy to the microorganism. The energy produced during co-metabolic processes cannot be used by the microorganism for further growth.

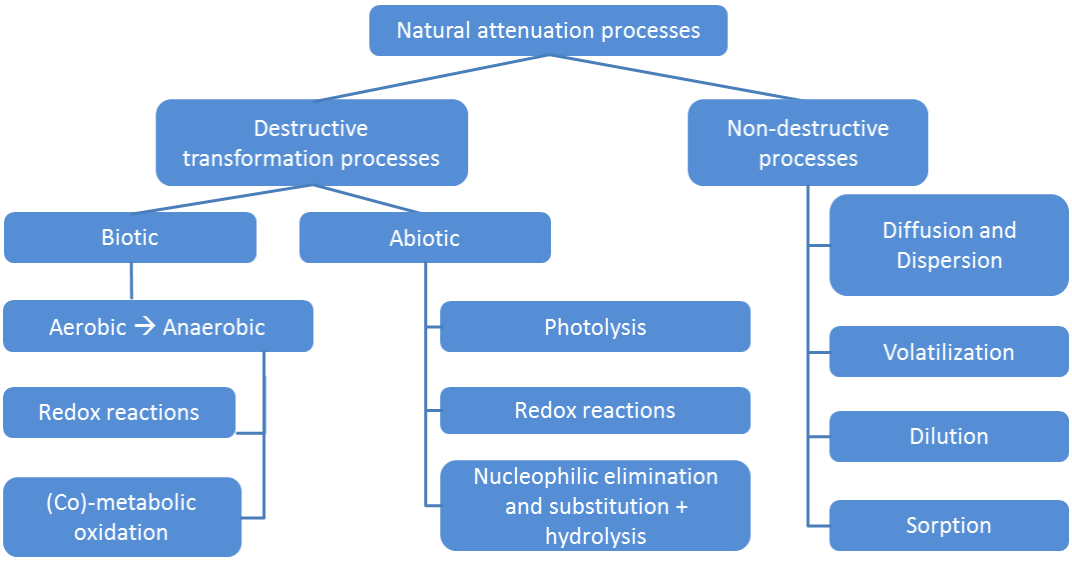

Figure 1.5: Common natural attenuation processes in the HZ. Source: *own.*

1.3.2 Transport Processes

Depending on their chemical characteristics contaminants can be present in the HZ in four phases; (i) the vapor phase, (ii) dissolved in water, (iii) as pure organic liquid (although not very common) and (iv) sorbed to the sediment. The degree of partitioning into each phase is

defined by a partition coefficient, i.e. the soil-water partition coefficient $K_d = \frac{C_b}{C_w}$ [L^3M^{-1}], the soil-gas partition coefficient $K_{bg} = \frac{C_b}{C_g} = \frac{K_d}{H}$ [L^3M^{-1}], Henry's constant (vapor phase) $H = \frac{C_g}{C_w}$ [-], log K_{ow} as the octanol-water coefficient (describing the partitioning between water and pure organic liquid) and the solubility in water. C_b, C_w and C_g [ML^{-3}] are the contaminant concentrations in the solid, aqueous and gas phases. The solubility is the mass of contaminant dissolved per volume of water.

Transport and attenuation processes of dissolved contaminants in the HZ are in principle similar to those occurring in aquifers. They can be represented by the advective-dispersive-reactive equation as shown in Eq. (1-10), which includes single-phase flow, single chemical species transport and equilibrium mass transfer reactions [*Miller et al.*, 2013].

$$n_e R \frac{\partial C}{\partial t} = \nabla \cdot (n_e D \cdot \nabla C) - \nabla \cdot (n_e v C) + n_e v_s C_s - \sum RP \tag{1-10}$$

Here R [-] is the retardation factor representing retarded transport due to sorption, v [LT^{-1}] is the fluid velocity, C [ML^{-3}] is the contaminant concentration, D [L^2T] is the dispersion coefficient, s indicates source/sink contributions and RP represents all reaction and mass transfer processes. Advection describes the movement of the dissolved contaminant through a unit area of porous medium in the longitudinal direction of v and becomes more pronounced in coarse grained more hydraulically conductive sediments. Hydrodynamic dispersion is the sum of diffusion processes and hydromechanical dispersion effects described in the previous section.

Formulas for multi-phase flow and multi-species transport as well as non-equilibrium behavior can be obtained from *Miller et al.* [2013] or a variety of textbooks [*Fetter*, 1999; *Zheng and Bennett*, 2002; *Bear and Cheng*, 2010]. The retardation factor can be calculated as

$$R = 1 + \frac{K_d \rho_b}{n_e} \tag{1-11}$$

with ρ_b [ML^{-3}] as the bulk density of the sediment. K_d can be described by a variety of sorption isotherms assuming equilibrium conditions, the use of which depends on the partitioning behavior of the contaminant as well as on the sorption capacity of the sediment and the speed of the sorption reaction. A comprehensive overview on various sorption isotherms can be found by *Zheng and Bennett* [2002].

The average contaminant transport velocity v_c [LT^{-1}] can then be estimated by $v_c = Rv$. The average time a dissolved contaminant effectively stays in the HZ is called the residence time t_R [T] and can be obtained via

$$t_R = \frac{n_e R V_0}{Q_L} \tag{1-12}$$

with Q_L [L^3T^{-1}] as the local discharge and V_0 [L^3] as the representative elementary volume, discussed in more detail in section 1.8. The concept of the distribution of residence time in HZs and its implications on HZ biogeochemistry is outlined in *Gomez et al.* [2012]. The average residence time of water in the HZ decreases with increasing hydraulic conductivity and can also be influenced by bedforms [*Boano et al.*, 2014]

An in-depth discussion of the mathematical representations of contaminant transport can be found by *Bear and Cheng* [2010], and *Zheng and Bennett* [2002]. Transport even more than flow is also highly dependent on heterogeneity and anisotropy of the subsurface material [*Engdahl and Weissmann*, 2010].

1.3.3 Natural Attenuation Capacity

The natural attenuation capacity (NAC) in the HZ is defined by a combination of water and contaminant residence time in the streambed, strong chemical gradients and a diverse microbial activity. It could be considered as the contaminant lowering capacity per meter flow path, similar to the definition given by *Chapelle and Bradley* [1998] for aquifers, although no official definition exists yet. The NAC can be assessed by evaluating the rate of each of the attenuation processes shown in Figure 1.5. As the rate of each process is site-specific and contaminant-specific the NAC has to be assessed for each case separately. *Newell et al.* [2002] distinguish among rate constants based on changes of contaminant concentration or mass over time at one specific point or along a path and biodegradation rate constants. Determining rate constants at one point versus time allows for an assessment of how fast remediation goals can be met. Rate constants versus distance allow for assessing plume behavior whereas biodegradation rates are used to estimate the effect of biodegradation on contaminant migration.

In many studies attenuation processes are assumed as simple first-order reactions with rate constants expressed in inverse time, often d^{-1}. *Newell et al.* [2002] and *Mulligan and Yong* [2004] provide extensive guidelines on how to determine each type of rate constant for first order reactions.

For biodegradation, the standard approach is to represent biological reactions by means of kinetic models. The most common kinetic models include first-order kinetics (1-13), Michaelis-Menten enzyme kinetics (1-14) with constant biomass concentration and Monod kinetics (1-15) that also takes into account microbial growth (1-16).

$$r_i = \lambda_i C_i \tag{1-13}$$

$$r_i = \frac{\lambda_i C_i}{K_{s,i} + C_i} \tag{1-14}$$

$$r_i = \frac{\lambda_i C_i X}{K_{s,i} + C_i} \tag{1-15}$$

$$r_X = \sum (Y_i r_i - bX) \tag{1-16}$$

Here r_i [$NL^{-3}T^{-1}$] is the species-dependent reaction rate, λ_i [different units] represents the rate coefficient (constant) of species i, C_i [NL^{-3}] is the species-dependent concentration, $K_{s,i}$ [NL^{-3}] is the species-dependent half-velocity constant, b [T^{-1}] is the cell decay rate, r_X [cells $T^{-1}L^{-3}$] is the net bacterial growth rate, Y_i [cells N^{-1}] is the species-dependent specific yield and X [cells L^{-3}] is the active microbial concentration. The reaction system depends on the contaminant as well as on the physico-chemical characteristics of the environment and a multitude of additional processes could be included into the kinetic models such as donor limitation, bacterial competition, inhibition and toxicity. These and others are described in the relevant literature [e.g. *Chambon et al.*, 2013]. Environmental conditions such as temperature also play an important role. A deeper insight is provided by *Bear and Cheng* [2010].

1.3.4 Variability in Rate Constants

In most remediation projects, rate constants are obtained from laboratory experiments, tracer tests (using a conservative tracer) or simple calculations using concentrations along flow paths under a steady state assumption. An assessment of plume extents and retention times is usually performed under the assumption of a uniform distribution and activity of subsurface microorganisms and averaged hydraulic properties. Although often sufficient in more homogeneous settings with little dynamics, rate constants defining the natural attenuation capacity in the hyporheic zone may vary significantly in space and time, much more than in aquifers. This is mostly due to varying characteristics of the water present in the HZ. Water quality parameters such as pH, temperature, electrical conductivity, dissolved oxygen content or dissolved and particulate organic matter differ in time and space for surface water and groundwater mixing in the HZ due to natural and anthropogenic effects, with dissolved oxygen (oxic → anoxic) and organic matter content usually declining across the HZ starting from the streambed top. As such, hotspots of variable biogeochemical activity are formed within the HZ, e.g. oxic/anoxic hotspots [*Lautz and Fanelli*, 2008].

Thus, these water quality parameters have a strong impact on redox zonation, which in turn influences microbial respiration and activity as well as biodegradation rates. Depending on the nature of the contaminant, type of microorganism and mode of biodegradation as well as available terminal electron acceptors a general redox zonation typically follows a sequence of (from the streambed top) oxygen reduction/aerobic respiration, denitrification, manganese

reduction, iron reduction, sulfate reduction and fermentation/methanogenesis. *Azadpour-Keeley et al.* [1999] provide an example of redox zonation for organic matter as well as a description of each of the processes involved.

Several studies have investigated the microbial community structure and distribution of unpolluted HZ sediments [*Fischer et al.*, 1996; *Findlay and Sinsabaugh*, 2006] as well as HZ sediments polluted with heavy metals [*Feris et al.*, 2003; *Feris et al.*, 2004], nitrate [*Iribar et al.*, 2008] or chlorinated ethenes [*Hamonts*, 2009; *Hamonts et al.*, 2014].

Although hydrodynamics and processes such as colmation have been related to microbial activity and sediment biofilm architecture [*Blenkinsopp and Lock*, 1994; *Battin and Sengschmitt*, 1999] and it is generally accepted that there exist biogeochemical hotspots within the HZ [*Claret and Boulton*, 2009]. However, studies relating the effects of variable hydraulic parameters to the natural attenuation potential in the HZ are scarce. *Claret and Boulton* [2009] related ranked K to gradients in microbial activity (looking at total organic matter, hydrolytic and dehydrogenase activity) and physicochemical variables (dissolved oxygen, electrical conductivity) along longitudinal flow paths at the Never Never River in Australia and confirmed that a higher K leads to shallower gradients in microbial activity and biogeochemistry, which might be expected as contact time of water (residence time) with the streambed sediment is reduced.

Variability/heterogeneity in HZ biogeochemistry parameters occurs not only in the form of hotspots but also at the scale of microenvironments such as individual grains and bacterial cells [*Boano et al.*, 2014]. However, such level of complexity has not yet been studied well and the fundamental processes at such scales are not yet well understood.

1.4 Coupled Water Flow and Heat Transport in the Hyporheic Zone

Heat transport through a saturated porous medium such as a streambed can occur by the processes of convection and conduction. Convection can be either forced or free. Forced convection of heat is caused by water flow through the pores, which occurs in most cases due to local or regional differences in the pressure gradient. Free convection occurs due to temperature-induced density and viscosity differences or salinity gradients but does not play a role in this work. Conduction follows Fourier's law [*Fourier*, 1822] and occurs either as molecular diffusion within the water filling the pore space or as heat exchange between (due to temperature gradients) solids or the solid and the liquid phase of the saturated streambed [*Anderson*, 2005; *Bons et al.*, 2013; *Rau et al.*, 2014]. The combined convective-conductive transport of heat through a saturated porous medium can then be written as

$$\frac{\partial T}{\partial t} = \nabla \cdot (D_T \nabla T) - v_T \nabla T \tag{1-17}$$

where T [Θ] is the temperature varying over time t [T], while v_T [LT^{-1}] represents the thermal front velocity based on convective processes and D_T [L^2 T^{-1}] denotes the thermal dispersion coefficient or diffusivity. The thermal front velocity is

$$v_T = q_T \frac{\rho_w c_w}{\rho c} \tag{1-18}$$

with q_T [LT^{-1}] as the exchange flux or specific discharge. It is essentially the same as the Darcy flux q_D (chapter 1.2) although in practice deviations occur due to different methods of assessment. In Eq. (1-18) $\rho_w c_w$ and ρc [$ML^{-1}T^{-2}\Theta^{-1}$] are the volumetric heat capacities of water and the water-sediment mixture, respectively. In general, a volumetric heat capacity is the product of the density ρ [ML^{-3}] of a substance and its specific heat capacity c [$L^2MT^{-2}\Theta^{-1}$], i.e. the amount of heat required to raise a unit mass of a substance by 1 K. Through the total porosity n these volumetric heat capacities are linked to that of the solids $\rho_s c_s$ via

$$\rho c = n\rho_w c_w + (1-n)\rho_s c_s \tag{1-19}$$

Similar to solute transport, heat transport is subject to diffusion. The thermal diffusivity denotes as

$$D_T = \frac{\kappa}{\rho c} \tag{1-20}$$

with κ [$MLT^{-3}\Theta^{-1}$] as the bulk or effective thermal conductivity linking the thermal conductivity of water κ_w to that of the solids κ_s. In general, the bulk thermal conductivity can depend on the porosity or water content, mineral type, grain size distribution as well as on structure effects, i.e. grain shape and the degree of cementation [*Côté and Konrad*, 2009]. However, from laboratory experiments *Côté and Konrad* [2009] concluded that structure effects seem to be negligible for ratios of $\kappa_s/\kappa_w < 15$, which holds true for most saturated streambeds. Various empirical and semi-empirical approaches relating κ to κ_w and κ_s have been discussed in the literature [e.g. *Woodside and Messmer*, 1961; *Cote and Konrad*, 2005; *Côté and Konrad*, 2009; *Tarnawski et al.*, 2011]. The most common approach used when describing heat transport through saturated sedimentary deposits so far seems to be to a geometric mean model [e.g. *Cote and Konrad*, 2005; *Rau et al.*, 2014] where

$$\kappa = \kappa_w^n \kappa_s^{(1-n)} \tag{1-21}$$

An alternative approach is given by *Anderson* [2005] and *Tarnawski et al.* [2011] based on the series-parallel model put forward by *Woodside and Messmer* [1961] with

$$\kappa = n\kappa_w + (1-n)\kappa_s \tag{1-22}$$

For the range of thermal conductivities found in laboratory experiments for fluvial and alluvial deposits (Table 1.1) the difference between both models is very small.

In general, measuring κ is relatively complex. Mostly, needle probes are applied in the field or the laboratory. These probes inject a current into the sample and relate thermal conductivity to the measured electrical conductivity. However, a world-wide accepted standard for these probes and how to interpret the probe-sample response data does not exist. These problems are partly solved by a verification of probe performance against reference materials, which however are also not always standardized.

Similar to solute transport a dimensionless number, in this case the thermal Péclet number Pe_T can be defined that relates conductive to convective heat transport as [e.g. *Anderson*, 2005]

$$Pe_T = \frac{\rho_w c_w}{\kappa} q_T L \tag{1-23}$$

with L [L] as the characteristic length, over which heat transport is considered. For $Pe_T > 1$ convective heat transport dominates over the conductive one and vice versa. According to *Bons et al.* [2013] and *Rau et al.* [2014], L is usually chosen as the average grain size diameter. While purely conductive heat transport can occur in low permeability sediments, the importance of convection increases with increasing permeability and velocity v of water in the streambed.

Eq. (1-20) can be expanded to include thermal dispersion due to the movement of water (forced convection) then reading [*Roshan et al.*, 2012]

$$D_T = \frac{\kappa}{\rho c} + f(\psi, q_T) \tag{1-24}$$

where f is a function based on the thermal dispersivity ψ [L] and the specific discharge. In many studies [e.g. *de Marsily*, 1986; *Anderson*, 2005; *Rau et al.*, 2010; *Vandenbohede and Lebbe*, 2010] this function is assumed linear. *Rau et al.* [2012b] conducted heat and solute tracer experiments in uniform coarse sand in the laboratory and deduced a quadratic function for the right term in Eq. (1-24). They also found that for their material, ψ can be neglected for $Pe_T < 0.5$. The significance of ψ on total heat dispersion at different spatial scales is an ongoing dispute in the scientific literature [e.g. *de Marsily*, 1986; *Hopmans et al.*, 2002; *Anderson*, 2005; *Vandenbohede et al.*, 2009; *Rau et al.*, 2014; *Irvine et al.*, 2015a]. In this thesis the author chooses to follow the study of *Anderson* [2005] and references therein and assumes the contribution of ψ to the total value of D_T negligible.

Rau et al. [2012b] also confirmed in their experiments earlier assumptions that conductive heat transport is faster than solute diffusion [*de Marsily*, 1986; *Anderson*, 2005] and that convective heat transport is retarded compared to advective solute transport. The thermal retardation factor R_T [-] with respect to q_T is then [*Vandenbohede and Lebbe*, 2010]

$$R_T = \frac{\rho c}{\rho_w c_w} \tag{1-25}$$

Thus, for the same water flux, Péclet numbers for solute and heat transport can vary significantly. In their laboratory experiments [*Rau et al.*, 2012b] found a difference in both Péclet numbers of up to several orders of magnitude and showed that heat transport can be dominated by conduction while solute transport is dominated by advection.

Table 1.1: Thermal properties of selected single phases and soils based on a meta-study of *Stonestrom and Constantz* [2003 and references therein]. Thermal properties of selected minerals can be found in *Cote and Konrad* [2005].

Single Phase	(Bulk) Density [10^6 gm^{-3}]	Porosity [-]	Water saturation	Volumetric heat capacity [10^6 Jm^{-3} °C^{-1}]	Thermal conductivity [Wm^{-1}°C^{-1}]	Thermal diffusivity [10^{-6}m^{2}s^{-1}]
Air	0.001			0.001	0.024	19
Liquid water	1			4.2	0.6	0.14
Ice	0.9			1.9	2.2	1.2
Quartz	2.7			1.9	8.4	4.3
Average soil minerals	2.7			1.9	2.9	1.5
Average clay minerals	2.7			2	2.9	1.5
Average soil organic matter	1.3			2.5	0.25	0.1
Porous Medium						
Sand	1.83	0.31	saturated	2.6	2.2	0.85
Sandy loam	1.38	0.48	saturated	3.2	1.8	0.55
Clay loam	1.21	0.54	saturated	3.2	1.4	0.42
Sand	1.5	0.43	dry	1.3	0.25	0.18
Silt loam	1.3	0.51	dry	1.1	0.26	0.23
Clay	1.16	0.56	dry	1.2	0.18	0.15

Heat transport as represented in Eq. (1-17) assumes local thermal equilibrium (LTE), i.e. at the boundary between the solid and liquid phase no temperature difference exists. For the slow flow velocities occurring in earth science applications this simplification seems justified as temperatures of both phases equilibrate quickly [*de Marsily*, 1986; *Bons et al.*, 2013; *Rau et al.*, 2014]. Remnants of the gas phase such as trapped air bubbles can be neglected. In principle, Eq. (1-17) is based on the idea of the representative elementary volume (REV) [*Bear and Cheng*, 2010]. Thermal properties of both phases are volume-averaged, an idea taken over from contaminant transport modeling [*Bear and Cheng*, 2010]. However, as most streambeds are heterogeneous environments and subject to thermal retardation in the solid phase as compared to the liquid phase, for larger pore velocities the assumption of a REV and LTE is increasingly violated. In a numerical modeling study *Roshan et al.* [2014] showed that the validity of LTE depends on the Reynolds number. For small Reynolds numbers ($Re < 0.01$) the assumption of LTE seems increasingly implausible. An alternative possibility, and

physically more correct, would then be to consider heat transport as a two-phase problem and couple the solid and liquid phase via a term representing thermal transfer through the boundary layer [e.g. *Levec and Carbonell*, 1985; *Kaviany*, 1995]. In this study, the idea of a REV is applied as the study site was a lowland stream with low flow velocities (chapter 3.5).

1.5 Mapping and Monitoring Hyporheic Zone Properties

Mapping and monitoring of HZ properties is commonly undertaken with the premise of understanding hydrological and/or biochemical characteristics of the HZ at various spatial and temporal scales. Sufficient data also allows for the study of processes by means of modeling [*Buss et al.*, 2009]. However, HZ parameters are dynamic in time and space and measurements at one scale are often not representative for a different one [*Williams*, 1984]. For example, hydraulic conductivity *K* would be one parameter that can differ at different spatial scales. As streambeds are often very dynamic environments, *K* can also vary in time, especially in the upper streambed layers that are influenced by colmation. The Darcy flux or exchange flux can also vary at sediment/reach scales in space and time. It is influenced by more regional factors (weather, ratio groundwater level/stream stage) as well as by very local factors such as streambed morphology. Other parameters showing a scale dependency include oxygen or carbon available in the streambed. They very much depend on the mixing behavior of surface water/groundwater in the hyporheic zone. The researcher's or manager's interest also plays a role as monitored parameters show different spatial gradients and thus do not always allow for an integrated consideration [*Bencala*, 1993]. To increase the degree of confidence in measured data and tackle the scaling issue, *Buss et al.* [2009] urge for a parallel use of point methods, lumped (average-based) methods and distributed methods whenever possible.

Common HZ properties determined by measuring and monitoring one or several parameters include **(i)** the structure and distribution of hyporheic fauna, **(ii)** geophysical properties, **(iii)** hydraulic properties, **(iv)** biogeochemical properties, and **(v)** streambed temperatures (chapter 1.5.3).

(i) Hyporheic fauna comprises microbes (bacteria, fungi, protozoa), micro-invertebrates (<50 µm in size), meio-invertebrates (50-1000 µm), macroinvertebrates (>1000 µm) and occasionally vertebrates using the HZ for reproduction and as a refugium [*Hancock et al.*, 2005; *Smith*, 2005]. Type and distribution of the hyporheic fauna (hyporheos) are determined by the specific hydrological and biochemical conditions in the HZ, including the availability of light, dissolved oxygen and organic matter (particulate and dissolved), mixing behavior of groundwater and surface water and subsequent contact time of water with streambed sediments as well as available pore space [*Ward et al.*, 1994; *Brunke and Gonser*, 1997; *Storey et al.*, 1999; *Malard et al.*, 2003; *Smith*, 2005]. Biodiversity commonly decreases with increasing depth and more anaerobic conditions.

(ii) Geophysical properties that help determine mixing patterns or groundwater discharge zone are commonly delineated with electrical resistivity tomography [*Harvey et al.*, 1997; *Acworth*

and Dasey, 2003; *Ward et al.*, 2010; *Cardenas and Markowski*, 2011]. Streambed lithology has been studied using geoelectrics [*Karan et al.*, 2013] and ground penetrating radar (GPR) [*Naegeli et al.*, 1996; *Brosten et al.*, 2009]. *Conant et al.* [2004] used GPR to describe for a reach of the Pine River, Canada subsurface lithology as well as the movement of a PCE plume in the subsurface. Both, GPR and methods based on electrical conductivity/resistivity are usually applied on the reach scale. On the catchment scale a use of these techniques would be possible via airborne measurement devices but the resolution would rapidly decrease. Using X-Rays similar to computer tomography is another potential technique to study flow paths in saturated sediments, mostly on the laboratory scale [*Beven and Germann*, 2013].

(iii) Delineation of hydraulic properties of the HZ includes determining parameters such as hydraulic gradient, hydraulic conductivity, porosity or grain size distribution. Additionally, EFs can be assessed by direct measurements or via a mass balance approach. *Kalbus et al.* [2006] and *Buss et al.* [2009] provide extensive reviews on measurement techniques adapted for hyporheic zone use for each of these parameters and discuss their advantages and limitations. These techniques are listed in Table 1.2, which includes a remark regarding the scale of application and additional literature sources.

The use of piezometers or monitoring wells in HZ research has been standard for many decades. Permanent or temporary piezometers/monitoring wells have been used to determine vertical and horizontal hydraulic gradients and water fluxes across the HZ via water level measurements [*Rosenberry and LaBaugh*, 2008]. They can also be used to conduct slug or pumping tests to determine hydraulic conductivity, to take water samples for the assessment of natural hydrochemical or biological parameters and of tracer tests. A dense network of multilevel monitoring wells can provide detailed information regarding the spatial and temporal variability of many subsurface parameters governing flow and transport [e.g. *Conant et al.*, 2004; *Rivett et al.*, 2008; *Schmidt et al.*, 2008].

In slug and bail tests a known volume of water or solid object is either introduced into or rapidly removed from a monitoring well and the subsequent water level response over time is measured. Depending on streambed and monitoring well properties a variety of analytical solutions exists [see *Butler*, 1998] that allow for a determination of hydraulic conductivity of the material along the filter screen. Grain size analyses are performed by dry/wet sieving of sediment samples. The application of one of the many existing empirical or semi-empirical analysis methods [see e.g. *Vienken and Dietrich*, 2011] then permits the determination of *K*. As during sieving the core samples are destroyed estimated *K* values do not necessarily represent actual *K* values on-site.

Classic permeameter tests are performed in the laboratory by enclosing a sediment sample between porous plates. Hydraulic conductivity is determined via Darcy's law either by applying a constant head to the soil sample and measuring steady throughflow or by measuring the head difference between two points over time (falling head test). Permeameter tests can also be conducted in-situ in the streambed by using standpipes of various shapes [*Hvorslev*, 1951; *Chen*, 2000]. Seepage meters serve in the direct quantification of exchange fluxes at the point scale. It is the only accepted method for determining seepage directly in the

field. Seepage meter designs range from simple half-barrels using a flexible plastic bag to capture seepage [*Lee*, 1977] to fully automated devices using heat-pulse [*Taniguchi and Fukuo*, 1993; *Taniguchi et al.*, 2003], electromagnetic [*Rosenberry and Morin*, 2004] or ultrasonic [*Paulsen et al.*, 2001] signals to measure discharge over time. Discussions on seepage meter design, handling and error sources are provided by *Rosenberry* [2008], and *Rosenberry and LaBaugh* [2008].

(iv) Hydrochemical parameters of interest in HZ studies include the pH value, redox potential and concentrations of dissolved oxygen and solids as well as of major ions, nutrients and contaminants in the pore water. Of additional interest can be geochemical parameters of the HZ sediment such as concentrations of sorbed contaminants, organic carbon content or cation exchange capacity as well as biochemical parameters such as metabolic rates that help to determine predominant contaminant attenuation processes. Table 1.3 summarizes common techniques applied to derive one or several of these parameters. These techniques are discussed in more detail by *Bridge* [2005], *Kalbus et al.* [2006], *Engelhardt et al.* [2011] and *Buss et al.* [2009].

Soil sampling is often used in conjunction with other sampling techniques to gain an insight into physical and biogeochemical processes governing flow and transport and contributing to natural attenuation of contaminants [*Bridge*, 2005]. Depending on the nature of investigation, different sampling techniques exist. If biochemical parameters are to be investigated one method applied frequently is the freeze coring technique where liquid nitrogen is used to freeze the soil column in the streambed and extract it for later analysis in the lab [*Buss et al.*, 2009]. For example, *Moser et al.* [2003] used extensive soil sampling to investigate biogeochemical processes in the HZ of the Columbia River at the Hanford site, USA. In contaminant transport and attenuation studies soil sampling is also often used to acquire material for microcosm studies or column tests [e.g. *Hamonts*, 2009; *Hamonts et al.*, 2009].

Experimental chambers are commonly used to study hyporheic metabolic rates. In its simplest form batch tests or microcosms use hyporheic zone sediment samples as substrate/reactant in laboratory experiments, e.g. to study the growth/decay of microorganisms and the attenuation of contaminants under controlled conditions [e.g. *Hamonts*, 2009, or as shown here in chapter 2]. More advanced chambers can be deployed in-situ in the streambed. These chambers are either pre-filled with substrate that afterwards reacts with the hyporheic environment or they just isolate a small part of the streambed for study under quasi-natural conditions [*Bridge*, 2005]. These in-situ chambers can be sampled for subsequent analysis in the lab or be equipped with in-situ measuring devices. If applied in-situ, these experimental chambers can become difficult to use when local flow regimes and biogeochemical conditions change, leading to erroneous estimates of metabolic rates [*Grimm and Fisher*, 1984; *Dodds and Brock*, 1998].

1.5.1 Tracer Tests

One of the main techniques to determine hydraulic and biochemical properties is the application of tracers. Tracer tests can aid in the delineation of flow paths in the stream and

the hyporheic zone, in the separation of streamflow components in the stream hydrograph and in the characterization of exchange fluxes between streams and aquifers. Typical conservative (i.e. non-reacting with streambed) tracers include saline solutes (NaCl, KCl, etc.) and fluorescent dyes (e.g. rhodamine). Environmental tracers include stable isotopes (^{18}O, ^{3}H or ^{2}H, ^{13}C, ^{15}N, ^{37}Cl and others), radioactive isotopes (^{222}Rn), electrical conductivity, pH, dissolved oxygen, heat or major ions (Cl^-, NO_3^-, etc.). Reactive and non-reactive tracers have been used to study the behavior of contaminants regarding their potential for retardation and transformation and to estimate residence times. *Triska et al.* [1989] co-injected nitrate and chloride into a reach of Little Lost Man Creek, CA to assess solute retention and nitrate transport through the HZ. *Fuller and Harvey* [2000] used bromide to study the uptake of several heavy metals in the HZ of Pinal Creek, AZ and found it to be most prominent in the first 15 cm of the streambed. *Jonsson et al.* [2003] studied hyporheic exchange and solute residence time using tritium and the reactive ($^{51}Cr(III)$) and noted that both tracers penetrated the HZ to different depths due to variations in sorption behavior. Other studies determined that in order to quantify EFs it were best to utilize a combination of tracers such as heat, chloride and electrical conductivity [*Cox et al.*, 2007] or heat, stable isotopes and various micropollutants [*Engelhardt et al.*, 2011]. Lately, stable isotopes have been increasingly used to prove the existence and trace the extent of natural attenuation in HZs receiving contaminated groundwater and to distinguish between attenuation processes such as dilution due to mixing of contaminated and uncontaminated water and biodegradation [*Kuhn et al.*, 2009]. The degree and rate of reductive dechlorination of chlorinated ethenes has been assessed by stable carbon ($^{13}C/^{12}C$) isotope analysis [*Hunkeler et al.*, 2005; *Abe et al.*, 2009; *Aeppli et al.*, 2010] or by combined carbon-chlorine isotope analysis ($^{13}C/^{37}Cl$) [*Hunkeler et al.*, 2011; *Badin et al.*, 2014]. The latter can distinguish between reductive dechlorination and aerobic oxidation processes. The degree of denitrification (uptake of NO_3^-) has been investigated using stable nitrogen isotopes ($^{15}N/^{14}N$) [*Böhlke et al.*, 2004] sometimes in combination with stable oxygen isotope ($^{18}O/^{16}O$) analysis [*Kaushal et al.*, 2011] or by nitrogen-oxygen isotope ($^{15}N/^{18}O$) analysis [*Buss et al.*, 2005]. $^{18}O/^{16}O$ isotope analysis has also been applied to distinguish groundwater-lake interactions [*Karan et al.*, 2014b], while *Engelhardt et al.* [2011] deduced groundwater-stream interaction from ^{2}H and ^{18}O analyses.

Table 1.2: Commonly mapped HZ hydraulic parameters and their assessment methods. Source: *own.*

Property	Assessment method	Explanation	Further literature	Scale
Water (Darcy) flux	Seepage meter measurements	Bag-type or automated seepage meters	*Rosenberry and LaBaugh* [2008]	Sediment
	Tests with conservative and environmental tracers	Artificial tracers such as fluorescent dyes and saline solutes or environmental tracers such as heat or stable & radioactive isotopes can be used.	*Berryman* [2005]	Reach
	Incremental streamflow	Determination of stream flow and discharge through subsequent cross sections.	*Harvey and Wagner* [2000]	Reach to catchment
	Hydrograph separation	Estimation of groundwater contribution to streamflow.	*Hornberger et al.* [1998]	Reach to catchment
Hydraulic gradient	Water level measurements in (multilevel) piezometers	Assessment of vertical and horizontal gradients possible, from which seepage can be determined.	*Rosenberry and LaBaugh* [2008]; *Buss et al.* [2009]	Sediment
Hydraulic conductivity *K*	Grain size analysis	*K* derived using empirical methods on sieved sediment samples.	*Vienken and Dietrich* [2011]	Sediment
	Pumping tests	*K* calculated from observations on water level drawdown and recovery in pumping and observation wells.	*Fetter* [2001]	Sediment to sub-reach
	Slug and bail tests	*K* determined from analyzing recovery of water level in piezometer after initial displacement.	*Butler* [1998]	Sediment
	Permeameter tests	*K* derived from constant or falling head tests applied on sediment samples.	*Freeze and Cherry* [1979]	Sediment

Property	Assessment method	Explanation	Further literature	Scale
	Constant head injection tests	*K* (horizontal) can be calculated from injection rate and test geometry.	*Cardenas and Zlotnik* [2003b]	Sediment
Porosity	Laboratory tests on sediment samples	Determined by relating dry mass to the total volume.	*Fetter* [2001]	Sediment
Flow velocity	In-situ tracer tests	Determined form travel time of tracer.	*Berryman* [2005]; *Buss et al.* [2009]	Reach

Table 1.3: Commonly mapped HZ hydro- and biochemical parameters and their assessment methods. Source: *own.*

Property	Assessment method	Explanation	Further literature	Scale
Concentration of solutes and phases	Grab samplers	Discrete sampling in surface water.	*Vrana et al.* [2005]	Sediment
	Passive samplers	Allow for diffusion and/or sorption of contaminants over time on filling material.	*Verreydt et al.* [2013]; *Verreydt et al.* [2010]; *Vrana et al.* [2005]	Sediment
	Reactive surface probes (thin films, gel probes)	Determine contaminant concentration, gradient and flux	*Bridge* [2005]	Sediment
	In-situ electrochemical sensors	A variety of optical sensors, electrodes and biosensors exists.	*Bridge* [2005]	Sediment to reach
	Integral pumping tests	Help to estimate contaminant plume discharge into stream along control planes.	*Bauer et al.* [2004]; *Kalbus et al.* [2007]; *Leschik et al.* [2009]	Sediment to sub-reach

Property	Assessment method	Explanation	Further literature	Scale
	Multilevel samplers and piezometers	Can be used for discrete sampling by means of pumps and packers or for deployment of sensors.	*Kalbus et al.* [2006]	Sediment
	Soil coring	Used to determine biogeochemical properties of sediments.	*Bridge* [2005]	Sediment
Reactivity	Tracer tests	Reactive tracers such as heavy metals can be used to determine sorption/retardation processes.	*Berryman* [2005]	Reach
	Reactive surface probes (redox gel probes)	Determine redox conditions	*Bridge* [2005]	Sediment
pH and redox potential	In-situ electrochemical sensors	A variety of electrodes exists.	*Bakker and Telting-Diaz* [2002]; *Bridge* [2005]; *Privett et al.* [2008]; *Tercier-Waeber and Taillefert* [2008]; *Vieweg et al.* [2013]	Sediment
Metabolic reaction rates	In-situ chambers	Use in-situ undisturbed sediments to simulate natural conditions.	*Bridge* [2005]	Sediment
	Microcosms	Prefilled with substrate.	*Bridge* [2005]	Sediment

1.5.2 Heat as a Tracer

Heat can be used as a tracer to study water flow in streambeds by measuring temperature differences between the top of the streambed (bottom of the overlying water column) and at some depth (vertical separation). Temperature differences in saturated streambeds are caused by the convection and conduction processes described in chapter 1.4. In streams with partially dry streambeds (ephemeral) or very shallow water levels, direct solar radiation onto the streambed can also strongly influence the temperature distribution [*Constantz*, 2008]. In general, a larger temperature gradient allows a temperature signal to penetrate deeper into the streambed before it is completely attenuated. Under natural flow conditions many stream and streambed temperature signals show a cyclic behavior, with the day-night (diel) and seasonal (summer-winter) cycles being the most prominent ones. The depth of signal propagation (in most streambeds only several 10 cm for the diel signal) depends also on the thermal parameters of the water-sediment mixture as well as on sediment properties (porosity, grain type, grain size distribution). The latter define water velocities through the streambed as well as the hydraulic connectivity between the stream, the HZ and the aquifer. In a losing stream a temperature signal starting at the streambed top penetrates deeper as convection and conduction processes both act essentially downwards. In a gaining stream, the upwelling of water of less variable temperature directs convection largely upwards (Figure 1.6). It should be noted that this is just a simple conceptual model of convection and conduction. Under natural conditions both processes act simultaneously in three dimensions on various scales leading to complex heat transport patterns. This complexity increases with streambed heterogeneity. Aside from a change in amplitude, a temperature signal also experiences a phase lag as it propagates through the streambed.

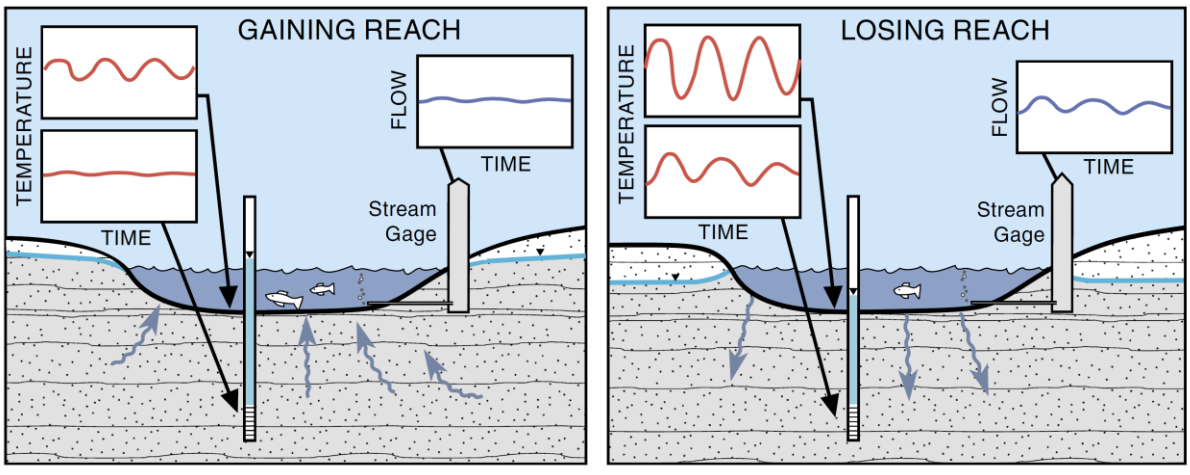

Figure 1.6: A temperature signal starting at the streambed top has a larger penetration depth for a losing reach (right) than for a gaining reach (left) before complete attenuation. In both cases the signal amplitude decreases and the signal experiences a phase shift. Source: *Stonestrom and Constantz* [2003]; *Rau et al.* [2014].

Researchers have been using stream and streambed temperatures to qualitatively delineate zones of GW-SW interaction [*Lapham*, 1989; *Bartolino and Niswonger*, 1999; *Alexander and*

Caissie, 2003; *Stonestrom and Constantz*, 2003]. Temperature envelopes have been constructed from periodic depth-dependent streambed temperature logs for daily and seasonal temperature cycles beneath a variety of streams. These temperature envelopes can be used to qualitatively distinguish downward from upward flux patterns (Figure 1.7).

Heat has been applied as a tracer in a vast number of quantitative HZ studies as outlined below:

(i) It has been used to quantify exchange fluxes for a variety of stream environments such as (a) streams exposed to tidal events [*Bianchin et al.*, 2010], (b) slow-flowing lowland streams [e.g. *Anibas et al.*, 2011; *Nützmann et al.*, 2014], (c) mountain streams [*Schmadel et al.*, 2014], (d) proglacial moraines [*Langston et al.*, 2013] or (e) ephemeral streams [*Constantz et al.*, 2001]. It has also been used to investigate flux patterns under extreme climatic conditions [*Bartsch et al.*, 2014] or during short-term extreme hydrologic events [*Barlow and Coupe*, 2009; *Karan et al.*, 2014a].

(ii) In several HZ studies, EFs deduced from temperature data have been compared to EFs deduced from other approaches such as vertical hydraulic gradients [*Fanelli and Lautz*, 2008; *Krause et al.*, 2011; *Krause et al.*, 2012], stream gauging [*Hatch et al.*, 2010] or hydrograph analysis [*McCallum et al.*, 2014]. Heat has also been jointly used with other tracers such as chloride [*Cox et al.*, 2007], stable isotopes [*Engelhardt et al.*, 2011], resazurin [*Gómez-Hernández et al.*, 1997] or water quality parameters including dissolved oxygen [*Schmidt et al.*, 2011], dissolved organic carbon [*Bartsch et al.*, 2014] or nitrate [*Karan et al.*, 2013].

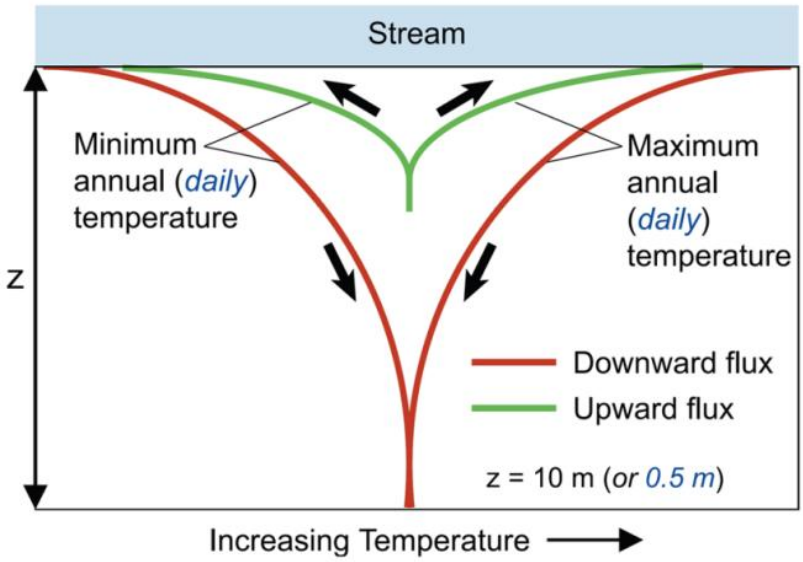

Figure 1.7: Hypothetical temperature envelopes for gaining (upward flux) and losing (downward flux) conditions. The daily temperature signal will have been completely attenuated quicker than the annual signal (e.g. at a depth of 0.5 m compared to 10 m). Source: *Constantz* [2008].

(iii) Other studies have focused on the quantification of EFs for different streambed morphological features and in-stream structures. *Daniluk et al.* [2013] used temperature data to calculate fluxes upstream and downstream of cross-vane structures (i.e. channel-spanning rock dams) in the framework of river restoration. *Gariglio et al.* [2013], *Marzadri et al.*

[2013] and *Naranjo et al.* [2013] used temperature data to study the spatial and temporal variability of EFs at pool-riffle sequences. *Cardenas and Wilson* [2007b] investigated water flow and heat transport through streambed dunes. The influence of natural and/or artificial in-stream structures (e.g. man-made dams or beaver dams) on the HZ thermal regime and EF estimates was studied by *Lautz et al.* [2010], *Fanelli and Lautz* [2008] and *Briggs et al.* [2013]. *Molina-Giraldo et al.* [2011] and *Shope et al.* [2012] related streambed fluxes to stream bank filtration processes

(iv) Heat as a tracer has also been used in the study of the transport and fate of contaminants in fluvial deposits. *Conant* [2004] and *Conant et al.* [2004] used mapped streambed temperatures in combination with groundwater and stream water sampling, soil coring and ground-penetrating radar measurements to study a PCE plume and its degradation products approaching the Pine River near Angus, Canada. *Hamonts et al.* [2012] and *Hamonts et al.* [2014] related temperature data collected in and near the streambed of the Zenne River, Belgium to the natural attenuation potential of the streambed with regard to chlorinated ethene contamination as well as to the encountered microbial community structure. For the same site, *Ebrahim et al.* [2013] and *Dujardin et al.* [2014] combined temperature measurements and numerical modeling to delineate vertical exchange fluxes (VEFs) across the streambed. *Kalbus et al.* [2007] and *Schmidt et al.* [2008] combined high-resolution streambed temperature measurements with results from integral pumping tests in the connected aquifer to study the potential mass fluxes and flow rates of chlorinated benzenes near Bitterfeld, Germany. In an additional study on the same site *Schmidt et al.* [2011] related hydraulic heads and streambed temperatures to redox conditions and chlorinated benzene concentrations. *Lewandowski et al.* [2011b] used streambed temperatures to delineate fluxes and investigate the fate and attenuation of pharmaceutical micro-pollutants in the stream Erpe, Germany originating from sewage inflow. *Engelhardt et al.* [2013] used streambed temperatures, hydraulic heads and water quality parameters to study acesulfame and wastewater transport from the Schwarzbach stream, Germany into its connected aquifer. *Briggs et al.* [2014] collected high resolution temperature data with a FO-DTS (chapter 1.5.1) at several locations in Cherry Creek, USA to determine EFs, which were then used to delineate the residence time of water in the HZ and its influence on nitrate production and turnover.

(v) Heat as a tracer has also found its way into other hydrologic areas e.g. to quantitatively study exchange flux patterns across lakes [*Anibas et al.*, 2009; *Sebok et al.*, 2013], wetlands [*Bravo et al.*, 2002; *Anibas et al.*, 2012] or hydrothermal mounts on the ocean floor [*Goto et al.*, 2005].

1.5.3 Measuring Streambed Temperatures

Nowadays, a variety of temperature measurement devices exists to obtain streambed temperatures, which can be used to quantify exchange fluxes (see subsequent sections). *Schmidt et al.* [2006] and *Anibas et al.* [2009; 2011] used different versions of mobile temperature probes, which were temporarily inserted into streambeds. With these probes they

were able to measure temperatures in several depths at one particular point in time (steady-state). By repeating this procedure at many locations they could map several transects in a short time. To collect temperature-time series (transient), measurement devices (e.g. StowAway TidbiTs, divers, precision thermometers, etc.) have been installed for prolonged times (up to several years) in in-stream piezometers [*Essaid et al.*, 2008; *Hatch et al.*, 2010 among others]. However, in such piezometers convection cells can occur in times when strong thermal gradients exist [*Constantz*, 2008]. Also, the piezometer material can cause a signal lag of up to 1.5 hours and extra damping (thermal skin effect) of the temperature signal [*Cardenas*, 2010]. It has thus become more common to install temperature measurement devices directly into the streambed. *Schmidt et al.* [2014] developed a multi-level temperature stick (MLTS, chapter 3.5.2) for direct installation into the streambed that can either be pushed in by hand or by using a retractable stainless steel casing. Steady-state and transient measurements were combined by *Conant* [2004] and *Lautz and Ribaudo* [2012].They mapped steady-state temperatures over larger areas of streambeds and collected time-series at a few selected points. By correlating mapped temperatures to VEFs obtained from the transient temperature measurements, they were able to delineate fluxes for all investigated locations and to create detailed interpolated maps of EFs.

To acquire quasi-continuous temperature data with much higher spatial resolutions than achievable with the aforementioned devices, researchers have started to use fiber-optic distributed temperature systems (FO-DTS) [*Selker et al.*, 2006b; *Selker et al.*, 2006a; *Tyler et al.*, 2009]. In such a system, a laser is connected to one or more fiber-optic cables. Pulsed laser light (wavelength around 1000 nm depending on instrument) is sent along the cable and Raman scattering effects are measured. When the incident light strikes matter, some of it is backscattered with frequencies slightly above (anti-Stokes backscatter) and below (Stokes backscatter) the original one. By calculating the anti-Stokes to Stokes ratio a prediction can be made regarding the temperature around the fiber where scattering occurred. Data quality depends on signal strength [*Rose et al.*, 2013] that decreases with increasing distance to the sensor, integration times, over which anti-Stokes to Stokes ratios are calculated, as well as instrument capabilities and cable diameters. Nowadays, instruments with a spatial resolution of ≤ 1 m and a temporal resolution of seconds to hours are commonly used. With proper instrument calibration temperature changes of 0.01°C can be observed. The main advantage of the FO-DTS system over other temperature measurement devices is its capability to continuously obtain data at many locations along the cable at the same time. Fiber-optic cables have been deployed along streambeds [*Lowry et al.*, 2007; *Slater et al.*, 2010; *Krause et al.*, 2012] or vertically installed into them [*Vogt et al.*, 2010; *Briggs et al.*, 2013; *Briggs et al.*, 2014]. The latter method has achieved temperature measurements with a spatial resolution of less than 0.02 m [*Briggs et al.*, 2012].

The previously presented methods passively use the natural temperature distribution in the HZ to deduce exchange fluxes. Recently *Lewandowski et al.* [2011a], *Angermann et al.* [2012a] and *Angermann et al.* [2012b] developed an active method where a heat pulse is emitted into the streambed and an array of 24 temperature sensors is used to monitor the resulting heat plume. With this tool, magnitude and direction of the water flux can be derived. Other

researchers [*Read et al.*, 2014; *Sayde et al.*, 2014] have started to explore the use of A-DTS. In such systems, heat is induced into the subsurface by heating a fiber-optic cable and comparing the temperature of the surrounding material (e.g. the water in a well) to its natural background temperature. Although promising, the use of heat as an active tracer in HZ studies is still in its infancy.

1.6 Modeling Hyporheic Zone Processes

In general, a model can be viewed as a simplified version of a complex real system used to simulate the system's behavior under certain input conditions represented by a set of pre-defined model parameters. Models can be helpful in understanding processes in the past and present and in making predictions regarding their future development. Flow and transport processes in the HZ can be simulated by a variety of model types and software packages. Ideally, all relevant processes should be considered simultaneously in both the surface water and groundwater compartments. However, due to data scarcity, limited time and resource constraints this often proves difficult [*Garraway et al.*, 2011].

1.6.1 Model Classification

A variety of model classifications and terminology exists in hydrology. One distinction made is that between white-box (physics-based models) that adhere to the conservation of mass and momentum, grey-box (lumped models) and black-box (empirical) models [*Willems*, 2000]. White box models are mostly continuous as they attempt to describe all processes acting in the system at all points. They can thus also be considered spatially distributed models. Their use requires prior information on main hydraulic and sedimentological characteristics of the subsurface.

Another distinction is that between deterministic and stochastic models [e.g. *Refsgaard*, 1996]. Deterministic models relate model output variables to model input via fixed mathematical model structure equations. Usually one set of input values and one set of model parameters produce one uniquely identifiable set of model output values. Stochastic models on the other hand describe some or all of the input values and parameters by a statistical distribution, considering the underlying processes random in nature. Model output is then not considered a single value but a range of value sets with a certain probability assigned to them and derived from different input/parameter combinations [*Rubin*, 2003].

HZ models can also be distinguished by how they connect (couple) the surface water and groundwater compartments. Fully coupled models are able to handle flow and transport in both surface and connected groundwater compartments simultaneously as well as their interaction. Pending data availability these models could consider all relevant processes of both compartments such as precipitation, evapotranspiration and other factors determining groundwater recharge as well as surface water and groundwater flow and transport processes. As such, a more realistic and often more accurate water balance of the entire system can be approximated and contributions of groundwater to streams could be quantified while

considering the entire local hydrological cycle. On the other hand computational requirements are much higher compared to non-integrated models, modeling time increases and calibration becomes more tedious with an increasing number of parameters. The type of coupling is often classified as **(i)** external, **(ii)** iterative or **(iii)** full [*Furman*, 2008].

(i) Externally-coupled models independently and successively solve for flow and transport processes in the two compartments. In most cases surface flow is solved first and results are then passed on to the subsurface model part. This is repeated for each time step [*Morita and Yen*, 2002]. Externally-coupled models are relatively easy to implement but often the used numerical solvers show problems with conversion, especially for large time steps [*Fairbanks et al.*, 2001]. External coupling or decoupling of fully coupled models can be useful if e.g. flow and transport in both compartments change on different time scales or if transport depends on flow but not vice versa (one-sided physical coupling), which might allow to save valuable computer resources.

(i) Iteratively-coupled models use separate iterative solvers for groundwater and surface water processes with heads or fluxes acting as internal boundary conditions between the two compartments. Each solver advances to the next time step when the iteration error is below a user-defined threshold.

(iii) Fully-coupled models solve all flow and transport processes of each compartment as well as their interactions simultaneously for each time-step. Full coupling is the most robust (least error-prone) of the three techniques; however, it also consumes the most resources and computing power. In fully-coupled models the same time-step can be used throughout the entire system, always defined by the most dynamic process within the system. Fully-coupled models can be especially valuable in regional catchment modeling and where groundwater-surface water interaction plays an important role.

One spatially distributed model type specifically developed for the HZ is the transient storage model (TSM) that was first introduced by *Bencala and Walters* [1983]. It has originally been used in studies of stream solute transport using conservative stream tracers [*Harvey et al.*, 1996; *Wagner and Harvey*, 1997]. Tracer data is commonly used for calibration of the TSM through inverse modeling. TSMs neglect the aquifer and assess hyporheic exchange flow and transport by using the stream as the main channel and the hyporheic zone as a transient storage zone connected to the channel via exchange processes. In the main channel, transport exists due to advection and dispersion. Exchange between channel and transient storage zone has been described by a mass transfer approach as performed e.g. by the 1D flow and transport model OTIS/MINTEQ/QTEQ [*Runkel*, 1998; *Runkel*, 2010].

TSMs are relatively simple conceptualizations of the real world and easy to use. However, they often lump together actual storage zones from various scales and use them for flow and transport modeling below the reach scale in environments where small scales of heterogeneity can be limiting. A variety of transient storage models is discussed by *De Smedt* [2007] regarding their application, advantages and limitations. *Gooseff et al.* [2005] performed sensitivity analyses to study the performance of various TSMs for conservative and reactive solute transport. In general, TSMs have been found to approximate solute concentrations

reasonably well on a short timescale but underestimate concentrations and ultimately EFs on longer timescales [*Bencala et al.*, 2011]. Parameters determined with a TSM at one location are often not directly transferrable to other locations (reaches, streams) and researchers have been searching for robust and transferrable correlations between the different parameters [*Boano et al.*, 2014].

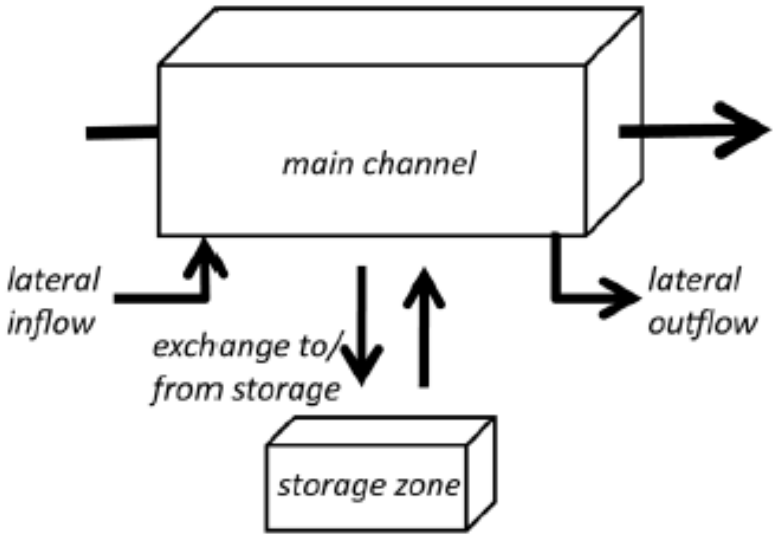

Figure 1.8: The transient storage model concept. Source: *Bencala et al.* [2011].

1.6.2 Frequently Used Model Codes

In physics-based models, flow and transport processes are commonly described by a set of partial differential equations, which can be solved analytically if the system is simple enough [*De Smedt*, 2007; *Kazezyilmaz-Alhan*, 2008], or numerically. One example for an analytical model would be the spreadsheet-based IGARF code developed by the Environment Agency of the UK. This code allows for the investigation of the influence of water abstraction on stream flow [*Buss et al.*, 2009].

Available software for numerical modeling includes the finite-difference code MODFLOW [*McDonald and Harbaugh*, 1988; *Harbaugh et al.*, 2000; *Harbaugh*, 2005] developed by the U.S. Geological Survey. It is the most frequently applied code to model GW-SW interactions [*Furman*, 2008; *Buss et al.*, 2009] and uses various packages to deal with HZ processes, including the river package, the stream package and several stream routing packages. These packages are mainly distinguishable by the way they conceptualize the HZ and assign boundary conditions. *Brunner et al.* [2010] describe their characteristics but also discuss general limitations when using MODFLOW in a HZ environment, which include (a) that only gravity driven flow through the streambed is assumed, which can lead to an underestimation of infiltration fluxes; (b) that streams are either connected or unconnected in the model

neglecting possible transitional stages; and (c) that any mismatch between actual stream width and the grid cell the stream is assigned to will produce water table errors.

Other software used for hyporheic zone modeling includes the fully coupled models Hydrogeosphere [*Therrien et al.*, 2010], MODHMS [*HydroGeoLogic*, 2000] and ParFlow [*Maxwell et al.*, 2009], as well as the externally-coupled models MIKE SHE [*Refsgaard and Storm*, 1995; *DHI*, 2009a, b], GSFLOW [*Markstrom et al.*, 2008] and Shetran [*Ewen et al.*, 2000]. Codes like SUTRA [*Voss and Provost*, 2008], HYDRUS [*Šimůnek et al.*, 2006] or COMSOL [*COMSOL-AB*, 2008] and others are less frequently used but as well constantly improved. To simulate chemical reactions as well as biodegradation, flow and transport models can be coupled with codes such as PHREEQC [*Parkhurst and Appelo*, 1999], MT3DMS [*Zheng and Wang*, 1999] or RT3D [*Clement*, 1997].

Many models are specifically tailored to research needs and serve only a limited research purpose. For example, *Salehin et al.* [2004] developed their own finite element model to study basic effects of sediment structure on hyporheic exchange. Specific problems for which existing software does not provide adequate solutions are often addressed using scripting software like MATLAB or programming languages like FORTRAN, C++ and Python.

1.6.3 Some Model Applications

Modeling has been shown to improve the understanding of exchange flow and transport processes and to help modelers assess residence times for a variety of conditions such as flow and transport near dams and meanders [*Wroblicky et al.*, 1998; *Boano et al.*, 2006; *Lautz and Siegel*, 2006; *Jin et al.*, 2009], for pool-riffle sequences [*Storey et al.*, 2003; *Tonina and Buffington*, 2007], for mountainous stream environments [*Kasahara and Wondzell*, 2003; *Wondzell et al.*, 2009], across point-bars [*Cardenas*, 2008a] or for micro-topographic effects [*Frei et al.*, 2010]. Numerous other HZ modeling studies have mainly been looking at the influence of hydrodynamics and heterogeneity in streambed geology, for various bedform types and/or stream curvatures on solute residence times and hyporheic exchange fluxes [*Elliott and Brooks*, 1997b; *Cardenas and Zlotnik*, 2003a; *Cardenas et al.*, 2004; *Cardenas and Wilson*, 2006; *Gooseff et al.*, 2006; *Cardenas and Wilson*, 2007a; *Cardenas*, 2008b; *Cardenas et al.*, 2008; *Sawyer and Cardenas*, 2009; *Jin et al.*, 2010; *Stonedahl et al.*, 2010; *Stonedahl et al.*, 2012; *Stonedahl et al.*, 2013]. Large scale bedforms such as point bars and their influence on EFs have also been studied using semi-analytical models [*Boano et al.*, 2010; *Marzadri et al.*, 2010].

Munz et al. [2011] showed in a modeling study for River Leith, UK that with an increase in head differences between stream and aquifer the spatial variability of exchange flux becomes less dependent on streambed topography. *Bardini et al.* [2012] discussed the influence of stream velocity and sediment permeability (assuming a homogeneous streambed) on nutrient cycling (nitrate, ammonium, DOC) and the redox zonation in the HZ for a dune. *Derx et al.* [2010] used Sutra2D3D to model 3D groundwater flow patterns in a gravel bar at the Danube as well as transport of a conservative tracer to better understand the impact of river water fluctuations on groundwater flow velocities, mixing zone evolution and dilution of solute

concentration. *Hantush* [2005] used linear response functions and the Laplace transform to find analytical solutions to stream channel flow and stream-aquifer exchange. *Wondzell et al.* [2009] studied tracer travel times for a mountainous stream reach using MODFLOW. They developed alternative homogeneous and heterogeneous models to estimate streambed *K* as well as depth and shape of the lower boundary for different model set-ups. *Hester et al.* [2013] used MODFLOW-GMS to simulate the mixing behavior of groundwater and stream water for homogeneous and heterogeneous streambed sediments. They found that flow paths originating in the aquifer only sometimes disperse in the HZ. Such dispersion is however needed for contaminants from the aquifer to attenuate in the HZ. *Käser et al.* [2014] showed with their 3D MODFLOW model that a streambed top parameterized with high resolution (streambed topography) and a HZ with a much more simplistic discretization are sufficient to delineate the pattern of EFs.

When modeling objectives suggest hyporheic zone processes not necessarily be fully integrated, when the streambed can be considered rather homogeneous, or when a lack of input data does not permit for heterogeneity to be taken into account, groundwater models can be used that consider the streambed a homogeneous structure and its hydraulic properties (e.g. hydraulic conductivity) can be determined by model calibration processes. However, the substitution of heterogeneous streambeds with homogeneous equivalents can be problematic as *Irvine et al.* [2012] showed in their theoretical modeling study on losing streams. They demonstrated that large errors of up to 34% in estimating infiltration fluxes (from river to aquifer) can occur in case of a discrepancy between the flow regimes of observed and modeled data.

1.6.4 Limitations of Models

Whereas early and crude numerical hydrological models were mainly constraint by insufficient computing power, a major problem today more frequently lies in finding an adequate discretization of the area to be modeled that still provides rather realistic results for each of the model elements while increasingly finer meshes/grids are used [*Beven*, 2001]. The issue of non-linearity focuses on how far inherently non-linear hydrologic systems can be successfully described through linearization and how much that influences the predictive capabilities of a model. The problem of scale deals with the issue of different representations of the same physical process at different scales and how this can be integrated into numerical models [*Blöschl*, 2001].

The problem of non-uniqueness of place accounts for the fact that often many optimal parameter sets exist that can describe the processes within a system equally well, even if the model structure could be perfectly determined. However, the latter is also near impossible as only limited measurements are available and measured data can hardly be reproduced in hydrological field studies as most processes are transient, i.e. variable in time. As such, the concept of equifinality has been introduced that accepts the existence of many imperfect model structures and many optimal parameter sets that are able to adequately describe the system in question (see e.g. *Beven* [2001] for an in-depth discussion). Over the last two

decades, the issues of non-uniqueness and equifinality have led to the development of a variety of approaches to improve parameter estimation by applying e.g. genetic algorithms, Markov Chain Monte Carlo methods or multi-objective optimization techniques following the Pareto principle [e.g. *Gupta et al.*, 1999; *Vrugt and Robinson*, 2007; *Vrugt et al.*, 2009; *Vrugt et al.*, 2013]. Other approaches such as GLUE ([*Beven and Binley*, 1992], see section 1.7.2) use many simulation runs and many parameter combinations to identify those parameter sets that can sufficiently well represent the studied processes without actual parameter optimization. Modeling is also subject to uncertainty, resulting from erroneous measurements, from parameter estimation when performed, and from the underlying model structure. These aspects are discussed further in the subsequent section.

1.7 Uncertainty

1.7.1 Concepts of Uncertainty

Describing and quantifying water flow, contaminant transport and attenuation processes in the HZ, is always subject to uncertainty. Uncertainty is an inherent part of any hydrological study and often its quantification is a requirement in management and decision making as there is no perfect information or perfectly described system. Quantifying uncertainty is always a subjective process as it cannot be objectively measured but has to be assessed by means of modeling [*Caers*, 2011]. On a most basic level, uncertainty arises from (i) the randomness and sometimes chaotic behavior of natural systems (intrinsic uncertainty) and (ii) from our incomplete knowledge of such natural systems (epistemic uncertainty) as e.g. discussed by *Bear and Cheng* [2010].

In field studies, one usually encounters measurement uncertainties or errors when using a certain measuring technique/device. These errors can arise from instrumental drift, improper instrument calibration or the use of different instruments as well as human measurement behavior. In modeling studies, researcher often distinguish among model uncertainty, parameter uncertainty, process uncertainty, and uncertainty regarding boundary and initial conditions [*Bear and Cheng*, 2010; *Voss*, 2011a, b]. Most uncertainty related to modeling is probably attributable to geologic heterogeneity of the subsurface, which in turn influences hydraulic and biogeochemical parameters [*Caers*, 2011].

Willems [2000] divides the total uncertainty encountered in modeling studies into three parts; **(i)** input uncertainty, **(ii)** parameter uncertainty, and **(iii)** model structure uncertainty (Figure 1.9).

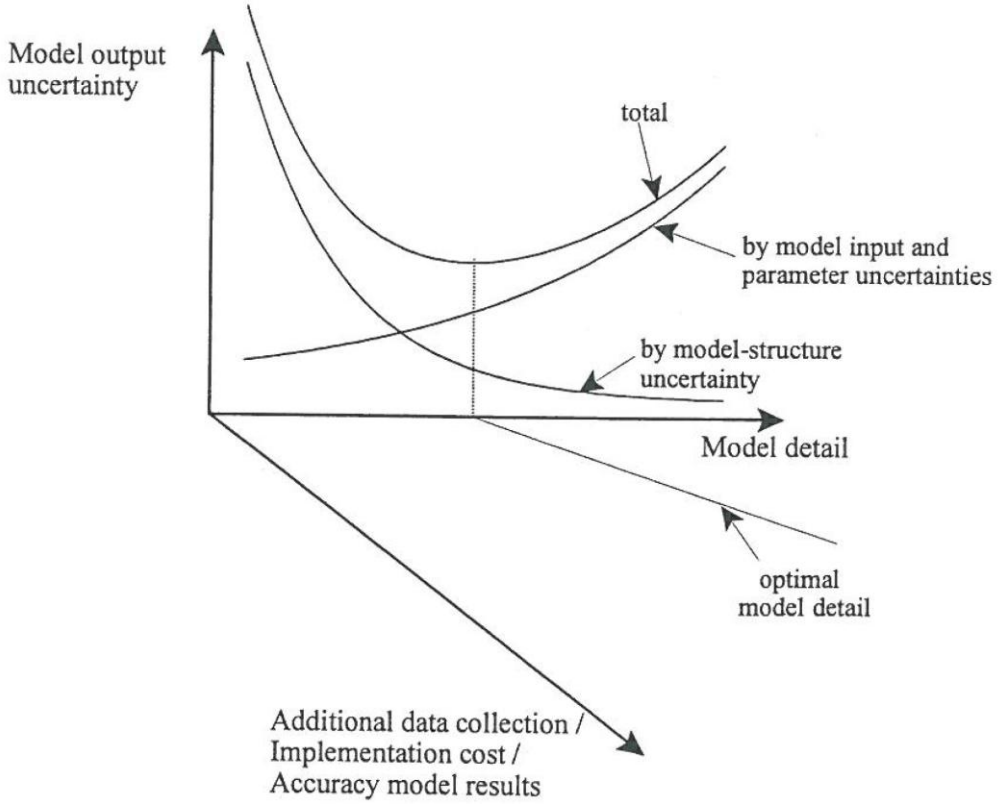

Figure 1.9: Different types of uncertainty. Source: *Willems* [2012].

(i) Input uncertainty arises from the uncertainty in external system description, i.e. from field measurements or input parameter estimation uncertainty. Also, data source and density (e.g. clustering, data with trends, etc.) could contribute to input uncertainties as well as raw data processing procedures. If input parameters are subject to spatial or temporal variability this is also reflected here.

(ii) Parameter uncertainty deals with errors in modeled parameters. These estimation errors can mostly be attributed to the parameter optimization algorithm used or to problems during model calibration, such as an improper calibration procedure and an insufficient calibration data set. Similar to input uncertainty, parameter uncertainty also has to consider data structure such as trends and clustering. The effects of sampling design and density on the estimation of VHG, VEFs and streambed *K* were studied by *Kennedy et al.* [2008], who found that in most GW-SW interaction studies for stream sections and reaches a delineation of realistic spatial parameter fields or reach average values might be more adequate and economical than point scale measurements correctly matched by a model.

(iii) Model structure uncertainty is the uncertainty in internal system description. It contains the remaining uncertainties after a theoretical error-free input, and after performing optimization and calibration. These remaining uncertainties include uncertainties regarding the conceptual model structure representing the physical processes within the model domain

as well as regarding the chosen boundary conditions. Physical processes can be uncertain due to a limit in knowledge or due to their actual randomness in nature [*Caers*, 2011].

1.7.2 Quantifying Uncertainty

To deal with these three types of uncertainty, *Ragas et al.* [1997] and *Willems* [2000, 2012] consider uncertainty from input or model parameters as operational uncertainty whereas model-structure errors produce fundamental uncertainty. When the former dominates, they suggest focusing efforts with regard to model improvement mainly on the collection of additional data. Alternatively one could reduce model complexity as for a fixed amount of available data, input and parameter uncertainties increase with increasing model detail.

Willems [2012] suggests finding an optimal balance between fundamental and operational uncertainties (Figure 1.9) in a probabilistic framework, using descriptive and spatial statistics. A variety of statistical parameters serving as uncertainty indicators have been developed and are in detail described in a multitude of textbooks [e.g. *Isaaks and Srivastava*, 1989; *Cressie*, 1993; *Rubin*, 2003; *Bear and Cheng*, 2010; *Caers*, 2011; *Chiles and Delfiner*, 2012]. Some of these that are used throughout this thesis are shortly described below.

Many of the uncertainty indicators are based on the use of the arithmetic mean m of a sample F containing realizations a determined by

$$m = \frac{1}{F}\sum_{k=1}^{F} a_k \tag{1-26}$$

Another often used central value that is more robust to extreme values is the median.

The variability of a parameter within a data set can be determined by calculating the range $r_a = a_{max} - a_{min}$, the interquartile range or the variance

$$y^2 = \frac{1}{F-1}\sum_{k=1}^{F} (a_k - m)^2 \tag{1-27}$$

where y is the sample standard deviation around the mean. Both mean and standard deviation are sensitive to outliers. Another indicator is the coefficient of variation that can be determined as $CV = \frac{y}{m}$. The symmetry of a distribution is given by the skewness whereas its peakedness is given by the kurtosis. Various graphical techniques such as an analysis of histograms and the cumulative distribution function (cdf), probability plots, scatter plots or Q-Q plots (for two parameters) can also aid in describing the data set. Studying the form (e.g. Gaussian, log-normal etc.) of the probability density distribution (pdf) is also often necessary for further stochastic analysis.

To investigate the relationship between two parameters one can determine Pearson's linear correlation coefficient

$$r_P = \frac{COV(a,b)}{\sqrt{y_a^2 y_b^2}} \tag{1-28}$$

or Spearman's rank correlation coefficient

$$r_R = \frac{1}{F}\frac{\sum_{k=1}^{F}\left(R_{a_k} - m_{R_a}\right)\left(R_{b_k} - m_{R_b}\right)}{y_{R_a} y_{R_b}} \tag{1-29}$$

where R_{a_k}, R_{b_k} are the ranks while m_{R_a} and m_{R_b} are the arithmetic means of the ranked data. In Eq. (1-28), $COV(a,b)$ is the covariance defined as

$$COV(a,b) = \frac{1}{F-1}\left(\sum_{k=1}^{F}(a_k - m_a)(b_k - m_b)\right) \tag{1-30}$$

For a vector containing two or more parameters that are transient in time one can then calculate a covariance matrix, via which the individual parameter variances can be obtained. If the uncertainty/error is assumed to be normally distributed, confidence bounds around the estimate can be constructed.

The root-mean-square error (RMSE) can provide a measure of how well a predicted value $\hat{\theta}_k$ (obtained through modeling) fits a variable θ_k that was determined by field or lab experiments. In such a case it is determined as

$$RMSE = \sqrt{\sum_{k=1}^{F}\frac{\left(\hat{\theta}_k - \theta_k\right)^2}{F}} \tag{1-31}$$

Related indices that use the estimation error (term inside the brackets in Eq. (1-31)) include the mean estimation error, the mean absolute error or the mean-square error. The Nash-Sutcliffe efficiency criterion E_{NS} [*Nash and Sutcliffe*, 1970] can also be used to analyze the predictive capabilities of a model. All these indices are linked to a deterministic predictive model.

If there is a spatial component to the studied parameter(s), stochastical analysis techniques are needed that can take into account spatial auto-correlation or cross-correlation (if more than one parameter is involved). Spatial auto-correlation means that a parameter value at a point A depends on a parameter value at a point $B = A + l$ at a certain lag distance l to A. In order to determine the error independent of spatial correlation the component related to spatial dependence has to be determined first. This can be done by using the auto-covariance (cross-covariance for several parameters) that applies the mean and assumes second-order

stationarity or the semi-variogram (cross-variogram) that only uses the distance l. The semi-variogram $\gamma(l)$ is defined as

$$\gamma(l) = \frac{1}{2n(l)} \sum_{k=1}^{n(l)} \left[a_{A_{k+h}} - a_{A_k}\right]^2 \tag{1-32}$$

where $n(l)$ is the number of pairs found for a certain lag distance. The variogram forms the basis of algorithms used for spatial continuity modeling such as various forms of kriging (see chapter 1.8) and sequential Gaussian simulations. If the spatial complexity cannot be fully delineated by using variogram analysis Boolean (object) models or 3D training images could prove a viable alternative (chapter 1.8). If prior information is available (e.g. parameter estimation ranges) and can be incorporated into the stochastic model, Bayesian techniques such as Markov-Chain algorithms can be used to conduct a more rigorous uncertainty analysis.

Another often applied technique in uncertainty estimation is a Monte Carlo simulation [see *Bear and Cheng*, 2010 for a mathematical outline], where a large number of realizations is constructed of the considered model domain with respect to a certain parameter. As each realization produces a forecast the collective behavior of all these forecasts then provides probabilistic information regarding the parameter's distribution. Monte-Carlo simulations are usually coupled to random field generators to produce a sufficiently large number of input realizations. One algorithm based on Monte-Carlo simulations is GLUE [*Beven and Binley*, 1992], the Generalized Likelihood Uncertainty Estimation procedure that takes into account equifinality (non-uniqueness of model solution) by defining an acceptable description of the system to be modeled instead of searching for an optimal solution. GLUE provides parameter distribution functions, not point estimates. It then employs importance sampling to identify a group of behavioral parameter configurations with regard to a certain acceptance threshold. Model parameter distributions are then estimated using weighting of these parameter configurations (Pseudo-Bayesian method). GLUE also provides an uncertainty analysis based on importance sampling and a sensitivity analysis based on screening (see also *Matott et al.* [2009]).

1.8 Spatial Heterogeneity

Most of the parameters describing flow, transport and attenuation processes in the HZ are heterogeneous, i.e. they attain different values at different locations within the same system of consideration. Heterogeneity has a direct influence on uncertainty. Heterogeneity of porous media is closely related to connectivity patterns found in nature. In a recent review *Renard and Allard* [2013] discuss the principles and definitions of connectivity and list a variety of static and dynamic connectivity metrics.

Geological heterogeneity leads to spatial and temporal parameter variability. In aquifers the effects of temporal parameter variability on flow and transport are often masked by stronger effects of spatial variability as shown in a modeling study by *Elfeki et al.* [2011]. As the HZ is a more dynamic system, temporal parameter variability should have in principle a stronger influence on flow, transport and attenuation. Several studies investigated the temporal variability of streambed temperatures and EFs [*Kalbus et al.*, 2008; *Hatch et al.*, 2010; *Anibas et al.*, 2011] and the natural attenuation behavior of chlorinated ethenes [*Hamonts et al.*, 2012] and nitrate [*Krause et al.*, 2009b] but systematic studies regarding their importance in comparison to spatial effects are still scarce. The remainder of this chapter will focus on spatial heterogeneity.

On a scale larger than that of a pore the behavior of each phase can be described by averaged state variables and material properties. For each of these variables and properties a homogeneous representative elementary volume (REV) can theoretically be found [*Bear and Cheng*, 2010]. This concept also becomes important as there often exists a discrepancy between the support volume underlying an observed data point and the minimum cell/block/element size in a numerical model (commensurability problem [*Beven*, 2000]). The optimal size of a REV is as such that the averaged parameter of interest remains approximately constant when the dimensions of the REV would be changed. Ideally, one could find the same REV for all averaged parameters or state variables of interest and its dimensions could then be used during discretization of the real world in the model. In practice, defining a single valid REV is mostly impossible as parameters and state variables are often heterogeneous. In those cases one could determine the correlation length, i.e. the scale at which two values of the same parameter at a distance from each other are still sufficiently correlated. *Engdahl and Weissmann* [2010] argued that the REV concept often works reasonably well in studies on the hydraulic behavior of a system but that it might be insufficient for effectively modeling transport processes. In the latter case small scale heterogeneities not captured by the resolution of the REV might well influence sorption or attenuation processes despite only marginally affecting average flow velocities.

To study the spatial heterogeneity of a parameter it is often necessary to find a model that adequately describes the parameter distribution in space, using direct or indirect information from field observations with a certain support volume together with certain interpolation and homogenization (upscaling) techniques, in order to estimate the parameter for model areas with no prior information. Numerous researchers describe the use of and theory behind the various methods that can be used to deal with spatial heterogeneity in flow and transport parameters in porous media [e.g. *Goovaerts*, 1997; *Kitanidis*, 1997; *Rubin*, 2003 and others; *Dagan and Neuman*, 2005; *de Marsily et al.*, 2005; *Bear and Cheng*, 2010; *Chiles and Delfiner*, 2012] and try to classify these methods to provide a better overview. One of the most extensive reviews on the applicability and functionality of various aforementioned methods for dealing with heterogeneity is provided by *Koltermann and Gorelick* [1996], who classify all methods into **(i)** structure-imitating, **(ii)** process-imitating, and **(iii)** descriptive methods (Figure 1.9).

(i) Structure-imitating methods rely on spatial statistics, probabilistic rules or deterministic constraints. They can be subdivided into **(a)** deterministic, **(b)** stochastic and **(c)** sediment pattern imitation methods.

(a) Deterministic methods include basic interpolation methods such as inverse distance weighting or trend surfaces and are not useful when uncertainty in the input data has to be considered.

(b) Stochastic methods can be subdivided again on the basis of whether they assume a statistical distribution of the parameter of interest that is either Gaussian or non-Gaussian. Gaussian methods assume the parameter of interest to be a continuous variable with the same mean, variance or variogram. The most commonly used Gaussian interpolation methods are various kriging and co-kriging algorithms (Figure 1.10). These algorithms produce a unique parameter map and smooth out small scale variability or extreme values. The quality of such a map often improves markedly with increased number of data points. Other Gaussian methods, such as turning bands [*Mantoglou and Wilson*, 1982; *Elfeki et al.*, 2011], Cholesky decomposition, spectral domain fast Fourier methods or sequential Gaussian simulation [see *Chiles and Delfiner*, 2012 for an outline] use random field generators to create multiple, equally likely maps. Contrary to kriging, that provides best estimates for each point and where the outcome is a map based on one random function or field, each map generated by a random field generator displays a texture similar to the true one and a conjunction of these maps or their information can help to produce a much better image of the parameter distribution.

Non-Gaussian methods are those able to describe discontinuous features. For example, Boolean and facies models were developed that used geometrical features to represent heterogeneous parameter distributions [e.g. *Haldorson and Damsleth*, 1990]. In these models, discontinuous sets of objects (e.g. clay lenses in a coarse grained matrix), also called (hydrostratigraphic) facies are drawn as a set of geometric features with varying shapes and positions embedded in a continuous matrix. Each facies is discretized and cells/nodes have hydraulic properties assigned, necessary for modeling. Additional tools that can deal with discontinuous features include indicator kriging relying on the indicator variogram and using pre-specified thresholds [*Journel and Isaaks*, 1984], and the Gaussian Threshold model [*Chiles and Delfiner*, 2012]. Markov chain models [see *Stewart*, 2009 for the mathematical background] can also describe discontinuities. They differ from variogram models by how they determine the transition probability within and between facies and would allow individual facies characteristics to be more influential during parameter estimation. As such, Markov chain models seem to model facies distributions closer to natural principles of sedimentology [*de Marsily et al.*, 2005]. Random field generators can also be made use of, e.g. in sequential indicator simulations. Simulated annealing uses an objective function to minimize the difference between statistics from a geological image and features desired in a subsurface map [*Koltermann and Gorelick*, 1996]. Often training images are applied, i.e. maps, borehole data or cross-sections that show the supposed geologic structure of the site or parts thereof, which will then be resembled by the geostatistical model.

(c) Sediment pattern imitation methods predict lithology and geometry of sedimentary deposits by building an image of sedimentation through time [*Koltermann and Gorelick*, 1996]. Although not directly conditioned on field data, some methods such as random walk or random avulsion can be calibrated to field measurements. In random walk models, paths of a large number of fluid particles are traced by approximating advection and by including dispersion through adding a random displacement after each time step [*Zheng and Bennett*, 2002]. Particles can also have assigned mass and velocity to account for sorption and decay effects. Random avulsion algorithms on the other hand are used to mimic stream channel migration (e.g. meandering) across a changing valley according to probabilistic and geometric rules.

(ii) Process-imitating methods model the physics of flow and transport as well as sediment forming processes. They are subdivided by *Koltermann and Gorelick* [1996] into geological process models, which are similar to the genesis models, and aquifer numerical model calibration methods. Genetic models are models which describe the geological processes forming the sediments within a study area [*Koltermann and Gorelick*, 1992; *Koltermann and Gorelick*, 1996]. These models can be based on empirical rules to represent processes like sediment transport and erosion, water level changes or climatic conditions [*Koltermann and Gorelick*, 1996; *Teles et al.*, 2001] and from their outcome sediment properties and distribution patterns (facies) could be derived. The advantage of genesis models is their ability in markedly better describing geological heterogeneity compared to geostatistical models, which could prove useful in complex and dynamic environments such as streambed and HZ sediments. However, compared to other methods mentioned here they are demanding on computer power and modeling time. Numerical model calibration methods are often integrated in the numerical models discussed throughout chapter 1.6. Usually these models start with maps produced by deterministic methods such as zonation or inverse distances or by some form of kriging. After flow and transport equations are solved for steady-state or transient conditions, a calibration process can be applied. A conditioning is not possible.

(iii) Descriptive methods include Boolean and facies models explained above.

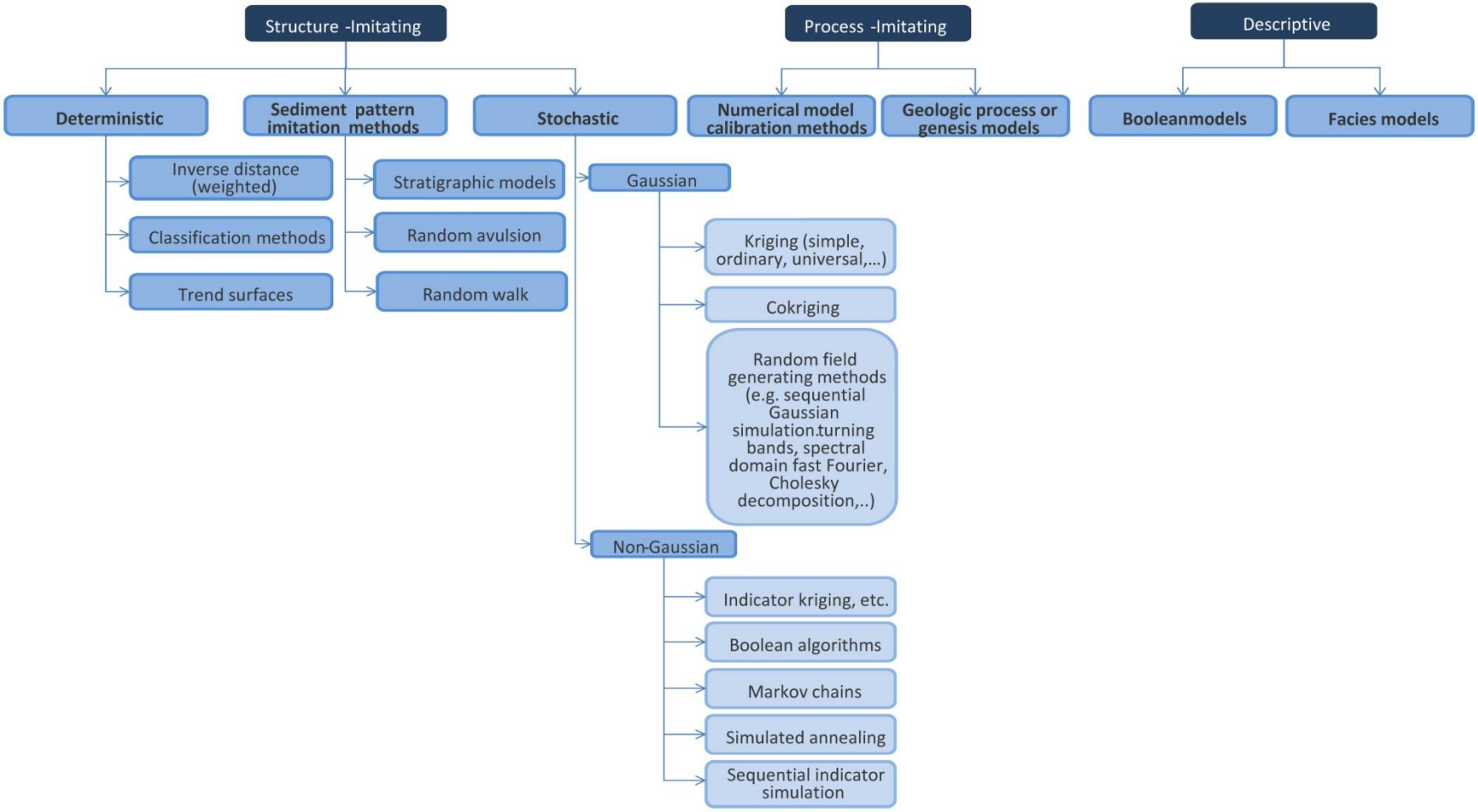

Figure 1.10: Classification of common methods used for assessing heterogeneity in the subsurface. Source: *Based on Koltermann and Gorelick* [1996].

1.9 Conclusions and Research Questions

This introductory chapter provides a concise outline of the hyporheic zone and the most frequently used concepts for describing water flow, contaminant and heat transport and contaminant attenuation. The shear amount of literature on aspects of HZ hydrology, ecology and biogeochemistry does not allow for a more detailed review here. For this, the interested reader is referred to the works of *Jones and Mulholland* [2000], *Buss et al.* [2009], *Boulton et al.* [2010] and *Boano et al.* [2014].

Despite much advancement over the last two decades, major knowledge gaps remain regarding the conceptualization and quantification of operational and fundamental uncertainty. Also, the consideration of heterogeneity inherent to HZ sediments and the respective hydraulic and geochemical parameters is sometimes omitted [see *Boano et al.*, 2014 for a discussion]. Recently, a larger part of the research community started shifting their interest from the sediment and reach scales towards the catchment scale. However, also at the former scales our understanding regarding uncertainty is still limited. When it comes to contaminant transport and attenuation, the subreach variability and uncertainty in reaction rate constants defining attenuation processes has only recently received increased attention, when researchers started to focus more on the biogeochemical hotspot concept [*Lautz and Fanelli*, 2008; *Krause et al.*, 2014]. The connections between the multitude of flow paths that are defined by the streambed geology and parameters such as hydraulic conductivity and exchange fluxes encountered in the HZ, and the formation of these hotspots and hot zones (i.e. larger areas) are also slowly unraveled [*Harvey et al.*, 2013]. In this framework, the development and application of new modeling tools of variable complexity (e.g. simple 1D models and analytical solutions, CFD (computational fluid dynamics) models, fully-coupled high resolution numerical models) and measurement/analysis techniques can strongly contribute to a better understanding and quantification of uncertainty.

1.10 Research Objectives and Thesis Outline

The main objective of this thesis is to study operational and fundamental uncertainty of water flow and contaminant transformation processes in the hyporheic zone of lowland rivers. The thesis will focus in particular on

1. The quantification of parameters defining the sequential reductive dechlorination reaction of chlorinated ethenes in streambed and aquifer sediments. In this context, reaction rate parameters will be determined for a variety of microcosm experiments and parameter uncertainty will be studied by using different kinetic models and a multi-objective self-adaptive multi-method search algorithm for parameter estimation.

2. The quantification of vertical exchange fluxes across streambeds using heat as a tracer. In this context, two new 1D models will be put forward that allow for flux

quantification in the frequency domain. They also determine parameter and model structure (fundamental) uncertainties.

3. The determination of streambed hydraulic conductivity on the sub-reach (stream section) scale using a high density data set. In this framework, the variability hydraulic conductivity determined from grains-size analyses and slug tests is investigated using descriptive statistics.

Figure 1.11 provides an overview on the work conducted in the remainder of this thesis. Each chapter contains an introduction, lists the specific objectives, provides an overview on the methodology used and discusses the results.

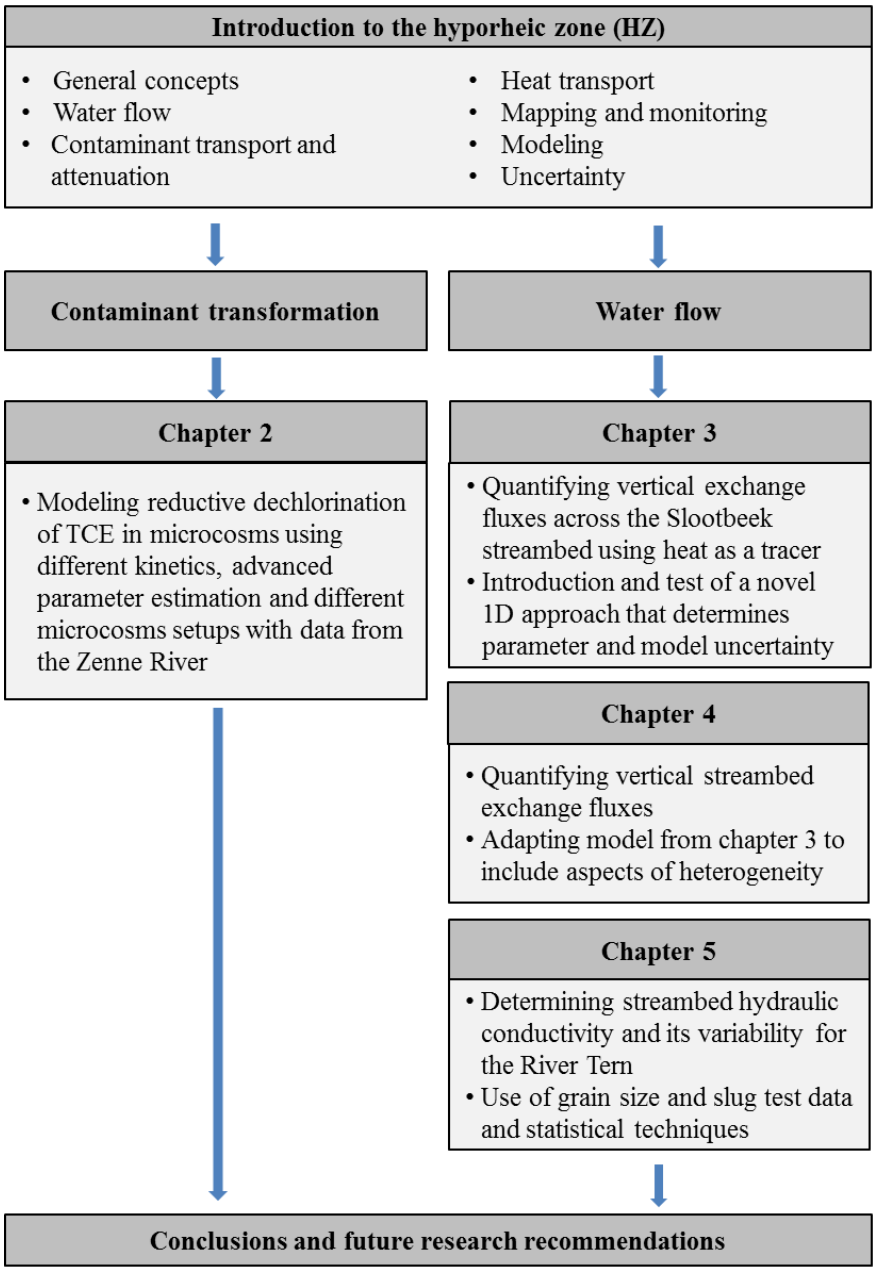

Figure 1.11: Overview of the different thesis chapters. Source: *own.*

This thesis includes data from the Zenne River study site in Belgium, the Slootbeek in Belgium and the River Tern in the UK (Figure 1.12). All sites are small lowland rivers in temperate climates that are partially regulated.

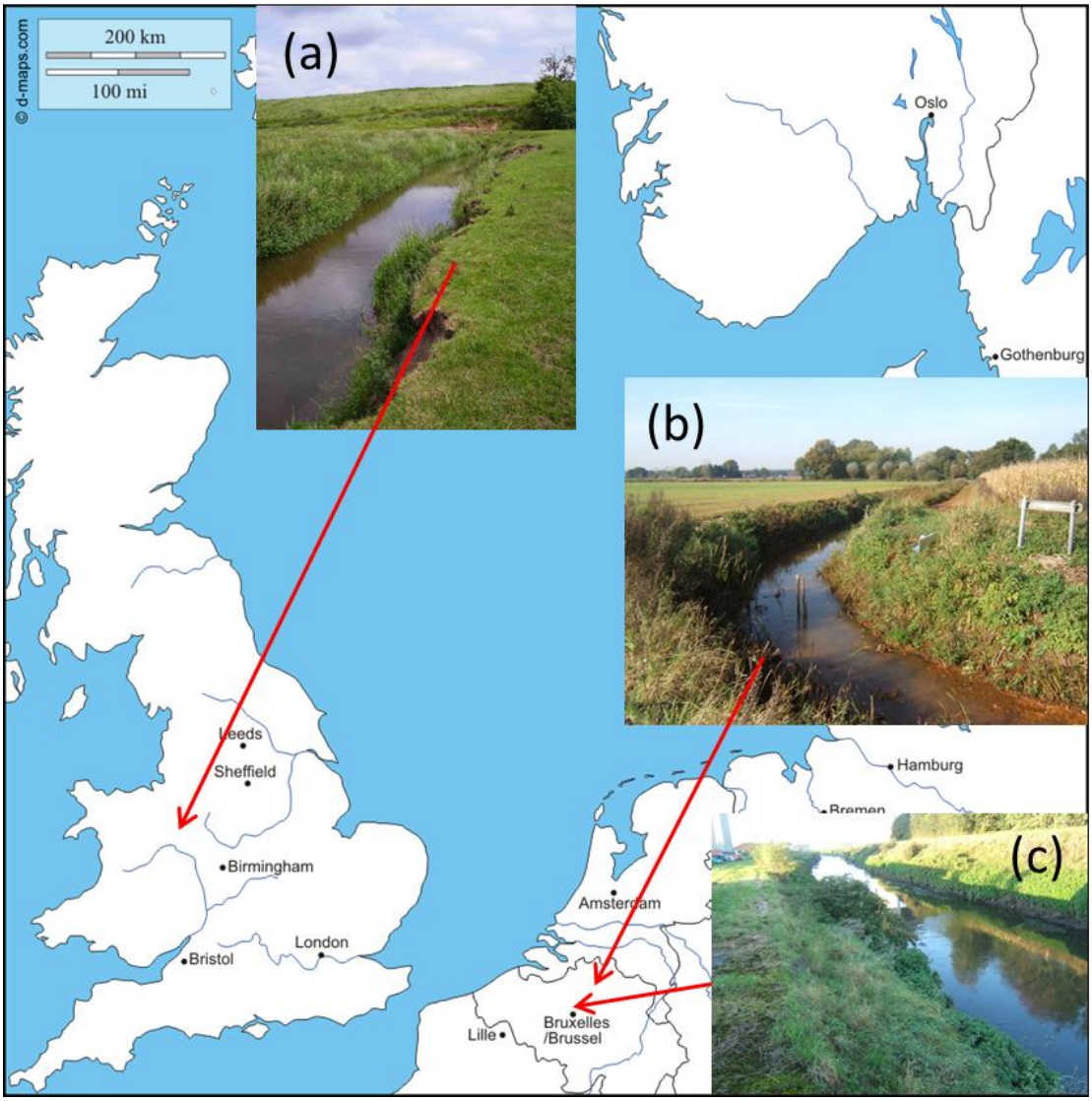

Figure 1.12: Data from the following field sites is included in this thesis: (a) River Tern, (b) Slootbeek, (c) Zenne River. Source: (a) *Riess* [2010]; (b), (c) *own.* Background map downloaded from http://d-maps.com/carte.php?&num_car=30226&lang=en.

Large parts of the work presented here have been published in or submitted to peer-reviewed journals as is indicated in the beginning of each chapter. The work is also part of the European Community's Seventh Framework Programme (FP7/2007-2013 under grant agreement n°265063) within the framework of the Marie Curie Initial Training Network ADVOCATE - Advancing sustainable in situ remediation for contaminated land and groundwater.

2 Modeling Anaerobic Biodegradation of Trichloroethene in Microcosms

This chapter is partly based on the following journal article:

Schneidewind, U.*, Haest, P.J.*, Atashgahi, S.*, Maphosa, F., Hamonts, K., Maesen, M., Calderer, M., Seuntjens, P., Smidt, H., Springael, D., Dejonghe, W. (2014): Kinetics of dechlorination by *Dehalococcoides mccartyi* using different carbon sources. *Journal of Contaminant Hydrology, 157, 25-36, doi: 10.1016/j.jconhyd.2013.10.006.*

* refers to equal contribution

2.1 Introduction

Contaminant transport processes in the hyporheic zone and the aspects of natural attenuation have already been discussed in chapter 1.3. To determine the attenuation potential of contaminants in the hyporheic zone or the connected aquifer it is common to conduct microcosm tests and column tests in the laboratory before actual field investigations are carried out. In such tests the contaminant attenuation behavior can be studied under controlled conditions. In the following sections of this chapter, the biodegradation of chlorinated ethenes in microcosms using aquifer and streambed material is discussed in more detail.

2.1.1 Chlorinated Ethenes

Chlorinated aliphatic hydrocarbons (CAHs) are organic substances that have been widely used as solvents in dry cleaning as well as degreasing agents in a variety of industries during manufacturing and machine maintenance [*Pankow and Cherry*, 1996]. Their wide-spread application and improper handling as well as their slow natural degradation have made them one of the most prevalent contaminant groups. Among CAHs, chlorinated ethenes (CEs, Table 2.1) such as PCE (perchloroethene), TCE (trichloroethene), cis-DCE (1,2 dichloroethene) or VC (vinylchloride) are some of the most prevalent organic contaminants found in soils and groundwater occurring especially at large industrial areas or megasites with multiple source zones [*Schiedeck et al.*, 1997]. Contamination by CEs has become a widespread environmental concern due to their potential adverse effects on human health and ecosystem functioning following exposure [*Adamson and Parkin*, 2000]. CEs are toxic and potentially carcinogenic [*Bouwer et al.*, 1981]. Water quality can be degraded, which can negatively affect drinking water supply as well as aquatic and riparian ecosystems.

As most CEs (except VC) are denser than water, they are categorized as dense non-aqueous phase liquids (DNAPLs). Below the water table, DNAPLs tend to migrate via preferential pathways towards the bottom of the aquifer where they can accumulate in long-living contaminant pools, from where they slowly dissolve into the groundwater [*Fetter*, 1999]. Dissolved CEs demonstrate low sorption and chemical reactivity. As the natural biodegradation potential at many contaminated sites is low, CE plumes can amount to several kilometers in length [*Mackay and Cherry*, 1989; *Conant et al.*, 2004]. When these plumes travel further through the aquifer, dissolved CEs can eventually discharge into streambeds and streams with baseflow such as shown for the River Tame [*Ellis and Rivett*, 2007; *Freitas et al.*, 2015].

Table 2.1: Some physico-chemical properties of common chlorinated ethenes. Source: *own.*

		PCE	**TCE**	**cis-DCE**	**VC**
Formula		C_2Cl_4	C_2HCl_3	$C_2H_2Cl_2$	C_2H_3Cl
Molecular mass	[g mol^{-1}]	165.8	131.4	96.9	62.5
Boiling point[a]	[°C]	121	87	60	-14
Melting point[a]	[°C]	-22.7	-87	-81	-153
Water solubility at 25°C[b]	[mg L^{-1}]	150	1000	3500	2700
Density at 20°C[b]	[g cm^{-3}]	1.62	1.46	1.28	0.91
Henry's law constant at 20°C[c]	[-]	0.533	0.314	0.14	0.891
log K_{ow}[d]	[-]	3.40	2.42	1.86	1.36

[a] *Fetter* [1999], [b] *USEPA* [1995], [c] *Staudinger and Roberts* [2001], [d] *ATSDR* [1997]

2.1.2 Natural Attenuation of Chlorinated Ethenes

Chlorinated ethenes can be degraded in aquifers and streambeds by biotic and abiotic transformation processes, as well as by sorption, volatilization, dispersion and dilution. Photolytic reactions play an insignificant role [*Bourg et al.*, 1992]. Biotic processes are much more relevant than abiotic ones.

The potential of dilution depends on the mixing behavior and the direction of flow (upwelling or downwelling). Once CEs are discharged into surface water, dilution is usually so strong that concentrations fall below detection limits in a very short time [*Conant et al.*, 2004; *Chapman et al.*, 2007; *LaSage et al.*, 2008]. Sorption of CEs in the streambed has been shown to be higher than in the connected aquifer due to additional organic carbon present in the HZ sediments [*Conant et al.*, 2004; *Ellis and Rivett*, 2007]. In various batch experiments TCE and PCE adsorption have been shown to follow a linear sorption isotherm [*Garbarini and Lion*, 1985; *Mouvet et al.*, 1993] but both are in general only weakly sorbed by soil and aquifer

solids and due to their hydrophobicity are neither strongly sorbed to organic-rich solids [*Bourg et al.*, 1992].

Under abiotic conditions CEs can be degraded by iron bearing minerals. Iron sulfide minerals, such as pyrite or mackinawite can reduce TCE in parallel via reductive elimination to ethene or by hydrogenolysis to cis-DCE [*Butler and Hayes*, 1999; *Jeong and Hayes*, 2007]. Iron sulfides are often used in engineered systems such as permeable reactive barriers or wastewater treatment lagoons and also frequently occur in anaerobic sediments, in e.g. natural wetlands. Removal of cis-DCE and VC using magnetite (Fe_3O_4) has been reported by *Lee and Batchelor* [2002]. Chlorinated ethenes can also be removed using phyllosilicate clays (biotite, montmorillonite, vermiculite) where iron(II) or iron(III) has replaced some of the aluminum or silicon atoms in the mineral lattice [*Lee and Batchelor*, 2004]. For more detailed information regarding the characterization of these degradation processes the interested reader is referred to *He et al.* [2009].

Biodegradation of CEs under aerobic conditions decreases with increasing number of chlorine substituents and occurs either as metabolic (growth-supporting) or co-metabolic oxidation (energy produced is not used for growth). Aerobic metabolic oxidation of PCE and TCE is only rarely observed [*Ryoo et al.*, 2000] and considered insignificant under natural conditions compared to other degradation processes [*Bourg et al.*, 1992]. For cis-DCE and VC metabolic oxidation has been reported to be induced by some strains of *Mycobacterium* and *Pseudomonas* [*Coleman et al.*, 2002a, b]. Aerobic co-metabolic CE oxidation is induced as a secondary process by catalytic enzymes such as monooxygenase that initially intent to oxidize growth-supporting substrates. Aerobic co-metabolic oxidation of CEs has been reported using e.g. *Methylosinus trichosporium OB3b* [*Chang and Alvarez-Cohen*, 1996] and has been successfully applied as an in-situ groundwater remediation technique [*Semprini et al.*, 2007].

Under anaerobic conditions CEs can be degraded by anaerobic oxidation [*Bradley and Chapelle*, 1998], fermentation [*Kaufmann et al.*, 1998] and reductive dechlorination. The latter is by far the most important biodegradation process for CEs [*Wiedemeier et al.*, 1998]. Biological reductive dechlorination is an electron-consuming process, in which a chlorine atom is removed and replaced by a hydrogen atom. CEs are sequentially reduced from PCE to TCE to DCE to VC to ethene to ethane (Figure 2.1). Although all three isomers of DCE can be formed, cis-1,2 DCE is the most prevalent one under natural conditions [*Bouwer*, 1994]. Reductive dechlorination of CEs can occur co-metabolically using e.g. iron- or sulfate reducing bacteria [*El Fantroussi et al.*, 1998] or via (de)halorespiration where anaerobic bacteria species such as *Desulfitobacterium, Dehalobacter, Sulfurospirillum, Geobacter* or *Dehalococcoides* use CEs as a terminal electron acceptor for growth [*El Fantroussi et al.*, 1998; *Holliger et al.*, 1999]. Depending on the bacteria species, halorespiration can be the result of reductive hydrogenolysis (i.e. replacement of chlorine with hydrogen) or dichloroelimination reactions (i.e. formation of a double bond between carbon atoms). Bacteria from the genus *Dehalococcoides mccartyi* are of particular interest for bioremediation as certain strains [see *Hamonts*, 2009 for a discussion] mediate complete

reductive dechlorination of PCE to ethene by reductive dehalogenase (RDase) enzymes [*Maymó-Gatell et al.*, 1997; *Hendrickson et al.*, 2002].

For an efficient degradation by halorespiration suitable electron donors are necessary in abundance (e.g. hydrogen, lactate or acetate), which are produced by hydrolysis or fermentation of the organic material present. However, at many field sites the amount of suitable electron donors is commonly very limited. Additionally, halorespirers need to compete with other organisms (e.g. methanogens) for these limited electron donors. Therefore, stimulated anaerobic reductive dechlorination has become an attractive option for the cleanup of polluted sites mainly due to its relatively low cost [*Pant and Pant*, 2010]. During the last two decades, a number of studies addressed the relative efficiency of various externally added electron donors, such as acetate [*He et al.*, 2002; *Lee et al.*, 2007], methanol [*Aulenta et al.*, 2005b], lactate [*Aulenta et al.*, 2005b] or butyrate [*Fennell et al.*, 1997; *Aulenta et al.*, 2005b; *Aulenta et al.*, 2005a]. Nevertheless, no conclusions could be drawn so far regarding the efficiency of electron donors such as H_2, rapidly fermentable carbon sources, slow release carbon sources or complex organic materials. In addition, information on indigenous sources such as dissolved natural organic carbon (DOC) to support reductive dechlorination is scarce.

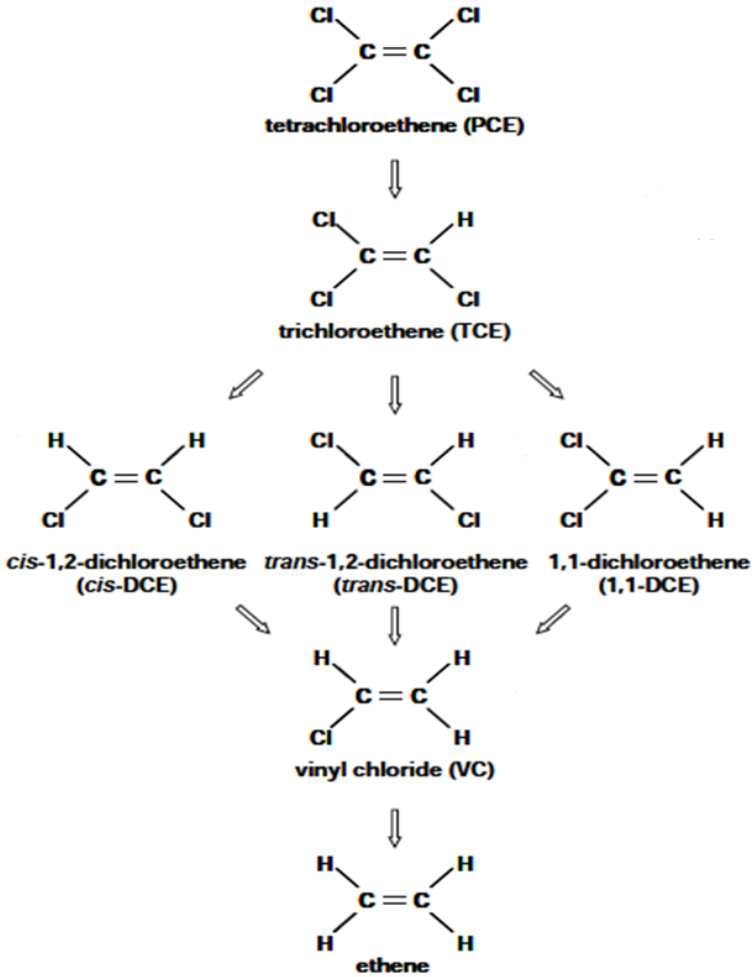

Figure 2.1: Sequential reductive dechlorination of PCE. Source: Modified from *Hamonts* [2009].

2.2 Objectives

In order to design and assess in situ remediation measures that include stimulating reductive dechlorination of CEs at the field scale, knowledge regarding the natural attenuation potential is essential. Given the limited data availability at the field scale and the complex microbial interactions, a need for practical tools that take into account the most relevant processes was identified [*Clement*, 2011]. Commonly, laboratory-scale microcosm experiments are first conducted to study site-specific dechlorination reactions in a controlled environment with known input conditions and to identify the most relevant processes. Rate coefficients defining these dechlorination reactions can be obtained by using kinetic models on the microcosm data (see chapter 1.3.3). These models are of variable complexity and as such need a variable amount of input data and computing resources. The application of these different models is thus also prone to different sources of uncertainty.

This chapter looks at the stimulated sequential reductive dechlorination of TCE to ethene by *Dehalococcoides mccartyi* in microcosm (batch) experiments using aquifer and streambed material and different carbon sources as electron donors. Three kinetic models of increasing complexity are applied to determine rate coefficients and find the most suitable numerical approximation that distinguishes the most influential driving factors of the dechlorination reaction. Some aspects of parameter and model structure uncertainty are discussed.

2.3 Study Site

Field work was carried out at locations SB2, SB3 and PB26 (monitoring wells), close to the Zenne River near Vilvoorde-Machelen, about 10 km North of Brussels, Belgium (Figure 2.2). Average elevation at the site is 16 m above sea level and the dominant soil type in the area is silty loam. The Zenne is a partially engineered lowland stream of about 100 km length and has a catchment area of about 600 km^2 [*Dujardin et al.*, 2011]. It is mostly a gaining stream except during high stream stage conditions. Near SB2, the Zenne River is dammed with steel pile walls causing mostly vertical exchange. There, stream stage varies between 0.5-2 m while stream flow is about 5 m^3s^{-1} under normal weather conditions [*Hamonts*, 2009]. The streambed consists mainly of medium to fine sands and silts. Local geology is defined by the Tielt Formation of about 25 m thickness, containing mostly silty-fine sands and glauconite. This formation is underlain by the Kortrijk Formation comprising mostly clay. Hydraulic conductivity in the aquifer is between 1-15 md^{-1} and groundwater velocity is about 30-60 m $year^{-1}$ [*Bronders et al.*, 2007].

At the site, a major industrial area existed between 1835 and the 1960's, where a considerable use of chemicals such as BTEX, PAH and CEs occurred. In the process, contaminants were released into the subsurface at four major (Figure 2.2) and several minor source zones. Over the years the contaminants moved through the subsurface forming a complex plume of at least 72 ha that is now discharging into the Zenne River. Most of the contaminants are sitting at a depth between 10 and 14 m below surface [*Bronders et al.*, 2007; *Dujardin et al.*, 2011]. PCE,

TCE and 1,1,1-TCA, originated mostly from the main sources S2-S4 (Figure 2.2) and are moving in direction North-West towards the Zenne River. While these readily degrade in the aquifer, VC, cis-DCE and 1,1 DCA have been found in the Zenne streambed [*Bronders et al.*, 2007; *Hamonts et al.*, 2009; *Hamonts et al.*, 2012].

Many aspects of the field site have been studied over the years. *Bronders et al.* [2007] characterized the site by means of classical and more advanced investigation techniques and contaminant transport modeling, and conducted risk assessments. *Dujardin et al.* [2011] refined the contaminant transport model to investigate the impact of landuse on groundwater recharge and contaminant fluxes. *Dujardin et al.* [2014] and *Ebrahim et al.* [2013] quantified groundwater-surface water exchange fluxes using temperature measurements while *Van Keer et al.* [2011] applied compound-specific stable isotope analysis to determine different source zones and characterize the plume. For an area near Post 26 (Figure 2.2), *Hamonts et al.* [2009] and *Kuhn et al.* [2009] determined the bioattenuation potential of the streambed sediment for VC and other CEs as well as the spatial distribution of different biotic and abiotic attenuation processes. In an additional study *Hamonts et al.* [2012] looked at the temporal variations of several natural attenuation processes at the site, while *Hamonts et al.* [2014] specifically investigated the composition of and the factors determining the site-specific microbial community. *Atashgahi et al.* [2013] could conclude from microcosm studies that VC had been degraded by anaerobic and aerobic microorganisms. The potential use of solid polymeric organics as sustainable electron donor sources when used as streambed capping material was investigated by *Atashgahi et al.* [2014].

2.4 Methodology

2.4.1 Microcosm Tests

For the microcosm tests aquifer material was previously collected by other researchers from VITO next to the monitoring wells at a depth of 7-8 m below surface (mbs) for PB26 and at 7.2 to 10.5 mbs for SB2 and SB3 using a Geoprobe Direct-push MacroCore system. All liners were transported to the lab and stored at 4 °C under a 100% nitrogen atmosphere before use. Sediments from the Zenne streambed were collected at Post 26 (Figure 2.2) using a 4 cm-diameter piston sediment sampler from Eijkelkamp.

From each location, 37 g of wet, well-mixed aquifer material was suspended in 90 mL of groundwater collected at the same location as the aquifer material in 160 mL bottles. Four different experimental conditions were set up for each of the three locations: natural attenuation, abiotic control, sediment, and lactate amendments. In natural attenuation microcosms no additional carbon source was added. In abiotic control microcosms, microbial growth was inhibited by adding formaldehyde (1% v/v). In lactate microcosms, sodium lactate was added to reach a final DOC of 300 mg/L. In sediment microcosms, aquifer material was replaced by 37 g of homogenized wet streambed sediment and the corresponding

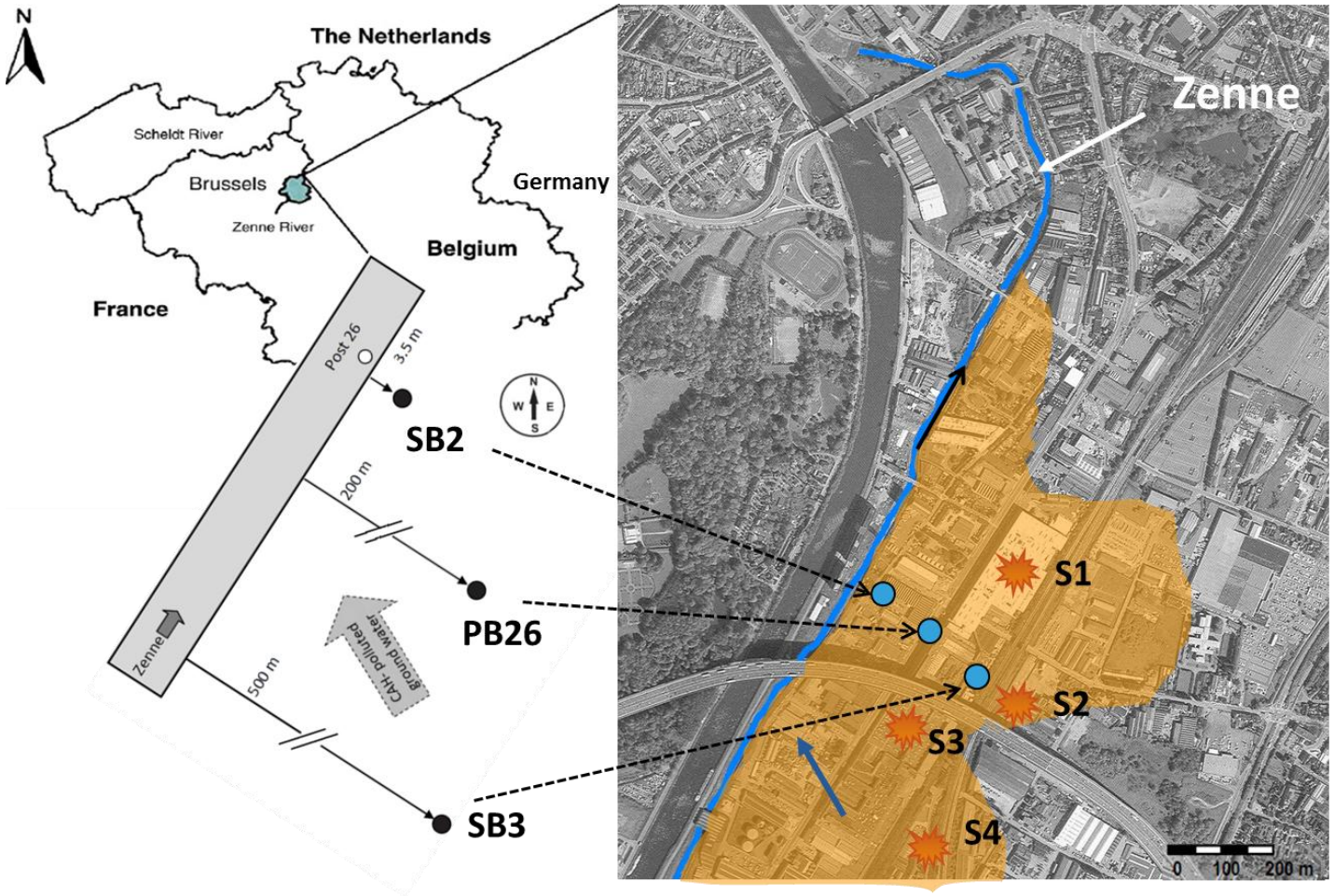

Figure 2.2: The Zenne River field site North of Brussels. Contaminants originate from four major source zones S1 to S4. The plume moves towards the Zenne River. Field work was carried out at locations SB2, PB26 and SB3 at different distances from the streambed near Post 26. Source: Modified from *Bronders et al.* [2007], *Dujardin et al.* [2014], *Hamonts* [2009] and *Schneidewind et al.* [2014].

groundwater from each selected location was added. Location PB26 was considered as a possible carbon source injection site for further studies and thus three additional conditions were tested: stimulation with molasses and stimulation by two types of streambed sediment extract, namely sedimented or centrifuged extract. In order to obtain the sediment extracts, 125 g of homogenized wet sediment was suspended for 3 days in 300 mL of PB-26 groundwater. The resulting suspension was either sedimented overnight, and the resulting supernatant was taken as sedimented extract, or centrifuged (7000 × g for 10 min) to obtain a supernatant as the centrifuged extract. Molasses was added in a similar way as lactate to reach a final DOC of 300 mg/L. As such, the limiting factors for complete dechlorination of TCE stimulated by an addition of carbon sources (lactate or molasses), other nutrients (centrifuged extract) and/or dechlorinating microorganisms (sedimented extract) could be assessed.

Each microcosm was spiked with 5 mg L^{-1} of TCE in the beginning and incubated in the dark at 12°C. Headspace samples were analyzed for the concentration of CEs, methane, ethene and ethane. After degradation of the first TCE spike, bottles were spiked with 11 mg L^{-1} of TCE and lactate and molasses were added in the respective treatments. This procedure was repeated once, resulting in three TCE, lactate or molasses spikes per microcosm. The treatments with sediment extract were only amended with 11 mg L^{-1} TCE due to the persistent presence of DOC. All microcosm experiments were performed in duplicate.

To determine the number of *Dehalococcoides mccartyi* per microcosm, DNA extraction and real-time quantitative PCR were performed as described by *Atashgahi et al.* [2013]. Additionally, *Eubacteria*, *Desulfitobacterium*, *Dehalobacter*, *reductive dehalogenase genes* (coding certain enzymes) as well as *mcrA* indicating methanogenesis [*Hamonts*, 2009; *Hamonts et al.*, 2014; *Schneidewind et al.*, 2014] were targeted.

Concentrations of TCE, cis-DCE, VC methane, ethene, ethane and methane were analyzed as described by *Atashgahi et al.* [2013]. DOC content was determined as described in *Schneidewind et al.* [2014]. All lab experiments were conducted by other researchers from VITO.

2.4.2 Modeling

2.4.2.1 Kinetic Models

Complex models have been developed to include any of the assumed driving factors of dechlorination such as donor availability, redox conditions, inhibition processes, microbial numbers or microbial activity [*Chambon et al.*, 2013]. To determine the parameters defining the sequential dechlorination from TCE to VC in the microcosms, three kinetic models of increasing complexity were applied here: (1) first order degradation, (2) Michaelis-Menten enzyme kinetics and (3) Monod kinetics where microbial growth is taken into account as described by *Haston and McCarty* [1999]. The degradation rates for first order kinetics were calculated according to Eq. (1-13) for each species with λ_i in [day^{-1}] and C_i in [mM].

Degradation rates for Michaelis-Menten enzyme kinetics were then calculated by extending first order kinetics for substrate concentration dependency and competitive inhibition using

$$r_i = \frac{\lambda_i C_i}{K_{s,i}\left(1 + \frac{C_{i+1}}{I_{i+1}} + \frac{C_{i+2}}{I_{i+2}}\right) + C_i} \tag{2-1}$$

with λ_i in [mmol cell^{-1} day^{-1}], $K_{s,i}$ in [mM] or [mmol L^{-1}], $C_{i,i+1,i+2}$ in [mM] as the aqueous concentrations of compound i and its parent compounds and $I_{i+1,i+2}$ in [mM] as the competitive inhibition constants of the parent compounds on the dechlorination of daughter products. Degradation rates for Monod kinetics were calculated with the modeled *Dehalococcoides mccartyi* concentration X_{mod} and applying Eqs. (1-15) and (1-16).

Both Michaelis-Menten and Monod kinetics include competitive inhibition but no Haldane or self-inhibition since CE concentrations were much lower than the inhibitive concentrations described in literature [*Yu and Semprini*, 2004; *Haest et al.*, 2010]. Volatilization of the CE compounds in the microcosms was accounted for by dividing r_i with $1 + H_i \frac{V_g}{V_{aq}}$, where H_i is the species dependent Henry constant at 12°C with 0.2 for TCE, 0.1 for cis-DCE, 0.7 for VC [*Staudinger and Roberts*, 2001] and 6.4 for ethene [recalculated after *Fry et al.*, 1995]. $V_g = 50$ mL and $V_{aq} = 90$ mL are the volumes of the gaseous and aqueous phase in each microcosm.

2.4.2.2 Parameter Estimation

Parameter estimates are obtained by modeling. By comparing simulated (modeled) results to observed data one attempts to find the best fit between both according to some criterion. This procedure is called model calibration, during which an inverse problem is solved. As all model parameters are optimized (fitted) simultaneously, the inverse problem, which is ill-posed, allows for several equally viable solutions meaning that combinations of different parameter estimates can be equally correct from a mathematical point of view. However, some of these might be problematic from a conceptual point of view. This has to be taken into account when analyzing the results later. An optimization of model parameters during calibration to describe the fit between modeled and observed results can be achieved by using **(i)** a manual trial-and-error approach, or **(ii)** automated calibration procedures.

(i) Manual calibration is often not feasible due to a large number of interacting parameters and time constraints. What is a good model fit might depend on chosen starting values and is often left to the subjectivity and conceptual understanding of the modeler, which can lead to calibrated parameters not always representing the optimal values providing the best possible fit to the observations [*Hill and Tiedeman*, 2007].

(ii) Automated calibration methods provide a more objective means of calibration. The optimal parameter set is usually derived by optimizing an objective function applying some numerical algorithm that finds the function's global extreme values, which however can

become tricky if local maxima/minima exist. Depending on the modeling approach automated calibration methods can be grouped into deterministic and stochastic methods. The former group uses local search algorithms such as the Gauss-Newton or Levenberg-Marquardt algorithms and includes the Maximum-Likelihood and Least-Square methods [*Zheng and Bennett*, 2002]. The latter group uses global search algorithms (e.g. genetic or evolutionary algorithms) and includes e.g. the self-calibrated method [*Gómez-Hernández et al.*, 1997] and the ensemble Kalman filter [*Evensen*, 2003]. Additionally, the performance of automated calibration procedures can also be influenced by whether parameters are bound by upper and/or lower maximum parameter values and the initial values assigned to the parameters to be calibrated.

For modeling of the reductive dechlorination in the microcosms three objectives were defined for each microcosm and considered simultaneously during calibration at all sampling occasions, i.e. the deviations of the modeled from the observed concentrations of TCE, cis-DCE and VC. Model deviation was calculated using the RMSE between observed and simulated data as shown in Eq. (1-31). The *Dehalococcoides mccartyi* concentration could not be taken as a fourth objective as only three data points per microcosm were available. It was thus just used to visually verify the outcome of the Monod model. First order and Michaelis-Menten kinetics were calibrated using only data from the third TCE spike since these were considered to represent a steady-state condition in the microcosms. The optimized results were then used as starting values for Monod kinetics, for which all three TCE spikes were modeled.

The parameters describing the Michaelis-Menten and Monod kinetics are highly correlated [*Robinson and Tiedje*, 1983; *Liu and Zachara*, 2001], impeding model calibration and making the use of a simple inverse calibration technique impossible. Especially the sequential nature of the dechlorination reaction and the competitive inhibition influence the observed concentrations. To overcome this limitation, a MATLAB-based global optimization algorithm called AMALGAM [*Vrugt and Robinson*, 2007; *Vrugt et al.*, 2009] was applied that can handle multiple objectives. AMALGAM is an evolutionary optimization method [see *Maier et al.*, 2014 for a recent review] that uses simultaneous multi-method search (Figure 2.3) by employing several optimization algorithms simultaneously. It includes a genetic algorithm [*Deb et al.*, 2002], a particle-swarm optimizer [*Kennedy et al.*, 2001], a differential evolution algorithm [*Storn and Price*, 1997] and an adaptive metropolis search algorithm [*Haario et al.*, 2001]. AMALGAM also employs self-adaptive offspring creation (Figure 2.3). While for the creation of the parent population all search algorithms contribute the similar number of optimized results, the more suitable optimization algorithms contribute more points to each subsequent daughter population than the less suitable ones indicating differences in reproductive success [*Vrugt and Robinson*, 2007]. As a result, AMALGAM produces point estimates of parameter combinations without information regarding the confidence of the result. Many optimization runs lead to numerous point estimates (many possible parameter combinations).

As multiple objectives are considered, AMALGAM searches for a set of optimal solutions on a Pareto-surface, where all objectives are met with equal efficiency and one objective cannot be improved without degrading at least one other objective. As no unique solution exists (problem of non-uniqueness, see *Beven* [2001] for a discussion) all points on a Pareto surface (front) are optimal solutions to the optimization problem. However, for further analysis and graphical representation it might be necessary to define a single most representative solution (representative parameter set). *Werisch et al.* [2014] discuss several alternatives, one of which is the use of a compromise solution [*Wöhling et al.*, 2008] that can be identified by the smallest Euclidean distance to a reference point, where all objectives are perfectly met. In the problem at hand that point would be where all RMSEs are zero, i.e. the zero-objective-point of the 3D space. The point on the Pareto surface closest to the zero-objective-point (i.e. with the smallest Euclidean distance) was then identified with a nearest-neighbor search. For the example shown here, the objective space did not have to be normalized as only concentrations were used in the objectives.

AMALGAM was applied for a similar optimization problem by *Haest et al.* [2010], who studied the self-inhibition of CEs in microcosms during reductive dechlorination. It was evaluated favorably compared to other multi-objective methods [*Wöhling et al.*, 2008] and was found to perform well in benchmark tests [*Krauße et al.*, 2012].

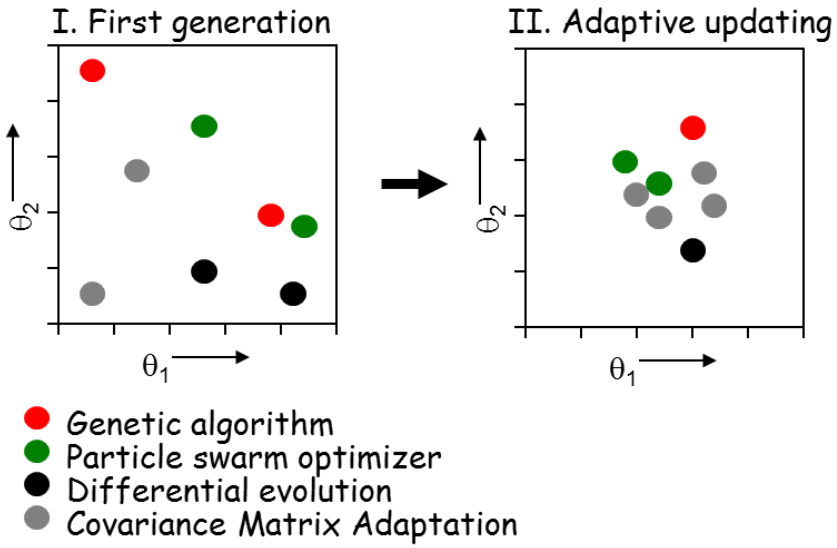

Figure 2.3: Basic concept of AMALGAM including multi-method search and adaptive offspring generation. Per run each of the four algorithms contributes with a number of solutions (offspring points). These points are put together in a combined daughter population, which is compared to the previous generation. This step is repeated many times. Depending on the optimization problem, the algorithms used contribute an unequal number of solutions (points) to each daughter population (they show different reproductive success). Source: *Vrugt* [2005].

2.4.2.3 Boundary Conditions

As parameter optimization with AMALGAM requires boundary conditions and initial values, upper and lower boundary values were assigned to each model parameter in all three kinetic models. This involved a literature study to find acceptable ranges of parameter values for the parameters in question. Additionally, several trial model runs were performed to see how many parameter combinations were close to the boundaries. With this in mind adequate intervals (parameter spaces) were defined, from which the parameter estimates were chosen by the models. Intervals for λ_i in the Michaelis-Menten kinetics model were determined as follows:

1. Representative results for λ_i [mmol cell^{-1} d^{-1}] found in the literature [*Garant and Lynd*, 1998; *Haston and McCarty*, 1999] were multiplied with the *Dehalococcoides mccartyi* concentration X_{obs} [cells L^{-1}] at the time of the third TCE spike observed in the individual microcosms to obtain λ_i in [mmol L^{-1} d^{-1}].
2. The upper and lower boundaries for these new microcosm-specific values were then defined by using a factor of 10,000 before model runs were started.

The same intervals were then used for λ_i and assumed in [d^{-1}] for the first order kinetics.

Intervals for λ_i [mmol cell^{-1} d^{-1}] in the Monod kinetic models were determined as follows:

1. Before performing spike one, X_{obs} was determined and set to 5×10^4 [cells L^{-1}], i.e. half of the detection limit, if no microorganisms were encountered at the start of the experiment.
2. Afterwards, the average X_{obs} for spikes one and two was calculated. This value was then divided from the λ_i [mmol L^{-1} d^{-1}] obtained from the Michaelis-Menten model.
3. These starting values were then multiplied/divided by a factor of 1000.

Intervals for half velocity constants, inhibition constants and decay rates were solely determined based on literature values [*Garant and Lynd*, 1998; *Haston and McCarty*, 1999; *Yu and Semprini*, 2004; *Haest et al.*, 2010]. For the yield coefficient, the upper and lower boundaries vary by a factor of three from the individual microcosm-specific yields initially calculated using observed microbial data from spikes one and two as well as measured CE concentrations. Interval ranges for all parameters of all three kinetic models are shown in Table 2.2. For the actual modeling all intervals were log-transformed as this is favorable for AMALGAM. By using the logarithm, numerical stability should be increased as the optimizer has to handle much smaller numbers. Also, when a parameter spans several orders of magnitude, a linear interval sampling would be "biased" because smaller values would be sampled less often than larger values.

Table 2.2: Tested parameter intervals for First-order, Michaelis-Menten and Monod kinetic models. Source: Adapted from *Schneidewind et al.* [2014].

		λ_{TCE}	$K_{s,TCE}$	I_{TCE}	$\lambda_{cis\text{-}DCE}$	$K_{s,cis\text{-}DCE}$	$I_{cis\text{-}DCE}$	λ_{VC}	$K_{s,VC}$	b_i [b]	Y_i
		a	[µM]	[µM]	*a*	[µM]	[µM]	*a*	[µM]	[d^{-1}]	[cells μmol^{-1}]
First-order	Min[c]	1.31E-05			1.02E-05			4.37E-06			
	Max[c]	6.63E+06			5.15E+06			2.21E+06			
Michaelis-Menten	Min[c]	1.31E-05	4.19E-01	3.70E+00	1.02E-05	3.78E-01	3.70E+00	4.37E-06	3.78E-01		
	Max[c]	6.63E+06	4.19E+01	3.70E+02	5.15E+06	3.78E+01	3.70E+02	2.21E+06	3.78E+01		
Monod	Min[c]	1.69E-14	4.19E-01	3.70E+00	1.31E-14	3.78E-01	3.70E+00	5.63E-15	3.78E-01	2.00E-02	6.01E+05
	Max[c]	4.06E-04	4.19E+01	3.70E+02	3.16E-04	3.78E+01	3.70E+02	1.35E-04	3.78E+01	5.00E-02	1.43E+09

a For the Monod model λ_i values are in [µmol $cell^{-1}$ d^{-1}], for Michelis-Menten [µmol L^{-1} d^{-1}], for First-order in [d^{-1}]
b Limits for decay are average values taken from literature sources
c Values are overall minimum and maximum values for all batches

2.4.2.4 Sensitivity Analysis

A sensitivity analysis is performed to study the response of model results to changes in input parameters. If model results are sensitive to a certain parameter more effort should be put on a proper characterization of that parameter to reduce uncertainty. If such a parameter has a high uncertainty associated with it, the predictive capabilities of the model will be reduced distinctly [*Zheng and Bennett*, 2002]. The same principle can be applied to study the reliability of a parameter or parameter combination estimated by inverse modeling. The relationship between observed data and modeled results can be assessed by error calculation, e.g. by using the RMSE. A strong increase in RMSE due to a minor change in the model parameter value (i.e. the RMSE is sensitive to that parameter) would mean that the initial parameter estimate had been reliable. An RMSE that is very insensitive to a parameter change means that the parameter is of less importance in the estimation process [Bear and Cheng, 2010].

For the microcosms a sensitivity analysis was performed using data from the third TCE spike in order to evaluate the relative importance of the parameters that were determined with the Monod model. The model was extended to investigate the effect of the electron donor concentration on the reaction rates [*Fennell and Gossett*, 1998; *Chambon et al.*, 2013] using

$$r_i = \frac{\lambda_i C_i X_{obs}}{K_{s,i}\left(1 + \frac{C_{i+1}}{I_{i+1}} + \frac{C_{i+2}}{I_{i+2}}\right) + C_i} \cdot \frac{C_d}{C_d + K_{s,d}} \tag{2-2}$$

with C_d [mM] as the concentration of the electron donor and $K_{s,d}$ [mM] as the half-saturation constant for donor usage in the dechlorination reaction. The Morris OAT scheme [*Morris*, 1991] was used for a global sensitivity analysis. This one-step-at-a-time scheme changes one input value per run and estimates the global effect of a parameter by averaging local sensitivities, i.e. elementary effects in a number of points in the parameter space. For one parameter a high mean of the distribution indicates that this parameter has an overall influence on the output while a high standard deviation indicates that either the parameter is interacting with other parameters or that the parameter's effect is non-linear. The analysis used 1000 starting points and the tested intervals were set to the maximum and minimum values that were obtained from the parameter optimization. C_d was initially set to 100 µM and decreased linearly to 0.1 µM by the end of the experiment. $K_{s,d}$ was varied from 5 to 50 µM. The latter value would approximate a donor limitation halfway through the experiment. The model shown in Eq. (2-2) is a conceptual representation of the donor limitation. In the microcosm experiments, neither the final electron donor (H2 or acetate) nor its utilization rate and the threshold level for the donor in the mixed community are known. Therefore, the proposed straightforward analysis of donor limitation was considered the most appropriate.

2.5 Results and Discussion

2.5.1 Microcosm Tests

The extent of the dechlorination reactions in the microcosms is shown in Figure 2.4. All carbon sources facilitated TCE dechlorination to cis-DCE and VC as prevalent intermediates, which were dechlorinated to ethene as the primary end-product, except in the sediment microcosms where ethane was the end product (Figure 2.4). This suggests that native dechlorinating populations are present in the aquifer of the Zenne site as was confirmed by qPCR analysis (Figure A2.1). No degradation of TCE or formation of any reduced products was observed under natural attenuation conditions indicating that the oligotrophic nature of the aquifer at the Zenne site could be impeding a complete degradation to ethene. Therefore, it was assumed that the addition of an external carbon source to the contaminated aquifer is inevitable in order to stimulate reductive dechlorination.

TCE dechlorination in the lactate-amended microcosms initially started with a long lag phase and proceeded to ethene for the first spike only in microcosms of PB26 (Figure 2.4E). The TCE degradation proceeded to ethene in all the lactate-amended microcosms after the third spike (Fig. 2.3A, C, E). The molasses-amended microcosms showed a short TCE dechlorination lag phase during the first spike but complete degradation to ethene after the second and third spikes (Fig. 2.4E). All microcosms containing streambed sediment instead of aquifer material show a shorter initial lag phase before degradation and a faster degradation overall demonstrating the increased dechlorination potential of the streambed. Microcosms of PB26 amended with sedimented extract degraded TCE at higher rates than the microcosms with centrifuged extract during the second and third TCE spikes. DOC concentration at the beginning and the end of each spike is shown in Figure A.2.2.

The concentration always reduces in all microcosms but dechlorination was only limited in microcosms using sediment extracts (location PB26) since the extracts were not renewed before each TCE spike. A carbon source limitation in those microcosms could also be derived from the absence of methane production while methane production was high in the other microcosms (except for SB3 and lactate), ranging to up to 1200 µmol/bottle (Figure A2.3). Methane production tended to decrease after the subsequent TCE spikes in the streambed sediment microcosms, whereas it remained stable or increased up to three-fold in the lactate- and molasses amended microcosms.

Bacterial growth (Figure A2.1) depends strongly on the substrate added and on the initial species concentration. Microcosms with streambed sediments already demonstrated a high number of *Dehalococcoides mccartyi* at the beginning of the first spikes and subsequent growth was much less than for other microcosms. This again indicates that under natural conditions the streambed of the Zenne is much more prone to dechlorination than the aquifer. *Dehalobacter* growth was not significantly stimulated but *Desulfitobacterium* numbers increased significantly in most microcosms. Additional results can be found in *Schneidewind et al.* [2014].

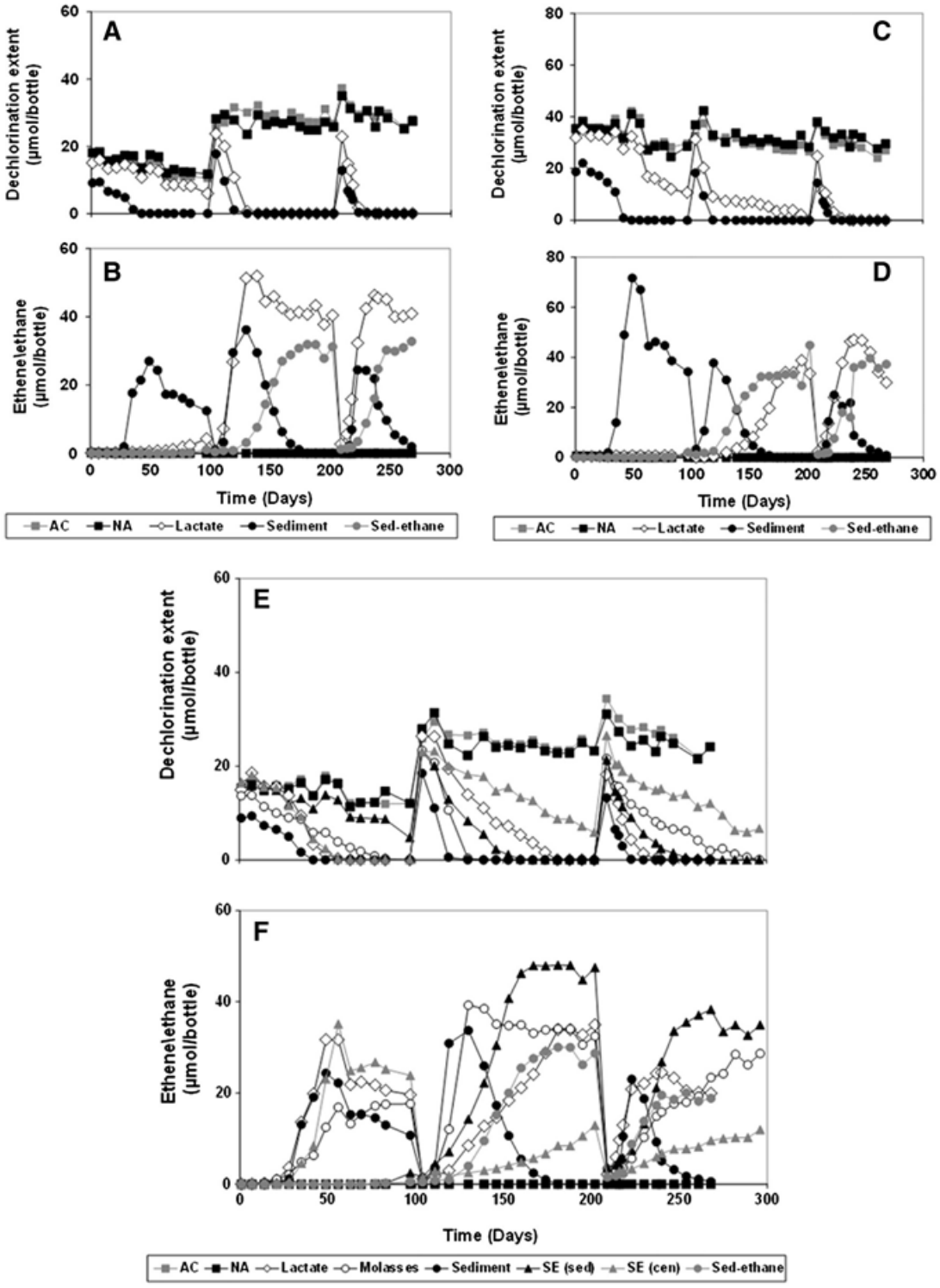

Figure 2.4: The extent of the dechlorination reaction in microcosms from locations SB2 (A), SB3 (C), and PB26 (E), and the accumulation of ethene and ethane (produced only in the sediment microcosms) (B, D, F). The data are presented as dechlorination extent in panels A, C, and E, i.e. the total moles of chloride from chlorinated compounds in the duplicate microcosms: [TCE] × 3 + [DCE] × 2 + [VC] and in panels B, D, and F as ethene × 6 and ethane × 6. AC: abiotic control, NA: natural attenuation, SE (sed): sediment extract obtained after sedimentation, SE (cen): sediment extract obtained after centrifugation, Sed-ethane: ethane formation in sediment microcosms. Source: *Schneidewind et al.* [2014].

The persistence of DOC in the tests with sediment extract indicated that the organic matter from the streambed sediment was less readily available for degradation than lactate or molasses. As such, the observed absence of methanogenesis in the microcosms stimulated with sediment extracts is similar to previous research that points to the competitive advantage of dechlorinators compared to methanogens when available resources are limited [*Duhamel and Edwards*, 2007; *Atashgahi et al.*, 2014].

2.5.2 Modeling

The results for λ_i in [d^{-1}] and in [mmol $cell^{-1}$ d^{-1}] for the First order kinetics are shown in Table A2.1 and a summary is provided in Table 2.3. The results (one per microcosm) represent only points on the Pareto surface closest to the origin. All graphs are provided by *Schneidewind et al.* [2014] in the supplementary information and in an additional .xlsx file. To obtain λ_i in [mmol $cell^{-1}$ d^{-1}], values in [d^{-1}] were divided by the yields [cells $mmol^{-1}$] calculated for each microcosm. Rate coefficients for TCE were highest in microcosms with streambed sediments although microcosms amended with lactate and sedimented sediments show same order of magnitude values. Microcosms amended with molasses and centrifuged sediments show values that are one order of magnitude lower. For cis-DCE and VC [d^{-1}] values are highest in lactate amended microcosms followed by microcosms with streambed sediments. Due to the different yields, streambed sediment microcosms can show a higher value in [mmol $cell^{-1}$ d^{-1}]. This demonstrates that taking into account microbial information in the determination of rate coefficients can lead to a different attenuation behavior. On average, rate coefficients for cis-DCE and VC are slightly higher than for TCE (Table 2.3).

RMSE values (can be found in an additional .xlsx file) for the three CEs are in the same order of magnitude except for some of the lactate amended microcosms where RMSE values for cis-DCE and VC are one order of magnitude smaller than for TCE. In general, the first-order model adequately described the observed dechlorination after the third spike, for which it was calibrated. Nevertheless, the data indicate a close to $zero^{th}$-order degradation in most treatments. Compared to literature values (Table 2.6), TCE rate coefficients are similar to other literature sources while cis-DCE and VC values are higher than those in *Wilson et al.* [1994] as the latter were determined in situ.

Microcosm-specific degradation parameters calculated with the Michaelis-Menten kinetics model are shown in Figure A2.2 and a summary is provided in Table 2.4. No clear trend is visible as to which amended carbon source or which substrate shows generally highest and lowest dechlorination potential. The maximal degradation coefficients of the Michaelis-Menten kinetics are mostly higher than values reported in literature (Table 2.6). This is most likely due to the normalization of the degradation rate to the measured *Dehalococcoides mccartyi* cell numbers in our experiment instead of using a conversion factor based on dry biomass that was used for other literature values. The latter could overestimate the fraction of *Dehalococcoides mccartyi* cells in a mixed community yielding lower normalized λ_i. RMSE values (can be found in an additional .xlsx file) for cis-DCE and VC are slightly smaller than

those for TCE. For microcosms amended with molasses and for those using centrifuged sediment extract RMSE values are up to an order of magnitude higher than for the other microcosms hinting towards more difficulties during optimization.

Table 2.3: Overall minimum, maximum, average values and standard deviations for optimized parameters for the First order kinetics model. Source: *own*.

Item	λ_{TCE} [d^{-1}]	λ_{cDCE} [d^{-1}]	λ_{VC} [d^{-1}]	λ_{TCE} [mmol $cell^{-1}$ d^{-1}]	λ_{cDCE} [mmol $cell^{-1}$ d^{-1}]	λ_{VC} [mmol $cell^{-1}$ d^{-1}]
Maximum	3.78E-01	3.93E+00	3.07E+00	1.75E-10	1.12E-10	3.25E-10
Minimum	2.74E-02	3.13E-02	5.24E-02	8.46E-14	3.89E-13	2.29E-13
Ar. Mean	1.84E-01	5.59E-01	6.28E-01	1.96E-11	2.17E-11	3.64E-11
σ	1.26E-01	9.22E-01	7.60E-01	4.77E-11	3.26E-11	7.97E-11

Microcosm-specific degradation parameters calculated with the Monod kinetics model are shown in Figure A2.3 and a summary is provided in Table 2.5. Maximal degradation coefficients for the Monod kinetics are more in line with literature values (Table 2.6). Values for microcosms using sedimented sediment extract are generally lowest, while for the other microcosms no clear trend is visible. Also, differences between duplicate batches can be up to three orders of magnitude due to different *Dehalococcoides mccartyi* numbers leading also to very variable yield coefficients. Results for the half-saturation, competitive inhibition constants and the yield coefficients are also in line with values from literature (Table 2.6). RMSE values (additional .xlsx file) for cis-DCE and VC are up to two orders of magnitude smaller than for TCE. This is probably due to the fact that the Monod model was used on the entire experiment while the other models were only used on the third TCE spike. As especially the TCE concentration shows a lag behavior for the first spike but not the subsequent ones parameter optimization for the entire experiment can be considered more complex and the data fitting is of less quality. Microcosms using sedimented streambed sediment extract show degradation coefficients of one to two orders of magnitude smaller than in the other treatments. This could be due to the lack of methanogenesis (chapter 2.4.2). Alternatively, the electron donor could have become a limiting factor since the DOC had declined to less than 5% of the starting concentration by the end of the experiment.

In general, First-order, Michaelis-Menten and Monod kinetics described the observed dechlorination with varying success. The half-saturation constants as substrate-dependent degradation parameters were better approximated using Michaelis-Menten kinetics. The calibrated Michaelis-Menten and First-order kinetics, however, could not approximate the lag-phase at the start of the experiment. This was better approximated using Monod kinetics, while the latter performed poorer for the subsequent spikes. This is also illustrated in Figure 2.5 for the microcosm of location PB-26 with sedimented extract. Spikes two and three were better approximated by the First-order and Michaelis-Menten models, while the beginning of

the experiment (there especially also the observed ethene concentration) was better approximated with the Monod model.

Table 2.4: Overall minimum, maximum, average values and standard deviations for optimized parameters for the Michaelis-Menten kinetics model. Source: *own*.

Item	λ_{TCE} [mmol cell^{-1}d^{-1}]	$K_{s,TCE}$ [mM]	I_{TCE} [mM]	λ_{cDCE} [mmol cell^{-1}d^{-1}]	$K_{s,cDCE}$ [mM]	I_{cDCE} [mM]	λ_{VC} [mmol cell^{-1}d^{-1}]	$K_{s,VC}$ [mM]
Maximum	8.24E-10	4.19E-02	3.70E-01	6.48E-09	3.78E-02	3.70E-01	6.93E-10	3.78E-02
Minimum	1.22E-13	2.10E-03	3.70E-03	6.46E-14	3.78E-03	4.27E-03	8.96E-14	3.78E-03
Ar. Mean	5.58E-11	1.37E-02	1.41E-01	3.77E-10	1.29E-02	1.03E-01	7.58E-11	1.42E-02
σ	1.93E-10	1.65E-02	1.59E-01	1.52E-09	1.15E-02	1.06E-01	2.08E-10	1.21E-02

Table 2.5: Overall minimum, maximum, average values and standard deviations for optimized parameters for the Monod kinetics model. Source: *own*.

Item	λ_{TCE} *a*	$K_{s,TCE}$ [mM]	I_{TCE} [mM]	λ_{cDCE} *a*	$K_{s,cDCE}$ [mM]	I_{cDCE} [mM]	λ_{VC} *a*	$K_{s,VC}$ [mM]	b [d^{-1}]	Y *b*
Maximum	6.87E-11	4.19E-02	3.70E-01	3.20E-08	3.78E-02	3.70E-01	4.84E-09	3.78E-02	5.00E-02	1.43E+12
Minimum	1.07E-13	4.36E-04	3.70E-03	6.12E-14	3.78E-04	3.70E-03	9.96E-14	3.78E-04	2.00E-02	2.27E+09
Ar. Mean	1.33E-11	1.81E-02	1.56E-01	2.48E-09	1.26E-02	8.64E-02	5.25E-10	1.29E-02	2.80E-02	2.18E+11
σ	2.25E-11	1.60E-02	1.32E-01	7.86E-09	1.60E-02	1.23E-01	1.25E-09	1.37E-02	1.28E-02	3.54E+11

a in [mmol cell^{-1} d^{-1}]
b in [cells mmol^{-1}]

As already discussed, parameter optimization with AMALGAM produces many possible solutions (non-uniqueness) on the Pareto front/surface that are able to approximate the observations. For example, Monod models were run with 10,000 iterations and produced about 3% possible solutions. To demonstrate the impact of non-uniqueness Figure 2.6 shows for microcosm PB26 with sedimented extract the 50 best parameter combinations from the automated calibration. All parameters but the degradation coefficients span a large part of the calibration interval (normalized), indicating a larger parameter uncertainty, and/or a strong correlation between parameters.

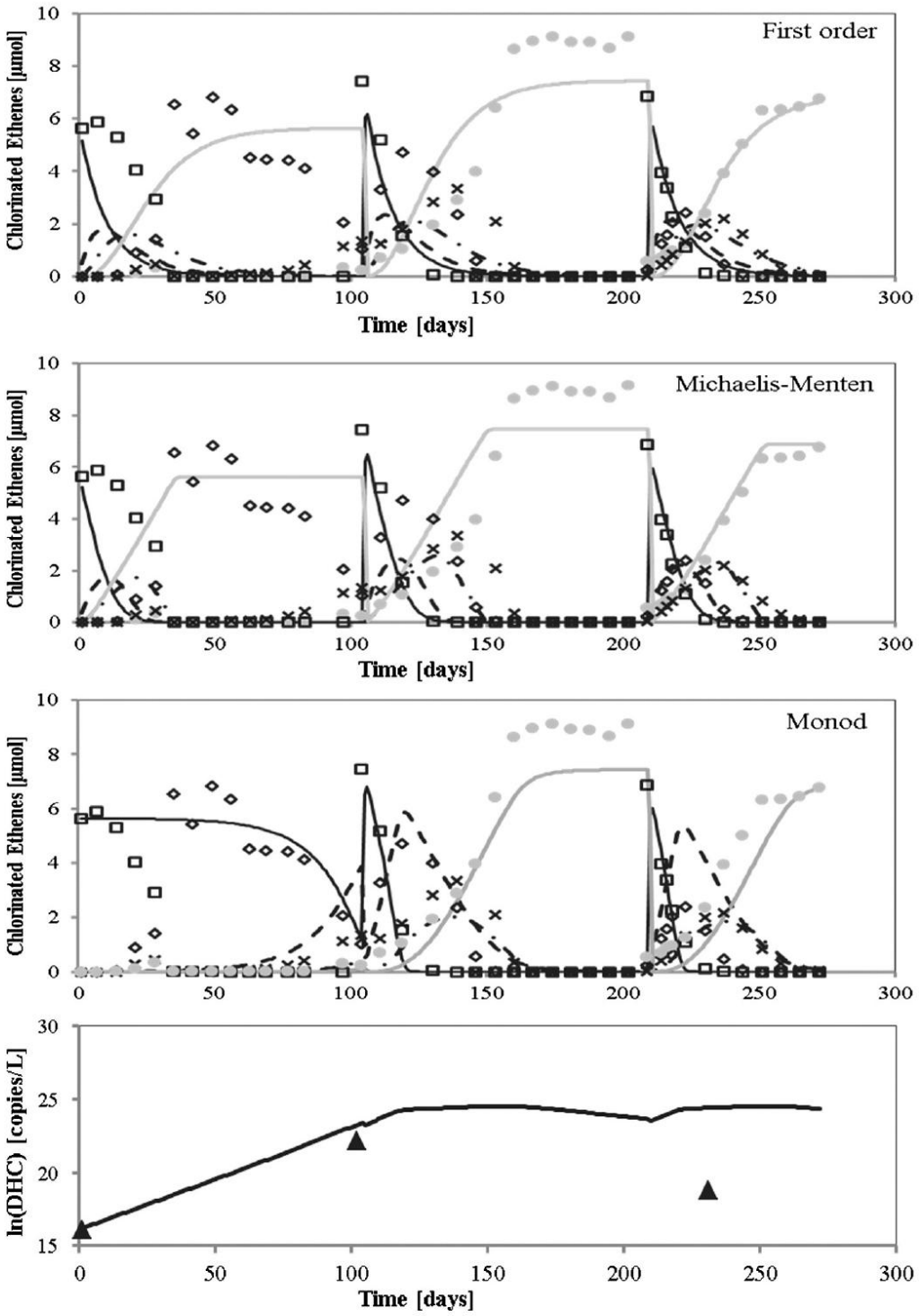

Figure 2.5: Model results for location PB26 batch 2 amended with sedimented extract using First-order (top), Michaelis-Menten (middle) and Monod (bottom) kinetics. Observed data: □ TCE, ◊ cis-DCE, × VC, ● Ethene and▲16S rRNA gene copy numbers of *Dehalococcoides mccartyi* (DHC). Modeled data: — TCE, - - cis-DCE, -·-·VC, ethene and — cell numbers of DHC. The 16S rRNA copy numbers were calculated from triplicate qPCR measurements and are presumed to represent DHC cell numbers in a one-to-one relationship. Source: *Schneidewind et al.* [2014].

Table 2.6: Range of optimized parameters obtained from modeling 18 batches compared to literature values. Only the points on the Pareto surface closest to the zero-objective point are considered here. Source: Adapted from *Schneidewind et al.* [2014].

	λ_{TCE} ***b***	$K_{s,TCE}$ **[mM]**	I_{TCE} **[mM]**	λ_{cDCE} ***b***	$K_{s,cDCE}$ **[mM]**	I_{cDCE} **[mM]**	λ_{VC} ***b***	$K_{s,VC}$ **[mM]**	**b** $[d^{-1}]$	**Y** [cells $mmol^{-1}$]
First-order model[a]	2.74×10^{-2} - 3.78×10^{-1}	-	-	3.13×10^{-2} - 3.93	-	-	5.24×10^{-2} - 3.07	-	-	-
Da Silva and Alvarez [2008][a]	7.90×10^{-1} - 15.89	-	-	-	-	-	-	-	-	-
Wilson et al. [1994][a,c]	8.00×10^{-3}	-	-	1.40×10^{-3} - 2.00×10^{-3}	-	-	5.00×10^{-4} - 2.00×10^{-3}	-	-	-
First-order model	8.46×10^{-14} - 1.75×10^{-10}	-	-	3.89×10^{-13} - 1.12×10^{-10}	-	-	2.29×10^{-13} - 3.25×10^{-10}	-	-	-
Michaelis-Menten model	1.22×10^{-13} - 8.24×10^{-10}	0.0021 - 0.042	0.0037 - 0.370	6.46×10^{-14} - 6.48×10^{-9}	0.0038 - 0.0378	0.0037 - 0.370	6.96×10^{-14} - 6.93×10^{-10}	0.0038 - 0.0378	-	-
Garant and Lynd [1998][d]	3.94×10^{-14}	0.0174	0.0174	2.47×10^{-14}	0.0119	0.0119	2.80×10^{-14}	0.383	-	-
Haston and McCarty [1999][d]	6.72×10^{-15}	0.0014	-	1.55×10^{-15}	0.0033	-	1.43×10^{-15}	0.0026	-	-
Monod-Model	1.07×10^{-13} - 6.87×10^{-11}	0.00044 - 0.0419	0.0037 - 0.370	6.12×10^{-14} - 3.20×10^{-8}	0.00038 - 0.0378	0.0037 - 0.370	4.84×10^{-9} - 9.96×10^{-14}	0.00038 - 0.0378	0.020 - 0.05	2.27×10^{9} - 1.43×10^{12}
Haest et al. [2010]	2.79×10^{-10}	0.0042	0.370	1.01×10^{-11}	0.0997	0.0997	2.74×10^{-12}	0.0997	0.029 - 0.05	7.76×10^{8} - 2.41×10^{10}[e]
Yu and Semprini [2004][d]	2.60×10^{-13}	0.0028	0.0028	4.60×10^{-14}	0.0019	0.0019	5.12×10^{-15}	0.602	0.024	2.86×10^{12}
Yu and Semprini [2004][d]	2.63×10^{-13}	0.0018	0.0018	2.90×10^{-14}	0.0018	0.0018	1.70×10^{-14}	0.063	0.024	2.86×10^{12}
Schaefer et al. [2009]	3.12×10^{-11}	0.0032	-	1.25×10^{-11}	0.002	0.0052	3.36×10^{-11}	0.0014	-	4.4×10^{9}[f]

a λ_i in $[d^{-1}]$
b in [mmol $cell^{-1}$ d^{-1}]
c determined in situ for aquifer material and anaerobic conditions
d Recalculated λ_i values according to *Duhamel et al.* [2004] assuming a conversion factor of 4.2×10^{-15} g dry weight of cell material per gene copy and a protein content of 50%
e Species-dependent yield reported
f Yield only reported for cis-DCE

A large parameter uncertainty can be the result of the experimental setup and of a lack of understanding all the underlying processes (model structure uncertainty or process uncertainty). There was no concentration gradient of the CEs to independently evaluate the effect of the half-saturation or inhibition constants. The eventual influence of these processes on the degradation reaction could thus not be decisively assessed from the observations. Parameter uncertainty could also result from the sequential reactions in the dechlorination reaction as is indicated by the significantly larger spread of the 50 best parameter values of the degradation rate coefficient for cis-DCE and VC degradation than for TCE degradation. The larger uncertainty for the parameters of the daughter products could also originate from the automated calibration itself since the observed concentrations of daughter products were small. The resulting outcomes of the simulated dechlorination reactions remain rather narrow indicating the small influence of competitive inhibition in this experiment since these parameters span the entire calibration interval, i.e. more than an order of magnitude difference. The Monod model could not adequately approximate the relation between the *Dehalococcoides mccartyi* numbers and the observed dechlorination rates as is also indicated by the large range in the simulated *Dehalococcoides mccartyi* numbers.

The inadequacy of the models to adequately approximate the overall dechlorination reaction could be due to a number of reasons. For example, the supporting microbial community could have played an important role as suggested by the fast degradation in the microcosms with streambed sediments. The positive influence of the supporting microbial community such as homoacetogens capable of providing *Dehalococcoides mccartyi* with acetate and vitamin B12 [*Ziv-El et al.*, 2012] could play an important part. In addition, other organohalide respiring bacteria could have degraded some of the chlorinated ethenes present, such as *Desulfitobacterium*, whose numbers increased significantly after the third TCE spike (Fig. A2.1). Moreover, the occasionally observed higher sum of *rdh* genes compared to *Dehalococcoides mccartyi* numbers suggests the presence of unknown organohalide respiring microorganisms harboring *rdh* genes in addition to *Dehalococcoides mccartyi*.

The influence of the electron donor concentration was evaluated in the sensitivity analysis for the Monod models (Figure 5 in *Schneidewind et al.* [2014]). Results showed that yield coefficient and maximal degradation coefficients of TCE and cis-DCE were the most influential parameters and that the electron donor concentration was of minor importance in this experiment, taking into account the model assumption that the electron donor concentration was non-limiting at the start of the experiment and decreased linearly.

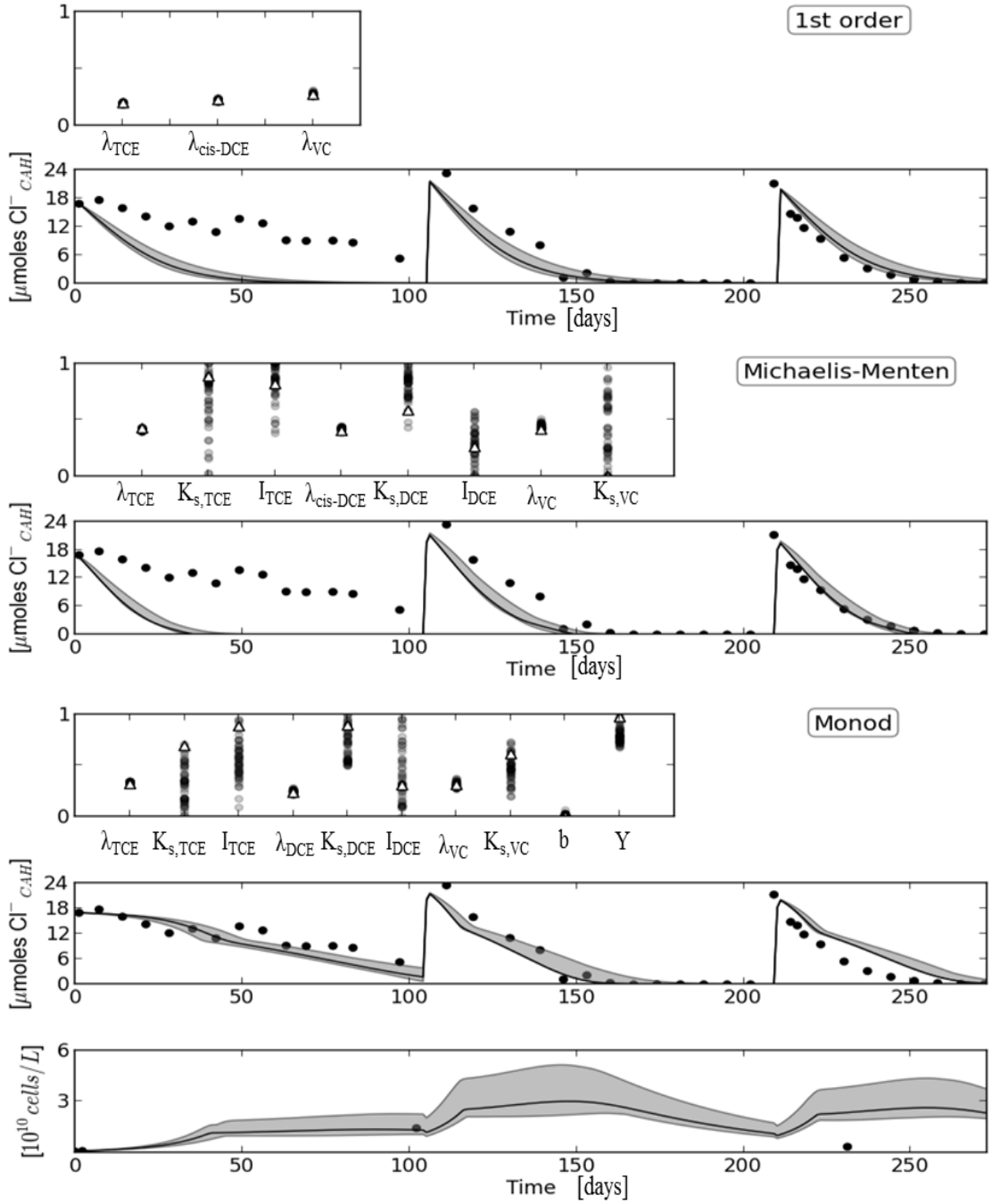

Figure 2.6: Parameter values of the 50 best combinations for each of the kinetic formulations and the related simulations for the overall dechlorination reaction using the chlorine atoms on the CE substrate as a proxy, i.e. [TCE] × 3 + [DCE] × 2 + [VC], and the *Dehalococcoides mccartyi* cells for the Monod kinetics. Parameter values were normalized to the interval that was considered acceptable in the automatic calibration. The parameter combinations are plotted in gray so that darker regions indicate a higher density of selected values with the selected 'optimal' combination of parameters indicated by the white triangles. The model simulations of the 50 best parameter combinations are bounded by the shaded region with the result of the 'optimal' parameter set indicated by the black line, and observed values for the treatment of sedimented sediment extract by black dots. Source: Adapted from *Schneidewind et al.* [2014].

2.6 Conclusions

An accurate simulation of microbial degradation is important to understand attenuation processes and determine the attenuation potential of hyporheic zones and their connected aquifers. Modeling can help to keep the uncertainties inherent to reactive transport within acceptable boundaries. It ensures credibility that is necessary in order to stimulate bioremediation as a trustworthy technique in soil and groundwater clean-up. In particular the time for a complete remediation to ethene should be approximated to a good extent. The results of the microcosm tests illustrate the need for biostimulation in the Zenne aquifer since no degradation of CEs was observed under natural attenuation conditions and dechlorination was achieved only using the different carbon sources.

Modeling results indicate that none of the discerned kinetics can approximate the entire experiment: First order and Michaelis-Menten kinetics can best approximate results from the third TCE spike, on which they were calibrated. Monod kinetics can best be used to approximate the first TCE spike where a lag time is present. The relation between *Dehalococcoides mccartyi* numbers and the optimized dechlorination parameters shows a large uncertainty. Not even the inclusion of donor limitation would significantly improve the simulations as shown by the sensitivity analysis. The inadequacies of the different model approximations suggest that factors other than CE-specific inhibition or growth of *Dehalococcoides mccartyi* influence the dechlorination reaction. Actually, all three kinetics performed poorly for observed degradation rates below 0.05 μmol day^{-1}, which also indicates that not all limiting factors had been included in the (lumped) degradation rate parameters of the different kinetics. For example, the supporting microbial community could have played an important role as suggested by the fast degradation in the microcosms with streambed sediments.

In effect, Monod kinetics should be derived from dedicated experiments including a concentration gradient of the electron donor and acceptor and extensive monitoring of the degrader's cell numbers or cellular activity. These experiments are capital and time-intensive but necessary to delineate the boundary conditions for the growth/activity described by Monod kinetics. If microbial growth is excluded, Michaelis-Menten kinetics should be preferred over first order kinetics to approximate the overall dechlorination reaction since it can incorporate the concentration dependent degradation rate (as indicated by the influence of K_s in the sensitivity analysis).

3 Quantifying Vertical Exchange Fluxes in a Lowland Stream Using Heat as a Tracer and the LPML Method

This chapter is partly based on the following journal articles:

1 Vandersteen, G.*, **Schneidewind, U.*,** Anibas, C.*, Schmidt, C., Seuntjens, P., Batelaan, O. (2015): Determining groundwater-surface water exchange from temperature time series: Combining a local polynomial method with a maximum likelihood estimator. *Water Resources Research, 51(2), 922-939, doi:10.1002/2014WR015994.*

2 Anibas, C.*, **Schneidewind, U.*,** Vandersteen, G., Joris, I., Seuntjens, P., Batelaan, O. (2016): From streambed temperature measurements to spatial-temporal flux quantification: Using the LPML method to study groundwater-surface water interaction. *Hydrological Processes, 30, 203-216, doi:10.1002/hyp.10588.*

* refers to equal contribution

3.1 Introduction

Exchange fluxes across streambeds can be measured in the field by means of seepage meters [*Lee*, 1977; *Rosenberry*, 2008; *Fritz et al.*, 2009]. They can also be quantified from other field measurements (see also chapter 1.5) such as hydraulic heads and gradients [*Krause et al.*, 2012; *Noorduijn et al.*, 2014] or by conducting tracer experiments [*Jonsson et al.*, 2003; *Engelhardt et al.*, 2011; *Langston et al.*, 2013]. One tracer that has received increased attention over the recent years is heat. Temperature as its proxy influences most physical and biochemical parameters in some form or other. Temperature measurements obtained from the top of a porous medium such as a streambed and at some depth can be used to quantify water fluxes by numerically or analytically solving for water flow and heat transport. One advantage of this method is that temperature is an easily, cheaply and accurately measureable parameter. Also, thermal parameters of streambed sediments are much more constraint than e.g. hydraulic conductivity [*Constantz*, 2008]. Chapter 1.4 already shortly introduced the basic theory behind heat transport in the HZ. Chapter 1.5.2 discussed the use of heat as a tracer while chapter 1.5.3 looked at methods used to obtain streambed temperatures.

This chapter deals with the quantification of vertical exchange fluxes (VEFs) from streambed temperature measurements through modeling. Chapter 3.1 presents established modeling concepts while the subsequent chapters introduce and discuss the theory behind and practical

application of a newly developed method that allows for the quantification of 1D VEFs in the frequency domain considering aspects of parameter uncertainty and model quality. The method is tested on data obtained from the Slootbeek, a small lowland stream in Belgium.

3.2 Modeling Streambed Temperatures to Quantify Exchange Fluxes

Exchange fluxes can be quantified by analytically or numerically solving Eq. (1-17). In general, analytical methods attempt to find the spatial and temporal distribution of a variable as a continuous function in space and time, for which in most cases such as when handling arbitrary geometry of the model domain a computer cannot solve the underlying non-linear partial differential equations (PDEs) that can be considered as exact solutions. Numerical methods overcome this limitation by approximating these exact solutions e.g. by using Taylor series expansions at a discrete number of points/nodes within the model grid resulting in a linear set of equations and afterwards interpolating results over the entire model domain [*Bear and Cheng*, 2010]. As such, numerical methods use a regular grid of cells or blocks (FD – finite difference method) or irregular mesh (FE – finite element and FV – finite volume methods) to discretize nature.

Numerical models allow for the discretization of complex three-dimensional streambed features and for fully coupling surface/subsurface water flow, heat and contaminant transport when necessary. Besides exchange fluxes numerical models often estimate other relevant hydraulic or thermal parameters with temperatures serving as an additional constraint. Table 3.1 lists the most common numerical codes used for heat transport modeling and the quantification of fluxes across streambeds. These codes are either modules of open-source packages (e.g. MODFLOW/MT3D, VS2DH, FEMME) or complete software packages for commercial use (e.g. HYDRUS). With the advance of powerful computer technology and the recent development of easy-to-handle user interfaces (GUIs) for the open-source codes such as 1DTempPro [*Voytek et al.*, 2014] and VS2DI [*Hsieh et al.*, 2000] for VS2DH, or MODELMUSE [*Winston*, 2009] for MODFLOW, the listed codes have become standard in the study of groundwater-surface water interaction. Other codes with similar potential such as FEFLOW [*Diersch*, 2014] or TOUGH2 [*Pruess et al.*, 1999] have not yet been fully exploited for heat transport in the hyporheic zone with the aim to quantify fluxes. Other researchers have applied less widely distributed numerical models to quantify fluxes such as *Ferguson and Bense* [2011] who used METRA/MULTIFLO [*Painter and Seth*, 2003] or *Kalbus et al.* [2008] who tested HEATFLOW [*Molson et al.*, 1992]. On yet other occasions, researchers have developed their own numerical codes/systems bespoke to their specific requirements [*Lapham*, 1989; *Holzbecher*, 2005; *Molina-Giraldo et al.*, 2011; *Cuthbert and Mackay*, 2013].

Despite their advantages numerical models are often complex in set-up and need a considerable amount of input data to produce meaningful results, which can make them costly. Another, often less laborious way to quantitatively approximate EFs is by making use of 1D analytical solutions to Eq. (1-17), while only considering the vertical direction. These

analytical solutions allow for a simple parameterization, assignment of model boundaries and a fast computation; thus big data sets can be handled and modeled with relative ease. According to *Rau et al.* [2014] the analytical solutions to the 1D case developed over the years can be categorized into **(i)** solutions to the steady state case with a constant temperature boundary and **(ii)** solutions to the transient case with a sinusoidal temperature boundary.

Table 3.1: Commonly used numerical codes to model heat transport in the hyporheic zone and quantify fluxes. For further description of these codes the reader is referred to the documentation column. Source: *own.*

Name	Type	Documentation	Studies on Exchange Fluxes
COMSOL Multiphysics	FE	comsol.com	*Cardenas and Wilson* [2007a]
FEMME-STRIVE	FD	*Soetaert et al.* [2002] *Anibas et al.* [2009] based on *Lapham* [1989]	*Anibas et al.* [2009], *Anibas et al.* [2011], *Anibas et al.* [2012], *Vandersteen et al.* [2015]
HYDROGEOSPHERE	FE	*Therrien et al.* [2010]	*Bartsch et al.* [2014], *Karan et al.* [2014a], *Irvine et al.* [2015a]
HYDRUS	FE	*Šimůnek et al.* [2006]	*Shanafield et al.* [2010], *Cranswick et al.* [2014]
MT3DMS/MODFLOW	FD	*Zheng and Wang* [1999] *Harbaugh* [2005]	*Shope et al.* [2012]
SUTRA	Hybrid FE/FD	*Voss and Provost* [2008]	*Nützmann et al.* [2014]
VS2DH	FD	*Healy and Ronan* [1996]	*Hatch et al.* [2006], *Barlow and Coupe* [2009], *Bianchin et al.* [2010], *Lautz* [2010], *Schornberg et al.* [2010], *Ebrahim et al.* [2013], *Naranjo et al.* [2013]
FD = finite difference; FE = finite element			

(i) Exchange fluxes have been obtained from point-in-time measurements [*Schmidt et al.*, 2007; *Anibas et al.*, 2011; *Lewandowski et al.*, 2011b] using variations of the steady state solution after *Bredehoeft and Papadopulos* [1965]. In its full form it is written as

$$\frac{T_z - T_u}{T_l - T_u} = \frac{e^{\left(\frac{q_z \rho_w c_w}{\kappa} z\right)} - 1}{e^{\left(\frac{q_z \rho_w c_w}{\kappa} z_l\right)} - 1} \tag{3-1}$$

with T_z[Θ] as the temperature at depth z [L], T_u, T_l[Θ] the constant temperatures at the upper boundary (z = 0) and the lower boundary z_l and q_z [L T^{-1}] as the flux in the vertical direction z. All other parameters are explained in section 3.2.1. In Eq. (3-1) it is assumed that the vertical temperature distribution only depends on q_z and that all other parameters are constant

(homogeneous subsurface). The temperature at a known depth z can be obtained by solving Eq. (3-1) for T_z. If also a measurement of the temperature at z exists, q_z can be found by minimizing the squared difference between both of these temperatures [*Schmidt et al.*, 2006; *Schornberg et al.*, 2010]. *Anibas et al.* [2009] applied this steady-state solution to data from two different field sites and found that it is only applicable under certain climatic conditions (e.g. in summer/winter in temperate climates) when the temperature difference between T_u and T_l is sufficiently large. *Schornberg et al.* [2010] pointed out that Eq. (3-1) provides most meaningful results under upward flow conditions with fluxes between 0.1 m d^{-1} and a maximum value depending on the measurement depth and resolution of the temperature sensor. They also showed that heterogeneity in streambed sediments produces increasing errors during flux quantification, especially for low flow conditions. *Ferguson and Bense* [2011] compared flux estimates using the steady state solution with those from a 2D numerical model and showed that the distribution of the streambed hydraulic conductivity K also impacts flux estimates. With increasing K the contribution of non-vertical heat transport (lateral conduction in their case) becomes more important and flux estimates from the analytical solution become increasingly erroneous.

(ii) If streambed temperature data are available in form of time series q_z can be estimated from any two temperature sensors with a known vertical separation Δz by applying some form of the solution after *Stallman* [1965]. For any depth z the transient temperature $T(z,t)$ can be obtained from [*Goto et al.*, 2005]

$$T(z,t) = Ae^{\left(\frac{v_T z}{2D_T} - \frac{z}{2D_T}\sqrt{\frac{\alpha+v_T^2}{2}}\right)} cos\left(\omega t - \phi - \frac{z}{2D_T}\sqrt{\frac{\alpha - v_T^2}{2}}\right) \tag{3-2}$$

with $\omega = \frac{2\pi}{P}$ as the angular frequency where P is the oscillation period of the temperature signal. A represents the magnitude of the amplitude of the temperature variations, ϕ the phase and $\alpha = \sqrt{v_T^4 + \left(\frac{8\pi D_T}{P}\right)^2}$. An amplitude ratio $A_r = \frac{A_2}{A_1}$ and a phase lag $\Delta\phi = \phi_2(z_2,t_2) - \phi_1(z_1,t_1)$ exist between both temperature signals (Figure 3.1), which can be used to calculate q_z as [*Hatch et al.*, 2006]

$$q_z = \frac{\rho c}{\rho_w c_w}\left(\frac{2D_T}{\Delta z}\ln A_r + \sqrt{\frac{\alpha + v_T^2}{2}}\right) \tag{3-3}$$

by using the amplitude ratio. When the phase lag is used, q_z is

$$|q_z| = \frac{\rho c}{\rho_w c_w}\sqrt{\alpha - 2\left(\frac{4D_T\pi\Delta\phi}{P\Delta z}\right)^2} \tag{3-4}$$

In Eqs. (3-3) and (3-4), D_T is defined as in Eq. (1-20). Using the phase lag, only the magnitude of the EF can be determined while using the amplitude ratio allows for a calculation of magnitude and direction. Both equations have to be solved iteratively.

A similar solution has been proposed by *Keery et al.* [2007] with

$$0 = \left(\frac{\rho_w c_w \ln A_r}{4\kappa\Delta z}\right)q_z^3 - \left(\frac{\rho_w c_w \ln^2 A_r}{4\kappa\Delta z^2}\right)q_z^2 + \left(\frac{\rho_w c_w \ln^3 A_r}{\kappa\Delta z^3}\right)q_z + \left(\frac{\pi\rho c}{P\kappa}\right)^2 - \frac{\ln^4 A_r}{\Delta z^4} \tag{3-5}$$

using the amplitude ratio and with

$$|q_z| = \sqrt{\left(\frac{\rho c\Delta z}{\Delta t\rho_w c_w}\right)^2 - \left(\frac{4\pi\kappa\Delta t}{P\Delta z\rho_w c_w}\right)^2} \tag{3-6}$$

with $\Delta t = \frac{P}{2\pi}\Delta\phi$ using the phase lag. To solve for q_z in Eq. (3-5) the roots of the third-order polynomial have to be calculated, one of which must be real while the other two can be real or conjugate complex [*Keery et al.*, 2007]. Both solutions need a sinusoidal temperature signal as input that contains a single frequency. In temperate climates under natural flow conditions the main frequencies of interest are the diel signal and the annual signal, both caused by variations in the incident solar radiation. As such, the frequency of interest has to be filtered out from the raw temperature data acquired at a field site. *Hatch et al.* [2006] experimented with several filter forms and finally suggested to use a cosine tapper band-pass filter on the raw temperature data. They mention that their filtering technique imposes edge effects at the beginning and end of each temperature-time series degrading the first and last 3-4 days of data and leading to erroneous EF estimates. *Keery et al.* [2007] used Dynamic Harmonic Regression (DHR), a generalized harmonic regression model [*Young et al.*, 1999]. This method uses the discrete Fourier transform and Kalman filtering techniques [*Kalman*, 1960] to describe the temperature variations (amplitudes, phases) with trigonometric functions of time. They also suggested discarding at least two periods at the beginning and end of the time series to minimize spurious effects introduced by filtering.

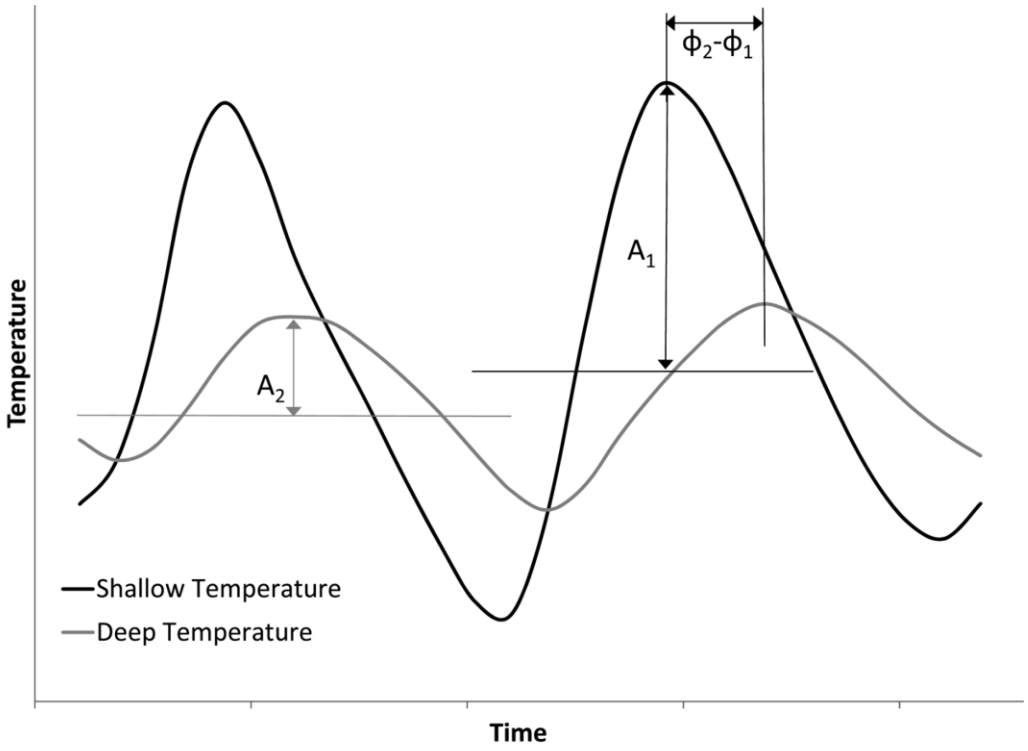

Figure 3.1: Amplitude attenuation and phase shift a temperature signal undergoes when it propagates through the streambed. Source: *Luce et al.* [2013].

The solutions after *Hatch et al.* [2006] and *Keery et al.* [2007] have been applied to quantify exchange fluxes in different stream environments [*Fanelli and Lautz*, 2008; *Hatch et al.*, 2010; *Jensen and Engesgaard*, 2011; *Lautz*, 2012; *Lautz and Ribaudo*, 2012; *Gariglio et al.*, 2013] and have been integrated into software packages such as VFLUX [*Gordon et al.*, 2012; *Irvine et al.*, 2015b] that allow for automatic filtering and handling of big data sets. *Luce et al.* [2013] extended the mathematical theory of both solutions by defining the ratio $\eta = \frac{\ln A_r}{\Delta\phi}$. This seemingly allowed them to explicitly calculate v in the streambed and to determine the thermal dispersion coefficient as represented in Eq. (1-20). So far, their method has only been applied on synthetic data and assumes that both amplitude ratio and phase lag between the two temperature sensors can be identified and provide the same magnitude of q_z in Eqs. (3-3) to (3-6). *Onderka et al.* [2013] used continuous wavelet transform to filter out the diel signal from a non-stationary (i.e. amplitudes of the diel signal change over time) long-term temperature-time series before using Eq. (3-2).

3.3 Assumptions and Limitations of the Transient 1D Analytical Solutions

The previously presented 1D transient analytical solutions [*Hatch et al.*, 2006; *Keery et al.*, 2007; *Luce et al.*, 2013] are subject to the following assumptions:

(A1) Streambed sediment characteristics are constant in space (homogeneous and isotropic) and time. Thus, a constant set of thermal parameters is applied over the entire domain.

(A2) Flow is uniform and steady leading to a spatially constant exchange flux.

(A3) Water and sediment temperatures are equal at all times (LTE concept).

(A4) The subsurface (domain) is assumed to be a semi-infinite halfspace where the upper boundary is the temperature sensors closest to the streambed top and the lower boundary is located in infinity. Thus, the VEF value obtained from two temperature sensors is representative for the entire homogeneous half-space.

As such, the solutions are subject to the following methodological limitations:

(L1) Only sinusoidal waves of a single frequency are used from the temperature data of both sensors. This single frequency has to be isolated from the raw temperature data by filtering. However, under field conditions streambed temperature signals are commonly a mix of many frequencies and the isolation of a single harmonics can lead to a loss of information in VEF calculations. Also, the filtering method can influence flux calculations as amplitude ratios and phase lags can be time-variant e.g. due to changing weather patterns [*Lautz*, 2012].

(L2) Several studies applying the solutions after *Hatch et al.* [2006] and *Keery et al.* [2007] on temperature-time series obtained under field conditions noticed discrepancies in q_z magnitudes obtained with the amplitude ratio to those obtained with the phase lag method [*Lautz*, 2010; *Rau et al.*, 2010; *Lautz*, 2012], which has been attributed to the concept of the *REV* as discussed before and to temperature sensor resolution [*Soto-Lopez et al.*, 2011].

(L3) VEFs are determined essentially from temperature data collected with two sensors separated by a known distance. If more than two sensors are available (as is common for modern field instruments), different sensor combinations can be used to calculate and compare flux estimates but not all information can be included simultaneously.

(L4) Many streambeds are heterogeneous and anisotropic environments as streambed-forming processes vary at different spatial and temporal scales. *Irvine et al.* [2015a] concluded from their modeling study that errors in flux estimates increase with the degree of streambed heterogeneity and are also influenced by the level of anisotropy in streambed structure. Heterogeneity leads to variable contributions of convection and conduction/diffusion to overall heat transport. As convective heat transport can be retarded compared to water flow [see e.g. *Vandenbohede and Lebbe*, 2010], heterogeneity can lead to larger estimation errors and is probably also likely to increase the fraction of non-vertical flow.

(L5) A temperature dependency of density, viscosity and hydraulic conductivity is not considered. To the knowledge of the author detailed studies regarding their influence on VEF estimates do not exist in the scientific literature.

(L6) Flow is assumed vertical. However, *Shanafield et al.* [2010] found in their numerical modeling study on a synthetic channel that fully vertical flow was in most scenarios only achieved beneath the stream center. Near stream banks and with increasing depth, horizontal and lateral flow components increase [see also *Cranswick et al.*, 2014]. *Roshan et al.* [2012] compared the performance of the solutions of *Hatch et al.* [2006] and *Keery et al.* [2007] to a 2D finite element model and found that for very small vertical velocities the 1D analytical solutions overestimate the velocity. Also, velocity (flux) errors are greater for gaining streams than for losing streams. *Cuthbert and Mackay* [2013] showed by comparing analytical solutions to a numerical model that not only non-vertical flow components can lead to VEF errors but also non-uniform flow, defined as divergent or convergent flow fields. *Rau et al.* [2012a] showed experimentally that even for a quasi-homogeneous subsurface the flow field becomes increasingly non-uniform with increasing velocity, which leads to greater errors in flux estimates.

These assumptions and limitations can lead to uncertainty in calculated vertical exchange fluxes. In principle, this uncertainty is a combination of model structure uncertainties, limitations of our conceptual understanding of heat transport in porous media, input uncertainties related to temperature measurements and parameter uncertainty related to the mathematical procedure used for flux estimation. *Shanafield et al.* [2011] investigated the impact of sensor accuracy on flux estimates. They showed that for the transient 1D analytical solutions, sensor accuracy limits the size of the amplitude that can be identified from the temperature record, which in turn influences flux estimates. The effect of sensor resolution was studied by *Soto-Lopez et al.* [2011], who demonstrate that the resolution highly influences the amplitude but only slightly the phase of the temperature signal. They concluded that using the phase lag method provides more reliable flux estimates than the amplitude method and suggest using the latter only to determine the direction of the flux. On the other hand, *Lautz* [2010] showed that under non-vertical flow conditions the use of the amplitude ratio is less prone to error than using the phase lag. The uncertainty in thermal parameters with regard to flux estimates has been studied by *Shanafield et al.* [2011], who showed that higher values of thermal diffusivity lead to less uncertainty in flux estimates. *Gordon et al.* [2012] included a routine to conduct Monte-Carlo analyses into the VFLUX software. As such, confidence intervals could be created around time-variant flux estimates. *Lautz* [2012] conducted column experiments to study heat transport in a controlled environment and showed that noise in the temperature signal can strongly influence flux estimates. She concluded that the use of adequate filtering techniques is imperative. Alternatively, the noise could be dealt with in other adequate ways.

The next sections discuss the LPML method, a novel transient method for the quantification of vertical exchange fluxes from temperature measurements in the frequency domain. This

method renders limitations L1 to L3 obsolete. It also allows for a direct quantification of parameter uncertainties and provides information regarding model quality. First, the LPML method is introduced mathematically and tested on a synthetic data set. Then, the LPML method is applied on measured data from the Slootbeek to study its performance. Finally, the method is used to delineate the spatial and temporal variability of VEFs and study the local flow system.

3.4 Using the LPML Method to Quantify Vertical Exchange Fluxes

This section introduces the LPML method that solves 1D coupled water flow and heat transport in the frequency domain. The LPML method combines a local polynomial (LP) signal processing technique [*Pintelon et al.*, 2010a, b] with a maximum likelihood (ML) estimator. The mathematical concepts of both the LP and ML parts are well developed but a combination of both parts with the aim to determine VEF is novel. A workflow of the method is presented in Figure 3.2 and described in the subsequent text. The method considers the streambed a homogeneous and semi-infinite halfspace. It also assumes that heat transport in the streambed can be described by a linear time-invariant (LTI) system using partial differential equations [*Pintelon and Schoukens*, 2012]. Linear systems theory [*Hespanha*, 2009] can then be used to determine the steady-state response of the thermal system in the frequency domain to a sinusoidal input. The advantage of representing the steady-state response of an LTI system to a sinusoidal excitation with a given frequency is that its steady-state response is also a sinusoidal waveform with the same frequency but with a possible amplitude and phase shift. This makes it possible to represent the response of an LTI system to a sinusoidal excitation through complex numbers as a function of the frequency. The LPML method is coded in MATLAB. It has been described and tested by *Vandersteen et al.* [2015] and applied on field data from the Slootbeek by *Schneidewind et al.* [2013] and *Anibas et al.* [2016].

3.4.1 Heat Transport in the Frequency Domain

Heat transport as presented in Eq. (1-17) can be re-written as

$$\frac{\partial T}{\partial t} = D_T \frac{\partial^2 T}{\partial z^2} - q_z \frac{\rho_w c_w}{\rho c} \frac{\partial T}{\partial z} \tag{3-7}$$

for the 1D case. Here D_T is quantified according to Eq. (1-20). Eq. (3-7) can be generalized and rearranged to

$$\frac{\partial^2 T}{\partial z^2} + \alpha \frac{\partial T}{\partial z} + \beta T + \gamma \frac{\partial T}{\partial t} = 0 \tag{3-8}$$

where the bulk parameters $\alpha, \beta \; and \; \gamma$ are constant, with $\alpha = -\frac{q_z}{D_T}\frac{\rho_w c_w}{\rho c}$; $\beta = 0$, and thus no longer considered, and $\gamma = -\frac{1}{D_T}$.

The excitation signal $T(z_0, t)$ to the system (i.e. the measured temperature signal at the upper boundary z_0; e.g. the streambed top) is assumed to be known and noiseless. When using its complex representation $T(z_0, t) = Re(e^{i\omega t})$ with $i = \sqrt{-1}$, the system response at any depth z can be represented in the frequency domain by

$$T(z, t) = Re(G(z, \omega)e^{i\omega t}) \tag{3-9}$$

with $G(z, \omega)$ as the frequency response function (FRF). A frequency response function is a non-parametric transfer function from the input at the boundary z_0 to the position z at discrete angular frequencies ω_k with $k = 1, \dots, F$ and F as the number of frequency lines used (i.e. depending on the length of the time series). Temperature measurements in the streambed are made at discrete points in time (here, at an equidistant time grid, i.e. interval between measurements is equal). To calculate FRFs the spectrum of the temperature signal is determined with the Fast Fourier transform algorithm (FFT) for a set of equidistant discrete frequencies. Each FRF contains a real and an imaginary part, which can be resolved into magnitude (amplitude in dB) and phase (in radians) information per frequency. For a single sine wave the amplitude of the FRF is a measure of the attenuation of the sinusoidal excitation of a particular frequency. The phase of the FRF measures the phase shift between the exciting sine wave and the response [*Pintelon and Schoukens*, 2012; *Vandersteen et al.*, 2015].

The complex representation in the frequency domain makes it possible to rewrite Eq. (3-8) into the ordinary differential equation (ODE)

$$\frac{d^2\Theta}{dz^2} + \alpha\frac{d\Theta}{dz} + (i\omega\gamma)\Theta = 0 \tag{3-10}$$

with $\Theta = \mathcal{F}\{T\}$ where $\mathcal{F}$ represents the Fourier transform. Alternatively, Eq. (3-10) can be represented by applying the FRFs as

$$\frac{d^2G}{dz^2} + \alpha\frac{dG}{dz} + (i\omega\gamma)G = 0 \tag{3-11}$$

If α and γ are assumed to be independent of z, the analytical solution to Eq. (3-11) for a semi-infinite homogeneous halfspace is given by

$$G(z, \omega, \theta) = e^{\lambda_1(\omega,\theta)z} \tag{3-12}$$

with

$$\lambda_1(\omega,\theta) = \frac{1}{2}\left(-\alpha - \sqrt{\alpha^2 - 4i\omega\gamma}\right) = \frac{q_z}{2D_T}\frac{\rho_w c_w}{\rho c} \pm \sqrt{\left(\frac{q_z}{2D_T}\frac{\rho_w c_w}{\rho c}\right)^2 + \frac{i\omega}{D_T}} \tag{3-13}$$

where $G(z,\omega,\theta)$ is the analytical expression of the FRF between the upper boundary temperature and the temperature at position z for a given parameter vector $\theta = [\alpha\ \gamma]$.

The concept of analytically solving Eq. (3-7) in the frequency domain for q_z and D_T by using transfer functions has already been demonstrated by *Wörman et al.* [2012], who used spectral scaling factors. However, their approach is only applicable to noiseless temperature signals assuming a sinusoidal input. Temperature-time series collected in the field are usually arbitrary signals with periodic and non-periodic (transient) parts. The latter can be caused by instrument drift or by very slow temperature fluctuations. They can thus be assumed to be a smooth function in the frequency domain. Additionally, raw temperature data contains additive noise that is assumed to follow a Gaussian distribution function in the frequency domain, known as a circular complex normal distribution. This is equivalent to a Gaussian distribution in the time domain but can also result from other distribution functions in the time domain [*van Berkel et al.*, 2014b]. Thus, a technique should be applied that separates periodic, non-periodic and noise parts from the measured temperature signal (input spectrum) before parameter estimation.

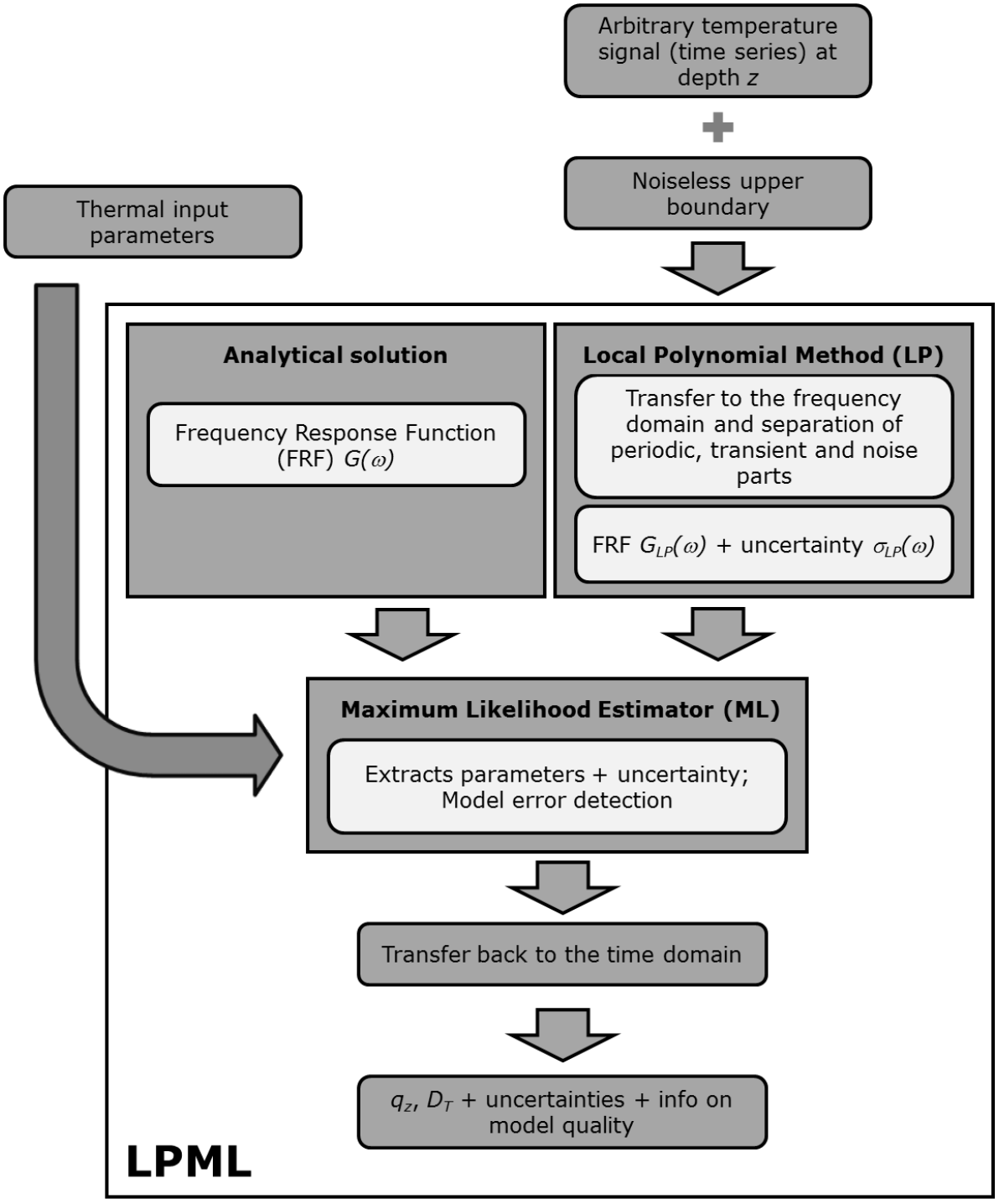

Figure 3.2: Flow chart presenting the concept of the LPML method showing the two main parts, the local polynomial method (LP) and the maximum likelihood estimator (ML) as discussed in Adapted from *Vandersteen et al.* [2015].

3.4.2 Extracting FRFs Using the Local Polynomial Method

In the absence of noise and transient parts, the output spectrum $Y(\omega)$ for each temperature sensor can be described by

$$Y(\omega) = G(\omega)U(\omega) \tag{3-14}$$

where $U(\omega)$ is the noiseless input signal and $G(\omega)$ is the FRF. However, as already explained in chapter 3.4.1, temperature data collected in the field deviates from a pure sine function (arbitrary signal) and also contains transient and additive noise parts in the frequency domain.

One possibility to separate the different signal components is by means of the local polynomial (LP) method. This method has been described in detail by *Pintelon et al.* [2010b, 2010a]. The LP method considers that the FRF $G(\omega)$ is a smooth function of the frequency that can be approximated locally by a low order (in this work a second order) polynomial system model $G_{LP}(\omega)$. The output spectrum $Y(\omega)$ can then be described by

$$Y(\omega) = G_{LP}(\omega)U(\omega) + Tr(\omega) + E(\omega) \tag{3-15}$$

in a small frequency band around the angular frequency ω of interest. Here $Tr(\omega)$ represents the transient parts, while $E(\omega)$ is the additive circular-complex normal noise. The separation of the FRF $G_{LP}(\omega)$ and the transient term $Tr(\omega)$, is possible since $G_{LP}(\omega)U(\omega)$ is a random spectrum while $Tr(\omega)$ is a smooth one. The solution of the resulting least squares problem is used to determine $G_{LP}(\omega)$ and $Tr(\omega)$. The residual analysis of the least squares problem then characterizes $E(\omega)$. Aside from the FRF $G_{LP}(\omega)$, the LP method also provides its variance $\sigma^2_{G_{LP}}(\omega)$. The variance is used as an indicator regarding the quality of the FRF and is inversely proportional to the square of the Signal-to-noise ratio (SNR). For frequencies where $\sigma^2_{G_{LP}}(\omega) > G_{LP}(\omega)$ the SNR is too large and the respective frequencies are eliminated from further use. The order of the polynomial is determined by analyzing the least-square errors resulting from fitting the polynomial function to the frequency lines used.

3.4.3 Parameter Estimation with the Maximum Likelihood Estimator

The FRFs $G_{LP}(z_n, \omega_k)$ and $G(z_n, \omega_k, \theta)$ at various depths z_n, for all considered angular frequencies ω_k can be used together with the variance $\sigma^2_{G_{LP}}(z_n, \omega_k)$ representing the noise information as input to a maximum likelihood estimator (ML) to estimate the parameter vector $\hat{\theta} = [\hat{\alpha} \quad \hat{\gamma}]$. In general, $\sigma_{G_{LP}}$ depends on the length of the temperature-time series, from which G_{LP} is deduced, as well as on the respective frequency, the depth of the output signal and the signal-to-noise ratio. The ML estimator requires knowledge regarding the pdf of the noise. The noise is assumed to be complex normally distributed and can be described by its covariance matrix. Once applying the ML principle, one can show that the covariance

matrix of the noise is used within the equations as weighting matrix. The ML estimator may provide better parameter estimates than other methods such as weighted least squares, depending on the form of the pdf of the noise. Properties of the ML estimator (invariance, consistency, asymptotic normality and efficiency) are discussed in *Pintelon and Schoukens* [2012].

The general idea behind a ML estimator is to maximize a known likelihood function, in this case the probability density function (pdf) with respect to $G(z_n, \omega_k, \theta)$. The parameter vector $\hat{\theta} = [\hat{\alpha} \quad \hat{\gamma}]$ is then determined by

$$\hat{\theta} = \min_{\theta} L_{ML}(\theta) \tag{3-16}$$

i.e. minimizing the ML cost function $L_{ML}(\theta)$ using nonlinear least squares minimization techniques such as Gauss-Newton or Levenberg-Marquardt optimization methods [*Fletcher*, 1980]. The ML cost function weighs the error with the uncertainty of the FRFs $G_{LP}(z_n, \omega_k)$ at different depths and frequencies. It can be represented as

$$L_{ML}(\theta) = \sum_{k=1}^{F} |e_{ML}(z_n, \omega_k, \theta)|^2 \tag{3-17}$$

where *F* is the number of frequency lines used (i.e. the length of the time series multiplied by the maximum frequency), |.| denotes the norm of a complex number, and e_{ML} the complex-valued weighted residual least-squares error which is

$$e_{ML}(z_n, \omega_k, \theta) = \frac{G_{LP}(z_n, \omega_k) - G(z_n, \omega_k, \theta)}{\sigma_{G_{LP}}(z_n, \omega_k)} \tag{3-18}$$

The uncertainties on $\hat{\alpha}$ and $\hat{\gamma}$ can be determined from the covariance matrix $COV(\hat{\theta})$. By using the analytical Jacobian matrix J_{ML}

$$J_{ML}(z_n, \omega_k, \theta) = \frac{\partial e_{ML}(z_n, \omega_k, \theta)}{\partial \theta} \tag{3-19}$$

during optimization one can determine the Fisher information matrix Fi using the following approximation:

$$Fi(\theta) \approx \sum_{k=1}^{F} J_{ML}^{h}(z_n, \omega_k, \theta) J_{ML}(z_n, \omega_k, \theta) \tag{3-20}$$

where J_{ML}^{h} represents the Hermitian transpose. The Fisher information matrix is a measure of the information contained in the data and can be used to determine the covariance matrix [*Pintelon and Schoukens*, 2012] via

$$COV(\hat{\theta}) = [Fi(\hat{\theta})]^{-1} \tag{3-21}$$

The ML concept can then be used to quantify $\hat{q}_z$ and $\widehat{D_T}$ according to

$$\hat{q}_z = \frac{\hat{\alpha}}{\hat{\gamma}} \frac{\rho c}{\rho_w c_w} \tag{3-22}$$

$$\widehat{D_T} = -\frac{1}{\hat{\gamma}} \tag{3-23}$$

The uncertainties on $\hat{q}_z$ and $\widehat{D}$ can be calculated with the covariance matrix $COV(\hat{q}_z, \widehat{D})$ via

$$COV(\hat{q}_z, \widehat{D_T}) = J_{\theta\to\theta'}^{h} COV(\hat{\theta}) J_{\theta\to\theta'} \tag{3-24}$$

where $J_{\theta\to\theta'}$ is the Jacobian matrix

$$J_{\theta\to\theta'} = \begin{bmatrix} \frac{1}{\hat{\gamma}} \frac{\rho c}{\rho_w c_w} & -\frac{\hat{\alpha}}{\hat{\gamma}^2} \frac{\rho c}{\rho_w c_w} \\ 0 & \frac{1}{\hat{\gamma}^2} \end{bmatrix} \tag{3-25}$$

and $J_{\theta\to\theta'}^{h}$ its hermitian transpose.

A cost function analysis can be performed to detect model structure errors (e.g. to see whether the assumption of purely 1D vertical water flow and heat transport is adequate). Such an analysis describes the goodness of fit between the actual model used and the analytical solution. The expected value L_E (from here-on called expected cost) and the variance of the cost in its minimizer $\hat{\theta}$ can be computed in the absence of modeling errors [*Pintelon et al.*, 1997; *Pintelon and Schoukens*, 2012] and compared to the actual value L_{ML} (from here-on called CostBest) obtained from Eq. (3-17). The expected cost function value can be obtained from [*van Berkel et al.*, 2014a]

$$L_E = \left(F - \frac{n}{2}\right) \tag{3-26}$$

where n is the number of free parameters (here $\hat{q}_z$ and $\widehat{D}$). Hence, the ML cost in its minimizers behaves like a χ^2 distribution with $F - n/2$ degrees of freedom. If $F \gg 1$, one can approximate both the expected mean value and the variance of the cost with *F*. *van Berkel*

et al. [2014a] and *Vandersteen et al.* [2015] suggest that a model is acceptable if L_{ML} falls within a 95% confidence interval around L_E, i.e.

$$L_E - 2\sqrt{L_E} < L_{ML}(\hat{\theta}) < L_E + 2\sqrt{L_E} \tag{3-27}$$

3.5 Verifying the LPML Method Using Synthetic Temperature Data

In this section the aim is to reproduce known values of VEF (q_z = -86.4 mm d^{-1}, representing inflow into a stream) and thermal conductivity (κ = 2.5 Wm^{-1}K^{-1}) with the LPML method. These known values were defined with the numerical heat transport model STRIVE, which is based on the ecosystem modeling platform FEMME [*Soetaert et al.*, 2002]. STRIVE uses the explicit finite difference approach after *Lapham* [1989]. For calculation in STRIVE a temperature-time series from the streambed top of the Aa River, Belgium was used as input and upper model boundary. This time-series ranges over 520 days (Figure A3.1) and is based on measurements from *Anibas et al.* [2009]. The lower boundary at 5 m depth was set constant to the average groundwater temperature of 12.2°C [*Anibas et al.*, 2011]. The model domain was vertically discretized in 500 model nodes with a thickness of 0.01 m each. The temperature distribution with depth was then calculated in STRIVE assuming constant values for q_z, κ and other relevant parameters ($n = 0.48; \rho c = 3.0 \times 10^6$ J/(K m^3)) over the entire modeling domain. Three of the resulting temperature-time series (depths: 0.05 m; 0.10 m and 0.20 m) were chosen as input to the LPML method. These time-series represent the shallow depths where temperature measurements are often performed under field conditions.

Applying the LPML method, values for $\hat{q}_z$= -86.4 mm d^{-1} and $\hat{\kappa}_z$ = 2.5 Wm^{-1}K^{-1} were estimated with small parameter uncertainties of $\sigma_{\hat{q}_z}$ = 0.01 mm d^{-1} and $\sigma_{\hat{\kappa}}$ = 0.0001 Wm^{-1}K^{-1}. These results show that the LPML method is able to retrieve the original parameters used in the simulation with STRIVE. The CostBest value of 2927 was not within the 95% confidence interval around the expected cost (2339 with a standard deviation of 48). This implies that some amount of residual modeling error is still present. This small discrepancy can be due to modeling errors in STRIVE introduced by the discretization of the partial differential equation during simulation. As the temperature-time series output created with STRIVE is noiseless, the actual model cost is dominated by numerical errors and not the noise contained in the temperature signal. It is assumed that by adding realistic noise levels the impact of the numerical error will be reduced and hence, CostBest and expected cost values would differ less.

By looking at the FRF G_{LP} in relation to its standard deviation $\sigma_{G_{LP}}$and the frequency range used in the analysis (Figure 3.3 (a)) for all three depths, one can see that G_{LP} reduces gradually for increasing depth and frequency. This was expected, as temperature signals are attenuated with depth. High frequency components are attenuated more strongly than low frequency components. For all three depths, $\sigma_{G_{LP}}$is well below G_{LP} with a local minimum at

the frequency of 1 d^{-1}. Standard deviations generally increase for higher frequencies as the output signal strength decreases while the noise level remains constant. At higher frequencies, less data is available to determine the frequency response. At the frequency of one per day, i.e. the diel signal, the excitation signal is strongest and thus $\sigma_{G_{LP}}$ is smallest. No frequency lines had to be excluded from further calculations.

A comparison of the FRFs G_{LP} and G versus the frequency range used in the analysis for all three depths (Figure 3.3 (b)) shows that both FRFs coincide well, however, differences between the respective FRFs steadily increase above a frequency of 1.1 d^{-1} as well as with depth. This is again due to increasing signal attenuation in depth and due to the fact that at higher frequencies less usable information is available compared to the constant noise. The results show that the LPML method is able to extract the correct values of exchange flux and thermal conductivity with minimal parameter uncertainties from a simulated data set.

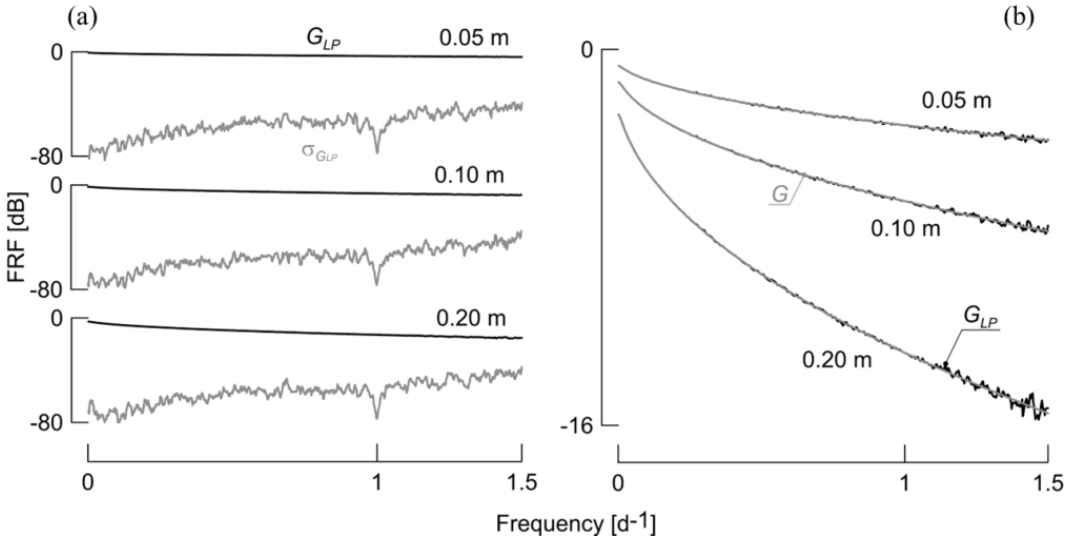

Figure 3.3: (a) FRF G_{LP} and $\sigma_{G_{LP}}$ for all three depths. G_{LP} always remained larger than $\sigma_{G_{LP}}$, so that no data had to be excluded from flux calculations. With increasing depth and frequency $\sigma_{G_{LP}}$ approaches G_{LP}. (b) Comparison between G_{LP} and G. Both FRFs are in good agreement. With increasing frequencies, G_{LP}becomes less smooth. Source: *Vandersteen et al.* [2015].

3.6 Using the LPML Method with Temperature Data from the Slootbeek

3.6.1 The Slootbeek Field Site

The LPML method was applied on temperature-time series obtained from the Slootbeek, the major tributary to the River Aa and part of the important River Nete catchment (Figure 3.4 (a)) in North-Eastern Belgium that covers an area of 1673 km^2. The Slootbeek has a length of approximately 3.9 km, a stream width between 3 m and 5 m and is fed by several drainage canals. Its stream stage is influenced by its location in a lowland agricultural landscape with elevations mostly around 10 to 15 m above mean sea level (Figure 3.4 (b)). Average discharge

at the confluence with the Aa River is about 0.05 $m^3 s^{-1}$ [*De Doncker*, 2010] and average stream velocity during installation of the measurement equipment was roughly 0.2 m s^{-1}. According to the Flemish geological data base DOV (accessed 2014) the local geology is defined by the Tertiary Formation of Kasterlee that comprises fine sands with fractions of clay, which is underlain by the Berchem Formation. Both form an aquifer of about 80 m thickness, which is bounded by the Boom Aquitard consisting of clay.

The investigated stream section is about 40 m long and about 150 m upstream of the confluence with the Aa River. It is canalized and comprises a stream bend where the stream sharply turns right before it continues straight towards the Aa River. The stream banks and the riparian zone of the Slootbeek are free of tall vegetation. The streambed is composed predominantly of fine sand and silt with occasional gravel deposits in the downstream part. It is overlain in most parts by a layer of organic matter with variable thickness and seasonally covered with macrophytes.

3.6.2 Field Work

Multilevel temperatures sticks (MLTS) from UIT, Dresden, Germany [*Schmidt et al.*, 2014] were installed into the streambed at locations ML1 to ML8 (Figure 3.4 (c), red dots). Each MLTS consists of a polyoxymethylene casing of 0.66 m length and 0.02 m outer diameter that holds eight TSIC-506 temperature sensors connected to an external data logger (Figure 3.5). The sensors are semiconducting resistors embedded in an integrated circuit and have an accuracy of 0.07 °C. Sensor (1) measured the open water temperature, which was not used for further analysis. Sensor (2) measured the temperature at the streambed top, representing the noiseless upper boundary temperature in the LPML method. Sensors (3) to (8) measured streambed temperatures at depths of 0.15, 0.17, 0.20, 0.25, 0.35, and 0.55 m. The MLTS used here were ready-to-install instruments but given sufficient financial resources they can also be custom-made. This would give the advantage that more sensors could be placed within the first 10-15 cm, where a significant part of the temperature signal can already be strongly attenuated depending on the direction of water flow. Measurement resolution was 10 min. Temperature read out occurred on-site every two to three weeks and data was immediately checked for consistency. The measurement setup as shown in Figure 3.4 (c) was active from February 17 to July 25, 2012 over a period of 158 days (140 days for ML2 as some data was faulty) before it was destroyed. The MLTS at location ML5 did not provide any data.

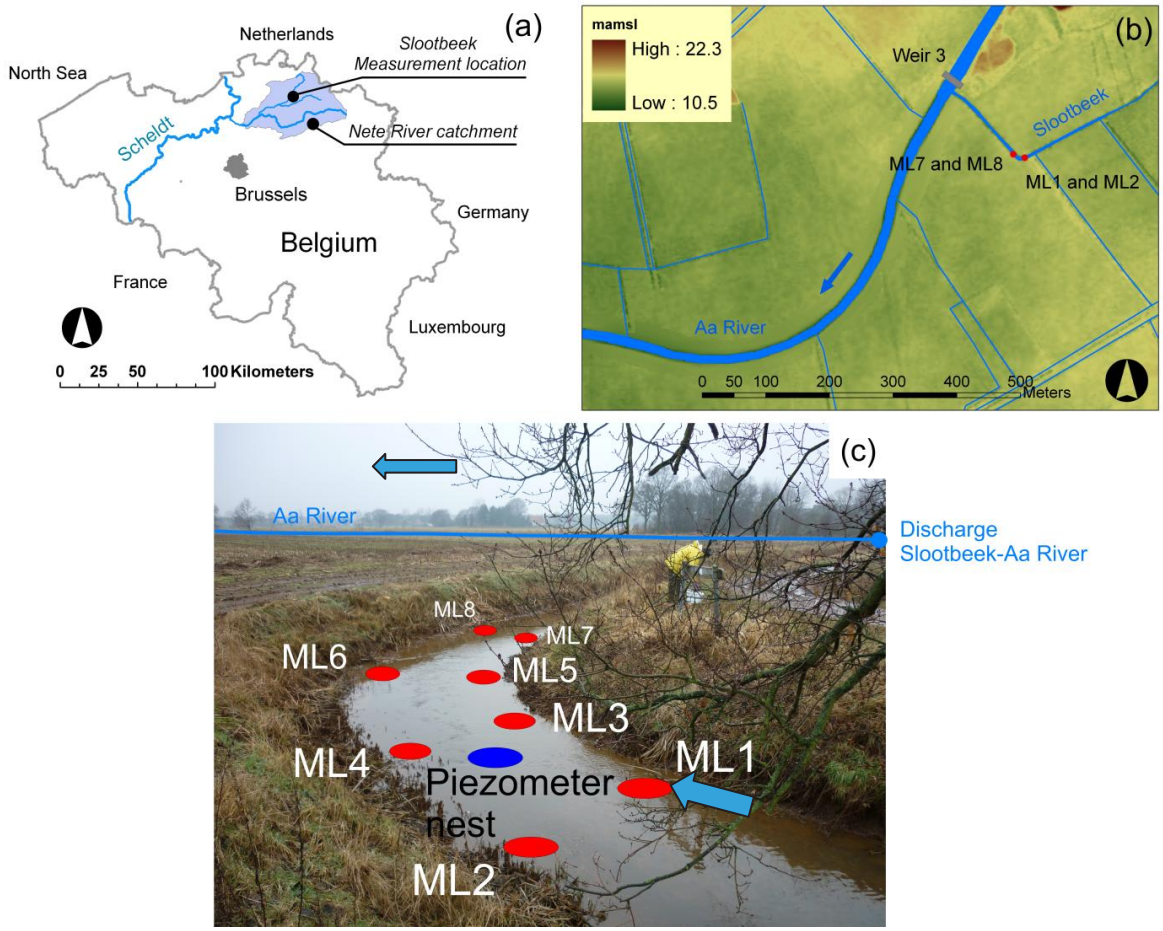

Figure 3.4: (a) The Slootbeek study site in the central part of the Nete River catchment. (b) Topographic map of the area including the studied stream section (in meters above mean sea level). The Slootbeek is a tributary to the Aa River. East of the discharge point the Slootbeek flows relatively parallel to the Aa River, while around 150 m before discharging into the Aa it makes a 90° turn towards it [*Anibas et al.*, 2016]. (c) Photo of the investigated stream section taken in February 2012 from the left stream bank. Locations of temperature measurements are indicated in red, while the blue ellipse indicates the location of a piezometer nest. The blue line in the background indicates the Aa River, flowing from right to left. The Slootbeek was about 4 m wide with a stream stage varying between 0.21 and 0.47 m at the ML locations.

For each MLTS there was an initial temperature offset between the different sensors. This offset was corrected by using independent temperature measurements obtained with an SWS (Schlumberger Water Services) data logger under near constant temperature conditions in a water bath. The average temperature of the SWS logger measured over one hour with measurements every 10 s was chosen as the reference temperature. Then, differences between individual sensors of the MLTS and the average SWS temperature were determined and added to the raw MLTS data during data processing. A second calibration at the end of the field work to correct for instrument drift could not be performed as the MLTS could not be recovered intact.

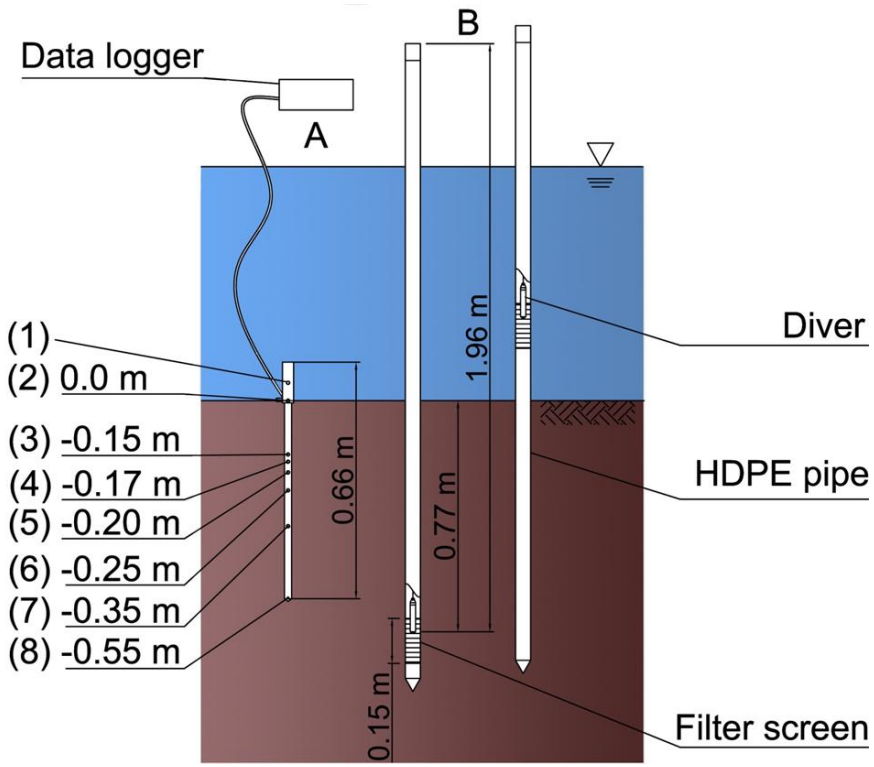

Figure 3.5: A multilevel level temperature stick (MLTS) is shown on the left (A). Sensor (2) measures the temperature at the streambed top. Sensors (3) - (8) measure temperatures in depths between 0.15 m and 0.55 m. The overall length of the instrument is 0.66 m. A piezometer nest (B) was installed between locations ML3 and ML4 to collect pressure head and temperature data. Source: *Anibas et al.* [2016].

A piezometer nest was installed between locations ML3 and ML4. It comprised two HDPE pipes of 2 inch diameter and was equipped with SWS data loggers to measure pressure head and temperature. While one logger measured at the streambed top, the other measured in 0.77 m depth. Measurements were conducted with a resolution of 30 min from June 11 till July 25, 2012 in the streambed and in the stream. Before that, measurements were only taken in the stream from March 6 to July 25, 2012 (the logger was attached to a wooden stick installed in the streambed). Pressure head data was corrected for the ambient air pressure measured with a baro logger located at Vrije Universiteit Brussel (VUB). A baro logger installed on-site was lost and no data could be recovered.

Groundwater levels and temperatures in the connected aquifer were monitored in well GW1, a HDPE piezometer installed at the right bank of the Slootbeek near its confluence with the Aa River (Figure A3.2). Pressure head data was collected from June 6 till July 25, 2012 with an SWS data logger in 10 min intervals. All measurement locations were mapped using triangulation and distances to fixed points (bridge, small weir at confluence with Aa River).

3.6.3 Results and Discussion of Field Measurements

3.6.3.1 Stream Stage and Vertical Hydraulic Gradient

Stream stage at the piezometer nest location (Figure 3.6) varied between 0.48 m and 1.20 m with a mean of 0.68 m and a standard deviation from the mean of 0.17 m. In-stream water temperatures varied between 4.5°C and 24.6°C with a mean of 13.3°C and a standard deviation of 3.7°C. In the deep piezometer, the water level above the streambed top ranged from 0.58 m to 1.18 m with a mean of 0.87 m and a standard deviation of 0.18 m (Figure A3.3). Water temperatures varied between 12.3°C and 13.6°C, with a mean of 13.1°C and a standard deviation of 0.5°C. Groundwater temperature in well GW1 varied slightly from 10.8°C to 11.2°C with a mean of 11.0°C and a standard deviation of 0.1°C (Figure A3.4). The water level in the aquifer ranged from 0.39 m to 1.02 m below surface, with a mean of 0.71 m and a standard deviation of 0.19 m.

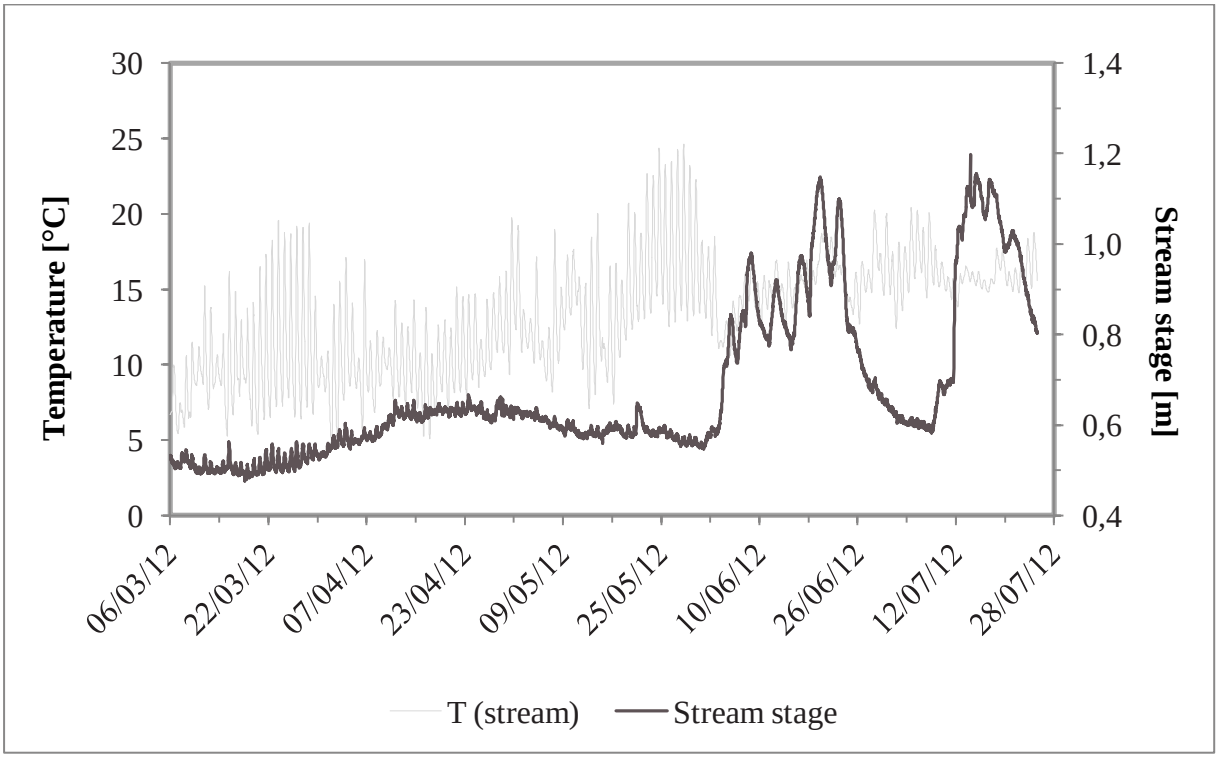

Figure 3.6: Stream stage and in-stream temperature measurements at the location of the piezometer nest. Stream stage from March until the beginning of June is fairly constant, while it strongly varies afterwards. Temperatures fluctuate more strongly during low stream stage than during high stream stage periods. Source: *own.*

For the period from June 11 till July 25, 2012 both stream stage and piezometric heads in the streambed are available, which allowed for a calculation of the VHG between the piezometers. The VHG was calculated as $\Delta h/\Delta L$ with Δh [L] as the elevation difference between the water table/stream stage and ΔL [L] as the distance between the filter screen midpoint of the streambed piezometer and the streambed top. The VHG (Figure 3.7) showed

variations between -0.11 representing upward flow and +0.22 representing downward flow, with an average -0.02 and a standard deviation of 0.05.

From stream stage observations, two distinct periods could be identified, (i) one with a fairly constant stream stage from March until the beginning of June 2012 and (ii) one with a strongly varying stream stage afterwards. Stream stage during (i) was influenced by the diel warming and cooling of the streambed, which caused a diurnal rise and fall of stream stage, indicating its dependence on GW-SW exchange. Rainfall seemed to play only a minor role since March 2012 was among the driest months in Northern Belgium. Period (ii) was characterized by extreme stream stage fluctuations with sudden rises of up to 1.20 m, which is almost three times the level observed earlier. However, daily precipitation records obtained from the meteorological station Ukkel [*KMI*, 2014] cannot account for such strong variations in stream stage. It is therefore hypothesized that the high stream stage events in June and July 2012 were a result from the blockage of the stream channel outlet causing backwater. Stream stage and groundwater levels near the outlet show that the rise in surface water level is running ahead of the groundwater levels by 2-6 hours (Figure 3.7). The VHG demonstrates losing conditions as soon as the stream stage rises indicating that stream water is flowing through the adjacent HZ into the aquifer. An effective blockage of the concrete outlet structure of the Slootbeek was indeed observed in January 2013 (after the measurement period) when plant and embankment material as well as parts of the measurement equipment clogged the confluence of the Slootbeek with the Aa River.

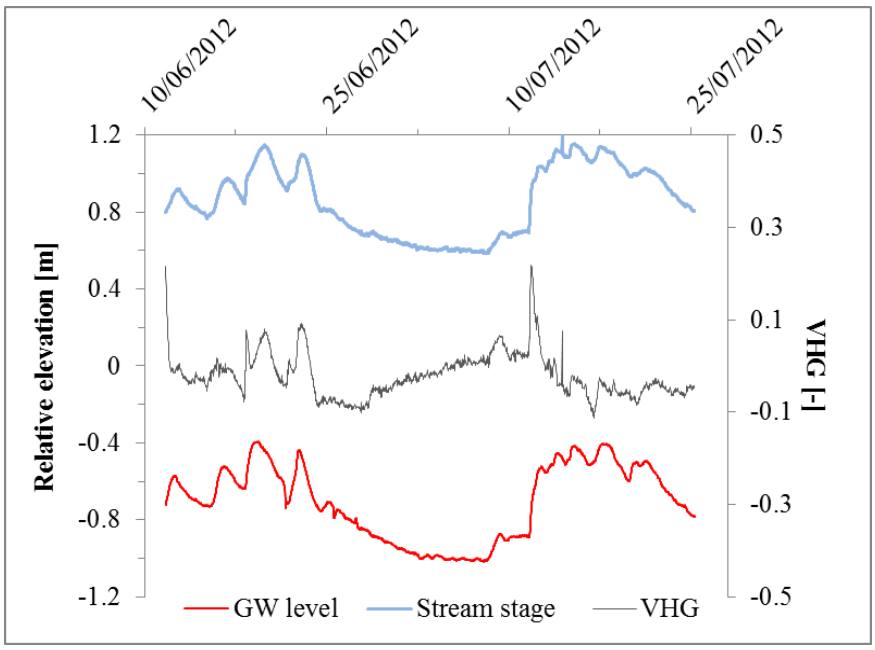

Figure 3.7: Vertical hydraulic gradient (VHG) and stream stage obtained from the piezometer nest for the period June 11 till July 25, 2012, as well as groundwater levels below land surface measured in well GW1 near the confluence with the Aa river. At times, the change in stream stage is running ahead of the groundwater levels by 2-6 hours. Source: *Anibas et al.* [2016].

3.6.3.2 MLTS Temperature Measurements

The recorded temperature-time series (Figures 3.8 and A3.5 to A3.10) show a wide range of measured temperatures despite the spatial proximity of the seven measurement points. ML1, ML2, ML3 and ML6 show strong temperature variations over time (diel and seasonal) while ML4, ML7 and ML8 only show relatively weak temporal changes. Temperatures ranged from 7°C to 11°C in February 2012 and from 15°C to 20°C at the beginning of June 2012. Since seasonal temperature differences follow approximately a sine wave, the general trend of the temperature from winter to summer is upwards. While until early March temperatures remained relatively constant at all locations, they increased with different intensity in spring. However, although temperature ranges for each location differed, average temperatures per depth across the locations are within 1.2°C (Table 3.2).

Location ML1 exemplarily shows the diel and seasonal temperature trends as well as the damping and delay of the signal with increasing depth (Figure 3.8). While the strongest temperature variations are encountered at the streambed top, at 0.55 m only small diel variations occur. The streambed temperatures equalize the average groundwater temperature measured in GW1 (11.0°C) at the end of March. The rising seasonal temperature trend is interrupted by periods of lower streambed temperatures; the most pronounced reduction occurred in the beginning of June 2012. In June and July one can also observe less daily temperature variations. This effect coincides with the sudden rise in stream stage due to backwater. Higher stream stage and stream volume lead to an additional damping of the diel temperature signal in-stream, before the signal reaches the streambed top. This can also be seen from the stream water temperature record (Figure 3.6), showing less diel fluctuations in June and July.

Table 3.2: Average temperatures per depth and location. Differences across locations are within 1.2°C. Source: *own.*

Depth [m]	T_ML1 [°C]	T_ML2 [°C]	T_ML3 [°C]	T_ML4 [°C]	T_ML6 [°C]	T_ML7 [°C]	T_ML8 [°C]
0.00	12.7	12.1	12.2	11.9	12.7	12.6	12.6
0.15	12.4	11.8	11.9	11.5	12.2	12.6	12.5
0.17	12.4	11.7	11.9	11.5	12.1	12.5	12.5
0.20	12.4	11.6	11.9	11.4	12.0	12.5	12.4
0.25	12.3	11.6	11.8	11.4	11.9	12.5	12.4
0.35	12.2	11.5	11.7	11.4	11.7	12.5	12.3
0.55	12.0	11.3	11.6	11.1	11.5	12.3	12.2

In general, variations in streambed temperature can be attributed to reach or sub-reach scale differences in VEF, differences in macrophyte growth, a heterogeneous and transient streambed sediment structure, spatial and temporal differences in stream water temperature

and variations in stream stage influencing the in-stream damping of the temperature signal. However, under natural conditions these variations do not occur suddenly.

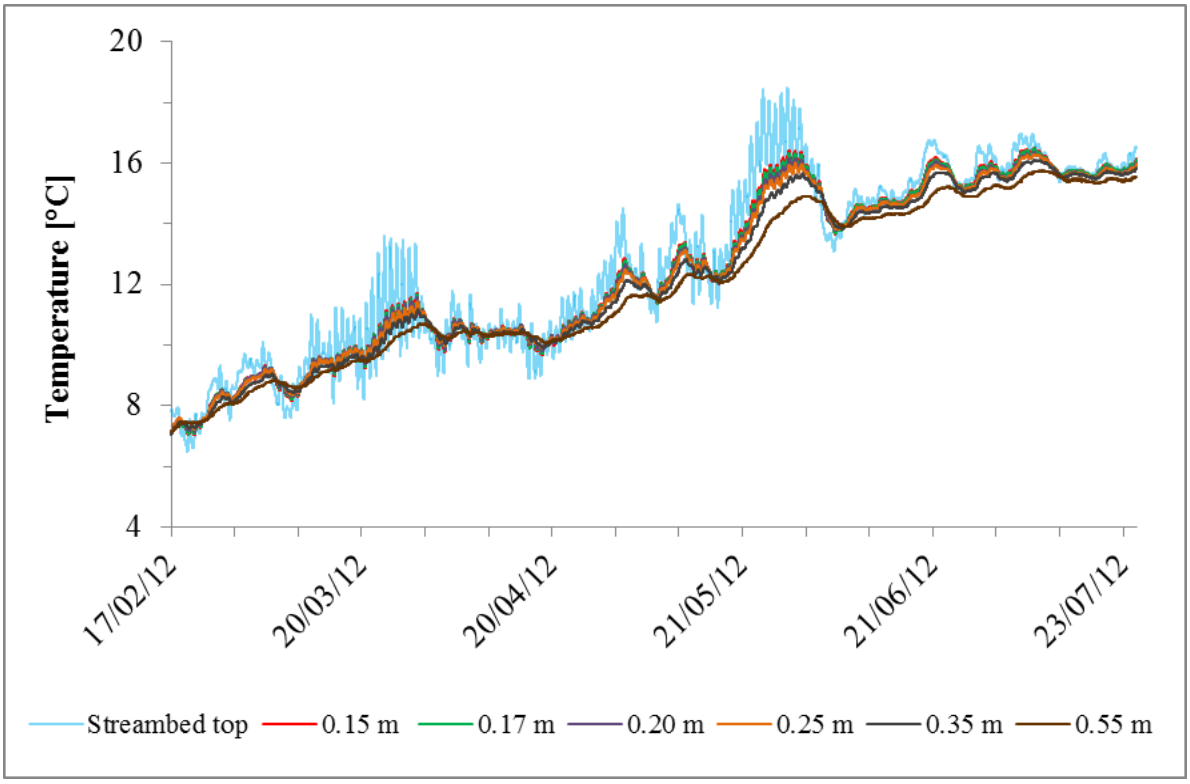

Figure 3.8: Temperature-time series collected at location ML1. Source: *Anibas et al.* [2016].

3.6.4 Comparing the LPML Method with STRIVE

For this analysis the temperature-time series from location ML1 was used with data covering a period of 90 days (February 17 to May 17, 2012, the analysis was performed while the MLTS was still installed). VEFs obtained with the LPML method were compared to those obtained with STRIVE. Constant values in the LPML method were $\rho_w c_w = 4.18 \times 10^6 \mathrm{Jm^{-3}K^{-1}}$ and $\rho c = 3.07 \times 10^6 \mathrm{Jm^{-3}K^{-1}}$ if $\rho_s c_s = 2.05 \times 10^6 \mathrm{Jm^{-3}K^{-1}}$ and n = 0.48 are assumed valid as used in chapter 3.5. For a better comparability of both models, the thermal conductivity was fixed to $\kappa = 1.8\ \mathrm{Wm^{-1}K^{-1}}$ (i.e. $D_T = 5.86 \times 10^{-7}\ \mathrm{m^2 s}$), a common value for the soil type (sandy loam, see Table 1.1) found at the measurement location [e.g. *Kasenow*, 2001; *Stonestrom and Blasch*, 2003] and supported by *Anibas et al.* [2011], who previously conducted experiments at the Aa river about 300 m away from the measurement location.

VEFs obtained with both models using the entire 90-day period show similar upwelling conditions, and vary by less than 1 mm d^{-1}. The VEF estimated with the LPML method is -44.3 mm d^{-1} with a standard deviation of 0.6 mm d^{-1}. The flux estimate obtained with STRIVE lies within two standard deviations of the LPML result (Table 3.3). The CostBest

value is about eight times higher than the expected model cost. This big difference indicates that the concept of purely 1D vertical water flow and heat transport might not be valid.

Table 3.3: Parameter estimates for location ML. Source: *Vandersteen et al.* [2015].

Parameter	Unit	STRIVE	LPML	LPML σ[a]	ExpCost	CostBest
q_z[b]	mmd^{-1}	-43.5	-44.3	0.6	809	6515
q_z[c]	mmd^{-1}	-	-36.3	0.8	809	6410
D	m^{2}s^{-1}	-	5.6×10^{-7}	1.7×10^{-9}		

[a] σ = standard deviation

[b] q_z = optimized vertical Darcy flux. Thermal diffusivity D was fixed to 5.86×10^{-7} m^{2}s^{-1}

[c] D and q_z were optimized simultaneously

Figure 3.9 (a) shows the frequency response G_{LP} and its standard deviation $\sigma_{G_{LP}}$ versus the frequency range. From the seven sensors used for the analysis only three are shown (i.e. 0.15 m, 0.25 m and 0.55 m). Again, it can be seen that G_{LP} reduces gradually with depth and with increasing frequency. The standard deviations are well below G_{LP} for 0.15 and 0.25 m, as well as for the other depths not shown. Only for 0.55 m depth and frequencies above 1.1 d^{-1} it can be observed that G_{LP} exceeds $\sigma_{G_{LP}}$. These frequency lines were discarded from VEF calculations. Figure 3.9 (b) compares the FRFs at 0.15, 0.25 and 0.55 m depth. It can be seen that at 0.25 m depth G_{LP} and G show the best agreement. G_{LP} is overestimated at 0.15 m depth, while it is underestimated at 0.55 m depth. It can also be noted that G_{LP} becomes more perturbed with noise for increasing frequencies as the usable signal information decreases. The larger differences between expected cost and CostBest and the higher discrepancies between G_{LP} and G as compared to the synthetic data set could be due (i) non-vertical flow making the 1D conceptualization invalid, (ii) geological heterogeneity violating the concept of a semi-infinite homogeneous streambed, and (iii) uncertainties in model parameterization. It can be seen that the additional noise component is especially pronounced in frequencies larger than 1.1 d^{-1}.

3.6.5 Comparing the LPML Method with an Amplitude-based Analytical Model

For this analysis the 90-day time series was used and VEFs obtained with the LPML method were compared to those obtained with the analytical amplitude method after *Keery et al.* [2007] as implemented in VFLUX, version 1.2.3 [*Gordon et al.*, 2012]. Besides temperature data, the analytical solution required additional input parameters that were chosen as $\rho_w c_w = 4.18 \times 10^6 \mathrm{Jm^{-3}K^{-1}}$, $\rho_s c_s = 2.05 \times 10^6 \mathrm{Jm^{-3}K^{-1}}$, $n = 0.48$ and $\kappa = 1.8\ \mathrm{Wm^{-1}K^{-1}}$. These

assumed values are representative for sandy loams as shown in Table 1.1 and deemed most representative for the measurement location.

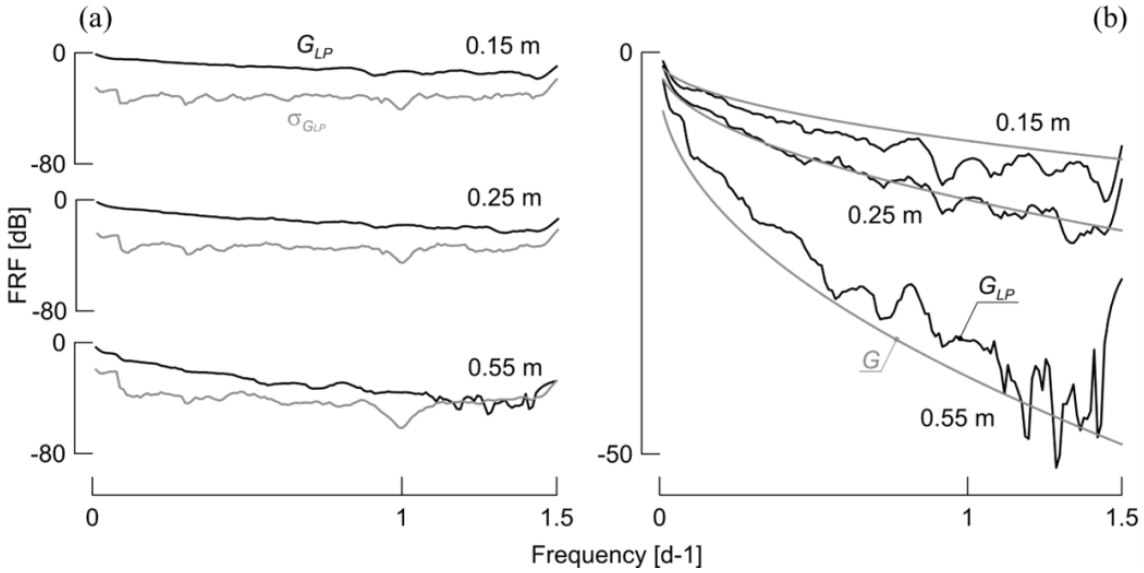

Figure 3.9: (a) FRF G_{LP} and $\sigma_{G_{LP}}$ for three depths from location ML1. At two depths, G_{LP} remains larger than its standard deviation $\sigma_{G_{LP}}$. At 0.55 m, $\sigma_{G_{LP}}$ becomes larger than G_{LP} for frequencies >1.1 d^{-1} and this information is excluded from VEF calculations. (b) Comparison of G_{LP} and G. G_{LP} becomes more variable with increasing frequencies and depth. At 0.25 m G_{LP} and G show best agreement. Source: *Vandersteen et al.* [2015].

As amplitude methods can only incorporate data from two sensors simultaneously, only temperature data from sensors two and five (streambed top and 0.20 m depth) was used in both models. Two scenarios were investigated with the LPML method, (i) only using a frequency of 1 d^{-1} and (ii) a frequency range of 1/90 d^{-1} to 1.5 d^{-1}. The amplitude method cannot use a frequency range in one model run. For a frequency of 1 d^{-1}, the amplitude method estimated a mean exchange flux of -70.7 mm d^{-1}, while the LPML method calculated a 15%-higher flux estimate of -80.9 mmd^{-1} with a standard deviation of 11.1 mm d^{-1}. The phase-lag method was not used with VFLUX for comparison as it yielded flux estimates for only about 50% of the time series with an average magnitude of 309.3 mm d^{-1}. This supports findings from *Lautz* [2012] and *Rau et al.* [2010], who also reported problems with the phase-lag method.

Deviations in VEFs estimated with both methods are a result of methodological differences. While the LPML method uses FRFs and information regarding the noise during parameter estimation, the amplitude method first isolates a single frequency of interest. Although this process is automated in VFLUX, it was difficult for the software to always properly identify the daily amplitudes of both time-series. *Gordon et al.* [2012] propose additional resampling of the temperature data to reduce noise and improve the data structure. Such procedures are not necessary with the LPML method and no data had to be excluded from the analysis.

When using the LPML method with the above-mentioned frequency range, the analysis results in a flux estimate of -61.4 mm d^{-1} with a standard deviation of 1.6 mm d^{-1}. This flux estimate is about 13% lower than with the amplitude method. The result shows that using a range of frequencies might considerably influence VEF estimates.

3.6.6 Using Different Frequency Ranges with the LPML Method

Although the vast majority of studies estimate VEFs by only making use of the daily temperature signal, other frequencies of the spectrum might also be substantially influential. *Lautz* [2012] and *Gordon et al.* [2012] highlight the usefulness of sub-daily signals while *Molina-Giraldo et al.* [2011] discuss the use of seasonal temperature signals for VEF quantification. Sub-daily oscillations can be prominent in dam-regulated rivers, rivers receiving discharge from waste-water treatment plants or industrial processes, systems fed by glacial melt water or very shallow streams that experience large direct solar radiation. Under these conditions fluxes might vary considerably over short periods of time. Seasonal oscillations on the other hand could be used to estimate fluxes from greater depths as these signals penetrate deep into the subsurface.

The LPML method can be used with a single frequency but also allows for the selection of multiple frequencies that carry information and discards those frequencies that mostly carry noise. It is thus not limited to isolating any one frequency before flux estimation. Figure 3.10 shows flux estimates obtained with the LPML method for the 90-day time series using 14 different frequency ranges from 1/90 d^{-1} to 15/90 d^{-1} up to 1/90 d^{-1} to 1.8 d^{-1}. The thermal diffusivity was set to $D_T = 5.86 \times 10^{-7}$ m^2s. In general, the VEF estimate increased when larger frequencies were included in the analysis. The largest flux value of -47.3 mm d^{-1} was obtained for a range from 1/90 to 1 d^{-1}, while the lowest flux value with -24.9 mm d^{-1} was obtained for a range from 1/90 d^{-1} to 30/90 d^{-1}. A reason why this particular period representing three-monthly to monthly frequencies shows the smallest VEF could not be determined. Above a frequency of 1.5 d^{-1}, VEF estimates stabilized around -45.0 mm d^{-1}. Standard deviations stabilized around 0.9 mm d^{-1} when the frequency range contained frequencies of 1 d^{-1} or higher. When only smaller frequencies were used standard deviations were up to two times larger. For the data set used here, including frequency components above 1.2 d^{-1} to determine the average flux provided little additional information as higher frequencies only exert a limited influence on the VEF estimate since these signals are attenuated more quickly with increasing depth.

For a specific site and data set, it is advisable to look either at specific frequencies of interest or test a variety of frequency ranges to find an adequate range that ensures that the signals of interest (daily, annual, event-based) are included in the analysis. This frequency range will usually be smaller for short time-series and shallow temperature measurements where low frequency components play only a minor role. An analysis using various frequencies and frequency ranges could also help identify previously unknown periodic events of importance at a specific site.

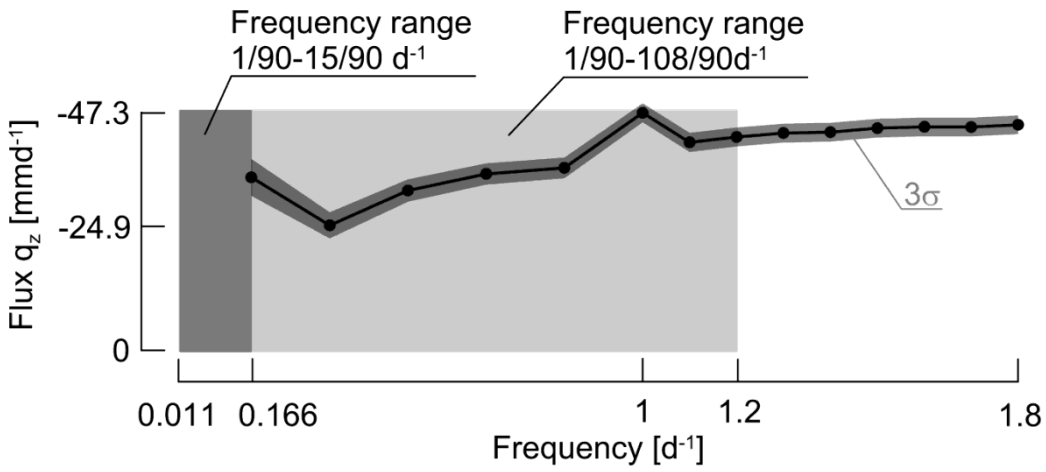

Figure 3.10: Vertical flux estimates for location ML1 using different frequency information. The dark grey box indicates the frequency range of 1/90 to 15/90 d^{-1}, while the light grey box shows the range of 1/90 to 108/90 d^{-1}. The corresponding flux values are indicated at the right hand limit of the boxes. The highest VEF is obtained using all frequency information in the range from 1/90 to 1 d^{-1}. As VEF estimates stabilize, including frequencies above 1.5 d^{-1} does not bring much additional gain. Source: *Vandersteen et al.* [2015].

3.6.7 Simultaneous Optimization of Flux and Thermal Diffusivity

The LPML method can simultaneously estimate α and γ and as such q_z and D_T (Eqs. 3.22 and 3.23). For the Slootbeek, so far, the thermal diffusivity had been fixed to $D_T = 5.86 \times 10^{-7}$ m^2s. When optimizing both parameters simultaneously for the 90-day time series, the VEF was estimated at -36.3 mmd^{-1}, which is about 20 % less than the VEF estimate in chapter 3.6.4 (Table 3.3). On the other hand, $\sigma_{\hat{q}_z}$ was with 0.8 mmd^{-1} about 33 % larger than $\sigma_{\hat{q}_z}$ in chapter 3.6.4. The thermal diffusivity was estimated to be 5.61×10^{-7} m^2s, which is about 4 % less than before. The standard deviation σ_{D_T} was 1.7×10^{-9} m^2s. With a value of 6410, the model cost proved to be 1.6 % smaller than in chapter 3.6.4. From this one example it seems reasonable to assume that a simultaneous optimization of both q_z and D_T provides reliable VEF estimates. However, a slight change in D_T may lead to a rather pronounced difference in the flux estimate, so q_z is sensitive with respect to D_T . It is thus recommended to verify estimates of D_T with independent measurements in the field or laboratory. However, such data was not available for the Slootbeek case.

3.6.8 Creating VEF Time Series with the LPML Method

The LPML method can be used to create time series of VEF by analyzing parts of temperature-time series in a consecutive manner (i.e. using a moving window by applying the Short Time Fourier Transform). The window length can be chosen relatively freely within the limits of the analyzed temperature-time series, depending on the frequency information used in the analysis. At least two complete periods of data (here 2 days) would be needed to estimate the FRFs and the transient parts, providing that the frequency range used is sufficiently large. However, increasing the frequency range only makes sense if the higher

frequency components contain usable information. Additionally, the mathematical requirements for the LPML method have to be fulfilled, i.e. sufficient degrees of freedom of the LP method [*Pintelon et al.*, 2010a]. In general, a shorter window will always provide a better temporal resolution of the flux but the output will become noisier. A trade-off has to be made between the frequency range included in the analysis and the window length.

For the 90-day temperature-time series from location ML1, the temporal variability of q_z ($D_T = 5.86 \times 10^{-7}$ m^{2}s) was calculated by applying a 10-day moving window (offset of 1 day) and using the same frequency range as above. Over the entire period, the VEF varied from -147 mm d^{-1} in mid-March to 21 mm d^{-1} (i.e. infiltration) at the beginning of April 2012 but mostly upwelling conditions prevailed (Figure 3.11). To evaluate the influence of the window length on the VEF estimate three different window lengths were used (note that the frequency range is different); 3 days, 10 days and 20 days. Shortening the window led to higher maxima and lower minima as well as stronger variations in flux estimates while increasing the window length smoothed the curve (Figure 3.11).

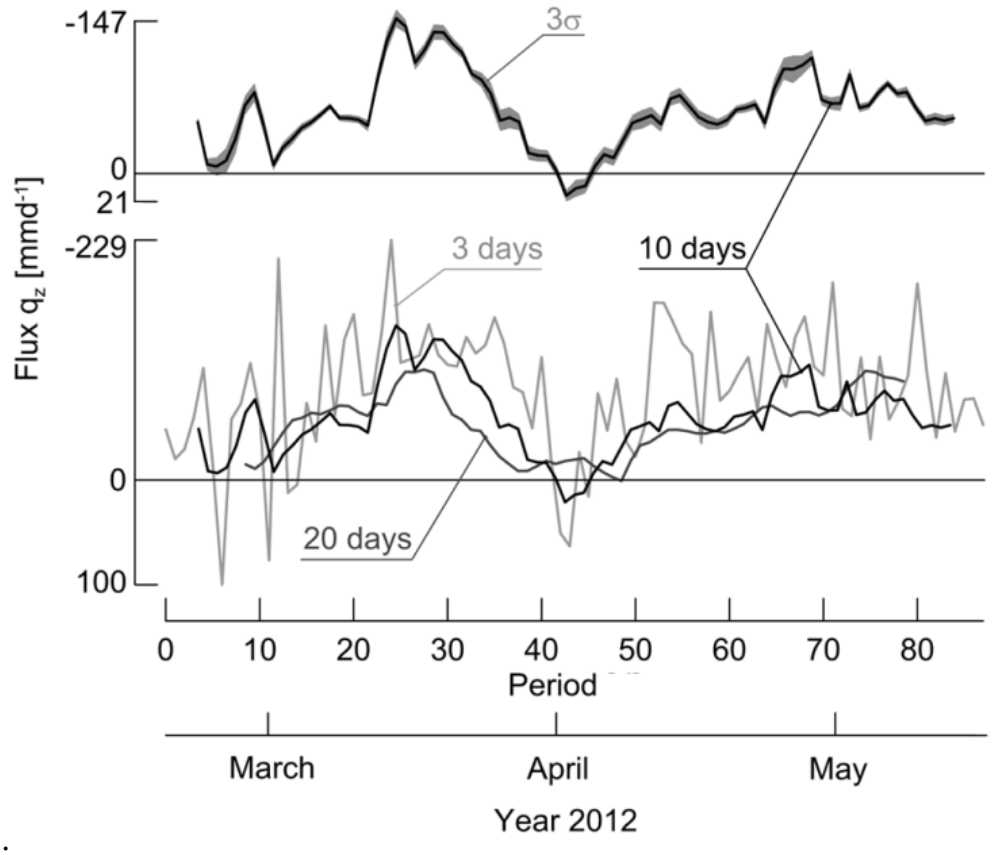

Figure 3.11: Moving windows (length: 3 days, 10 days, 20 days) are used to create VEF time series for ML1. Range and variability of VEF decrease with increasing window length. However, the general trend is preserved. Source: *Vandersteen et al.* [2015].

However, the general trend over time was preserved as can be seen especially for periods 20 to 50. Standard deviations also depend on the window length. As the window length

increased, the average of the standard deviations in percent decreased. In general, percent standard deviations are highest for near zero flux estimates. In those cases a distinction between upwelling or downwelling conditions can prove difficult.

3.6.9 Spatial and Temporal Variability of VEFs

In the following analyses the bulk thermal conductivity was set to κ = 1.72 $Wm^{-1}K^{-1}$ (based on the estimated D_T in chapter 3.6.7, while ρc was set to 3.07×10^6 $Jm^{-3}K^{-1}$ (same as in chapter 3.6.4) for locations ML1 and ML2. Locations ML3 to ML8 had a higher organic matter content; thus κ = 1.40 $Wm^{-1}K^{-1}$ and ρc = 3.20×10^6 $Jm^{-3}K^{-1}$ assuming a clay-loam from Table 1.1.

3.6.9.1 Long-Term, Seasonal and Monthly Fluxes

Long-term, seasonal and monthly vertical exchange fluxes and their uncertainties were estimated for all seven locations. Long-term flux estimates are based on the entire temperature-time series as input and ranged between -291.2 mmd^{-1} (ML6) and 12.3 mmd^{-1} (ML7) with uncertainties varying from 0.4 % (ML6) to 5.2% (ML7) as presented in Table 3.4. ML3 and ML7 show losing conditions, while the other locations show gaining conditions. Locations with losing conditions also show a much smaller flux magnitude, making the investigated stream section overall gaining with an average long-term exchange flux of -81.2 mmd^{-1}.

By dividing the datasets into periods covering parts of astronomical seasons (only spring is complete), flux estimates show strongly gaining conditions in winter (February 17 to March 20, 2012), except at location ML3. Estimates ranged from -332.5 mmd^{-1}(ML6) to 11.2 mmd^{-1} (ML3) with an average over the measurement locations of -137.8 mmd^{-1}. Uncertainties on the estimates varied from 0.6% (ML8) to 9.8% (ML7). During spring (March 21 to June 20, 2012), exchange fluxes decreased to -119.0 mmd^{-1} (ML6) and 11.8 mmd^{-1} (ML3) with an average of -41.4 mmd^{-1}. Standard deviations ranged from 0.3% (ML8) to 4.4% (ML7). During the summer period (June 21 to July 25, 2012), flux estimates ranged from -270.3 mmd^{-1} (ML6) to 101.7 mmd^{-1} (ML7) with an average of -15.5 mmd^{-1}. Standard deviations for this period varied from 1.3% (ML6) to 6.7% (ML3) and only four of the seven locations showed gaining conditions.

These seasonal flux estimates showed on average a strong trend from strongly gaining conditions in winter towards only slightly gaining or even losing conditions in summer. Seasonal differences in exchange flux where already observed in the Aa River, where winter estimates were around 25% larger than summer estimates [*Anibas et al.*, 2011]. For the Slootbeek, seasonal variations were much more pronounced as the average summer flux was only about 11% of that of the winter flux. This demonstrates that the investigated stream section of the Slootbeek is much more dependent on groundwater inflow than the sections of the Aa River investigated previously. In general, the Aa River is much longer, has a much

higher discharge and many tributaries. Such characteristics commonly reduce the dependence on groundwater inflow as compared to a stream such as the Slootbeek. However, as indicated in Figure 3.6, the two events showing high stream stages in the Slootbeek in June and July 2012 also influence GW-SW interaction. When the stream stage suddenly increases it can be expected that an otherwise gaining stream will receive less groundwater and will eventually become losing when the stream stage rises above the piezometric head of the connected aquifer.

Table 3.4: Long-term and seasonal flux estimates and their uncertainties obtained from temperature-time series for seven locations in the Slootbeek, Belgium. Source: *Anibas et al.* [2016].

Location	Long-term		Winter 2012		Spring 2012		Summer 2012	
	q_z [mmd^{-1}]	σ_{qz} [mmd^{-1}]	q_z [mmd^{-1}]	σ_{qz} [mmd^{-1}]	q_z [mmd^{-1}]	σ_{qz} [mmd^{-1}]	q_z [mmd^{-1}]	σ_{qz} [mmd^{-1}]
ML1	-25.4	0.47	-46.3	1.37	-21.5	0.38	33.8	0.96
ML2	-89.9	0.68	-143.7	1.78	-67.4	0.71	-49.6	1.99
ML3	10.1	0.21	11.2	0.92	11.8	0.23	9.1	0.61
ML4	-47.1	0.41	-86.0	2.33	-45.1	0.34	-30.2	1.80
ML6	-291.2	1.17	-332.5	3.12	-119.0	0.36	-270.3	3.42
ML7	12.3	0.64	-142.2	13.89	7.5	0.33	101.7	2.66
ML8	-137.1	0.75	-225.1	1.44	-56.4	0.37	97.1	4.16
Average	-81.2		-137.8		-41.4		-15.5	
RSD	1.32		0.83		1.10		8.16	

q_z = vertical exchange flux
σ_{qz}= standard deviation on the estimates
RSD = relative standard deviation or absolute coefficient of variation

By looking at monthly flux estimates (Table 3.5) it could be observed that while at ML3 estimates remained almost constant in time, at other locations such as ML7 and ML8 conditions changed strongly from gaining to losing. This indicates that not only fluxes but also their trends can vary strongly at a relatively small spatial scale. The most gaining conditions that are also the largest absolute flux estimates (max q_{zgc}) and the smallest gaining or largest losing conditions per location were concentrated in February and July, respectively (Table 3.6). A pattern emerged, showing predominantly gaining conditions at the outer bank of the Slootbeek (i.e. ML2, ML4, ML6 and ML8) and less gaining or even losing conditions at the inner bank (i.e. ML1, ML3 and ML7).

Table 3.5: Monthly estimates and their uncertainties obtained from temperature-time series for seven locations in the Slootbeek, Belgium. Source: *Anibas et al.* [2016].

Location	February-12		March-12		April-12		May-12		June-12		July-12	
	q_z [mmd^{-1}]	σ_{qz} [mmd^{-1}]	q_z [mmd^{-1}]	σ_{qz} [mmd^{-1}]	q_z [mmd^{-1}]	σ_{qz} [mmd^{-1}]	q_z [mmd^{-1}]	σ_{qz} [mmd^{-1}]	q_z [mmd^{-1}]	σ_{qz} [mmd^{-1}]	q_z [mmd^{-1}]	σ_{qz} [mmd^{-1}]
ML1	-20.6	2.33	-40.0	0.67	-33.6	0.79	-52.5	0.79	24.1	0.92	34.7	0.68
ML2	-130.2	3.34	-120.4	1.32	-214.1	1.66	-57.7	1.36	-16.8	0.82	-	-
ML3	-8.8	1.95	4.4	0.56	16.5	0.49	19.6	0.73	11.3	0.67	2.0	0.52
ML4	-113.3	3.50	-108.5	1.16	-64.8	1.00	-67.6	1.02	-26.9	1.22	-17.3	1.18
ML6	-448.9	11.69	-409.9	3.42	-197.8	0.98	-222.9	1.22	-169.1	2.72	-141.4	3.14
ML7	-143.1	7.19	-46.1	7.03	24.1	1.29	6.4	1.20	36.2	1.87	87.1	2.66
ML8	-289.0	4.65	-196.1	1.25	-81.7	1.24	-112.9	1.14	3.0	2.25	110.9	5.70
Average	-164.9		-130.9		-78.8		-69.6		-19.8		12.7	
RSD	0.94		1.06		1.21		1.17		3.51		7.09	

q_z = vertical exchange flux
σ_{qz}= standard deviation on the estimates
RSD = relative standard deviation or absolute coefficient of variation

The smallest absolute EFs $|q_z|$ indicating the period with least vertical water exchange was encountered in late spring and early summer, except at location ML1 where smallest EFs were calculated for February. The change in flow direction from gaining to losing was most prominent at the downstream locations ML7 and ML8, but occurred also at ML1. This again is linked to the two events with high stream stage in June and July 2012 when mostly losing conditions occurred.

Table 3.6: Occurrence of maximum and minimum fluxes for each of the seven locations of the Slootbeek Source: *Anibas et al.* [2016].

Location	max q_{zgc} [mmd^{-1}]	Month	max q_z [mmd^{-1}]	Month	min $\|q_z\|$ [mmd^{-1}]	Month
ML1	-52.5	May	34.7	July	20.6	February
ML2	-214.1	April	-16.8	June	16.8	June
ML3	-8.8	February	19.6	May	2.0	July
ML4	-113.3	February	-17.3	July	17.3	July
ML6	-448.9	February	-141.4	July	141.4	July
ML7	-143.1	February	87.1	July	6.4	May
ML8	-289.0	February	110.9	July	3.0	June

max q_{zgc} = maximum exchange flux for gaining conditions
max q_z = maximum exchange flux for losing conditions or minimum flux for gaining conditions
min $|q_z|$ = minimum absolute exchange flux

3.6.9.2 Short-Term Flux Variations

The LPML method allows for the analysis of data sets of different length. However, a minimum amount of data is necessary for the statistical estimation of parameter uncertainties and to ensure an adequate signal to noise ratio. To study the temporal variability of exchange fluxes in more detail, a rectangular window with the length of ten days was moved along the temperature-time series with an increment of one day.

The time series of estimated fluxes of ML3 and ML6 highlight the results of this analysis indicating the range, trend and variations of vertical fluxes across the streambed of the Slootbeek (Figure 3.12). The colored bands encompassing the solid lines show the uncertainties on the flux estimates. No linear relationship between flux magnitudes and their uncertainties could be deduced. While for ML3 the Pearson correlation coefficient r^2 is 0.00, for ML6 it is 0.07. Using other functions (exponential, polynomial, power) also did not show a relationship between both variables. For both time series the EF is variable in time, highlighting strong differences at both temporal and spatial scale. While ML6 showed mostly discharging conditions ML3 was predominantly recharging. Common to ML3 and ML6 but

also to the other modeled time series was an increasing trend (i.e. from negative values, hence losing situation to less negative or even positive values) during the course of the observation period. Higher exfiltration fluxes occurred in winter and spring while lower values or even infiltration occurred in summer (Figures 3.12 and 3.13). However, for ML3 this trend was relatively weak. The absolute fluxes were higher and their temporal variations stronger for ML6 than for ML 3. In July 2012, both locations showed comparable exchange flux and ML6 even changed flow direction from exfiltration to infiltration shortly thereafter. While for most of the time both curves are fairly synchronized, short periods existed (e.g. at the end of May or at the end of June) where ML6 showed increasing exfiltration fluxes while ML3 showed an increase in infiltration.

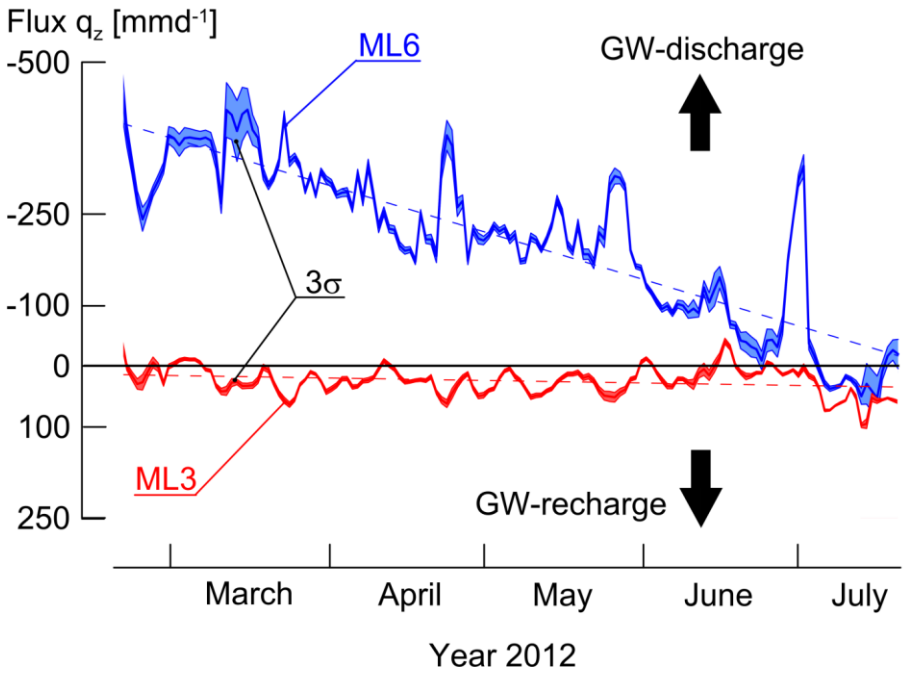

Figure 3.12: The LMPL model output for ML3 and ML6 shows extremes calculated for the Slootbeek, where ML6 shows highest fluxes and ML3 lowest ones. All measurement locations show increasingly exfiltrating conditions over time; for ML6 this trend is very strong, while for ML3 the trend is only weak. Both curves end in mostly recharging conditions of comparable magnitude. Opposing rising and falling short term trends suggest a flow-through system from the left (ML6) to the right stream bank (ML3). Source: *Anibas et al.* [2016].

In general, all locations showed decreasing exfiltration over the entire observation period with a 95% probability determined by applying a Mann-Kendall test [*Mann*, 1945; *Kendall*, 1975]. By comparing the flux estimates for pairs of opposite sensors (Figure 3.13) it can be seen that most flux variations within the pairs are well synchronized, with the best agreement between ML3 and ML4. Fluxes on the outer stream bank are generally higher in magnitude and more variable. The upstream points ML1-ML4 show lower flux values and absolute variations than the downstream locations ML6-ML8. ML1 and ML2 showed strongly opposing trends from mid-March until the beginning of April. While the flux at the outer bank (ML2) rose, the flux at the inner bank (ML1) decreased. This trend was reverted throughout April. In the beginning

of May, both locations showed gaining conditions before ML2 became more erratic. The high stream stage events in June and July are least visible in this MLTS pair. At ML7 the flux showed a fairly erratic behavior in the first month of the time series, visible also in the high uncertainty bounds on the estimates and the fairly low correlation with its counterpart ML8 (Fig.3.13 (d)). Here, the LPML model seemingly had problems to converge, as is indicated by the gap in the graph of ML7. Later however, ML7 tends to fit well with the time series of ML8. From the beginning of June onwards both lines almost completely correspond and end in strong and rather erratic fluctuations of exfiltration fluxes.

The exchange flux pattern shown here could be due to two main reasons: (i) The synchronous rise or decline of exchange flux in the same direction affecting the entire stream section is caused by changes of in-stream hydraulic conditions (e.g. a changing stream stage) because of meteorological events or the blocked outlet. Both effects would also cause concurrent changes in EF values; the locations closer to the outlet would be more affected. (ii) Gaining conditions at the outer stream bank and partly losing conditions at the inner stream bank as encountered for MLTS pairs ML3 & ML4 and ML7 & ML8 (Figure 3.13) from March to the beginning of June are an indicator for a local flow-through system. In such a system groundwater enters the Slootbeek via the outer bank and leaves it through the inner bank of the examined stream bend. Such systems have been described e.g. by *Woessner* [2000] and *Winter et al.* [1998].

From mid-June on until the end of July indications for a flow-through system were less pronounced as losing conditions were found at both stream banks due to the higher stream stage. The flow-through mechanism with higher exfiltration at the outer bank and lower at the inner bank is supposedly caused by regional groundwater flow and the morphology of both the Slootbeek and the Aa River. The regional groundwater flow direction is WSW; the Aa River shows GW-SW water exchange in its bends such as the one downstream of the outlet of the Slootbeek [*Anibas et al.*, 2011; *Mutua*, 2013]. There, flow lines converge and stronger hydraulic gradients towards the south are present because of the topography. The bend of the Slootbeek is exposed to the same flow field as the Aa River bend.

For most of its length the Slootbeek runs almost parallel to the Aa River, so a strong hydraulic connectivity between both for the right bank of the Slootbeek can be assumed. The left stream bank of the Slootbeek is more influenced by regional groundwater flow. This would explain the occurrence of different fluxes and different trends on both sides of the stream. Streambed sedimentation and erosion as well as plant growth also could affect the observed pattern. The overall decreasing exfiltration trend at all measurement locations is potentially caused by the combined effect of decreasing precipitation from December to April and increasing evapotranspiration from April onwards.

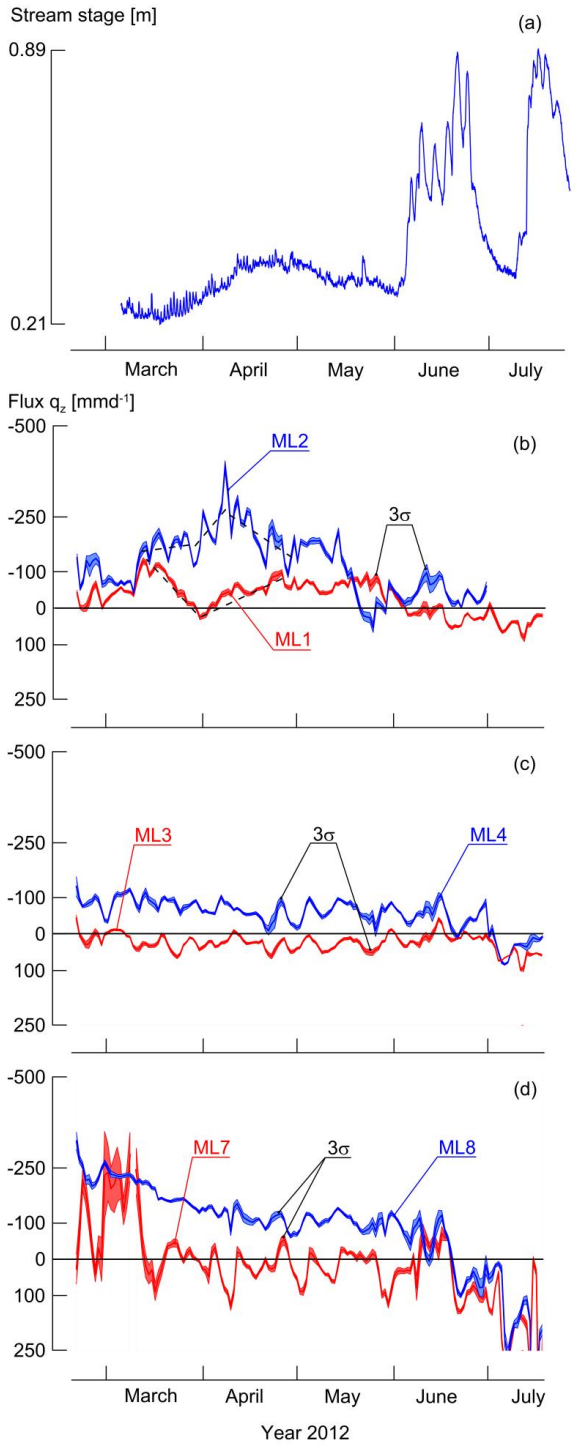

Figure 3.13: (a) Stream stage showing two distinct phases: a less variable one until May 2012 influenced by rainfall is succeeded by two events of high stream stages. The paired short term fluxes for ML1 and ML2 (b), ML3 and ML4 (c) and ML7 and ML8 (d) show increasing trends. (b) and (c) are characterized by synchronous changes in VEF where the outer bank of the stream has higher flux magnitudes. The measurement locations at the outer bank are indicated in blue colors, the location at the inner bank in red. In June and July the two high stream stage events can be observed, considerably changing the flux towards more losing conditions. Source: *Anibas et al.* [2016].

3.6.9.3 Spatial Pattern of VEFs

At the investigated section of the Slootbeek, fluxes varied spatially to different extents. To compare flux variations the relative standard deviation or absolute coefficient of variation (RSD) was used. This parameter relates the standard deviation to the mean as an indicator (Tables 3.4 and 3.5).

From Table 3.5, it can be observed that the average long-term discharge is -81.2 mmd^{-1} with an RSD of 1.32, indicating strong spatial variation among the seven locations. From the average seasonal flux estimates it can be concluded that variations in summer (8.16) were much higher than in winter (0.83) or spring (1.10). This can be explained by the stronger fluctuations in stream stage with periods of reversed flow conditions between stream and aquifer. Monthly flux averages (Table 3.5) emphasize this observation as June and July show much higher spatial variability than the previous months.

Figure 3.14 shows the spatial distribution of exchange flux as an interpolated map of the examined stream section using the calculated long-term values (Table 3.4). For the interpolation a multilog radial basis function was used (Golden Software Surfer 8.04). This function is an exact interpolator that can produce reasonable maps with only a few measurement points. It uses relative distances from a data point to a node on the interpolation grid, which can be rescaled by a predefined anisotropy (here the anisotropy ratio is 2.5). Similar to kriging algorithms a search ellipse can be defined. Additionally, a shaping factor R^2 (here 1.1) can be used to smoothen the interpolated surface. More information on radial basis functions can be obtained from *Buhmann* [2009]. ArcMap 10.1 (ESRI) was then applied to determine the net exchange over the stream section covering an area of 624 m^2. The interpolation was based on only seven locations, which did not allow for a detailed (statistically representative) delineation of the spatial heterogeneity. However, a robust first estimate of the exchange pattern for the study site could still be delineated.

Gaining conditions were encountered towards the outer stream bank, with flux estimates above -250 mmd^{-1} at ML6, surpassing all other locations. Locations near the inner bank showed either slightly gaining (ML1) or slightly losing conditions (ML3 and ML7). From the interpolated area an average groundwater discharge of -92 mmd^{-1} was estimated. This value is about 13% higher than the average flux over the seven locations (Tab. 3.4) and only 1.5% higher than the flux (-91 mmd^{-1}) estimated independently with the LPML method using an average temperature-time series built from the time-series of the seven locations. The estimated flux value of -92 mmd^{-1} was also used to determine the net exchange over the studied stream section, which amounted to 57 m^3d^{-1}. Assuming this to be a representative value for the whole Slootbeek and using a constant channel width of 3 m over the entire stream length, the Slootbeek receives around 25% of its discharge at the outlet from vertical flux. This result suggests that the Slootbeek is more dependent on net exchange than its receptor, the Aa River, which has an average flux of -65 mmd^{-1} [*Anibas et al.*, 2011] and receives around 15% of its discharge from the fluvial aquifer. Using heat as natural tracer,

Anibas et al. [2011] also showed that the Aa River receives most water where a river bend is exposed to the regional groundwater flow. This is in fact the area downstream of the discharge point of the Slootbeek in the Aa River. The highest values were described for the left bank of the Aa River with about -110 mmd^{-1}, with little variation between winter and summer seasons.

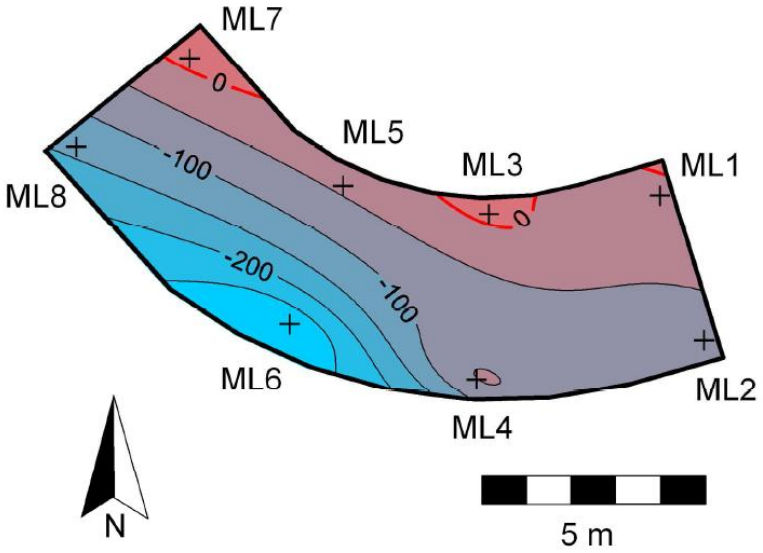

Figure 3.14: Spatial interpolation of the long-term fluxes reveals a tendency of stronger discharge on the outer (left) bank (in blue) and lower discharge or slight recharge (zero flux is indicated as a red line) at the right bank of the Slootbeek. This is an indication for a flow-through system. In magnitude, fluxes at ML6 exceed the other locations, possibly because of converging flow lines of the regional GW-flow. Data from seven measurement locations (ML1-ML8) were used; at ML5 no data could be collected. Source: *Anibas et al.* [2016].

3.6.10 Exchange Flux from Piezometric Head

The VHG as shown in Figure 3.7 was used to determine the average VEF for the piezometer location (Figures 3.4 and 3.5) from June 11 till July 25, 2012. To do so a hydraulic conductivity value of 1×10^{-5} ms^{-1} was assumed. This value is representative for fine sand, the major streambed component found at the piezometer location. Applying Darcy's law, an average VEF of -18 mmd^{-1} could be calculated, with a maximum gaining flux of -97 mmd^{-1} and a maximum losing flux of 188 mmd^{-1}. Estimates from temperature-time series analyses for ML4 located about one meter away from the piezometer nest for the same period showed an average VEF of -51 mmd^{-1} with an uncertainty on the estimate of 1.5 mmd^{-1}. These variations in VEF estimates could be explained by the different nature of the two methods. Flux estimates using Darcy's law depend on an adequate characterization of the hydraulic conductivity, which is much more variable for different streambed sediments than their thermal counterpart. On the other hand, the thermal method requires knowledge on the thermal conductivity and volumetric heat capacity, two parameters which are difficult to determine in the field.

3.7 Conclusions

This chapter provided a short background of how streambed temperatures can be used to quantify 1D vertical exchange flux by a variety of analytical models. These models make certain assumption and thus are limited in their applicability. To overcome some of these limitations the LPML method was newly adapted to the field of stream hydrology. This method solves 1D water flow and heat transport in the frequency domain and has the following advantages compared to the transient analytical solutions discussed before [*Hatch et al.*, 2006; *Keery et al.*, 2007; *Luce et al.*, 2013]:

(i) The LPML method utilizes more spectral information of the temperature measurements than just one frequency.

(ii) The LPML method can handle non-periodic transient temperature signals.

(iii) The LPML method can simultaneously use temperature-time series information from several depths to quantify exchange fluxes.

(iv) The LPML method can provide both estimates of VEFs and thermal diffusivity/conductivity as well as their uncertainties.

(v) The LPML method also provides information regarding the model quality using cost-function analysis.

(vi) The LPML method can be used on the entire temperature-time series or on shorter periods by applying a moving window.

The LPML method was successfully tested on a synthetic data set and afterwards applied to delineate spatial and temporal variations in VEF over a stream section of the Slootbeek. It was found that long-term flux estimates ranged from -291 mmd^{-1} to 12 mmd^{-1} while average seasonal fluxes ranged from -138 mmd^{-1} in winter to -16 mmd^{-1} in summer. Highest gaining conditions of -165 mmd^{-1} averaged over all locations occurred in February 2012 while highest losing conditions of 13 mmd^{-1} were observed in July 2012. The stream section was gaining during most of the observation period. Two high stream-stage events could also be observed, which were most probably caused by blockage of the stream outlet. This blockage led to a change in flow direction from gaining to losing conditions. Results also indicate the existence of a time-variable flow-through system with water flowing from the outer bank towards the inner bank. Such systems are still poorly described in the scientific literature. By relating the results to previous studies [*Anibas et al.*, 2011; *Mutua*, 2013] it could be observed that the Slootbeek receives relatively more water from the fluvial aquifer than the Aa River. This suggests a general relation between stream size and the amount of water (in percent of the total water found in the stream) a stream receives by GW-SW interaction, which should be further studied by the scientific community.

Similar to other existing 1D models, the LPML method is subject to methodological limitations including the assumption of a homogeneous subsurface and the disregard of non-

vertical flow components. These assumptions could lead to erroneous flux estimates. As such, a comparison or validation with flux estimates from other methods such as vertical hydraulic gradients is advised. The application of the covariance matrix and the cost function analysis allow for a quantification of parameter and model structure uncertainty. However, it should be noted that these values should only be seen as indicative (i.e. showing a certain trend) and not as true uncertainty values. To determine the true overall uncertainty one would have to quantify the other uncertainties discussed in chapter 3.3 (e.g. input uncertainty due to sensor accuracy and resolution, model structure uncertainty due to 1D assumption, etc.). This could be achieved by conducting a variety of simulations (sensitivity analysis) using synthetic data and known input conditions that could be adapted independently. Additionally, a comparison of flux estimates with those obtained from 2D and 3D water flow and heat transport models would be necessary, as discussed previously.

4 LPMLE3 – A Novel Method to Quantify Vertical Water Flux in Streambeds Using Heat as a Tracer

This chapter is partly based on the following work:

Schneidewind, U., van Berkel, M., Anibas, C., Vandersteen, G., Schmidt, C., Joris, I., Seuntjens, P., Batelaan, O., Zwart, H.J. (2015): LPMLE3 - A Novel Method to Quantify Vertical Water Fluxes in Streambeds Using Heat as a Tracer. In review with *Water Resources Research.*

4.1 Introduction

One of the main limitations of the LPML method [*Vandersteen et al.*, 2015] as well as the analytical 1D methods to solve Eq. (1-17) and calculate VEFs [*Hatch et al.*, 2006; *Keery et al.*, 2007; *Wörman et al.*, 2012; *Luce et al.*, 2013] is their assumption of a homogeneous and isotropic streambed of infinite extent (semi-infinite halfspace) with constant fluxes and thermal parameters (see discussion in chapter 3.3). However, streambeds are often very dynamic and heterogeneous environments. They show variable patterns of mixing of groundwater and surface water and are constantly reshaped by processes such as sediment erosion and deposition as well as colmation (chapter 1.2). Thus magnitude and direction of exchange flux may vary along the measured temperature profiles. This flux variability and the availability of high-resolution temperature data in the vertical direction through the use of novel measurement devices [*Vogt et al.*, 2010; *Briggs et al.*, 2012; *Schmidt et al.*, 2014] makes it beneficial to develop and apply models that can account for streambed heterogeneity. Several numerical models exist [e.g. *Voytek et al.*, 2014] that fulfill this requirement but these models often need a considerable amount of input data other than temperature and can be costly in setting up.

In this chapter the LPMLE3 method is introduced and applied. The **LPMLE3** (Figure 4.1) method is a novel method scripted in MATLAB that can be used to quantify vertical water fluxes in streambeds in the frequency domain without assuming the subsurface to be a homogeneous semi-infinite half space. It uses a local polynomial (**LP**) model to separate periodic, non-periodic and noise parts contained in a temperature signal and to determine the system response in the frequency domain. The LP model is combined with a maximum likelihood estimator (**MLE**) that quantifies fluxes and their uncertainties for finite domains

considering information from three (**3**) temperature sensors. Each finite domain has a temperature boundary condition (in form of temperature-time series) at its top and bottom, while the flux is estimated from a third temperature-time series within the domain showing the system response. By using finite domains, thermal parameters and fluxes are considered locally constant in space. This is a more realistic assumption for a dynamic streambed. The LPMLE3 method extends the method presented by *van Berkel et al.* [2014a] with the LP method [*Pintelon et al.*, 2010a] that allows for the use of non-periodic temperature-time series.

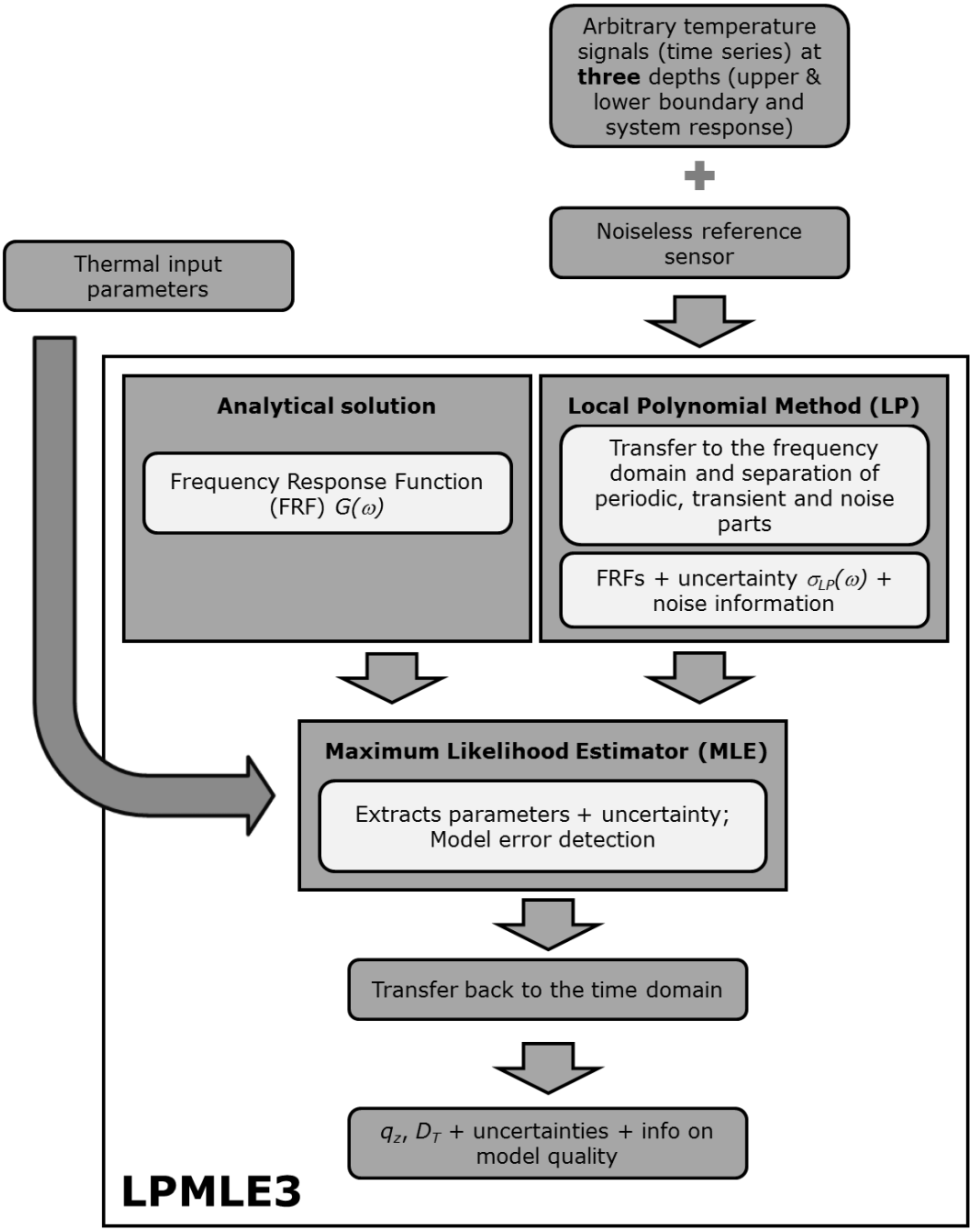

Figure 4.1: Flow chart presenting the concept of the LPMLE3 method. Source: *own.*

4.2 The LPMLE3 Method

The general analytical solution to Eq. (3-10), not assuming a semi-infinite halfspace but assuming periodic temperature signals without noise, can be written as

$$\Theta(z,\omega,\theta) = C_1 e^{(\lambda_1 z)} + C_2 e^{(\lambda_2 z)} \tag{4-1}$$

where

$$\lambda_{1,2}(\omega,\theta) = \frac{1}{2}\left(-\alpha - \sqrt{\alpha^2 - 4i\omega\gamma}\right) = \frac{q_z}{2D_T}\frac{\rho_w c_w}{\rho c} \pm \sqrt{\left(\frac{q_z}{2D_T}\frac{\rho_w c_w}{\rho c}\right)^2 + \frac{i\omega}{D_T}} \tag{4-2}$$

with $\theta = [\alpha \quad \gamma\,]$ and z as the depth. C_1 and C_2 are free variables determined from the temperature measurements at sensor x, i.e. $\Theta(z = z_{x-1})$ and $\Theta(z = z_{x+1})$ at the upper and lower boundary, respectively.

Methods that consider the streambed homogeneous and semi-infinite only require the determination of C_1 using $\Theta(z_{x-1})$. This mathematical simplification is not used here. As such, also C_2 needs to be determined, which allows the streambed to be divided into several finite sub-domains. Thermal parameters and VEF now only need to be constant within each sub-domain. For each finite sub-domain it holds that

$$\begin{aligned}\Theta(z_x,\omega,\theta) = &\left(\frac{e^{(\lambda_1 z_{x+1})}e^{(\lambda_2 z_x)} - e^{(\lambda_2 z_{x+1})}e^{(\lambda_1 z_x)}}{e^{(\lambda_2 z_{x-1})}e^{(\lambda_1 z_{x+1})} - e^{(\lambda_2 z_{x+1})}e^{(\lambda_1 z_{x-1})}}\right)\Theta\left(z_{x-1},\omega,\theta\right) \\ &- \left(\frac{e^{(\lambda_1 z_{x-1})}e^{(\lambda_2 z_x)} - e^{(\lambda_2 z_{x-1})}e^{(\lambda_1 z_x)}}{e^{(\lambda_2 z_{x-1})}e^{(\lambda_1 z_{x+1})} - e^{(\lambda_2 z_{x+1})}e^{(\lambda_1 z_{x-1})}}\right)\Theta\left(z_{x+1},\omega,\theta\right)\end{aligned} \tag{4-3}$$

In analogy to Eq. (3-14) one can now write for depths $z_{x-1}; z_x$ and z_{x+1}

$$Y(\omega) = G_1(\theta,\omega)U_1(\omega) - G_2(\theta,\omega)U_2(\omega) \tag{4-4}$$

where $Y(\omega) = \Theta(z_x,\omega,\theta)$ is the output spectrum at the sensor showing the system response while $U_1(\omega) = \Theta(z_{x-1},\omega,\theta)$ and $U_2(\omega) = \Theta(z_{x+1},\omega,\theta)$ are the input spectra at the boundaries. $G_1(\theta,\omega)$ and $G_2(\theta,\omega)$ are the analytical expressions of the FRFs between the boundary temperatures and the temperature at location z_x.

The true parameter vector $\theta = [\alpha \quad \gamma\,]$ can be determined by comparing the predicted output $\Theta(z_x, \omega, \theta)$ from Eq. (4-3) to the real temperature measurements. Hence, in the absence of modeling errors and for periodic excitations (e.g. by using a pure sine function) it follows

$$0 = \Theta(z_x, \omega, \theta) - \Theta_{meas}(z_x, \omega) \tag{4-5}$$

However, temperature-time series collected in the field contain periodic $G(\omega)$ and transient parts $Tr(\omega)$ and are perturbed with noise $E(\omega)$ (chapters 3.4.1 and 3.4.2). This noise is assumed to be additive and to follow a Gaussian distribution function in the frequency domain, known as a circular complex normal distribution. This is equivalent to a Gaussian distribution in the time domain but can also result from other distribution functions in the time domain [*van Berkel et al.*, 2014b]. Similar to chapter 3.4.2 and Eq. (3-15), the LP method [*Pintelon et al.*, 2010b, a] is used to separate $Tr(\omega)$ and $E(\omega)$ from the measured input spectra $U(\omega)$ for all sensor locations. For that, the thermal transport between sensors is assumed to be linear and a noiseless reference temperature is assumed to exist. Between this reference sensor and any sensor at a certain depth z a non-parametric FRF can be estimated. In the case here, the input sensor at the streambed top is assumed to be noiseless. The output spectra at the different sensors are then

$$Z(\omega) = G_{LP}(\omega)U_{ST}(\omega) + Tr(\omega) + E(\omega) \tag{4-6}$$

where $U_{ST}(\omega)$ is the input at the streambed top and $Z(\omega)$ is the output spectrum obtained at the different sensors.

In a second step, the obtained FRFs and the noise information on these FRFs are used as input to a maximum likelihood estimator to estimate the parameter vector $\hat{\theta} = [\hat{\alpha} \quad \hat{\gamma}]$. This parameter vector is then determined by minimizing the log-likelihood cost function $V_{ML}(\theta, \omega_k)$ by means of non-linear least-squares optimization techniques as outlined in *van Berkel et al.* [2014a] via

$$\hat{\theta} = \min_{\theta} V_{ML}(\theta, \omega_k) \tag{4-7}$$

where

$$V_{ML}(\theta, \omega_k) = \frac{1}{F}\sum_{k=1}^{F} |e_{ML}(\theta, \omega_k)|^2 \tag{4-8}$$

where F is the number of frequency lines used (see Eq. (3-26) in the estimation. The estimation error $e_{ML}(\theta, \omega_k)$ is calculated as

$$e_{ML}(\theta,\omega_k) = \frac{\Theta(z_x,\omega_k,\theta) - \Theta_{meas}(z_x,\omega_k)}{\sigma_e(\theta,\omega_k)} = \frac{Y(\omega_k) - G_1(\theta)U_1(\omega_k) + G_2(\theta)U_2(\omega_k)}{\sigma_e(\theta,\omega_k)} \tag{4-9}$$

where $\sigma_e(\theta,\omega_k)$ is the variability (in this case the standard deviation) that considers the different noises. As such it is defined as [*van Berkel et al.*, 2014a]

$$\sigma_e(\theta,\omega_k) = \sqrt{\sigma_Y^2 + \sigma_{U_1}^2|G_1^2| + \sigma_{U_2}^2|G_2^2| - 2Re\left(G_1\sigma_{U_1U_2}^2\overline{G_2} + \sigma_{YU_1}^2\overline{G_1} - \sigma_{YU_2}^2\overline{G_2}\right)} \tag{4-10}$$

where $\overline{G_{1,2}}$ are the complex conjugates of $G_{1,2}$. The variances and co-variances in Eq. (4-10) are estimated for each ω_k. The analytical Jacobian matrix was used as shown in Eqs. (3-19) to (3-21) to minimize the cost function, and to determine the covariance matrix $COV(\hat{\theta})$ of the parameter vector $\hat{\theta} = [\hat{\alpha} \quad \hat{\gamma}]$. The MLE concept can then be used to quantify $\hat{q}_z$ and $\widehat{D_T}$ and their uncertainties according to Eqs. (3-22) to (3-25).

The estimated parameters $\hat{q}_z$ and $\widehat{D_T}$ are only valid results for the respective finite domain, for which temperature data has been used. Aspects regarding the optimal interval size are discussed by *van Berkel et al.* [2014a]. They point out that parameter estimates improve with the distance between the upper and lower boundaries, as the attenuation of the temperature signal is more pronounced (the signals still need to be significantly large to have a significant signal-to-noise ratio). On the other hand, as the domain size increases, the assumption of constant parameters can be increasingly violated.

Again, a cost function analysis can be performed to study model structure uncertainty by comparing the theoretical expected value V_E of the cost function can be compared to the actual value V_{ML} obtained from Eq. (4-8). The expected cost function value can be obtained analogous to Eq. (3-26) by

$$V_E = \left(F - \frac{n}{2}\right) \tag{4-11}$$

Van Berkel et al. [2014a] suggest that a model is acceptable if V_{ML} falls within a 95% confidence interval around V_E. When V_{ML} falls outside this range it might be useful to decrease the distance between upper and lower boundary. However, smaller domains increase the uncertainty of the parameter estimates and hence a compromise needs to be made.

4.3 Verifying the LPMLE3 Method Using Synthetic Temperature Data

The LP and MLE3 parts were tested independently by *Pintelon et al.* [2010a, b] and *van Berkel et al.* [2014a], respectively, and Monte-Carlo analyses showed that the uncertainties can be well predicted. To investigate the performance of the LPMLE3 method here, a synthetic temperature distribution was calculated with the numerical model STRIVE as described in chapter 3.5. This temperature distribution was based on predefined parameter settings for upwelling flux (q_z = -86.40 mm d^{-1}) and thermal diffusivity (D_T = 8.333 × 10^{-7} m^2 s^{-1}). Vertical streambed fluxes were quantified with the LPMLE3 method for seven successive finite streambed sub-domains (0.1-0.2 m, 0.2-0.3 m …0.7-0.8 m) by **(i)** only using a frequency of 1 d^{-1} as is common in studies using amplitude/phase lag methods and **(ii)** by using a frequency range from 1/520 d^{-1} to 1.5 d^{-1}.

For case **(i)** flux estimates obtained with the LPMLE3 method deviated between 0.03% and 1.32% from the predefined flux value (Figure 4.2, Table A4.1), while estimated diffusivities differed between 0.06% and 1.98% (Table A4.1). Although deviations are small, they increase with depth and both parameters are slightly overestimated. This is probably a result from the attenuation of the daily signal with depth. Although here the daily signal is by far the most pronounced one in the upper streambed, lower frequencies seem to increase their influence on the flux estimate with increasing depth.

For case **(ii)** this effect could not be observed. Flux estimates deviated between 0.00% and 0.10% while estimated D_T deviated between 0.00% and 0.05% (Table A4.2). For both parameters a relation to depth was not found. Standard deviations on the parameter estimates increased with depth but for case (ii) they were 2-3 orders of magnitude smaller compared to case (i). The small differences of q_z and D_T for case (ii) as compared to the predefined values based on the simulations with STRIVE can be a result from truncation of the temperature data (after the third digit) during extraction from the STRIVE model. Additionally, numerical errors produced by STRIVE when approximating the partial differential equation for heat transport on a grid could have an influence. For case (i) the use of only the diel signal introduces small additional errors.

When performing a cost function analysis the expected value of the cost function is 779 (i.e. 520 days multiplied with the highest frequency used, which is 1.5 d^{-1} in this case. The result is subtracted by 1, i.e. the number of free parameters divided by two (see Eq. (4-11)). The actual model cost (CostBest) values are between 22% and 438% higher than the expected cost value. For a field data set one could assume that these differences are due to the influence of non-vertical flow components that would make the assumption of 1D vertical flow increasingly less valid. However, for the synthetic data set the temperature-time series output created with STRIVE is noiseless and the actual model cost is dominated by numerical errors and not the noise contained in the temperature signal. By increasing the noise, actual and expected cost values would differ less.

Figure 4.2 also shows the comparison to flux estimates obtained with the semi-infinite amplitude method of *Hatch et al.* [2006] as implemented in VFLUX [*Gordon et al.*, 2012]. From the deviations it can be seen that using the amplitude method for depth dependent flux calculations can lead to noticeable errors. In our case VFLUX-fluxes deviated between 1.15% and 11.27% (Table A4.3) from the original flux value.

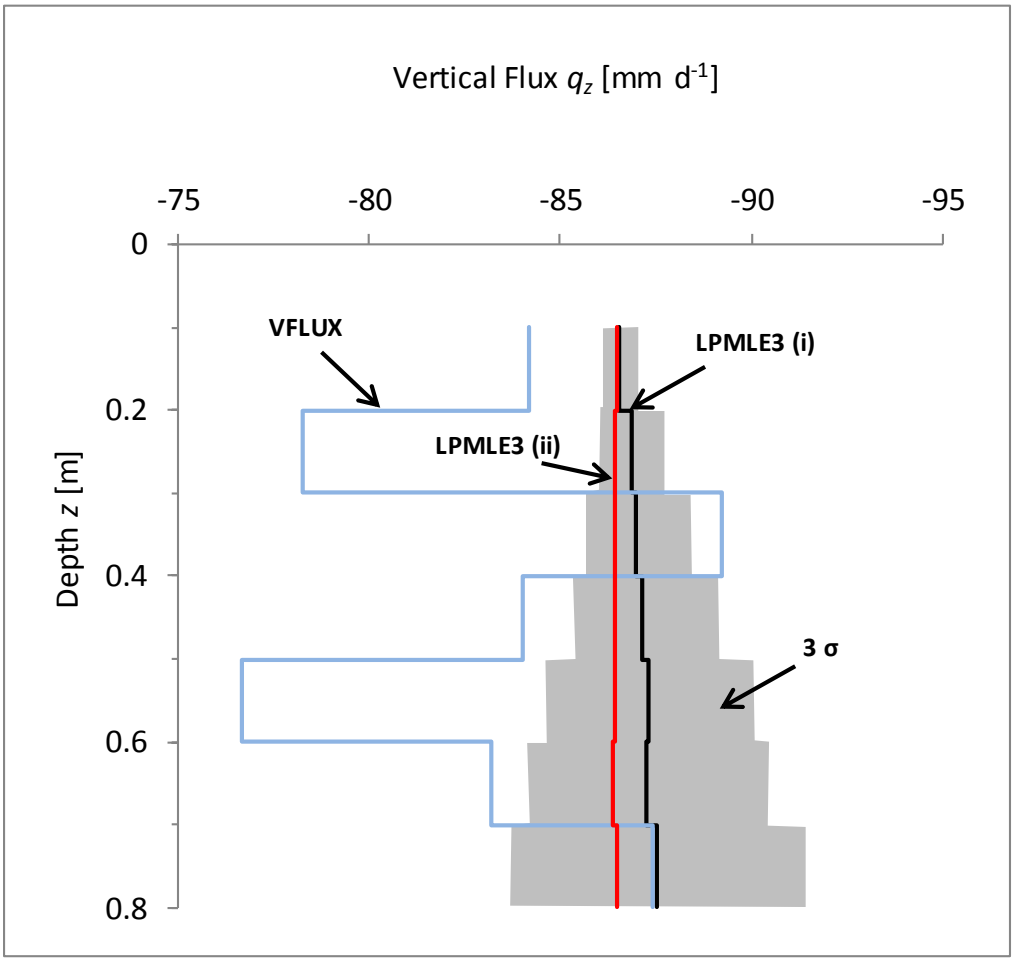

Figure 4.2: Flux estimates obtained with the LPMLE3 method and VFLUX using the amplitude method after *Hatch et al.* [2006]. VFLUX and LPMLE3 **(i)** results were calculated using only a frequency of 1 d^{-1}. LPMLE3 **(ii)** results were obtained using a frequency range. Source: *own.*

From these results it can be concluded that the LPMLE3 method can quantify vertical streambed fluxes and thermal diffusivities with reasonable accuracy if thermal dispersivity is neglected (Eq. 1-24). However, it has to be stressed here that unlike numerical models the LPMLE3 method does not follow the principle of conservation of mass between consecutive sub-domains. As such, the flux estimates represented here should not be considered to cross the boundary of one sub-domain and enter the next one. Here, fluxes rather express vertical flow components within a certain finite sub-domain. Hence, rather than referring to vertical exchange flux indicating an exchange between streambed layers or between streambed and stream, the term vertical streambed flux has been used. Only where the sub-domain in

question has the streambed top as upper boundary, the vertical flux can be considered an exchange flux. In the next step the LPMLE3 method is applied on a field data set.

4.4 Using the LPMLE3 Method with Temperature Data from the Slootbeek

4.4.1 Field Work

Field work was conducted at the same stream section of the Slootbeek that was introduced in chapter 3.6.1. At location ML10 (Figure 4.3) an MLTS (Figure 3.5) was installed in the vicinity of two piezometer nests (Piezo 1 and 2) to acquire a temperature time series at the respective depths over a period of 25 days (23 Oct – 17 Nov 2012) with a resolution of 5 min.

Next to the temperature stick a bag-type seepage meter (chapter 1.5) was installed. It followed a design discussed in *Rosenberry and LaBough* [2008] and comprised a vented half-barrel metal cylinder covering a surface area of 616 cm^2. First seepage measurements commenced three weeks after device installation to allow for sufficient sediment and flow equilibration. Seepage was collected in a plastic bag with a volume of 4 L. The bag was tested for leaks and then pre-filled with 100 mL of water before installation to minimize measurement errors from its initial expansion as discussed by *Shaw and Prepas* [1989] and *Cable et al.* [1997]. After testing various time intervals it was found that a minimum time interval of 20 min was needed for stable seepage measurements, i.e. to minimize the impact of possible errors introduced during retrieval of the bag and determination of the bag volume in a graduated cylinder. Data collection took place over 4 days (14 Nov – 17 Nov 2012).

Figure 4.3: Streambed temperatures were measured at location ML10. Next to the temperature stick a seepage meter similar to the one shown here was installed into the streambed. Source: *own*.

4.4.2 Average Vertical Flux Estimates

The temperature data shown in Figure 4.4 were collected at location ML10 and used for the estimation of vertical streambed fluxes. Over the 25-day observation period, temperatures

ranged from 6.1°C to 15.4°C with an average of 11.1°C and a standard deviation of 1.0°C. The sensor at the streambed top showed the highest temperature fluctuations due to the influence of the diel cycle while the temperature signal was increasingly attenuated with increasing depth. Because of the season, sensors closer to the streambed top showed mostly lower temperatures than deeper sensors; the vertical temperature gradients were in general relatively small. The sensor at 0.55 m depth showed temperatures that were closest to the average regional groundwater temperature of 12.2°C.

For flux calculations the thermal diffusivity was fixed to 5.863×10^{-7} m^2 s^{-1}, a value representative for the streambed of the Slootbeek. This was done as independent field measurements of thermal parameters for validation were not available. Vertical fluxes were estimated for five streambed sub-domains (SD1 to SD5, Figure 4.5 and Table 4.1) using sensor triplets. For each triplet the first and third sensors represent the upper, respectively lower boundary of the sub-domain while the second sensor is used for parameter estimation.

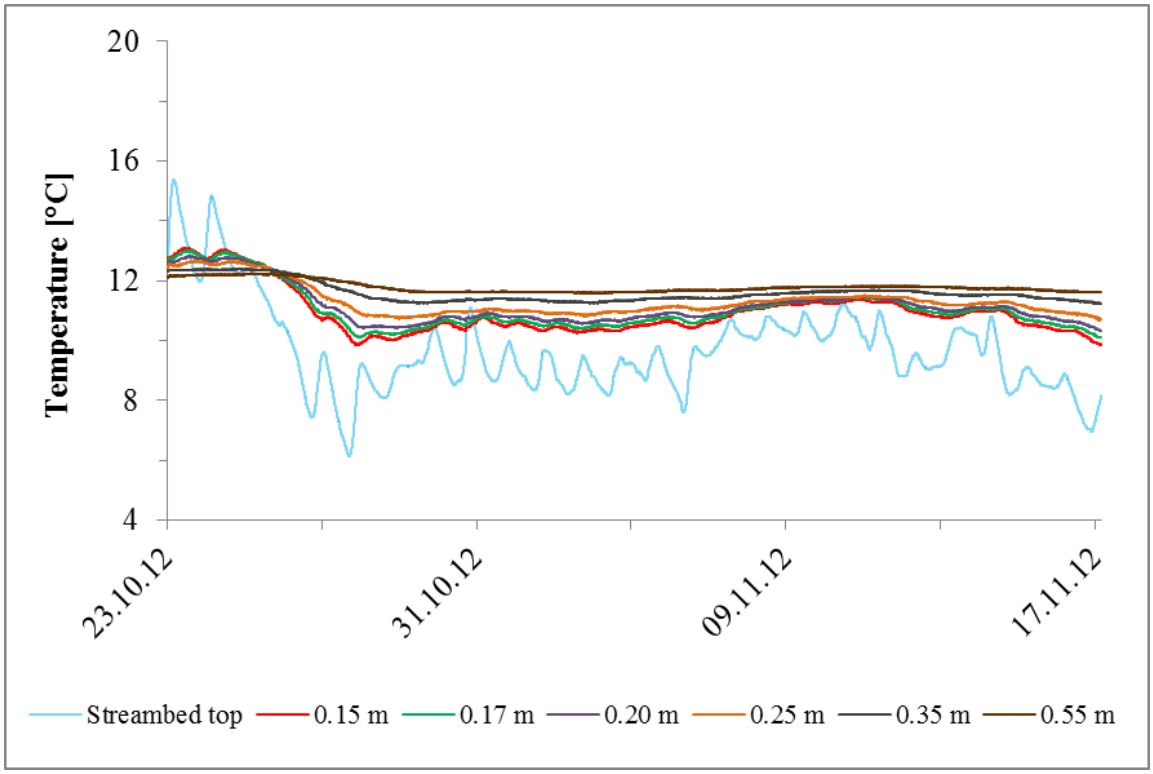

Figure 4.4: Temperature data collected at location ML10 at the streambed top and six depths. Source: *own.*

When only sensor triplets with consecutive numbering are considered (i.e. sensors 2, 3, 4 or 3, 4, 5 etc.), estimated fluxes varied between -105.4 mm d^{-1} for SD2 and -299.7 mm d^{-1} for SD3 (Figure 4.5) with percent standard deviations ranging from 3% for SD1 to almost 51% for SD2. Although the standard deviations are relatively high, a decreasing trend of fluxes with depth in the streambed can be identified.

Additionally, fluxes were estimated for ten streambed sub-domains using sensor triplets with non-consecutive numbering (e.g. 2, 3, 5 etc., see Table 4.1) considering finite domains of variable size. For sub-domains with flux estimates based on more than one possible sensor combination (e.g. SD12), estimates within that sub-domain can vary as the respective temperature signals also differ. In those cases, it seems appropriate to use average flux estimates for further analysis. For the ten additional sub-domains estimated fluxes varied between -158.0 mm d^{-1} for SD12 (sensors 3, 4, 8) and -308.0 mm d^{-1} for SD7 (sensors 2, 4, 6). Sub-domains that include sensor two, i.e. the sensor at the streambed-stream interface show much lower standard deviations than other sub-domains. This is a result of the attenuation of the temperature signal with depth that makes flux estimates in general more uncertain. Notice that any sensor combination is possible for LPMLE3, including overlapping sub-domains.

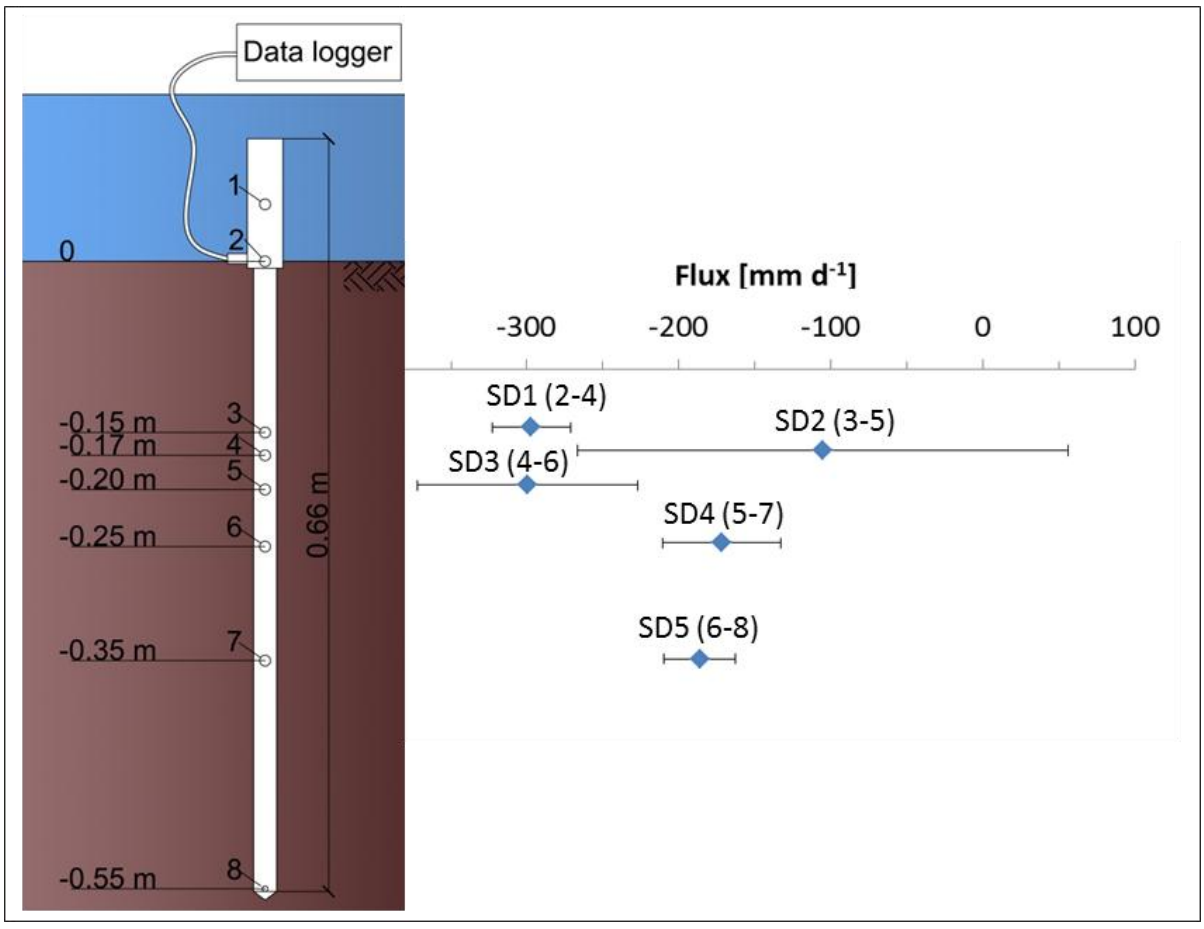

Figure 4.5: Flux estimates from temperature data collected with an MLTS between 23 Oct – 17 Nov 2012 indicate a decreasing trend with depth in the streambed. Data from sensor one were excluded from the analysis. Sensor two was located at the streambed top. Vertical streambed fluxes were estimated for five streambed sub-domains using triplets of consecutive sensors. Flux estimates vary with depth and sub-domain size and show a variable degree of parameter uncertainty (uncertainty bounds as 3 × σ). Source: *own.*

The LPMLE3 results show a considerable variation in vertical flux for the different streambed sub-domains, which can be significant when including uncertainties (Figure 4.5) on the

estimates (shown as three times the standard deviation). Variations in flux estimates are hypothesized to be a result of the following factors:

(i) Depth-dependent non-vertical flow components exist: The influence of non-vertical flow components [*Lautz*, 2010; *Roshan et al.*, 2012] and non-ideal flow fields [*Cuthbert and Mackay*, 2013] has been found to be able to considerably influence flux estimates as discussed in chapter 3.3. A violation of the assumption of purely vertical flows could also be deduced from the cost function analysis. Actual model cost values vary between 32 and 2065 (average is 670), while the expected value is 36.

(ii) Heterogeneity and anisotropy exist in streambed sediments as already discussed in chapter 3.3. Heterogeneity in streambed sediments produces flux errors especially for low flow conditions [*Schornberg et al.*, 2010] and with anisotropy [*Irvine et al.*, 2015a].

(iii) Thermal parameters may not be constant with depth. During modeling, thermal parameters were set constant assuming a sandy loam as deduced from Table 1.1 ($\rho_w c_w$ = 4.18 × 10^6 $Jm^{-3}K^{-1}$, ρc = 3.07 × 10^6 $Jm^{-3}K^{-1}$, κ = 1.8 $Wm^{-1}K^{-1}$). However, changes in the composition of streambed sediments or in porosity can lead to variations in the volumetric heat capacity of the water-sediment matrix and/or the effective thermal conductivity and diffusivity producing erroneous flux estimates. It is therefore advisable to determine thermal parameters from field or lab experiments to independently validate model estimates.

(iv) Temperature measurements contain errors due to instrument drift, instrument resolution and accuracy as discussed in chapter 3.3. Here, the impact of measurement errors was reduced by calibrating the multilevel temperature stick in a water bath of known temperature. Also, initial accuracy was equal for all sensors and drift should not have played a major role for the relatively short observation interval of 25 days.

(v) The modeling procedure produces erroneous flux estimates. As already discussed before, temperature measurements contain noise that is assumed to follow a Gaussian distribution. However, a non-Gaussian noise distribution could also occur, in which case this assumption is violated.

4.4.3 Comparison with Seepage Meter Measurements

SD9 represents the entire length of the temperature stick between the streambed top and the deepest sensor at 0.55 m. The time-averaged flux estimate amounts to -263.9 mm d^{-1} with a sample standard deviation of 13.09 mm d^{-1}. In comparison, flux estimates obtained with the LPML method as described by *Vandersteen et al.* [2015] that assumes the entire subsurface to be a homogeneous semi-infinite halfspace amount to -314.9 mm d^{-1} with an uncertainty on the estimate of 3.42 mm d^{-1} or 1.08%.

Fluxes from seepage meter measurements (11 in total) ranged from -341.4 mm d^{-1} to -405.0 mm d^{-1} with an average flux of -378.5 mm d^{-1} and a sample standard deviation of 19.30 mm d^{-}

[1] or 5.10%. Hence, all three approaches produce flux estimates in the same order of magnitude.

Table 4.1: Estimates of vertical fluxes for different streambed sub-domains using sensor-triplets with consecutive and non-consecutive sensors (see also Figure 4.5). Source: *own.*

Sub-domain	Sensors	Size [m]	q_z [mm d^{-1}]	σ_{qz} [mm d^{-1}]	σ_{qz} [%]	Average q_z [mm d^{-1}]	CostBest
SD1	2,3,4	0.17	-297.1	8.61	2.90	-297.1	268
SD2	3,4,5	0.05	-105.4	53.72	50.97	-105.4	32
SD3	4,5,6	0.08	-299.7	24.14	8.05	-299.7	116
SD4	5,6,7	0.15	-171.7	12.92	7.52	-171.7	90
SD5	6,7,8	0.30	-186.4	7.80	4.19	-186.4	70
SD6	2,3,5	0.20	-257.7	3.91	1.52	-278.8	1118
	2,4,5		-299.8	6.49	2.17		538
SD7	2,3,6	0.25	-250.7	2.79	1.11	-284.3	2065
	2,4,6		-308.0	3.63	1.18		1746
	2,5,6		-294.3	4.10	1.39		1487
SD8	2,3,7	0.35	-254.9	2.91	1.14	-271.9	1928
	2,4,7		-269.8	3.09	1.14		1938
	2,5,7		-265.1	3.20	1.21		1913
	2,6,7		-297.8	4.12	1.39		1290
SD9	2,3,8	0.55	-252.1	3.29	1.30	-263.9	1472
	2,4,8		-256.8	3.41	1.33		1461
	2,5,8		-255.6	3.76	1.47		1296
	2,6,8		-283.0	4.53	1.60		973
	2,7,8		-271.8	4.50	1.66		815
SD10	3,4,6	0.10	-190.7	25.06	13.14	-222.3	84
	3,5,6		-253.9	13.38	5.27		251
SD11	3,4,7	0.20	-170.2	14.22	8.36	-188.8	115
	3,5,7		-192.5	7.44	3.87		358
	3,6,7		-203.8	7.87	3.86		262
SD12	3,4,8	0.40	-158.0	10.32	6.53	-185.8	124
	3,5,8		-182.2	7.18	3.94		259
	3,6,8		-196.9	7.38	3.75		192
	3,7,8		-206.1	6.16	2.99		221
SD13	4,5,7	0.18	-217.0	13.78	6.35	-212.4	176
	4,6,7		-207.8	9.78	4.71		178
SD14	4,5,8	0.38	-188.0	12.01	6.39	-196.4	156
	4,6,8		-199.3	8.91	4.47		138
	4,7,8		-202.0	6.98	3.46		152
SD15	5,6,8	0.35	-187.8	9.77	5.20	-191.7	86
	5,7,8		-195.6	6.93	3.54		98

Size = size of streambed sub-domain
q_z = estimated vertical exchange flux
σ_{qz} = standard deviation of q_z
CostBest = actual value of cost function analysis; the expected value is 36

4.4.4 Temporal Variability of Vertical Streambed Fluxes

Similar to chapter 3.6.8, time-series were created to study the temporal variability of streambed fluxes by applying a moving window and the Short Time Fourier Transform. Here, a 10-day rectangular moving window was applied on sub-domains SD1 to SD5 (Figure 4.6) using frequencies of up to 1.5 d^{-1} and assuming a constant thermal diffusivity of 5.863×10^{-7} $m^2 s^{-1}$. The window was always moved by one day. For sub-domain SD1 (0 to 0.17 m depth) fluxes varied between -496.6 mm d^{-1} and -233.4 mm d^{-1} (Figure 4.6) with percent standard deviations ranging from 2.6 % to 4.7 %. Flux estimates for SD2 to SD5 are more variable and parameter uncertainties are higher (Figure 4.6 and Table 4.2).

For SD2, conditions change from gaining at the beginning to losing towards the end of the time series. In general, flux estimates for all sub-domains do not follow the same trend and considering that the confidence intervals (3σ = 99.7 %) only partly overlap, flux estimates can at least partly be considered significantly different. This would hint towards a complex flow pattern. The assumption of purely vertical flow might thus be violated. As already indicated in Fig.4.5, uncertainties for SD2 are very high (σ ranges from 11.7 to 125.9 % of the flux value) and fluxes are highly variable. This might indicate that the sub-domain size might be too small (it is only 5 cm). Hence, the boundary conditions and any measurement and parameterization errors may considerably influence the estimates.

Table 4.2: Summary of estimates of time-variant VEFs and their uncertainties for different streambed sub-domains as shown in Figure 4.6. Source: *own*.

Name	Range q_z [mm d^{-1}]	Range σ_{qz} [mm d^{-1}]	Range σ_{qz} [%]
SD1	-496.6 to -233.4	8.5 - 19.6	2.6 - 4.7
SD2	-554.4 to 540.2	49.6 - 126.4	11.7 - 125.9
SD3	-385.5 to -180.4	22.5 - 70.5	6.0 - 39.1
SD4	-492.0 to -104.0	11.0 - 31.6	3.7 - 19.2
SD5	-323.5 to -67.2	9.8 - 53.1	3.9 - 49.9

q_z = estimated vertical flux
σ_{qz} = standard deviation of q_z
[%] = percent of q_z value

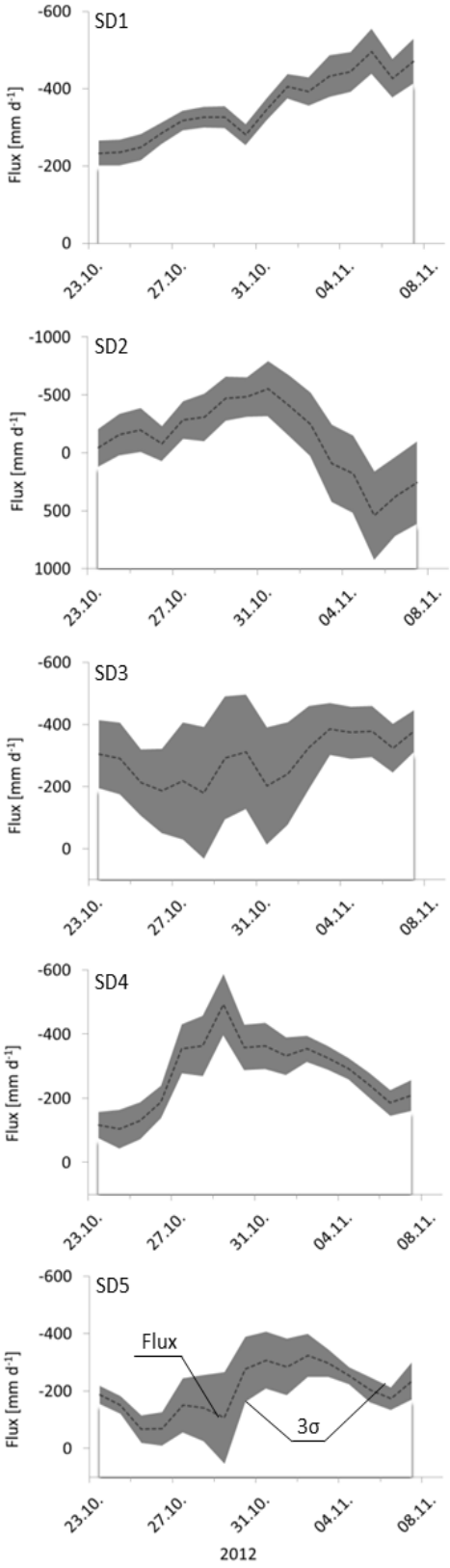

Figure 4.6: Temporal variability of vertical fluxes and their uncertainties (3σ) for streambed sub-domains SD1 to SD5. Source: *own.*

4.5 Conclusions

The LPMLE3 method was developed, tested and applied for the quantification of VEFs. Aside from the advantages of the LPML method the LPMLE3 method also allows for the consideration of streambed sediment heterogeneity by dividing the streambed into finite layers or sub-domains. For each of these finite sub-domains fluxes and thermal parameters are constant. Each finite sub-domain uses two temperature sensors as boundary conditions, while parameters (flux, thermal diffusivity) are estimated using information from a third sensor within the domain. Unlike previous methods that assume the subsurface to be homogeneous and semi-infinite, the LPMLE3 approach is thus not constrained by this assumption.

For location ML10 of the Slootbeek average flux estimates obtained for subdomains of different extent varied between -105.4 mm d^{-1} for and -308.0 mm d^{-1} and were in the same order of magnitude as seepage meter measurements obtained at the same location. When calculated as time series, fluxes varied considerably but showed mostly upwelling conditions.

The presented results show that the LPMLE3 method can serve as a tool to estimate vertical streambed fluxes for sub-domains of a multi-level sensor device. As such it is possible to obtain first information regarding the spatial distribution of fluxes in the vertical direction. Highly variable flux estimates of consecutive or partly overlapping sub-domains could indicate that the assumption of purely vertical flow is invalid or that small-scale heterogeneities in the streambed sediments exist. For further analysis it might then be necessary to employ more complex 2D/3D numerical models that allow for a discretization of the streambed.

Similar to other 1D methods, the LPMLE3 method is bound to the assumption of vertical flow only. As discussed in chapters 3.3 and 3.7 it has been shown that this assumption is sometimes violated, especially in a heterogeneous streambed. Also, flux estimates might be influenced by the proximity of a boundary sensor as seemed to be the case for sub-domain SD7. Further research is needed to investigate the exact influence of the upper/lower boundary condition and determine adequate domain sizes.

5 Variability of Hydraulic Conductivity in Streambeds

Some of the results discussed in this chapter are only present in digital form and can be found in an additional .xlsx file. Due to the sheer amount of data it was not possible to include everything in the appendix.

5.1 Introduction

As already discussed in chapter 1.2.4, streambed hydraulic conductivity *K* is one of the most important parameters defining flow and transport processes in the hyporheic zone. Information on *K* can aid in the characterization of groundwater-surface water interactions through e.g. the quantification of water and solute exchange fluxes [*Landon et al.*, 2001; *Ryan and Boufadel*, 2006; *Kalbus et al.*, 2009] or the delineation of interstitial flow [*Findlay*, 1995; *Conant*, 2004]. Via exchange fluxes, streambed *K* can be linked to the attenuation and transformation of contaminants as has been shown by *Kennedy et al.* [2009a, b] for nitrate. Streambed *K* has also been found to influence the composition and distribution of interstitial fauna [*Boulton et al.*, 1998; *Hancock et al.*, 2005; *Claret and Boulton*, 2009; *Boulton et al.*, 2010] and can be associated with long-term changes in riparian vegetation [*Webb and Leake*, 2006]. Additionally, quantifying *K* in the HZ can be of relevance to solving civil and geotechnical engineering problems such as in the assessment of structural stability.

Table 5.1 lists common ranges of horizontal and vertical streambed *K* found in literature, and their assessment methods (see also chapter 1.5). Values of streambed *K* can vary over several orders of magnitude for different stream environments and values obtained in most studies fall within the range given and discussed by *Calver* [2001]. Most of these studies focused either on method comparison, verification and improvement or on studying specific stream environments. As such, the majority of studies tends to oversimplify heterogeneity in geology, morphology and hydraulic parameters of the streambed or the alluvial aquifer connected to a stream [*Buss et al.*, 2009; *Engdahl et al.*, 2010]. However, as discussed in chapter 1, a certain degree of heterogeneity is common to most natural environments. As such geological heterogeneity can strongly influence the spatial and temporal variability of streambed *K*. Heterogeneity can also cause considerable parameter and model structure uncertainty.

Only few studies specifically consider this aspect on the reach or sub-reach scale (several 10 m). *Genereux et al.* [2008] conducted a study in two sections of West Bear Creek, NC, USA

on the spatial and temporal variability in streambed *K* carrying out 487 falling head tests in piezometers installed in the streambed.

Table 5.1: Streambed *K* ranges found in literature and their assessment methods. Source: *own.*

Author	*K*-Range [m d^{-1}]	Study site	Assessment method
Calver [2001]	8.64×10^{-5} - 8.64×10^{2}	Meta study based on previous field and modeling experiments	
Chen et al. [2013]	K_v: 8×10^{-5} - 61.4	Platte River, USA and tributaries	Permeameter tests in lab
	K_v: 3×10^{-4} - 110.8		In-situ falling head permeameter
Cheng et al. [2011]	K_v: 2.9 - 41.9	Platte River, USA	In-situ falling head permeameter
Conant [2004]	K_h: 5×10^{-3} - 17.5	Pine River, Canada	Slug tests
Dong et al. [2012]	K_v: 0.4 - 48.0	Clear Creek, USA	In-situ falling head permeameter
Genereux et al. [2008]	K_v: 1×10^{-2} - 66.2	West Bear Creek, USA	In-situ falling head permeameter
Landon et al. [2001]	K_v: 1.0 - 280.0	Platte River, USA and tributaries	In-situ permeameter[a]
	K_h: 7.0 - 30.0		Slug tests[a]
	K_g: 1.0 - 240.0		Grain size analysis[a]
	K_v: 1.0 - 175.0		Seepage meter/VHG[a,b]
Leek et al. [2009]	K_h: 0.3 - 1200.0	Touchet River, USA	Slug tests[a]
Lu et al. [2012a]	K_g: 0.6 - 1140.0	Platte River, USA	Grain size analysis
	K_h: 1.9 - 564.0		In-situ permeameter, L-shaped
Lu et al. [2012b]	K_h: 4.0 - 564.5	Platte River, USA	In-situ permeameter, L-shaped
	K_v: 0.9 - 188.7		In-situ falling head permeameter
Pliakas and Petalas [2011]	K_g: 15.0 - 754.3	Nestor River, Greece	Grain size analysis
	K_v: 57.6 - 410.2		Permeameter tests in lab
Ryan and Boufadel [2006]	K_v: 0.1 - 28.5	Indian Creek, USA	In-situ falling head permeameter
Song et al. [2009]	K_g: 19.9 - 285.3	Elkhorn River, USA	Grain size analysis
	K_v: 2.7 - 104.9		In-situ falling head permeameter
Wang et al. [2014]	K_v: 0.7 - 29.7	Manasi River, China (disconnected river)	In-situ falling head permeameter

[a] Values were obtained from graphs and thus can be slightly inaccurate
[b] VHG = vertical hydraulic gradient

K varied spatially over four orders of magnitude (10^{-2} to 10^{2} md^{-1}) throughout the investigated parts of the creek with higher variability in the stream center. This was attributed to differences in grain size distribution. Temporal variability in *K* over a whole year using bi-monthly measurements at certain locations was also pronounced. The study also demonstrated that streambed obstacles (beaver dam) showed decreased K values upstream compared to downstream. Sebok et al. [2015] studied spatial and temporal variabilities of streambed K for two sections (straight and meandering) of the Holtum stream in Denmark in Winter and Summer. They combined slug test measurements (all at 0.5 m depth below streambed) with in situ permeameter tests, grain size analysis and VHG measurements to relate vertical and horizontal streambed *K* to channel morphology and sediment properties. Their results showed high spatial variability in streambed *K* and temporally varying *K* values that could be attributed to the dynamic sedimentation/scouring occurring in the stream. Both studies only partly focused on the three-dimensional variability of streambed *K* over their study areas.

5.2 Objectives

As shown above only few studies have investigated the small-scale spatial distribution of streambed *K*. However, a delineation of its spatial distribution might be important in studies of contaminant transport and attenuation in the HZ as hydraulic parameters influence the formation of hotspots of chemical reactions and microbiological activity (see chapter 1.3.4) thus influencing the spatial distribution of the contaminant mass flux entering a stream. The objective of this chapter is to study streambed *K* on sub-reach and sediment scales for a small section of the River Tern, a lowland river in Western UK and to see whether its spatial distribution can be delineated by combining different methods of determining *K* on a dense grid. Results are statistically analyzed. This analysis also provides some basic information regarding parameter uncertainty.

5.3 Study Site

The study focuses on a small section of the River Tern, a major lowland river in Western England (Figure 5.1A). River Tern is a tributary to the River Severn and part of the Shropshire Groundwater Scheme (SGS) that has been studied by the UK Environment Agency regarding the availability of potable water for the region [*Streetly and Shepley*, 2005]. The study reach (2°53'W, 52°86'N) is situated about 1 km north-west of Stoke-on-Tern where the river cuts through agricultural lands and shows no significant meandering. It is adjacent to a reach where research has been carried out by the University of Birmingham

(Figure 5.1B). Their investigations have focused on the description of the local hyporheic community [*Krause et al.*, 2011], on the determination of groundwater-surface water exchange fluxes by streambed temperature measurements [*Angermann et al.*, 2012a; *Krause et al.*, 2012; *Krause and Blume*, 2013], on streambed nitrogen cycling [*Krause et al.*, 2013] as well as on the attenuation potential of chlorinated solvents [*Weatherill et al.*, 2014]. Other reaches of the River Tern were used to study heat transport through the streambed [*Keery and Binley*, 2007; *Keery et al.*, 2007] and the retardation potential of the streambed sediments [*Smith and Lerner*, 2007, 2008].

Regional topographic elevation of the SGS varies between 35 m and 410 m above ordnance datum (mAOD) with most of the River Tern valley at an elevation around 60 m. At the studied section, streambed elevation was assessed over ten months in 2008 and 2009 [*Riess*, 2010] and varied between 57.73 m and 58.31 mAOD over the entire site and measurement time. Stream channel width was about 4 m and channel morphology nearby was defined by occasional in-stream vegetation, pool-riffle-pool sequences and high stream bank inclinations [*Krause et al.*, 2013]. The local aquifer comprises Permo-Triassic sandstone of the Bridgnorth and Kidderminster formations of about 150 m thickness. It is overlain by Quaternary drift deposits of alluvial nature mainly comprising gravels, sands and silts. Local clay and peat lenses can also be encountered. The thickness of the drift deposits can be up to 5 m but it shows high spatial variation, as does sediment type [*Streetly and Shepley*, 2005]. Average stream stage varied from May 20008 to May 2009 between 58.52 and 59.06 m AOD based on in-stream piezometer measurements conducted by *Riess* [2010].

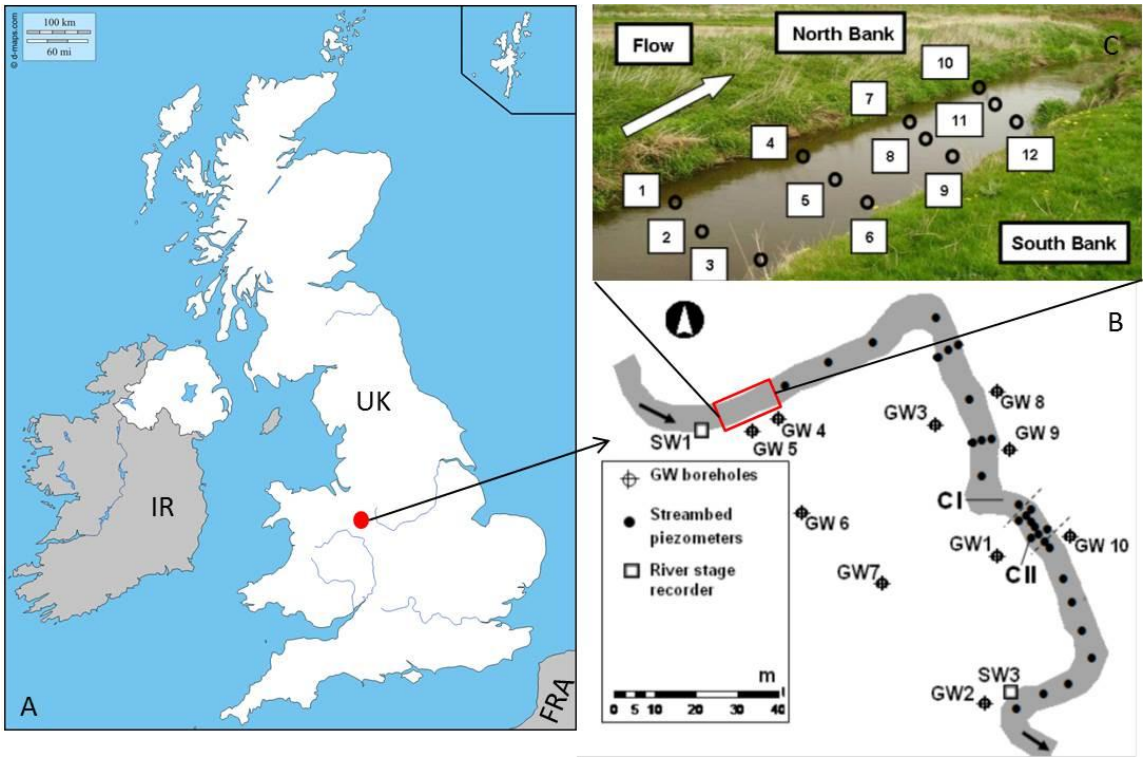

Figure 5.1: River Tern study site (red rectangle) in the UK. The area downstream was intensively researched by the University of Birmingham (see text). Source: modified from *Krause et al.* [2012] and *Riess* [2010]. UK map (A) downloaded from http://d-maps.com/carte.php?num_car=2562&lang=en [10 August 2015].

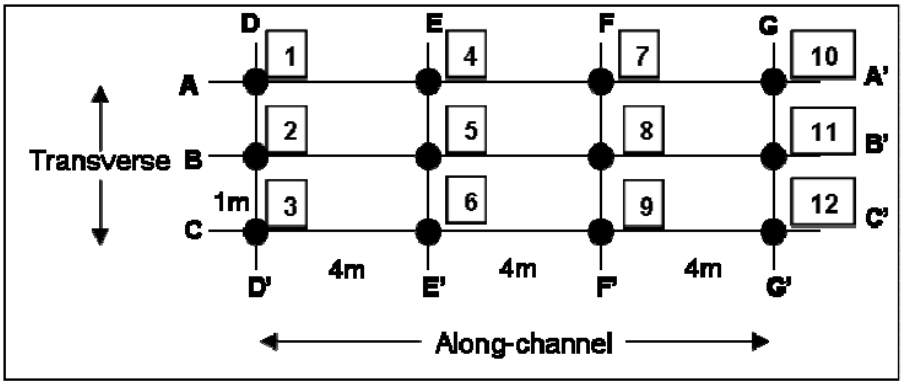

Figure 5.2: Transects along and across the stream section. Source: *Riess* [2010].

5.4 Methodology

5.4.1 Grain Size Analysis

One soil core was taken from the streambed at each of the twelve locations indicated in Figure 5.1C by means of percussion coring as described in *Riess* [2010]. The distance between sampling locations along the stream was approximately 4 m, while across the stream it was about 1 m. Core lengths varied between 0.5 and 0.89 m. After extraction, cores were immediately visually inspected to log the lithology and then cut into 138 sections of 4-10 cm length for further processing in the lab. After oven-drying, sections were dry-sieved by *Riess* [2010] using mesh sizes of 5, 3.35, 2, 1.18, 0.6, 0.43, 0.3, 0.21, 0.15, 0.063 mm.

To obtain non-directional streambed hydraulic conductivity values K_g [LT^{-1}], first the percentage of the total mass retained by each sieve was used to produce cumulative grain size curves and samples were classified according to EN ISO 14688-1 [2013]. K_g values were then estimated for each core section using information from the cumulative grain size curves as well as the empirical models after *Beyer* [1964], *Hazen* [1893], the USBR model [*Vukovic and Soro*, 1992] and the semi-empirical model after Kozeny-Köhler [*Kozeny*, 1953] as presented in *Kasenow* [2001]. The formulas and relevant parameters for each model are listed in Table 5.2. Their applicability and limitations are discussed in detail in *Vienken and Dietrich* [2011] and *Lu et al.* [2012a]. Other models also found in the scientific literature were not utilized as their application range and data requirements did not match the available data.

A general formula for calculating K_g can be found in *Bear and Cheng* [2010] as

$$K_g = \frac{g}{\vartheta} C f(n) d_x^2 \tag{5-1}$$

where g is the gravitational constant [LT^{-2}], ϑ is the kinematic viscosity [L^2T], d_x [L] is the grain diameter of the relevant fraction used in the model, while C and $f(n)$ are the dimensionless shape factor and porosity function, respectively.

Table 5.2: Formulas used to estimate hydraulic conductivity K_g from grain size data. Source: *own.*

Name	Formula	K_g in	Relevant parameters	Application criteria
Hazen	$K_g = C_H d_{10}^2 (0.7 + 0.03T)$ $C_H = 400 + 40(n - 26);\ n$ in [%]	md^{-1}	d_{10} in mm	$U < 5$ $0.1 < d_{10} < 3\ mm$
Beyer	$K_g = C_B d_{10}^2$ $C_B = 0.0045 \log \frac{500}{U}$	ms^{-1}	d_{10} in mm	$U < 20$ $0.06 < d_{10} < 0.6\ mm$
USBR	$K_g = 0.0036\, d_{20}^{2.3}$	ms^{-1}	d_{20} in mm	$U < 5$
Kozeny-Köhler	$K_g = 5400 \frac{n^3}{(1-n)^2} d_{10}^2$	md^{-1}	d_{10} in mm	

T = Temperature in [°C], K_g = hydraulic conductivity from grain size analysis, C = shape factor, n = porosity, U = coefficient of uniformity, $d_{10,20}$ = grain diameters where 10% resp. 20% of the sample mass falls below

For the models used here the porosity n was estimated where necessary according to *Vukovic and Soro* [1992] using

$$n = 0.255(1 + 0.83^U) \tag{5-2}$$

where $U = \frac{d_{60}}{d_{10}}$ is the coefficient of uniformity, while d_{60} and d_{10} are obtained from the cumulative grain-size distribution curves representing the grain diameters where 60%, respectively 10% of the sample mass falls below. Two major methodological limitations occur:

(i) Grain size analyses only allow for the estimation of non-directional (isotropic) hydraulic conductivities as during dry-sieving, the original sediment characteristics (packing, void ratio, colmation effects) are destroyed, and

(ii) all models were used under the assumption of a constant temperature of 10°C in the streambed because of lack of additional information. This value was derived from in situ porewater sampling of deep multi-level sampling points (Dr. Steve Thornton, U. Sheffield, pers comm.). Small errors might be introduced in the estimates where streambed temperature variations occur, e.g. when diel cycles influence the hydraulic conductivity via the kinematic viscosity. An increase in temperature by 2°C would lead to a change in kinematic viscosity by about 6%. These errors increase with decreasing stream stage as more direct solar radiation reaches the streambed. The kinematic viscosity can also vary with depth as a temperature

signal is attenuated when it propagates through the streambed. However, to the best knowledge of the author, studies on spatial and temporal variations in streambed kinematic viscosity have not yet been published.

5.4.2 Slug Tests

At each of the locations indicated in Figure 5.1C, a piezometer nest was installed into the streambed by *Riess* [2010] comprising three HDPE tubes of 3.5 m length (inner diameter 11 mm). Each HDPE tube had a screened section covered by a 100 µm nylon mesh, acting as a sediment filter. Screened sections were installed at each location at 0.35-0.40 m, 0.65-0.70 m and 0.95-1.00 m depth within the streambed, to represent "shallow", "middle" and "deep" piezometers, respectively. At locations 2, 5, 8 and 11 an additional tube was installed for groundwater sampling with a screened filter section at 1.95-2.00 m below the streambed top. Prior to conducting slug tests, the piezometers were left undisturbed to equilibrate for a period of almost two months. Falling head slug tests were conducted with three replicates in each piezometer by *Riess* [2010] to determine the radial hydraulic conductivity K_r [LT^{-1}] of the streambed around the screened sections. K_r can be considered the omnidirectional horizontal hydraulic conductivity K_h. For the analysis here, the semi-analytical solution after *Springer and Gelhar* [1991] was used as shown in *Butler et al.* [2003] and implemented in the software AQTESOLV Pro 4.0 where

$$K_r = \frac{t_d}{t}\frac{r_c^2 ln\left(\frac{R_e}{r_w}\right)}{2bC_D} \tag{5-3}$$

Here, t_d is the dimensionless time parameter calculated as

$$t_d = t\sqrt{gL_e} \tag{5-4}$$

with t as the actual time, g as the gravitational constant and $L_e = \left(\frac{t}{t_d}\right)^2 g$ [L] as the effective water column length in the piezometer or well. In Eq. (5-3), r_c [L] is the effective radius of the well casing (corrected for the radius of the transducer cable if a data logger is used) while $r_{we} = r_w a$ [L] is the effective piezometer radius that depends on the measured piezometer radius r_w [L] and the dimensionless anisotropy factor $a = \frac{K_v}{K_h}$ where K_v [LT^{-1}] is the vertical hydraulic conductivity component. The anisotropy ratio becomes important when the model is used for a piezometer or partially penetrating well (i.e. not the entire streambed thickness is screened). As the true anisotropy at the field site was unknown, K_h was estimated using two anisotropy factors for comparison, with $a = 1$ and 0.1. A value of $a = 0.1$ (i.e. K_v is ten times smaller than K_h) is often assumed when no other information on K_v is available. R_e in Eq. (5-3) is the effective radius parameter after *Bower and Rice* [1976], b [L] represents the

screen length and C_D is a dimensionless parameter describing the damping behavior of the type curve. If needed, it can include frictional well loss according to *Butler* [2002]. The Springer-Gelhar model can be used for unconfined aquifer conditions and assumes homogeneity over the filter length. Here, the model was used with two different saturated streambed thicknesses of B = 2.5 m and 25 m to study the influence of that parameter on K_h.

5.4.3 Statistical Analyses

Results of K_h and K_g as well as their logarithmic values obtained over the entire study area were first depicted graphically in histograms to obtain probability density functions and cumulative distribution functions. Afterwards, descriptive parameters were determined for each distribution, which included mean, median, standard deviation, standard error on the mean $\left(\frac{y}{\sqrt{F}}\right)$, kurtosis, skewness, range, maxima and minima, coefficient of variations and the inter-quartile range using MS Excel. Normality tests were conducted to clarify whether each distribution is significantly different from a normal or log-normal distribution. For this, a two-sided Student *t*-test (at the threshold of 0.05) was performed on each distribution to check whether the skewness and kurtosis (as defined in Excel) were both significantly different from zero, i.e. the values for the normal distribution. Then, Pearson correlation coefficients were calculated between K_g values derived from the models as well as logarithmic K_g values.

Additional to the entire study area, several descriptive parameters were calculated for K_h and K_g as well as for their logarithmic values for each of the transects (seven in total) and measurement locations (12 in total) shown in Figure 5.2. To calculate Pearson correlation coefficients between K_g and K_h or their logarithmic values for the entire study area respectively for the different transects, original K_g values were resampled to be representative for core sections of 5 cm length (i.e. the filter length in the slug tests) using weighting factors. All correlation coefficients were calculated using the software SGeMS [*Remy et al.*, 2009]. Mathematical descriptions of the different coefficients and parameters used can be obtained from e.g. *Caers* [2011] or *Chiles and Delfiner* [2012].

5.5 Results and Discussion

5.5.1 Sediment Cores

From the original 138 core subsections, 134 could be used further analysis. Based on the mesh sizes of the sieves, the soil could be classified into fine sand (FSa), medium sand (MSa), coarse sand (CSa), particles that represent at least fine gravel (FGr), and fines (< 0.063 mm). In general, the streambed sediment at the investigated stream section can be considered moderately diverse. From the 134 samples, 16 had as main grain fraction (i.e. grain size with the highest percentage in sieving) fine sand; eight were fine gravel or gravel with larger grain diameters, three were mainly coarse sand, and 103 were composed mainly of medium sand. In

four samples the main grain fraction was either gravel or coarse/medium sand but could not be determined unambiguously as it was not clear from sieving which weight percentage resulted from fine gravel and which from larger gravel grains. Only two samples contained just one grain fraction (medium sand). 51 samples contained one minor grain fraction with 5% mass or more, 29 samples contained two minor fractions, 45 samples contained three minor ones and seven samples contained four minor grain fractions. Table A5.1 (see additional .xlsx file) shows the classification of all samples, the sample length, the sample depths below the streambed top as measured in May 2008 at the locations of the middle piezometers in the piezometer nests and the elevations above ordnance datum. At nine of the twelve locations, at least one core sub-section with gravel as the major grain size fraction could be found although they are not evenly distributed in depth. Fines were found to a considerable amount at locations 3, 5, 9 and 11 with the highest amount of fines encountered in sub-section 1.9.10 (15% mass).

For each sample a cumulative grain size curve was created in MS Excel (using Bezier curves, other methods are described e.g. in *Botula et al.* [2013]) from the sieve analysis results (Figure 5.3 as an example, the rest can be found in the additional .xlsx file) showing the cumulative weight [%] per grain diameter, assuming spherical grains. From these grain size curves, diameters d_{10}, d_{20}, d_{60} were determined, which were then used to calculate K_g values according to Table 5.2. Table A5.2 (in the additional .xlsx file) provides the uniformity coefficients, porosities and respective grain diameters of each sample. Arithmetic means, medians, minima, maxima and standard deviations for the entire site can be found in Table 5.3. Porosity values are in range for values of sands and gravels commonly found in the literature [e.g. *Fetter*, 2001]. Results for uniformity values show that not for all samples K_g values could be calculated later with the Hazen and USBR models as sometimes *U* values were outside the acceptable ranges (Table 5.2). The same descriptive statistical parameters were calculated for each location (in the additional .xlsx file), which provided no further valuable insight. Looking at the parameter values for each transect it can be seen that for F-F' and G-G' grain size ranges are slightly wider than for the other transects.

Quality of the grain size data is different for each core. For locations with a higher percentage of fines, additional laboratory tests to determine fractions and K_g values might have provided some additional insight about heterogeneity. Likewise, the largest mesh opening of 5 mm retained between 0% and about 45% of the grains (location 1.2.10), indicating that for some samples coarser fractions than fine gravel (2 mm - 6.3 mm grain size) likely existed, which would have somewhat influenced the classification as well as subsequent calculations of K_g.

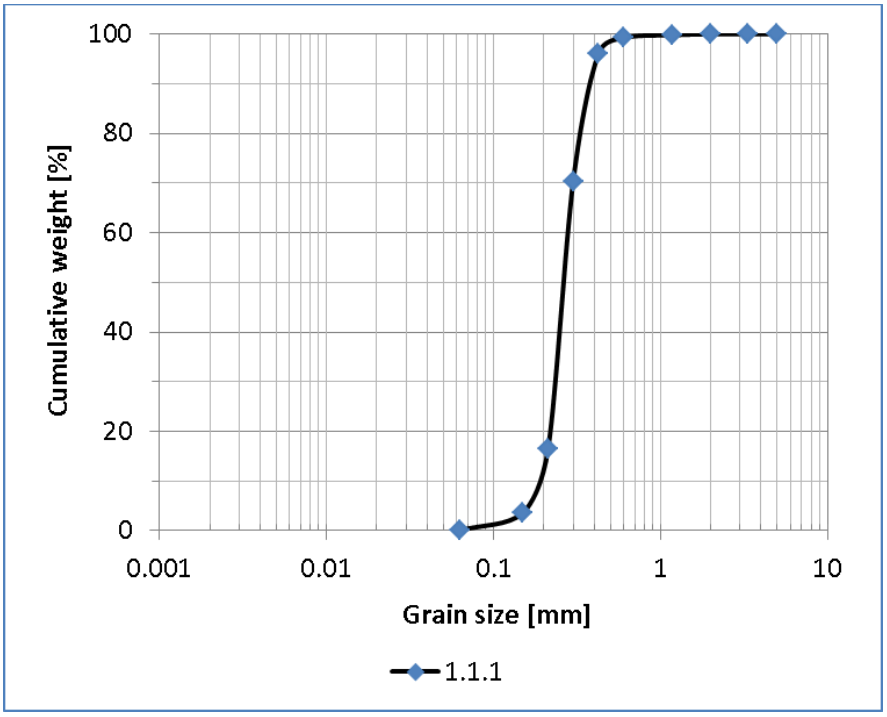

Figure 5.3: Cumulative grain size curve for sample 1.1.1 (location 1). Curves for the remaining samples can be found in an additional .xlsx file. Source: *own.*

Table 5.3: Summary statistics over the entire stream section showing various grain diameters, the porosity *n* and the uniformity coefficient *U*. Summary statistics per location and per transect can be found in an additional .xlsx file. Source: *own.*

	d_{10} [mm]	d_{20} [mm]	d_{60} [mm]	U [-]	n [-]
Samples	133	134	133	132	132
m	0.17	0.22	0.60	3.76	0.40
Median	0.17	0.22	0.37	2.38	0.42
a_{max}	0.32	0.50	4.00	19.35	0.45
a_{min}	0.06	0.08	0.18	1.33	0.26
y	0.07	0.09	0.71	3.52	0.05

m = mean, *y* = standard deviation, *a* = value,
n = porosity, *U* = coefficient of uniformity,
$d_{10,20,60}$ = grain size diameters

5.5.2 Hydraulic Conductivity from Grain Size Analyses

For each core sub-section, K_g values were calculated using the models shown in Table 5.2. Results for each sample can be found in Table A5.3 in the additional .xlsx file. Table 5.4 provides a summary showing the respective descriptive parameters per model. While the models after Beyer and Kozeny-Köhler use a sample size of 132, the Hazen and USBR models use a smaller sample size as not for all core subsections the conditions listed in Table

5.2 were fulfilled. K_g values over all models vary between 1.1 md^{-1} and 154.7 md^{-1} (see also Figure 5.4). The USBR model shows the smallest range of K_g values. Also, K_g values are one order of magnitude lower than with the other models. The difference between mean and median is highest for the Kozeny-Köhler model indicating a larger spread of the values than in the other models. The coefficient of variation indicating the variability of the data with respect to the mean is highest for the Kozeny-Köhler model with almost 100% (i.e. the standard deviation is almost as large as the mean).

From the histograms (Figure 5.5) it can immediately be seen that K_g values calculated after Beyer, Kozeny-Köhler and with the USBR model show a distribution that is strongly positively skewed (i.e. the tail goes to the right), while the skewness for the Hazen model is less. It could be assumed that at least the former three models follow a log-normal distribution, for which this type of skewness is typical, while the Hazen model shows a bimodal distribution. Figure 5.6 shows for each model the distributions of the $ln(K_g)$ values and all of them follow much more the shape of a normal curve. However, results of the two-sided Student *t*-tests showed that neither of the models showed a normal distribution (as expected) and that only the K_g values after Hazen and the USBR model follow a log-normal distribution. For those two models back-transformed K_g values show slightly elevated means, medians, standard deviations and coefficients of variations as compared to the original distributions.

Table 5.4: Summary statistics over the entire stream section showing K_g obtained with different empirical/semi-empirical models. Values of $ln(K_g)$ are back-transformed to the original units where appropriate. Source: *own.*

	Unit	**K_g(B)**	**K_g(H)**	**K_g(K)**	**K_g(USBR)**	**lnK_g(H)**	**lnK_g(USBR)**
Samples	[-]	132	83	132	107	83	107
m	[md^{-1}]	29.0	44.4	38.5	10.3	45.6	10.9
SEM	[md^{-1}]	2.1	3.0	3.3	0.8		
Median	[md^{-1}]	24.0	40.6	26.0	9.1	36.3	7.4
y	[md^{-1}]	24.0	27.2	38.3	8.1	34.5	11.7
Kurtosis	[-]	0.4	0.2	1.0	4.3		
Skewness	[-]	1.0	0.9	1.3	1.6		
r_a	[md^{-1}]	95.7	109.2	153.2	48.5		
a_{min}	[md^{-1}]	3.2	6.6	1.5	1.1		
a_{max}	[md^{-1}]	98.9	115.8	154.7	49.6		
CV	[%]	82.8	61.3	99.5	78.8	75.8	107.3
IQR	[md^{-1}]	36.2	33.7	52.2	9.8		

m = mean, SEM = standard error of the mean, y = sample standard deviation,
r_a = range, IQR = interquartile range, CV = coefficient of variation, B = Beyer,
H = Hazen, K = Kozeny-Köhler

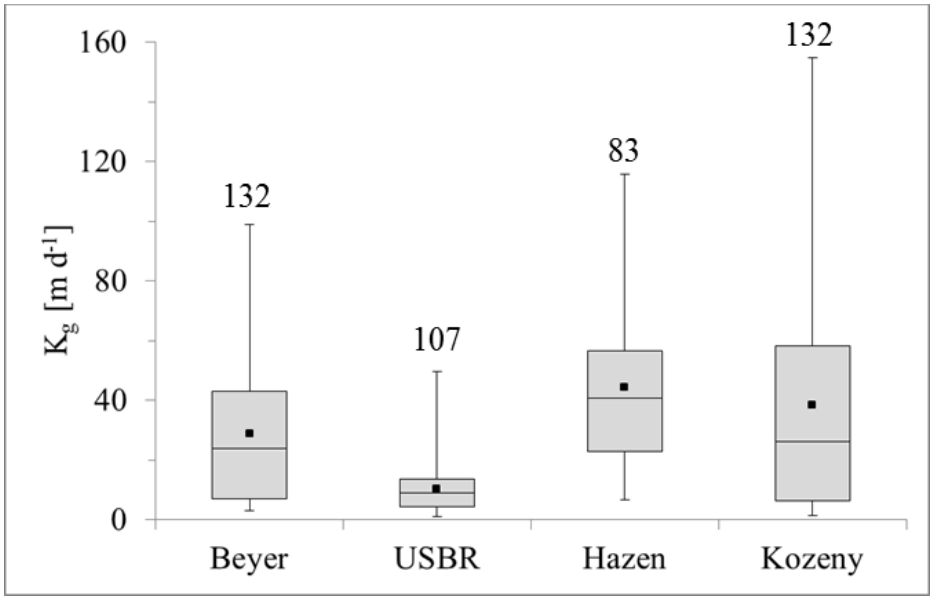

Figure 5.4: K_g values obtained with different empirical/semi-empirical models. Boxplots show maxima, minima, means (black dots), medians, as well as values for quartiles one and three forming the interquartile range. Numbers on top of the boxplots indicate the number of samples each boxplot is based on. Source: *own.*

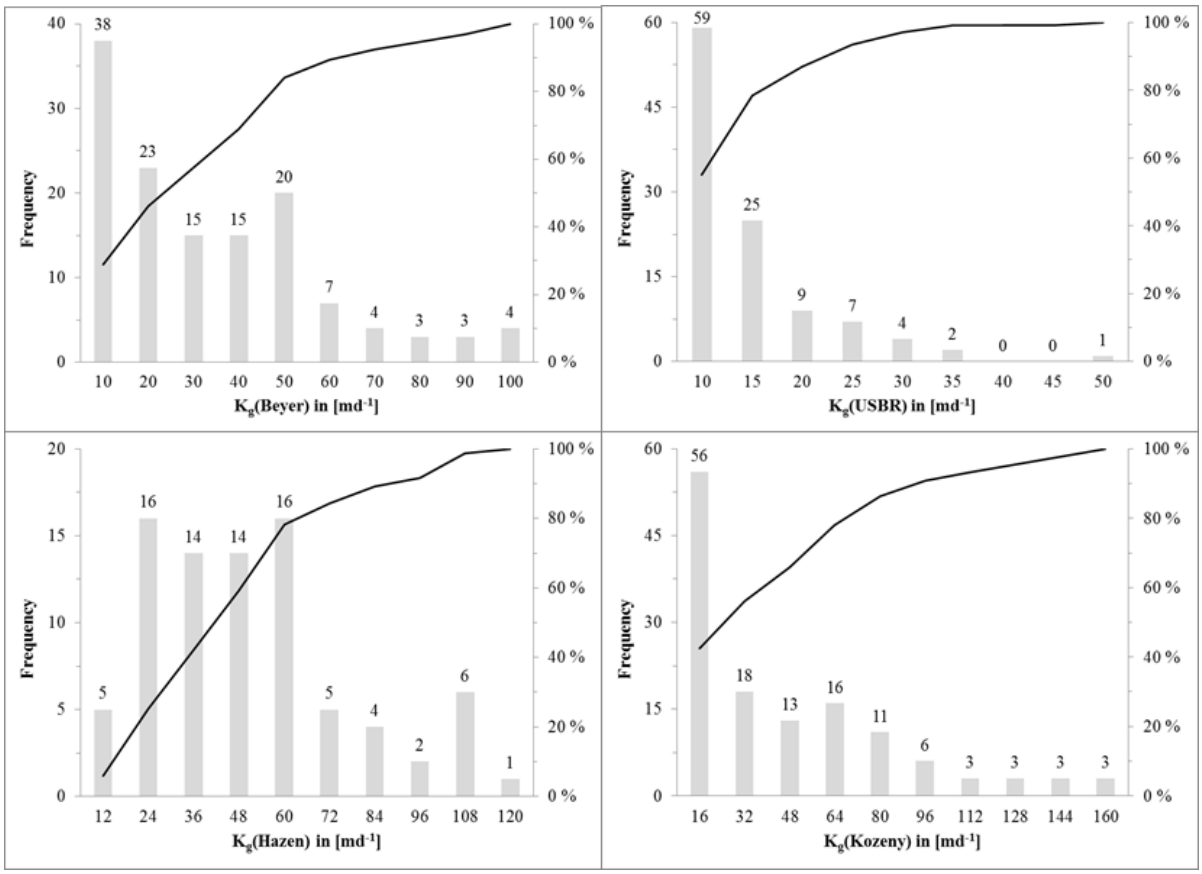

Figure 5.5: Histograms showing probability distribution and cumulative distribution for K_g values. Source: *own.*

To study the correlation between K_g or $ln(K_g)$ values obtained with the different models, scatter plots were created (Figure 5.7 and Figures A5.1 to A5.11) and Pearson linear correlation coefficients were calculated (Table 5.5).

Table 5.5: Pearson linear correlation coefficients for K_g and $ln(K_g)$ values. Source: *own.*

	Hazen	**USBR**	**Kozeny**	**Beyer**
Hazen	1.00			
USBR	0.83	1.00		
Kozeny	0.97	0.88	1.00	
Beyer	0.97	0.94	0.94	1.00
ln -values	**Hazen**	**USBR**	**Kozeny**	**Beyer**
Hazen	1.00			
USBR	0.61	1.00		
Kozeny	0.61	0.87	1.00	
Beyer	0.68	0.95	0.94	1.00

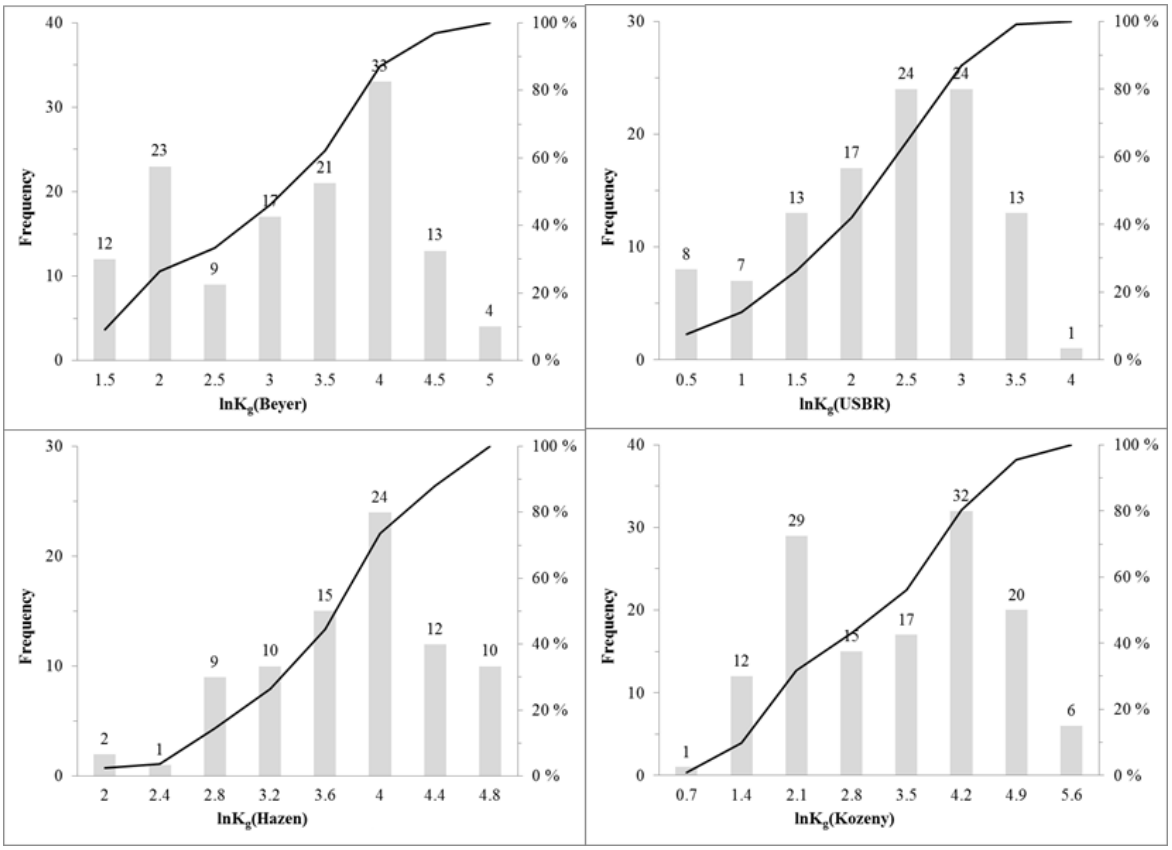

Figure 5.6: Histograms showing probability and cumulative distributions for $ln(K_g)$ values. Source: *own.*

Linear correlations between the different models are mostly high with coefficients ranging from 0.83 to 0.97 for K_g values. For $ln(K_g)$ values correlations are equally high except when the Hazen model is used. Here coefficients vary only between 0.6 and 0.7. A reason for this

could be the different calculation methods. In general, a high correlation between the different models is expected as calculation methods are not fundamentally different and all are based on a certain grain diameter obtained from the same cores

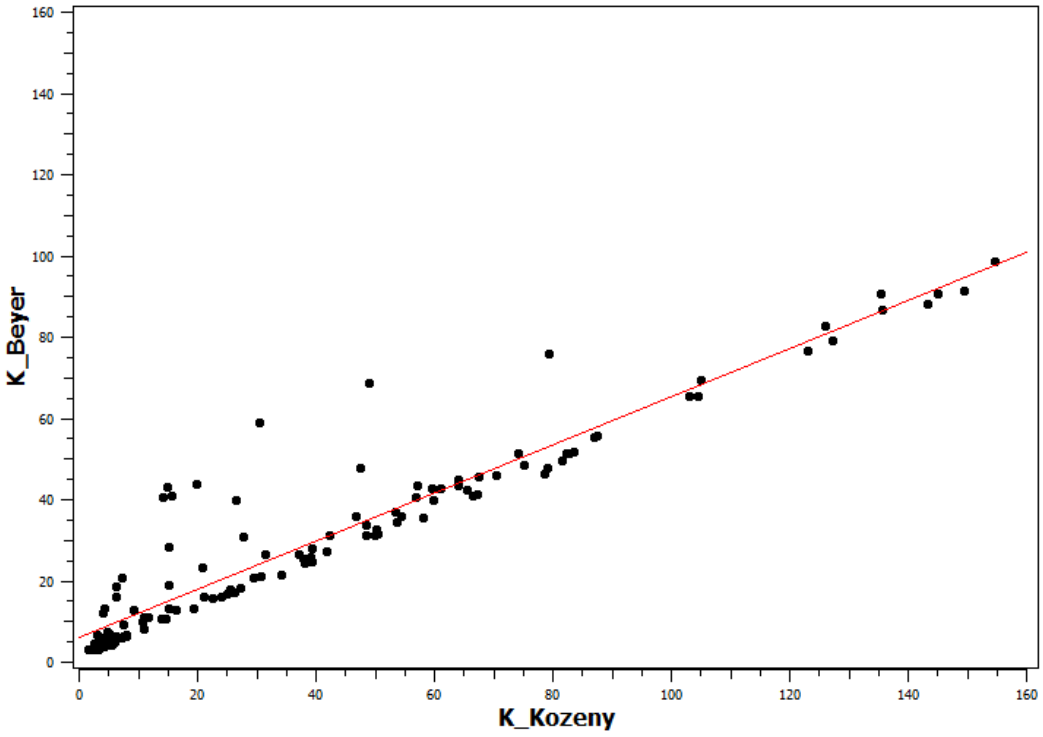

Figure 5.7: Scatter plot correlating K_g values [md^{-1}] obtained after Beyer with those obtained after Kozeny-Köhler. The red line indicates the linear regression line. Black dots represent those core sub-sections where for both models a K_g value was obtained. Source: *own.*

By looking at K_g values from the transects and the individual locations (Figure 5.2) it can be seen that average values are all in the same order of magnitude and that the highest average per model and the lowest average per model are not further apart than by a factor of four (Tables A5.4 and A5.5). This indicates that at least on average there is no high variability in K_g over the samples. However, this does not stipulate the absence of small-scale variations or certain structures in the sediments.

In general, the obtained K_g range (1.1 md^{-1} to 154.7 md^{-1}) is smaller than ranges found in other studies [*Landon et al.*, 2001; *Song et al.*, 2007; *Lu et al.*, 2012a] that used similar models. This would indicate less variability or heterogeneity of the streambed sediment at the investigated section.

5.5.3 Hydraulic Conductivity from Slug Tests

Results of a total of 108 slug tests obtained at the 36 locations were analyzed with the Springer-Gelhar model to calculate K_h values. Exemplarily, the curve fitting result is shown for location 10, shallow piezometer, test 2 (Figure 5.8). A table with all curve fitting

parameters and results can be found in the additional .xlsx file. From the 108 calculated K_h values, 104 could be used for further analysis. In four cases, results from the first slug test had to be omitted as they produced K_h values that were much lower than those of the subsequent two tests. Own field experience showed that this can happen if the filter section is clogged or coated with fine material, which usually disappears when the piezometer is developed (i.e. short pumping or water injection before a series of tests). If the development was not 100% complete, the first slug tests in a test series produce smaller K_h values that are not representative for the formation.

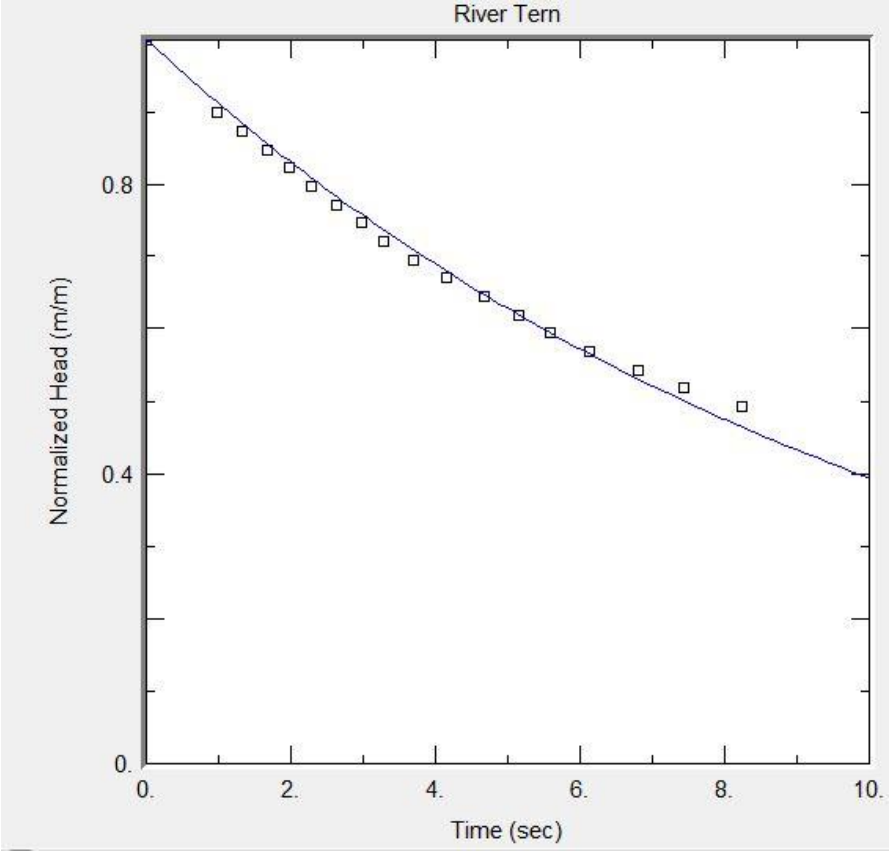

Figure 5.8: Type curve fitting result for location 10, test 2 in the shallow piezometer. Shown is the normalized piezometric head versus time. Analyses were performed using AQTESOLV Pro 4.0. Source: *own.*

For each series of tests an average K_h value was calculated (36 in total). Figure 5.9 shows the distribution of these average values as well as the same descriptive parameters shown in Table 5.4 assuming an anisotropy ratio of one (no anisotropy) and a streambed thickness of 2.5 m. Although the histogram is positively skewed, a two-sided Student *t*-test confirmed no significant deviation of K_h from a normal distribution at a level of 0.05.

	Unit	K_h
Samples	[-]	36
m	[md^{-1}]	6.0
SEM	[md^{-1}]	0.5
Median	[md^{-1}]	5.1
y	[md^{-1}]	3.2
Kurtosis	[-]	-0.7
Skewness	[-]	0.9
r_a	[md^{-1}]	11.4
a_{min}	[md^{-1}]	1.1
a_{max}	[md^{-1}]	12.5
CV	[%]	53.5
IQR	[md^{-1}]	4.5

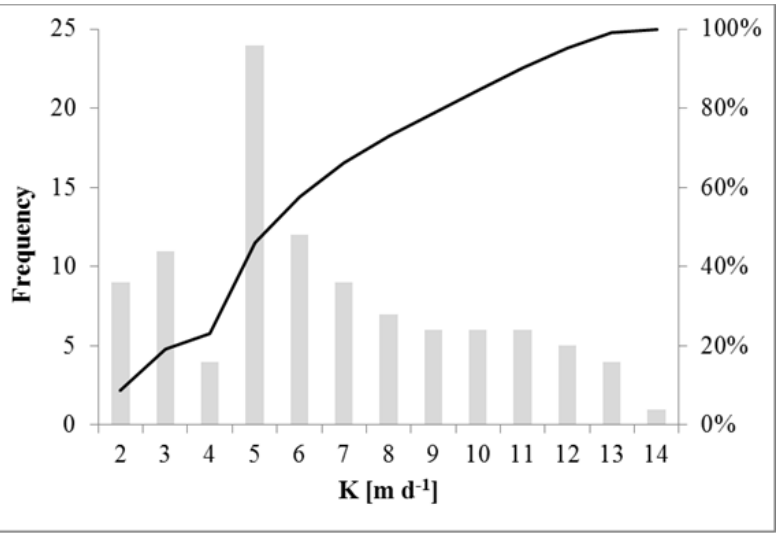

Figure 5.9: Histogram and summary statistics of K_h values from slug tests assuming $a = 1$. Source: *own.*

An anisotropy ratio of less than one, i.e. $K_h > K_v$, leads to a general increase in estimated K_h values as the well/piezometer radius used in the model has to be adapted [*Bower and Rice*, 1976; *Zlotnik*, 1994]. For $a = 0.1$, estimated K_h values increased between 62% and 70% (average increase was 66%). With rising filter depth the increase becomes slightly smaller as the depth to screen bottom and screen distance to water table increase reducing the anisotropy effect. On the other hand, a change in streambed thickness has a much smaller influence on K_h. An increase of the saturated streambed thickness B from 2.5 m to 25 m here led to a decrease in K_h ranging from 2.2% to 10.0% (average decrease of 5.6%). The decrease was higher for deeper locations as the increase in depth to screen bottom and screen distance to water table become more influential for K_h calculation. By analyzing K_h values at the three depths (Table 5.6) a steady increase in K_h seems present. This is probably due to the reduced effect of colmation leading to a decrease in fine material with depth as has also been shown in the analysis of the sediment cores. However, by taking a closer look at the individual locations, an overall increase of K_h with depth could only be observed for locations 3, 4, 8, 9 and 10. At locations 1, 2 and 5, K_h values were highest for the middle piezometers, while at locations 6, 7, 11 and 12, K_h values were lowest for the middle piezometers. At location 12, the K_h value was highest at the shallow piezometer closest to the streambed top. These results indicate some heterogeneity in the streambed sediment structure leading to variability in K_h. Aside from colmation this variability can also be caused by variable amounts of hyporheic and/or groundwater-surface water exchange flow in the streambed. For further insight, a quantitative analysis regarding the predominant exchange flow would have to be performed, which is, however, outside the scope of this thesis.

In general, K_h values estimated here, were not as variable as compared to values and ranges found in other studies [*Landon et al.*, 2001; *Leek et al.*, 2009]. However, a comparison of the absolute values is difficult as the other studies do not provide information regarding the considered degree of anisotropy.

Table 5.6: K_h ranges and average values for the three different filter depths depending on the anisotropy ratio *a*, and the saturated streambed thickness *B*. Source: *own.*

Depth [m]	a	B [m]	K_h [m d^{-1}]	K_{hav} [m d^{-1}]
0.35-0.40	0.1	2.5	1.9 - 12.5	7.0
	1	2.5	1.1 - 7.4	4.1
	1	25	1.1 - 7.2	4.0
0.65-0.70	0.1	2.5	2.3 - 18.2	10.4
	1	2.5	1.4 - 11.1	6.3
	1	25	1.3 - 10.4	6.0
0.95-1.00	0.1	2.5	6.6 - 20.6	12.6
	1	2.5	4.0 - 12.5	7.7
	1	25	3.7 - 11.5	7.0

K_h values measured at a depth of 1.95-2.00 m at all locations on transect BB' (Figure 5.2) ranged from 25.3 md^{-1} to 27.9 md^{-1} assuming $a = 0.1$, while at this transect, K_h values ranged from 7.2 md^{-1} to 15.1 md^{-1} for the depth of 0.95-1.00 m. This indicates that with increasing depth the variability in K_h seems to decrease as colmation and HEF no longer play a major role.

5.5.4 Bivariate Relationship and Spatial Data Analysis

To allow for a comparison between K_g and K_h, via linear correlation, $K_g$values were resampled to 5 cm to obtain the same sample size as the K_h values (screen length is 5 cm). As initially most core sections were longer than 5 cm, the number of K_g samples used in correlation analysis increased. A correlation was performed for the entire site as well as for each transect. Considering the entire site (Table 5.7), no linear correlation between K_g and K_h, respectively their logarithmic values was found. Looking at the individual transects (additional .xlsx file) also no clear trend could be observed. For some transects a positive correlation was encountered while for others the correlation was negative. This was mostly due to the fact that only five to seven data points (i.e. depths with K_g and K_h values present) were available for correlation per transect, which seemed to be an insufficient amount. Additionally, correlation might also have been influenced by the fact that K_g values were deduced from disturbed samples while K_h values were determined in situ. Results shown here, support the general notion in the scientific community that correlating K_g to K_h values proves difficult if not impossible due to methodological differences.

Table 5.7: Pearson correlation coefficients between *K* values of the different assessment methods based on resampled data. Source: *own.*

	K_Beyer	*K_USBR*	*K_Hazen*	*K_Kozeny*	*lnK_B*	*lnK_U*	*lnK_H*	*lnK_K*	*K_fh2*	*lnK_h*
K_Beyer	1.00									
K_USBR	0.96	1.00								
K_Hazen	1.00	0.94	1.00							
K_Kozeny	0.95	0.92	0.99	1.00						
lnK_B	0.92	0.88	0.93	0.85	1.00					
lnK_U	0.90	0.90	0.93	0.87	0.97	1.00				
lnK_H	0.93	0.85	0.93	0.92	1.00	0.94	1.00			
lnK_K	0.87	0.84	0.91	0.89	0.94	0.94	0.99	1.00		
K_h	0.00	-0.08	-0.20	0.10	0.08	-0.01	-0.18	0.20	1.00	
lnK_h	0.10	0.01	-0.21	0.20	0.18	0.08	-0.20	0.29	0.95	1.00

5.6 Conclusions

Analysis of the site-specific streambed hydraulic conductivity on a small scale (sub-reach and sediment core scale) showed a mild variability in comparison to values found in other studies that used similar methods of characterization. When different methods of assessment (e.g. slug tests and grain size analysis) are used additional uncertainty is introduced and a direct comparison or correlation of obtained *K* values can be difficult even if the same sample support is considered. In general, the use of slug tests to determine streambed *K* values seems to produce more representative data as measurements are performed in situ and samples are not disturbed thus allowing for the consideration of anisotropy. For the data presented here, also the coefficient of variation of $K_h$values is about half of that of the K_g values. *K* values obtained from grain size analysis can be used as an indicator to the conditions at a site. However, as a correlation of K_g values to values obtained in situ is often inconclusive, analysis of the spatial variability of streambed hydraulic conductivity based on K_g values (e.g. through the use of variograms) should be performed with care. Here, further analyses regarding the spatial variability of streambed *K* by means of variograms and kriging did not produce meaningful results.

In general, knowledge on the spatial variability of streambed hydraulic conductivity on the sub-reach and sediment scales can be useful to determine local hotspots that might become important for contaminant attenuation processes. However, at the site presented here no streambed sediment structures with distinctly different *K* could be delineated. This could be related to the following aspects:

- The field site was situated in a straight section of the stream. In meandering sections the variability of streambed *K* is assumed larger than in straight sections [see also *Sebok et al.*, 2015] due to a more diverse flow pattern and stronger differences in erosion and deposition patterns.
- The number of locations where $K_h$values were obtained was insufficient to determine the spatial variation with respect to the entire field site or individual transects. In case of K_g, sampling locations were distributed too evenly on the grid. Additionally, K_g

values obtained from grain size analysis might not provide representative information regarding the spatial variability of streambed hydraulic conductivity due to the method of sampling and analysis, in which a large part of the spatial information can already be destroyed.

6 General Conclusions and Future Research

6.1 General Conclusions

The aim of this thesis was to study water flow and contaminant transformation in the hyporheic zone of lowland rivers at the reach, subreach and sediment scales under uncertainty. To do so, the focus was laid on three major parameters of interest in HZ research, i.e. streambed hydraulic conductivity, exchange fluxes across streambeds and reaction rate coefficients defining contaminant attenuation. These parameters can be quantified through a variety of field, lab and/or modeling techniques. Likewise many methods exist to quantify operational and fundamental uncertainties, whereby the quantification of fundamental uncertainties proves often much more challenging.

Some general conclusions regarding uncertainty can already be stated before any further uncertainty quantification:

- All results obtained from field and/or lab measurements contain intrinsic uncertainty depending on the measurement procedure and the person conducting the experiment. One way to overcome these problems is to repeat experiments. However, in HZ research many experiments are basically non-repeatable as the HZ is a dynamic system that can change significantly over very short times (hours to days).
- There will always be some degree of operational or parameter uncertainty due to the simple fact that parameters usually cannot be measured over the entire scale of interest. Instead, certain interpolation techniques are used that ideally should at least reproduce the measured values at the measurement locations.
- Operational and fundamental uncertainties are often quantified by means of modeling. However, here it has to be kept in mind that looking at the quantified uncertainties alone for a comparison between different models is still somewhat subjective as many hydrological problems are ill-posed [*Ebel and Loague*, 2006] and subject to non-uniqueness. On the one hand, any model will only represent the modeler's own understanding of the system under investigation. As the modeler chooses his or her preferred conceptual and mathematical representation of reality (i.e. the preferred model), alternative models, possibly equally capable in describing the investigated system are omitted. As there is more than one possible model parameterization for the study area, the problem is not uniquely identifiable [*Ebel and Loague*, 2006; *Voss*, 2011b]. On the other hand, even the modeler's preferred model or parameterization can produce several equally well performing estimated parameter value combinations; the solution is said to be non-unique [*Carrera and Neuman*, 1986].

With that kept in mind the following conclusions can be drawn:

Transformation of Chlorinated Ethenes:

The quantification of parameters defining the sequential reductive dechlorination reaction of chlorinated ethenes by *Dehalococcoides mccartyi* in streambed and aquifer sediments is often not straight forward as the model results have shown. For once, results depend on available electron donors or the material microcosms were amended with. For example, this has led to First order degradation coefficients varying over three orders of magnitude (compare with Table 2.3, columns 2-4).

In general, such model algorithms (such as AMALGAM here) should be used that allow taking into account multiple objectives. These algorithms can then produce a number of viable Pareto-efficient solutions that define a range for each of the model parameters, which could then be used further in transport models.

For example, when streambed sediments and contaminated water from location SB2 were used, modeling of microcosm #2 with the First order approach (third spike only) led to 301 Pareto-efficient solutions out of 3000 iterations. Results for the individual degradation coefficients then varied between 3.2×10^{-1} $d^{-1} < \lambda_{TCE} < 3.3\times10^{-1}$ d^{-1}, 4.8×10^{-3} $d^{-1} < \lambda_{cDCE} < 2.1\times10^{-1}$ d^{-1} and 2.9×10^{-3} $d^{-1} < \lambda_{VC} < 5.3\times10^{-1}$ d^{-1}, while coefficients of variation varied between 0.3 % and 125.7 %. This means that with a sufficient number of iterations, many equally valid model solutions can be determined, accounting for non-uniqueness while indicators such as the coefficient of variation can provide information regarding parameter uncertainty. The number of viable solutions decreases with increasing model complexity and depends also on the number of iterations chosen. The parameter range is of course also influenced by the assigned boundary conditions. Thus, sufficient effort should be put into finding adequate boundary conditions through literature studies or preliminary calculations.

Additionally, improving kinetic models by including simultaneous growth/decay of other microorganisms could lead to better estimates and a more realistic description of the entire system. However, as model complexity is increased, so will be computing time and additional data will be needed. A trade-off will have to be made at some point regarding the actual benefits for non-scientific studies.

Quantification of exchange flux using heat as a tracer:

Heat is a useful tracer when it comes to the quantification of exchange fluxes across streambeds, especially due to its easy application. The quantification of exchange fluxes through temperature modeling is a well-accepted method within the scientific community. Even though heat transport in the streambed is fundamentally a three-dimensional process, often enough it seems sufficient to determine the vertical component of the exchange flux with simple 1D models. Here, the development and implementation of the LPML and LPMLE3 methods have allowed for the possibility to directly quantify parameter uncertainty by using the maximum-likelihood estimator and the covariance matrix. Additionally,

fundamental model structure uncertainty can in principle be assessed by using a cost function analysis, although additional research is required regarding the interpretation of the results.

As shown in Figure 1.3, exchange flux depends on a variety of factors. Over the several months of temperature measurements performed in the course of this thesis, the most influential ones had to be weather defining recharge and base flow contribution, the local hydrological regime with varying vertical hydraulic gradients, stream stage and streambed sediment load defining erosion and colmation processes and leading to short-term changes in streambed morphology. If colmation is strong, hydraulic conductivity variations in the first centimeters of the streambed can also play a critical role although further studies are required to determine the actual impact.

The LPML method was applied on temperature-time series collected from the streambed of the Slootbeek, a small Belgium lowland stream. Vertical flux estimates were in line with those found in other studies ranging from several mm per year to up to 1 m per year. The magnitude of the flux also increased gradually with downstream direction. Additionally, a flow-through system could be observed at least over parts of the measurement period (see chapter 3.6.9). The results can prove useful for further studies regarding the interactions between the Slootbeek and the Aa River on a regional scale. The LPMLE3 method allows for the quantification of vertical fluxes for parts of the streambed (sub-domains). Estimates for the Slootbeek were in the order of magnitude of seepage meter measurements. However, as the LPMLE3 method does not adhere to the principle of conservation of mass, estimated fluxes between streambed sub-domains might not always represent actual measurable vertical flux, especially, in case of a strong non-vertical flow component. Nonetheless, both models could be valuable tools for the scientific community, especially as they can simultaneously include multiple frequencies in data analysis and not just one signal (e.g. day-night signal) has to be isolated for flux estimation as was the case with previous methods.

The uncertainty in estimated exchange fluxes represented by the standard deviation was mostly between two to three orders of magnitude smaller than the actual estimated flux. In general, parameter uncertainties will become higher for smaller flux estimates. Near zero exchange, standard deviations might well be much larger than actual flux estimates leading to uncertainty regarding the direction of the flow (upward or downward). Uncertainty in the flux estimate can also depend on the configuration of the temperature measurement device used as shown in chapter 4. If in multi-sensor devices individual sensors are very close together, as was the case for subdomain SD2, uncertainty (standard deviation) might suddenly become very large (in the case of SD2, more than 50 %). However, further studies are needed to define a minimum size of the sub-domains used with the LPMLE3 method.

The impact of non-vertical flow components on the exchange flux estimates was not studied here but can potentially have a strong influence as shown by *Lautz* [2010]. As such, the uncertainty of the flux estimate due to the choice of the model can exceed the uncertainty of the parameter estimate e.g. due to the choice of the estimation algorithm.

Variability in streambed hydraulic conductivity:

The aim in chapter 5 was to determine streambed hydraulic conductivity on the sub-reach (stream section) scale using a high density data set and to study its variability. Although the data set at hand was ultimately insufficient to conduct meaningful advanced geostatistical analyses by, e.g. using variogram analysis and kriging the study can still be used to draw several conclusions. For once, the degree of variability in streambed *K* will depend on the general characteristics of the study site such as streambed morphology and channel planform. Also, the variability in streambed *K* is closely linked to the spatial and temporal patterns of exchange flux as these co-define the influence of colmation/erosion processes. This connection can be further studied for the field site as relevant data on vertical hydraulic gradients is partly available. The study conducted here can also be useful for later investigations that focus on transport and attenuation processes of nitrate occurring at the site.

In general, it seems preferable also on the sub-reach and sediment scales to use measurement techniques such as slug-tests that allow for directly determining streambed *K* in the field, even though they might be more costly or labor intensive. With slug tests a better spatial correlation could be obtained afterwards and anisotropy could be accounted for in the study here. Additionally, hydraulic conductivity estimates from slug tests also led to slightly lower coefficients of variation (about 50 %) than those from grain size analyses (60 % to 100 %, depending on the model)

6.2 Future Research

From the conclusions drawn above the following ideas are suggested regarding future research:

Transformation of CEs in the hyporheic zone:

The use of more complex kinetic models requires a better understanding of the factors affecting the cellular activity and concurrent growth of the dechlorinating bacteria. This, however, needs more research into the behavior of *Dehalococcoides mccartyi* in mixed microbial communities to elucidate their favorable growth conditions [*Islam et al.*, 2010]. Aside from further studying the fundamental attenuation processes of CEs by *Dehalococcoides mccartyi* further research should also focus on improving the modeling process. The modeling code (AMALGAM) applied here requires the definition of multiple objectives and already uses multiple evolutionary algorithms. However, as the model code produces many likely solutions on the Pareto front further research could focus on developing robust procedures to decide, which of these Pareto solutions should be included in decision making processes, e.g. when it comes to defining remediation procedures. Additionally, it

could be determined (order of magnitude) what is a sufficient number of iterations as this influences computing time.

Quantification of exchange flux using heat as a tracer:

Future research with regard to the LPML method could focus on the following issues:

- The LPML method could be tested on temperature data from other stream environments for comparison.
- It could also be tested on data with higher spatial resolution in the vertical such as obtained with a FO-DTS by *Briggs et al.* [2012]. This would allow for a better understanding of the connection of sensor spacing and parameter uncertainty and help to determine a minimum spacing between two temperature sensors.
- Using the LPML method on longer time-series could help in the understanding of annual exchange processes.
- An additional study on the effect of different window lengths and frequency ranges on a temperature-time series of one year or longer could help to better understand the long-term exchange processes acting at the Slootbeek.
- A comparison of 1D models that includes the LPML method with 2D and 3D models could help to determine the validity of the assumption of 1D vertical flow and provide a better understanding of the model structure uncertainty expressed now by the expected and actual cost values.
- To improve the understanding regarding expected and actual cost values, further studies that collect temperature data under controlled flow conditions could clarify whether the difference between both could actually serve as an indicator for non-vertical flow.

The LPML method could also be adapted to study other flow and transport processes in the frequency domain that rely on time-series.

The LPMLE3 method allows for the quantification of vertical streambed fluxes considering heterogeneity (i.e. by dividing the subsurface into several sub-domains with different characteristics). Here, future research could additionally focus on the following aspects:

- An analysis of variations in flux estimates of partially overlapping sub-domains could prove helpful to better understand the overall spatial variability of vertical flux.
- For practitioners interested in the temporal variability of fluxes future studies could investigate the interplay between the size of the sub-domain, temperature data quality and the windowing technique applied.

Future field studies could also focus on the vertical and temporal variability of thermal diffusivity. For a comparison however, values for thermal conductivities and volumetric heat capacities for each finite domain should also be obtained from field or laboratory experiments. Similar to chapter 3.6.9, the spatial and temporal patterns of vertical streambed

fluxes could be assessed with the LPMLE3 method. Figure 3.16 could then be enhanced to represent a crude 3D image of streambed flux. Such a 3D pattern could be combined with depth-dependent information from in-stream piezometers to deduce streambed hydraulic conductivity patterns.

Variability in streambed hydraulic conductivity:

A future study could focus on conducting many slug tests at small spatial scales and not on a predefined grid to acquire data suitable for variogram analysis. If such a study has already been conducted at a very similar field site an alternative could be to use a training image and techniques such as multiple point geostatistics.

Parameter interaction

Further research could also focus more on the general interplay between hydraulic and biochemical parameters that define contaminant attenuation in the HZ and the formation of hot-spots. A better understanding of how microbial activity is influenced by biochemical and hydraulic parameters would allow for the development of improved concepts for microbial stimulation as a remediation technique. However, the quasi-uniqueness of each field site in terms of geological, physical and biochemical characteristics provides a strong obstacle to be overcome here.

Among other factors, contaminant attenuation depends on the hydraulic conductivity and exchange flux that determine the residence time. Here, a simple numerical experiment is conducted for a one dimensional streamline in the hyporheic zone using HYDRUS 1D to demonstrate how important the parameter dependence and thus the quantification of parameter variability and uncertainty can become. Assumed is a streambed of 2 m thickness, where only vertical upward flow occurs and no initial contamination exists. Then for one day 5 mg of VC are introduced at the lower end of the streambed. Assuming constant water flux at the streambed top, constant pressure head at the streambed bottom, no contaminant entering the stream, only first order degradation and no other transformation processes occurring, the following scenarios can be considered:

(i) The exchange flux is assumed to be -81.2 mm d^{-1}, i.e. the average long-term value obtained at the Slootbeek (Table 3.4). The First order rate coefficient for VC is assumed to be λ_{VC} = 7.4×10^{-2} d^{-1}, i.e. the average from the Pareto-efficient solutions of microcosm #2 obtained when streambed sediments and contaminated water from location SB2 were used. K_h is varied over the entire range described in Figure 5.9 (i.e. 1.1 md^{-1} to 12.5 md^{-1}) assuming a minimum, maximum and an average K_h scenario. Simulations showed that at 1 m depth (i.e. the middle of the streambed), breakthrough occurs after 4 days and maximum concentrations only minimally increase from 0.57 mgL^{-1} for the lowest K_h value to 0.62 mgL^{-1} for the highest K_h value. After 12 days, only 10% of the concentration remains. As uncertainties on K_h were

about 50% of the mean, they will have no strong additional influence on the estimated concentrations.

(ii) If an average K_h of 6.0 md^{-1} is assumed together with λ_{VC} = 7.4×10^{-2} d^{-1} but now the exchange flux is changed from -81.2 mm d^{-1} to -291.3 mm d^{-1} (i.e. the maximum long-term value from the Slootbeek), breakthrough at 1 m is already reached after 1.7 days and maximum concentrations are much higher with 2.3 mgL^{-1}. After 4.2 days only 10% of the concentration remains. A 3.5 times bigger exchange flux leads to a much smaller residence time and less contaminant mass is degraded in the same volume of streambed sediment. If in the example here the standard deviation on the exchange flux is 10 %, breakthrough would increase/decrease by about half a day and maximum concentrations would increase/decrease by about 10-15 %.

(iii) Now, an average K_h of 6.0 md^{-1} is assumed together with an exchange flux of -81.2 mm d^{-1} but λ_{VC} is varied between 2.9×10^{-3} d^{-1} and 5.3×10^{-1} d^{-1}. Using a degradation coefficient of 5.3×10^{-1} d^{-1}, breakthrough is reached after 3 days, for λ_{VC} = 7.4×10^{-2} d^{-1} breakthrough is reached after 4 days, while for λ_{VC} = 2.9×10^{-3} d^{-1} breakthrough is reached after 4.3 days. The relation here is thus not linear. Maximum concentrations change from 0.16 mgL^{-1} over 0.59 mgL^{-1}, to 0.77 mgL^{-1}. Although the difference between the maximum λ_{VC} and the average λ_{VC} is smaller than between the average λ_{VC} and the minimum λ_{VC}, the relative impact of the change is higher.

In the example here, the influence of the exchange flux and the mixing behavior (not tested here) on contaminant attenuation is much bigger than the influence of the hydraulic conductivity of the streambed. The latter will probably only become considerably more influential in case of strong colmation effects when K_h can locally drastically decrease. On the other hand, the determination of variability and uncertainty in reaction rate coefficients λ_{VC} seems to become increasingly important with decreasing variability in exchange flux.

Appendix - Chapter 2

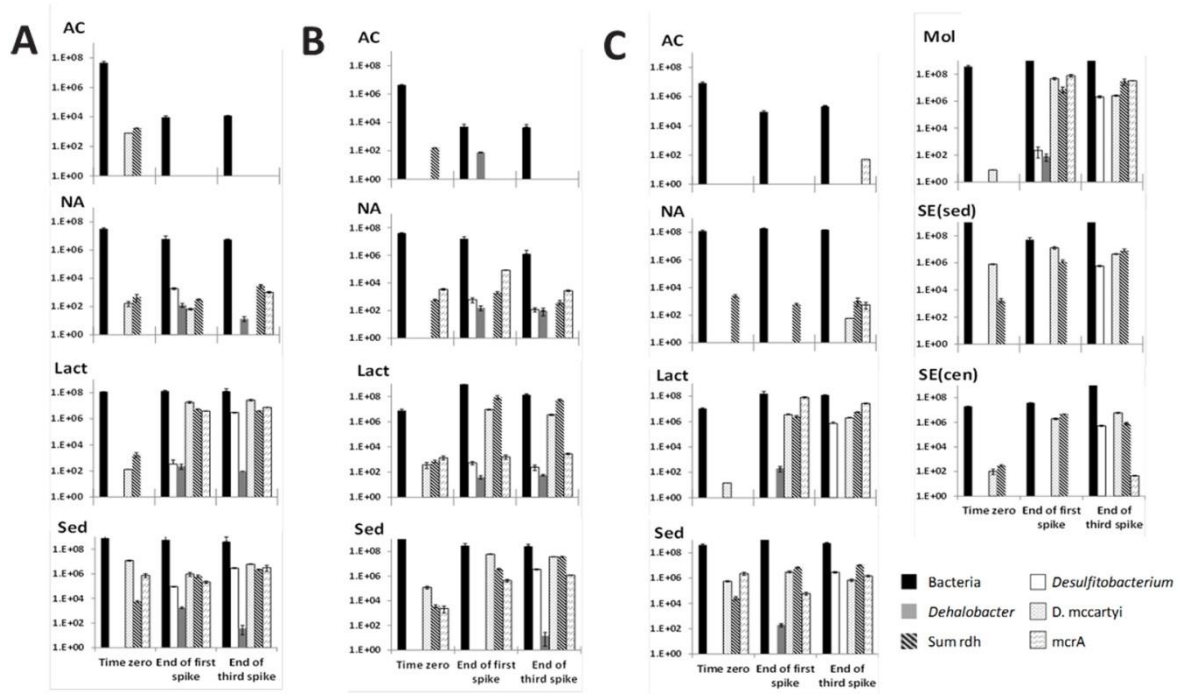

Figure A2.1: 16S rRNA gene copy numbers of eubacteria, Dehalococcoides mccartyi, Desulfitobacterium, Dehalobacter and sum of rdh (tceA, vcrA, and bvcA) and mcrA genes as determined by qPCR in the microcosms Samples were taken at the start of the experiment, and at the end of the first and third TCE spikes. Each bar represents the average of the results of triplicate qPCRs performed on one sample of each of the duplicate microcosms (n = 6). NA: natural attenuation, AC: abiotic control, Lact: lactate, Sed: streambed sediment, SE (sed): sediment extract obtained after sedimentation, SE (cen): sediment extract obtained after centrifugation, Mol: molasses. Source: Modified form *Schneidewind et al.* [2014].

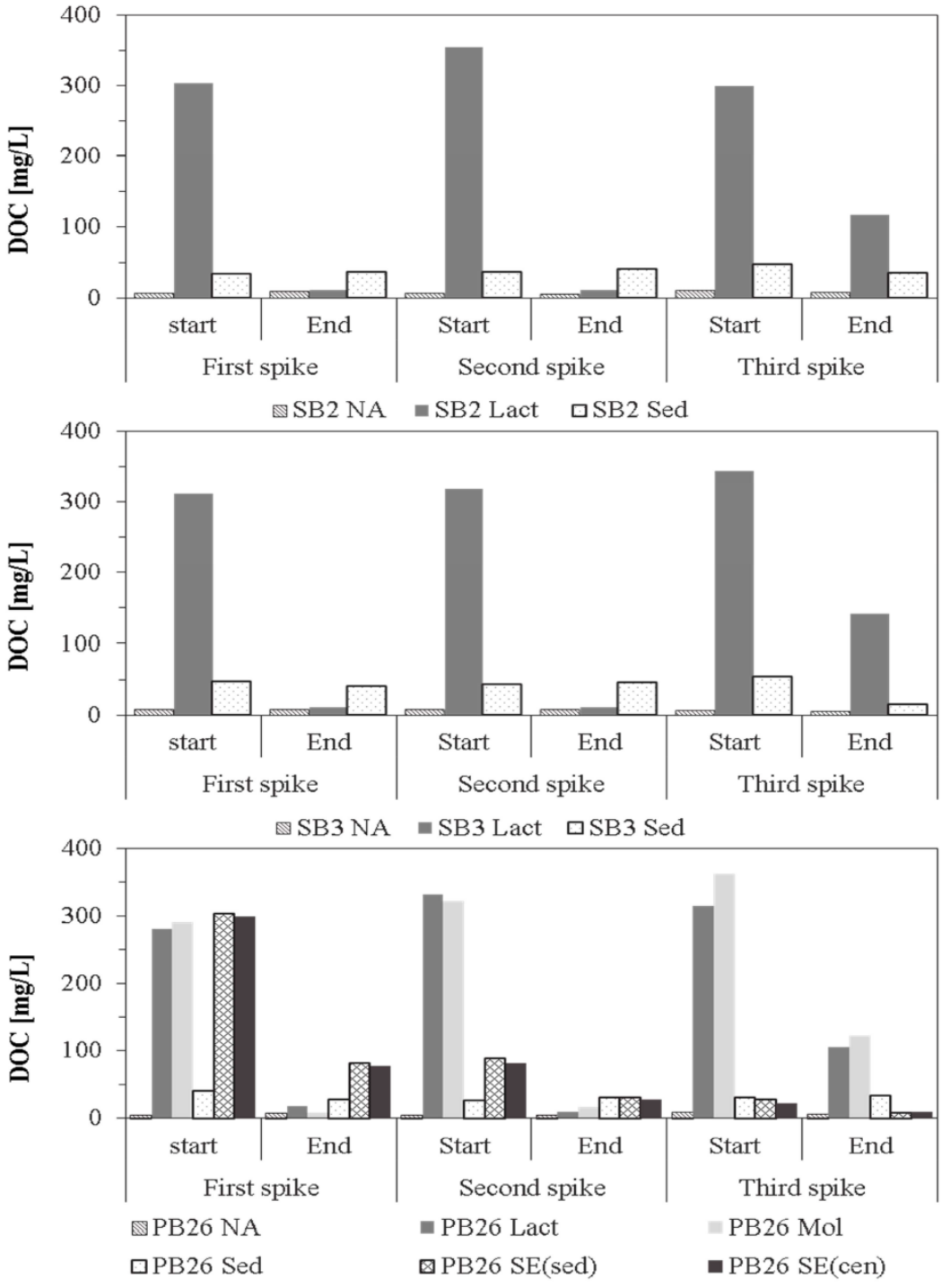

Figure A2.2: Dissolved organic carbon (DOC) concentrations in microcosms for locations SB2, SB3, and PB26 NA: natural attenuation, Lact: lactate amendment, Mol: molasses amendment, Sed: streambed sediment, SE(sed): sediment extract obtained after sedimentation, SE(cen): sediment extract obtained after centrifugation. Source: *Schneidewind et al.* [2014].

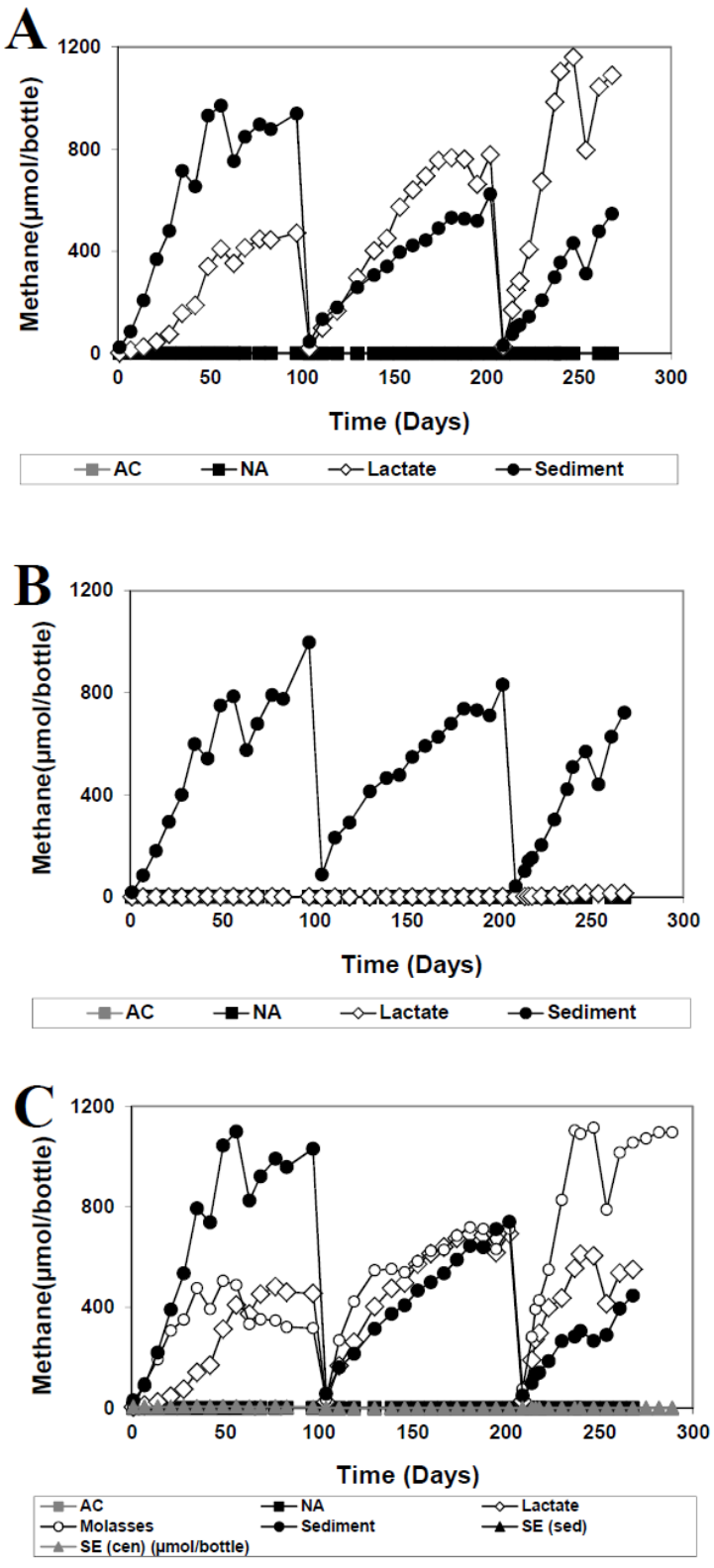

Figure A2.3: Methane production in microcosms from location SB2 (A), SB3 (B), and PB26 (C). NA: natural attenuation, AC: abiotic control, SE (sed): sediment extract obtained after sedimentation, SE (cen): sediment extract obtained after centrifugation. Source: *Schneidewind et al.* [2014].

Table A2.1: Results of First order kinetics model were obtained using AMALGAM for optimizing the third TCE spike in each microcosm. Each result is the point on the Pareto surface closest to the zero-objective point. Source: *own.*

Location & Batch		Setup[a]	λ_{TCE} [d^{-1}]	λ_{cDCE} [d^{-1}]	λ_{VC} [d^{-1}]	λ_{TCE} [mmol $cell^{-1}$ d^{-1}]	λ_{cDCE} [mmol $cell^{-1}$ d^{-1}]	λ_{VC} [mmol $cell^{-1}$ d^{-1}]
PB26	1	LAC	1.05E-01	1.03E+00	9.46E-01	3.80E-12	3.73E-11	3.41E-11
PB26	2	LAC	9.46E-02	7.61E-01	5.26E-01	6.85E-12	5.51E-11	3.80E-11
PB26	1	MOL	4.03E-02	1.85E-01	1.09E-01	8.46E-14	3.89E-13	2.29E-13
PB26	2	MOL	5.89E-02	2.35E-01	1.86E-01	4.20E-13	1.68E-12	1.32E-12
PB26	1	SED	3.78E-01	1.90E-01	4.81E-01	7.30E-12	3.68E-12	9.30E-12
PB26	2	SED	3.16E-01	2.02E-01	5.86E-01	1.75E-10	1.12E-10	3.25E-10
PB26	1	SESED	1.41E-01	9.46E-02	8.85E-02	1.73E-12	1.16E-12	1.09E-12
PB26	2	SESED	1.10E-01	1.41E-01	1.44E-01	1.06E-12	1.36E-12	1.39E-12
PB26	1	SECEN	4.69E-02	3.13E-02	5.24E-02	1.38E-11	9.21E-12	1.54E-11
PB26	2	SECEN	2.74E-02	3.20E-02	7.51E-02	1.57E-12	1.83E-12	4.29E-12
SB2	1	LAC	1.41E-01	8.20E-01	2.01E+00	7.02E-13	4.08E-12	1.00E-11
SB2	2	LAC	1.08E-01	3.93E+00	3.07E+00	6.69E-13	2.44E-11	1.91E-11
SB2	1	SED	3.74E-01	1.69E-01	4.55E-01	1.21E-10	5.44E-11	1.47E-10
SB2	2	SED	3.24E-01	1.58E-01	4.16E-01	1.63E-12	7.95E-13	2.10E-12
SB3	1	LAC	1.42E-01	2.85E-01	3.02E-01	2.40E-12	4.82E-12	5.10E-12
SB3	2	LAC	2.28E-01	1.37E+00	6.37E-01	1.27E-11	7.64E-11	3.54E-11
SB3	1	SED	3.54E-01	2.05E-01	6.31E-01	2.55E-12	1.47E-12	4.55E-12
SB3	2	SED	3.19E-01	2.14E-01	5.90E-01	7.45E-13	4.99E-13	1.38E-12

a Abbreviations: LAC = lactate, MOL = molasse, SED = sediment, SESED = sedimented sediment, SECEN = centrifuged sediment

RMSE values can be found at \PhD_Schneidewind\Thesis\Data\Chapter 2 in rmse.xlsx.

Table A2.2: Results of the Michaelis-Menten kinetics model obtained using AMALGAM for optimizing the third TCE spike in each microcosm. Each result is the point on the Pareto surface closest to the zero-objective point. Source: *own.*

Location & Batch		Setup[a]	λ_{TCE} [µmol cell^{-1}d^{-1}]	$K_{s,TCE}$ [µM]	I_{TCE} [µM]	λ_{cDCE} [µmol cell^{-1}d^{-1}]	$K_{s,cDCE}$ [µM]	I_{cDCE} [µM]	λ_{VC} [µmol cell^{-1}d^{-1}]	$K_{s,VC}$ [µM]
PB26	1	LAC	4.88E-09	2.97E+01	1.30E+02	4.14E-09	1.23E+01	3.05E+01	1.21E-08	3.78E+01
PB26	2	LAC	1.39E-09	2.10E+00	3.70E+00	3.28E-09	4.71E+00	1.30E+02	3.59E-09	5.78E+00
PB26	1	MOL	1.67E-08	4.14E+01	1.17E+02	1.17E-08	6.88E+00	8.43E+01	6.54E-09	8.40E+00
PB26	2	MOL	1.07E-09	4.19E+01	5.63E+00	1.31E-09	3.37E+01	3.70E+02	5.97E-10	2.07E+01
PB26	1	SED	6.09E-09	2.10E+00	3.73E+00	5.04E-09	1.47E+01	9.31E+00	3.70E-09	3.90E+00
PB26	2	SED	5.73E-08	2.17E+00	3.70E+00	5.51E-08	9.85E+00	3.17E+01	3.96E-08	5.50E+00
PB26	1	SESED	1.17E-09	6.10E+00	3.69E+02	4.85E-10	2.51E+01	1.94E+02	2.69E-10	1.17E+01
PB26	2	SESED	2.28E-09	1.68E+01	1.86E+02	1.19E-09	7.20E+00	1.45E+02	6.15E-10	8.83E+00
PB26	1	SECEN	2.09E-09	4.14E+01	3.70E+02	4.64E-10	4.58E+00	1.16E+02	7.98E-10	6.62E+00
PB26	2	SECEN	2.66E-10	3.88E+01	2.60E+02	9.67E-11	3.85E+00	5.28E+00	1.17E-10	3.46E+01
SB2	1	LAC	1.37E-10	2.10E+00	3.50E+02	1.81E-10	3.78E+00	4.27E+00	2.00E-10	7.50E+00
SB2	2	LAC	7.12E-10	2.10E+00	3.70E+00	4.04E-09	6.95E+00	3.05E+02	1.37E-09	4.13E+00
SB2	1	SED	8.23E-10	2.12E+00	3.71E+00	4.07E-10	3.82E+00	6.98E+00	8.24E-10	2.62E+01
SB2	2	SED	2.79E-09	2.10E+00	3.70E+00	3.85E-09	3.78E+01	1.94E+02	4.58E-09	2.89E+01
SB3	1	LAC	1.07E-09	3.74E+00	3.70E+02	2.52E-09	3.85E+00	7.96E+01	7.18E-10	5.09E+00
SB3	2	LAC	8.24E-07	7.07E+00	3.53E+02	6.48E-06	3.33E+01	5.01E+01	5.96E-07	3.78E+00
SB3	1	SED	1.22E-10	2.10E+00	6.32E+00	6.46E-11	7.18E+00	9.01E+01	8.96E-11	4.62E+00
SB3	2	SED	8.04E-08	2.12E+00	3.70E+00	2.02E-07	1.28E+01	5.80E+00	6.93E-07	3.16E+01

a Abbreviations: LAC = lactate, MOL = molasse, SED = sediment, SESED = sedimented sediment, SECEN = centrifuged sediment

RMSE values can be found at \PhD_Schneidewind\Thesis\Data\Chapter 2 in rmse.xlsx.

Table A2.3: Results of the Monod kinetics model. They were obtained using AMALGAM for optimizing the third TCE spike in each microcosm. Each result is the point on the Pareto surface closest to the zero-objective point. Source: *own.*

Location & Batch		Setup[a]	λ_{TCE} *b*	$K_{s,TCE}$ [µM]	I_{TCE} [µM]	λ_{cDCE} *b*	$K_{s,cDCE}$ [µM]	I_{cDCE} [µM]	λ_{VC} *b*	$K_{s,VC}$ [µM]	b [d^{-1}]	Y [cells µmol^{-1}]
PB26	1	LAC	2.30E-09	4.76E-01	1.94E+02	9.33E-07	2.42E+00	1.18E+01	2.44E-06	3.80E-01	4.63E-02	3.24E+07
PB26	2	LAC	1.56E-08	4.36E-01	6.77E+01	1.15E-05	4.45E-01	1.42E+02	4.84E-06	3.98E-01	5.00E-02	5.85E+06
PB26	1	MOL	1.07E-10	4.19E+01	3.70E+02	3.85E-08	3.78E-01	2.11E+02	1.10E-08	2.16E+00	4.42E-02	1.43E+09
PB26	2	MOL	1.90E-09	4.19E+01	3.70E+00	3.20E-05	3.78E-01	3.70E+02	1.37E-06	3.78E-01	2.00E-02	5.37E+07
PB26	1	SED	1.46E-09	5.71E-01	1.67E+02	8.04E-10	3.78E+01	3.70E+02	9.24E-10	1.26E+01	2.01E-02	1.45E+08
PB26	2	SED	6.87E-08	4.14E+01	3.70E+02	1.03E-08	5.41E-01	3.70E+00	3.75E-07	2.81E+01	2.00E-02	5.40E+06
PB26	1	SESED	4.76E-10	3.43E+00	7.41E+01	1.14E-10	3.51E+01	9.05E+00	2.77E-10	1.58E+01	2.01E-02	2.40E+08
PB26	2	SESED	3.39E-10	1.02E+01	2.20E+02	7.83E-11	2.32E+01	1.52E+01	9.96E-11	6.35E+00	2.00E-02	3.08E+08
PB26	1	SECEN	4.46E-08	1.46E+01	1.73E+02	9.72E-09	7.64E-01	5.25E+00	6.67E-09	9.81E-01	5.00E-02	2.27E+06
PB26	2	SECEN	6.12E-08	9.30E+00	1.39E+02	1.22E-08	4.90E-01	1.85E+02	2.40E-08	1.98E+01	4.91E-02	6.09E+06
SB2	1	LAC	1.21E-09	2.55E+01	5.63E+01	1.16E-09	1.50E+00	9.23E+01	3.04E-09	1.03E+01	2.01E-02	9.90E+07
SB2	2	LAC	1.75E-09	2.73E+01	1.08E+01	3.37E-09	4.62E-01	8.60E+01	8.93E-08	3.78E+01	2.34E-02	7.42E+07
SB2	1	SED	3.30E-08	2.57E+01	1.86E+01	9.56E-09	1.93E+01	6.87E+00	2.71E-07	3.78E-01	2.00E-02	9.31E+06
SB2	2	SED	6.50E-10	3.72E+01	3.41E+02	2.83E-10	3.73E+01	4.27E+00	2.27E-09	3.78E+01	2.01E-02	5.74E+08
SB3	1	LAC	1.58E-09	4.62E+00	2.83E+01	8.35E-09	2.84E+01	1.87E+01	4.67E-10	3.34E+01	2.00E-02	3.61E+07
SB3	2	LAC	2.48E-09	3.34E+01	1.70E+02	1.16E-08	3.78E+01	1.49E+01	3.93E-10	3.78E-01	2.05E-02	1.47E+07
SB3	1	SED	9.15E-10	3.05E+00	4.10E+01	1.04E-10	3.78E-01	3.70E+00	1.60E-09	2.08E+01	2.00E-02	3.40E+08
SB3	2	SED	1.12E-09	4.48E+00	3.67E+02	6.12E-11	4.22E-01	5.51E+00	2.61E-10	3.97E+00	2.01E-02	5.57E+08

a Abbreviations: LAC = lactate, MOL = molasse, SED = sediment, SESED = sedimented sediment, SECEN = centrifuged sediment
b in [µmol cells^{-1} d^{-1}]

RMSE values can be found at \PhD_Schneidewind\Thesis\Data\Chapter 2 in rmse.xlsx.

Appendix - Chapter 3

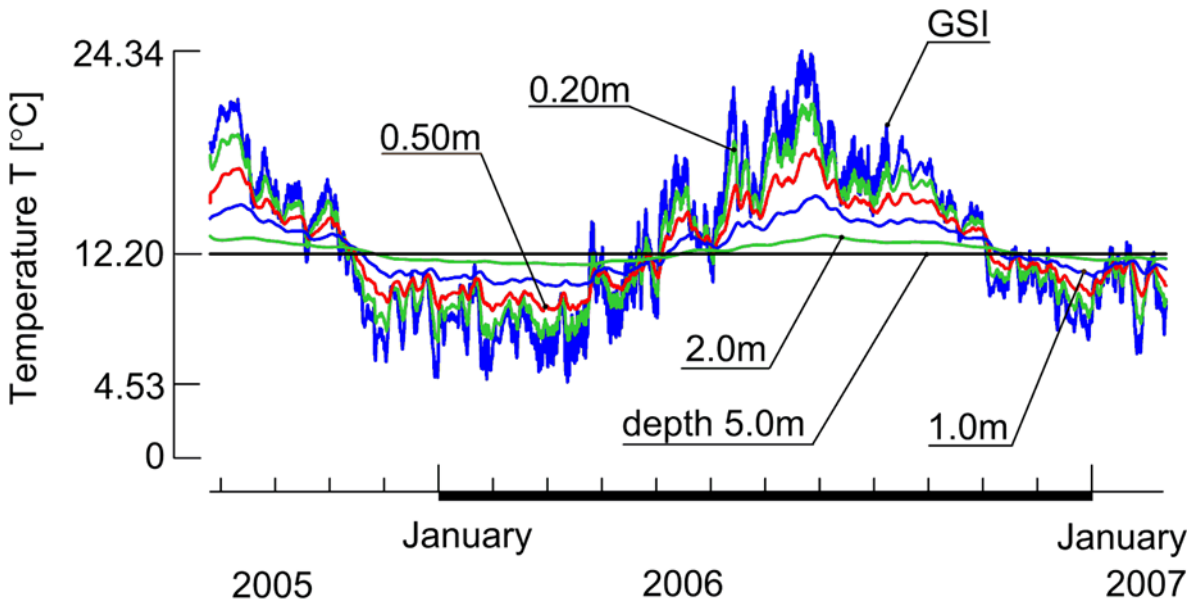

Figure A3.1: Temperature-time series (520 days) of several depths that were created with the numerical model STRIVE by *Anibas et al.* [2011]. Time series at 0.05 m, 0.10 m and 0.20 m were the used as input to the LPML method to estimate known values of $\boldsymbol{q_z}$ and $\boldsymbol{\kappa}$ (chapter 3.5). Source: *Vandersteen et al.* [2015].

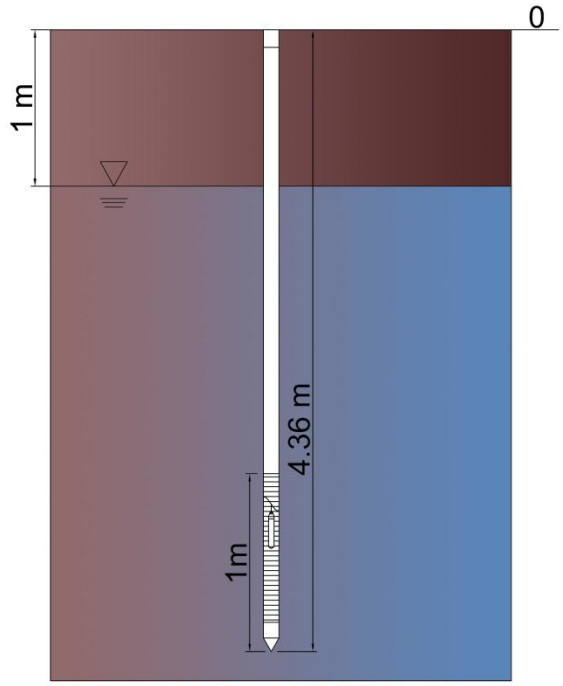

Figure A3.2: Well GW1 installed next to the confluence with the River Aa to measure groundwater temperatures and pressure head (chapter 3.6.2). Source: *own.* Not to scale.

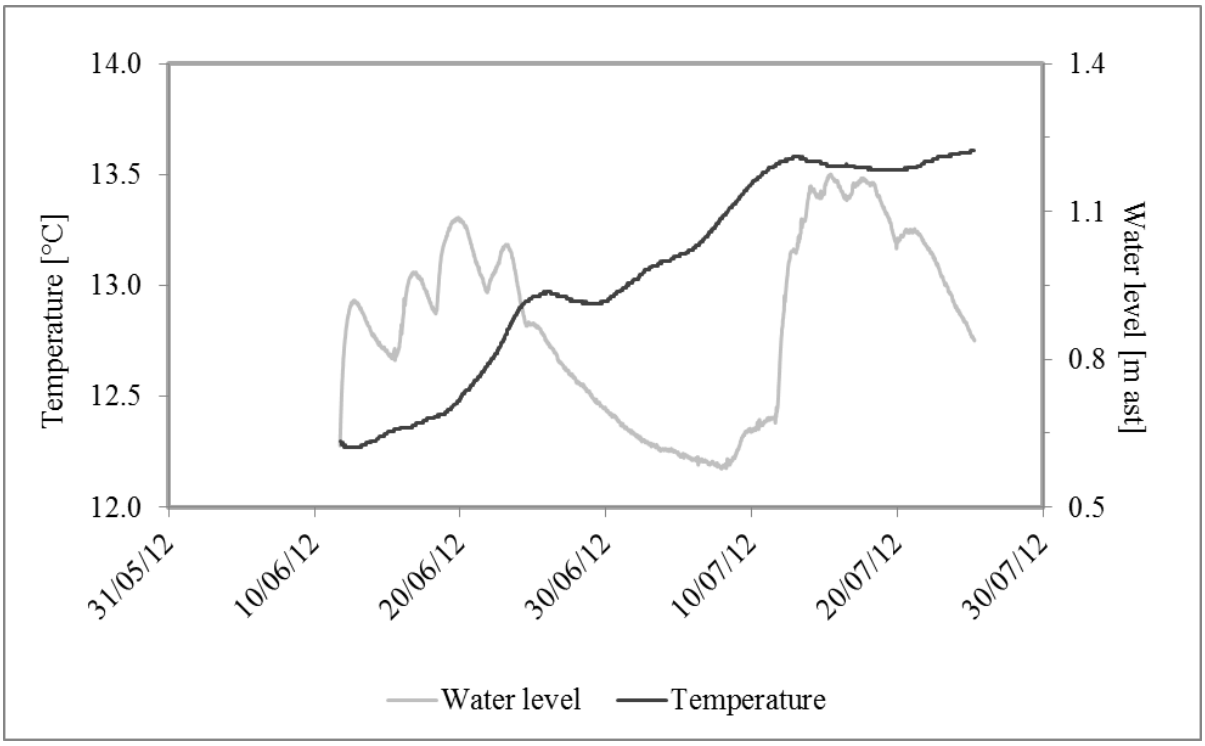

Figure A3.3: Water temperatures and water levels above streambed top measured in the deep streambed piezometer (chapters 3.6.2 and 3.6.3.1). Source: *own*.

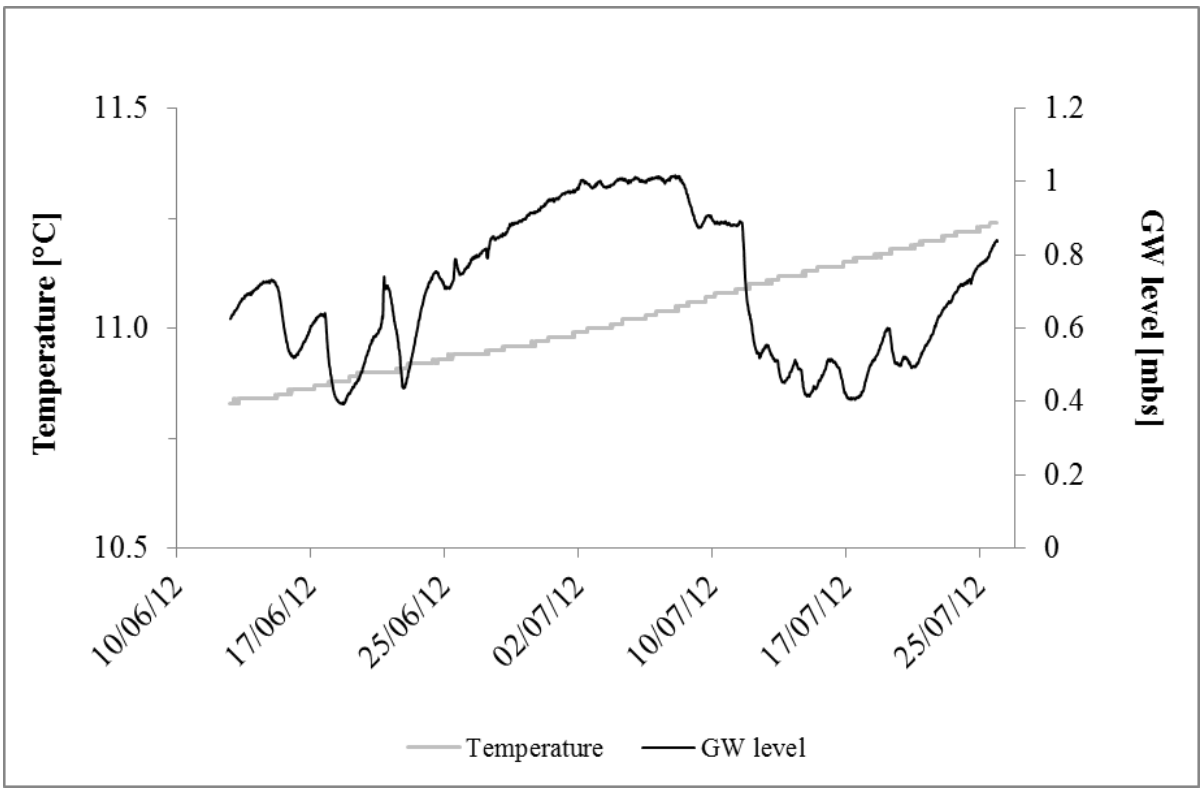

Figure A3.4: Groundwater temperatures and groundwater water levels below land surface measured in well GW1 (chapter 3.6.3.1). Source: *own.*

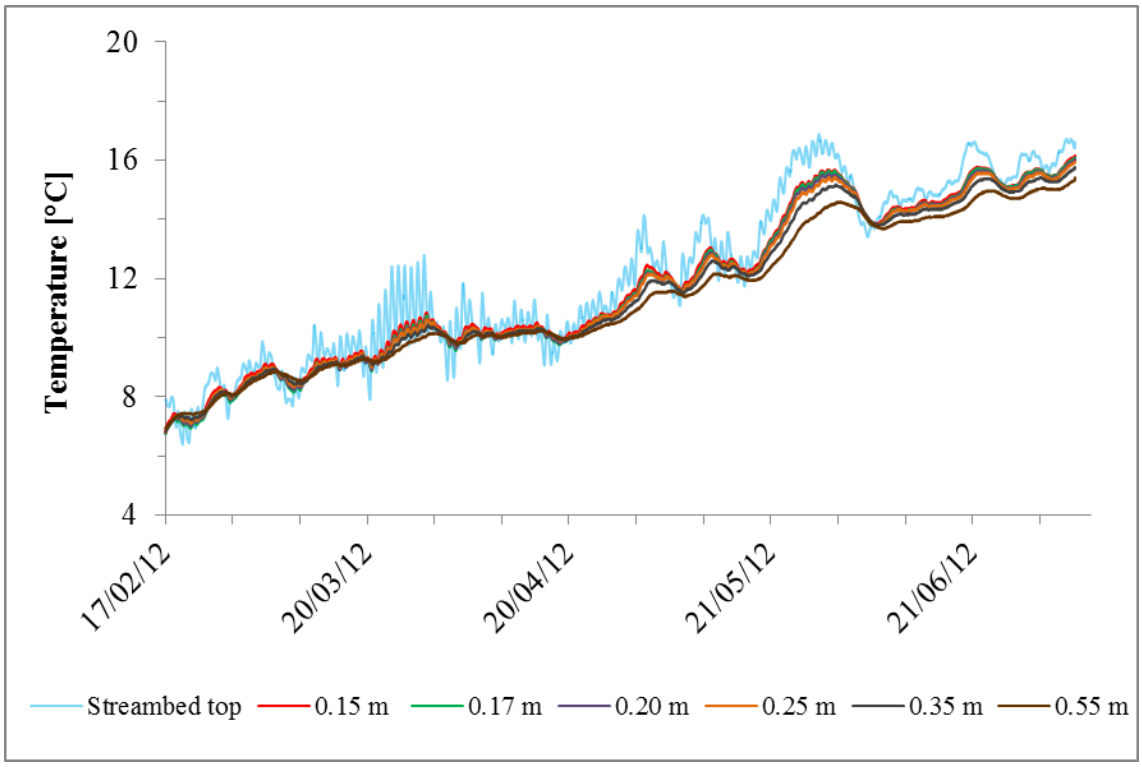

Figure A3.5: Temperature-time series collected at location ML2 (chapter 3.6.3.2). Source: *Anibas et al.* [2016].

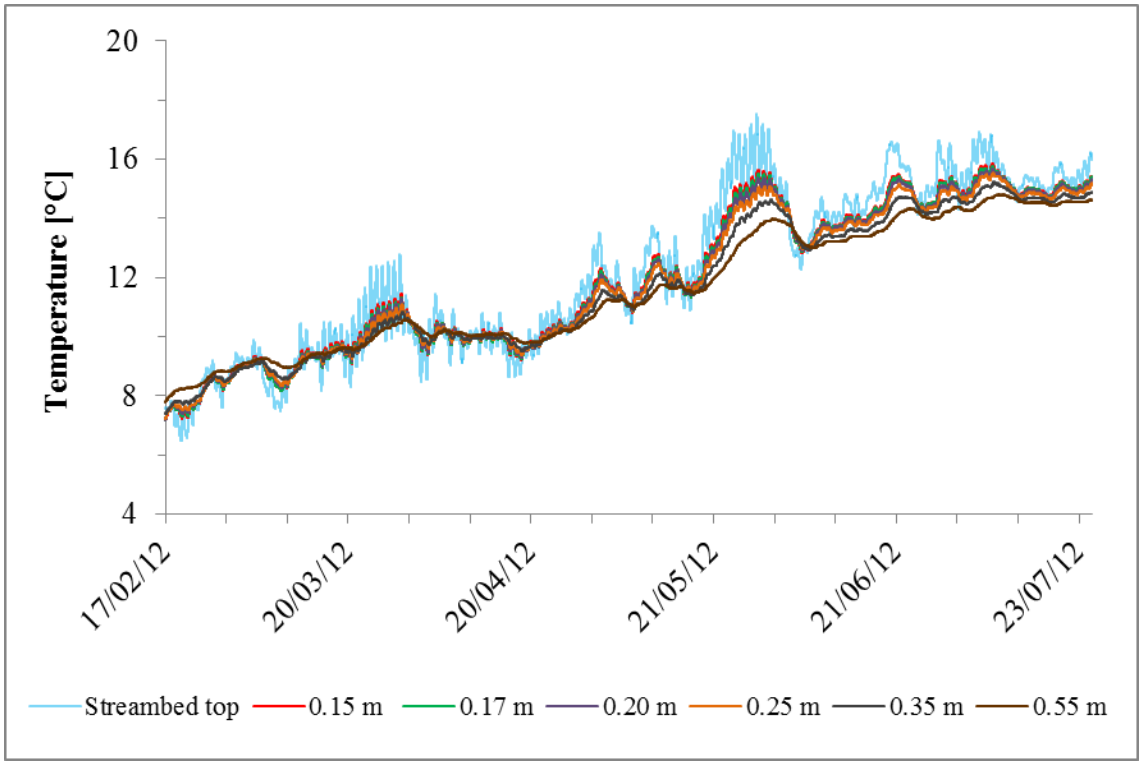

Figure A3.6: Temperature-time series collected at location ML3 (chapter 3.6.3.2). Source: *Anibas et al.* [2016].

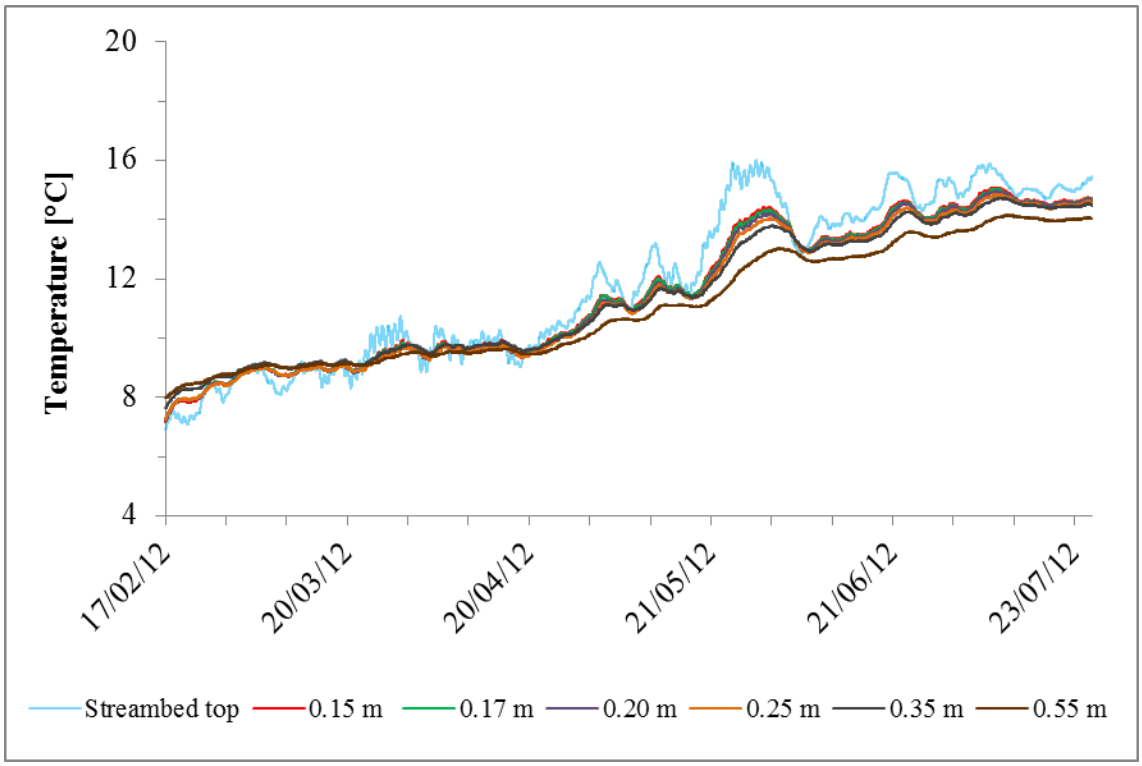

Figure A3.7: Temperature-time series collected at location ML4 (chapter 3.6.3.2). Source: *Anibas et al.* [2016].

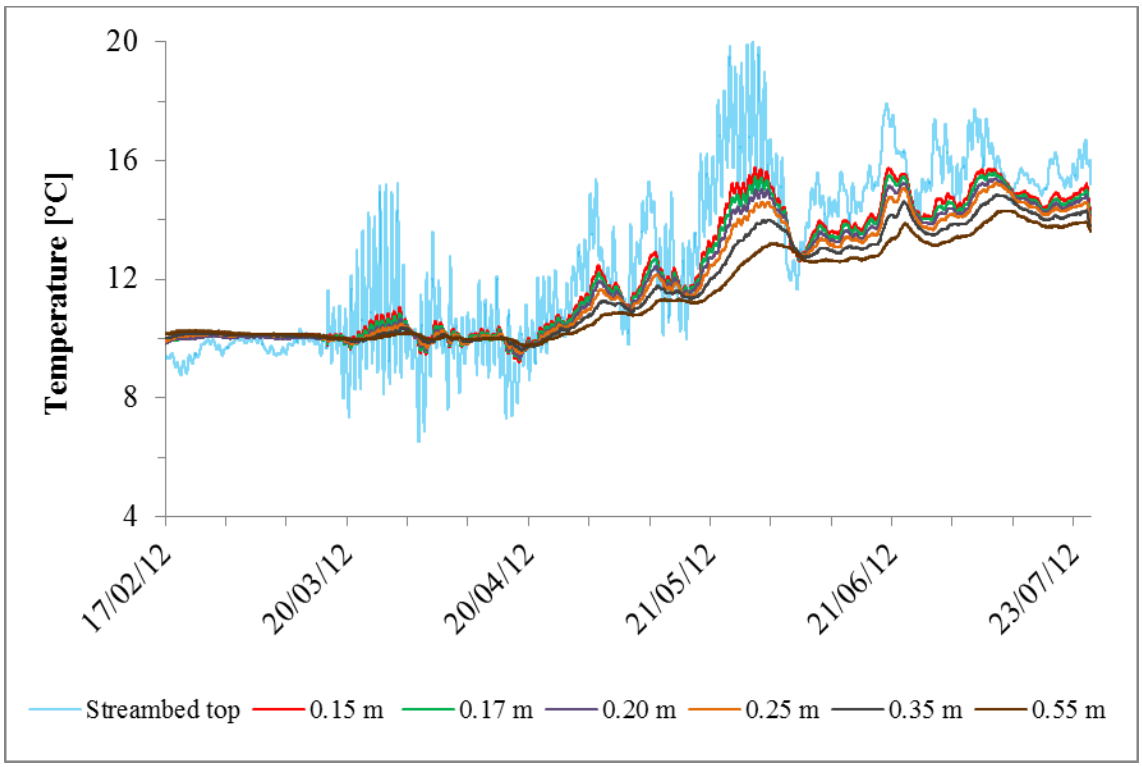

Figure A3.8: Temperature-time series collected at location ML6 (chapter 3.6.3.2). Source: *Anibas et al.* [2016].

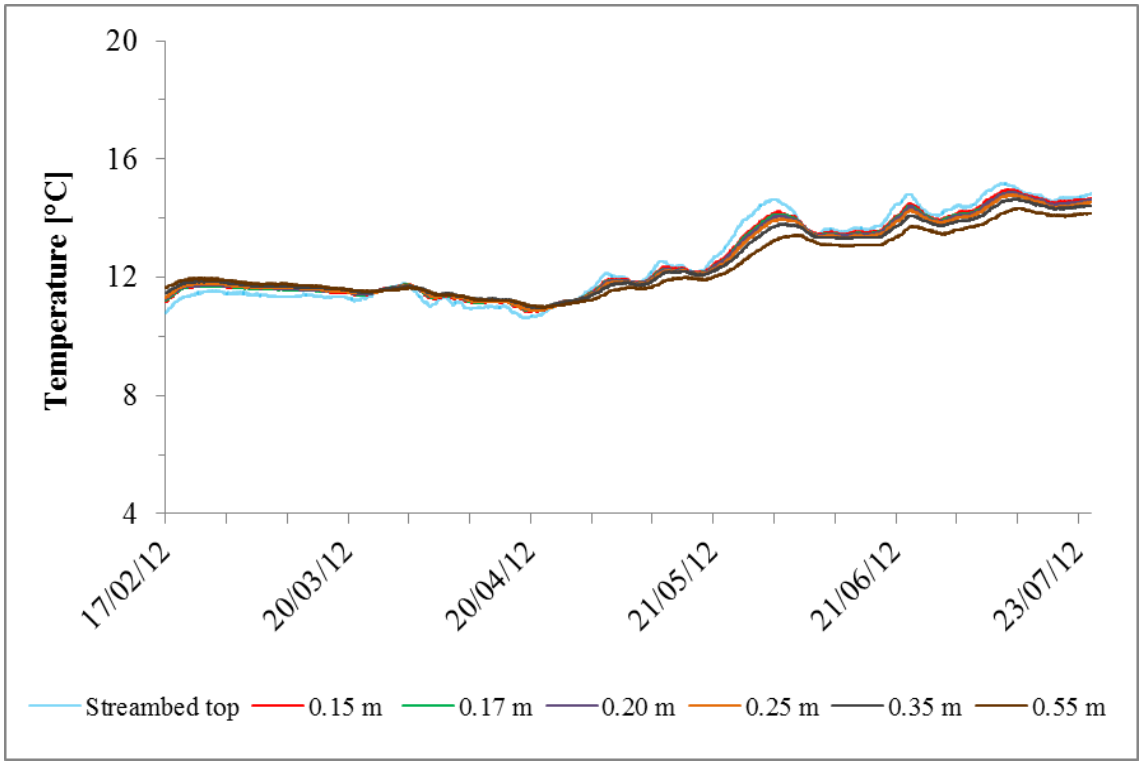

Figure A3.9: Temperature-time series collected at location ML7 (chapter 3.6.3.2). Source: *Anibas et al.* [2016].

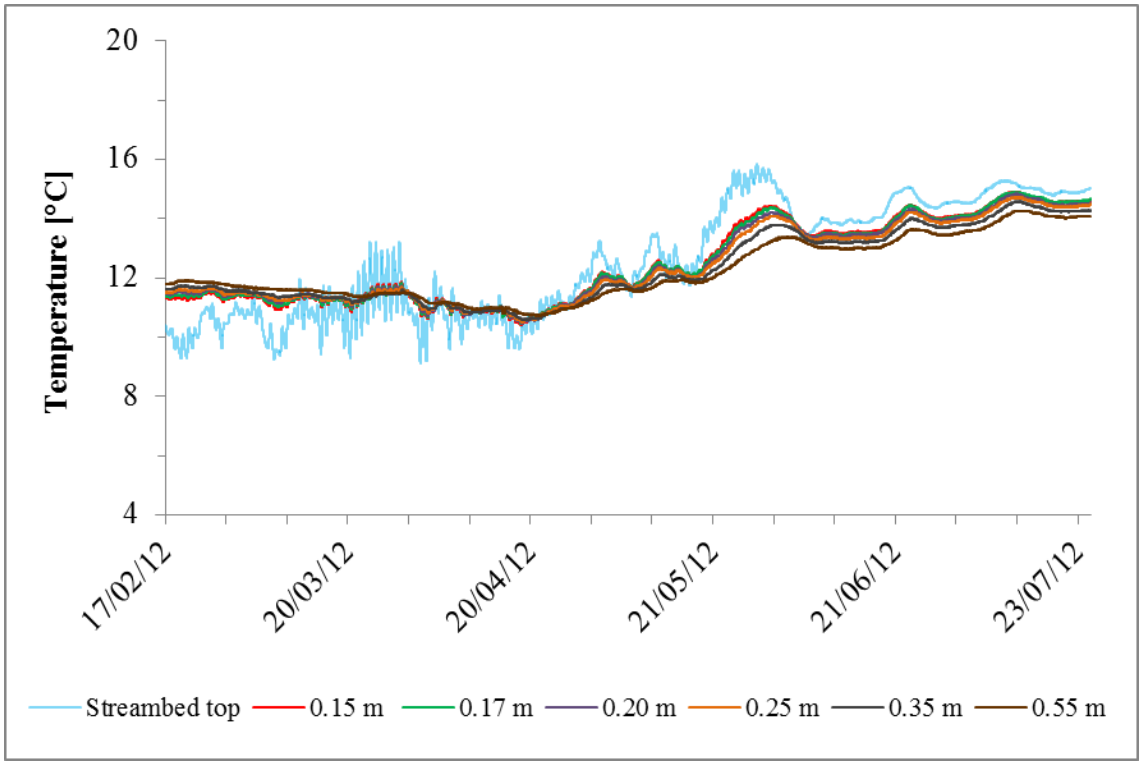

Figure A3.10: Temperature-time series collected at location ML8 (chapter 3.6.3.2). Source: *Anibas et al.* [2016].

Appendix - Chapter 4

Table A4.1: Estimates of average vertical fluxes and thermal diffusivities for consecutive finite streambed domains estimated with the LPMLE3 method using a frequency of 1 d^{-1}. Source: *own*.

Depth [cm]	q_z [mm d^{-1}]	D_T [m^2 s^{-1}] × 10^{-7}	q_z dev. [%]	D_T dev. [%]	σ_{qz} [mm d^{-1}]	σ_{DT} [m^2 s^{-1}] × 10^{-8}	σ_{qz} [%]	σ_{DT} [%]
10-20	-86.53	8.354	0.15	0.25	0.16	0.156	0.19	0.19
20-30	-86.84	8.391	0.51	0.69	0.28	0.269	0.32	0.32
30-40	-87.00	8.412	0.69	0.95	0.46	0.438	0.52	0.52
40-50	-87.17	8.437	0.89	1.24	0.62	0.593	0.71	0.70
50-60	-87.30	8.458	1.04	1.50	0.90	0.866	1.03	1.02
60-70	-87.28	8.464	1.01	1.57	1.06	1.018	1.21	1.20
70-80	-87.54	8.498	1.32	1.98	1.28	1.238	1.47	1.46

Depth = Interval size per sensor triplet, e.g. 10-20 = upper boundary at 10 cm, lower boundary at 20 cm and third sensor at the mid-point, i.e. 15 cm.

q_z = vertical flux, D_T = thermal diffusivity, dev. = deviation from STRIVE values (q_z = -86.40 mm d^{-1}, D_T = 8.333 × 10^{-7} m^2 s^{-1})
σ = standard deviation, σ [%] = standard deviation in [%] of parameter value

Table A4.2: Estimates of average vertical fluxes and thermal diffusivities for consecutive finite streambed domains estimated with the LPMLE3 method using a frequency range from 1/520 d-1 to 1.5 d-1. Source: *own*.

Depth [cm]	q_z [mm d^{-1}]	D_T [m^2 s^{-1}] × 10^{-7}	q_z dev. [%]	D_T dev. [%]	σ_{qz} [mm d^{-1}] × 10^{-2}	σ_{DT} [m^2 s^{-1}] × 10^{-10}	σ_{qz} [%]	σ_{DT} [%]
10-20	-86.48	8.334	0.10	0.01	0.25	0.072	0.00	0.00
20-30	-86.43	8.334	0.04	0.00	0.41	0.156	0.00	0.00
30-40	-86.43	8.334	0.03	0.01	0.62	0.247	0.01	0.00
40-50	-86.41	8.334	0.01	0.00	0.94	0.408	0.01	0.00
50-60	-86.43	8.334	0.03	0.01	1.08	0.489	0.01	0.01
60-70	-86.40	8.332	0.00	0.01	1.62	0.763	0.02	0.01
70-80	-86.48	8.333	0.09	0.05	2.18	1.067	0.03	0.01

Depth = Interval size per sensor triplet, e.g. 10-20 = upper boundary at 10, lower boundary at 20 cm and third sensor at the mid-point, i.e. 15 cm.

q_z = vertical flux, D_T = thermal diffusivity, dev. = deviation from STRIVE values (q_z = -86.40 mm d^{-1}, D_T = 8.333 × 10^{-7} m^2 s^{-1})
σ = standard deviation, σ [%] = standard deviation in [%] of parameter value

Table A4.3: Estimates of average vertical fluxes and thermal diffusivities for sensor pairs obtained using the amplitude method after *Hatch et al.* [2006] as implemented in VFLUX version 1.2.3 [*Gordon et al.*, 2012]. Only the frequency of 1 d-1 was used. Source: *own.*

Depth [cm]	q_z [mm d^{-1}]	q_z dev. [%]
10 & 20	-84.18	2.56
20 & 30	-78.24	9.45
30 & 40	-89.23	3.27
40 & 50	-84.02	2.75
50 & 60	-76.66	11.27
60 & 70	-83.21	3.69
70 & 80	-87.39	1.15

Depth = depth of sensors
q_z = vertical flux
dev. = deviation from STRIVE values
(q_z = -86.40 mm d^{-1})

Appendix - Chapter 5

Table A5.1: Classification of the soil samples, sample length, sample depth below streambed top and elevation of each sample. The elevation of each sample was calculated by subtracting the sample depth from the elevation of the streambed top in May 2008 (middle piezometer). The sample depth was calculated by adding the sample length to the midpoint of the first sample.

See file: \PhD_Schneidewind\Thesis\Data\Chapter 5\chapter_5_supplement.xlsx

Table A5.2: Specific grain diameters, uniformity coefficients and porosity values for each core sample.

See file: \PhD_Schneidewind\Thesis\Data\Chapter 5\chapter_5_supplement.xlsx

Table A5.3: Shape factors, K_g and $\ln(K_g)$ values calculated using the models shown in Table 5.2.

See file: \PhD_Schneidewind\Thesis\Data\Chapter 5\chapter_5_supplement.xlsx

Table A5.4: Average, maximum and minimum K_g per transect for different grain size models. Source: *own.*

Transect	K(Beyer) [m/d]	K(USBR) [m/d]	K(Hazen) [m/d]	K(Kozeny) [m/d]
Average values				
A-A'	25.1	8.6	32.4	31.9
B-B'	30.7	11.5	45.0	39.2
C-C'	31.1	11.1	59.9	44.3
D-D'	30.3	10.3	45.7	43.1
E-E'	21.4	7.2	35.0	26.6
F-F'	25.0	9.6	38.6	32.2
G-G'	37.5	13.2	53.9	50.1
Maximum values				
A-A'	76.6	21.8	89.9	123.1
B-B'	91.0	49.6	106.1	143.2
C-C'	98.9	30.6	115.8	154.7
D-D'	65.5	20.3	76.7	103.1
E-E'	55.7	16.0	65.3	87.5
F-F'	90.7	26.0	106.3	144.9
G-G'	98.9	49.6	115.8	154.7
Minimum values				
A-A'	3.6	1.1	6.6	2.2
B-B'	3.2	1.2	9.4	1.5
C-C'	3.3	1.1	12.3	2.9
D-D'	3.3	1.1	12.3	2.5
E-E'	3.2	1.1	7.2	2.6
F-F'	3.6	1.1	12.0	2.2
G-G'	3.3	1.2	6.6	1.5

Table A5.5: Average, maximum and minimum K_g per location for the different grain size models. Source: *own.*

Location	K(Beyer) [m/d]	K(USBR) [m/d]	K(Hazen) [m/d]	K(Kozeny) [m/d]
Average values				
1	28.8	11.2	37.2	37.2
2	41.9	11.9	54.2	66.0
3	21.2	8.1	43.7	28.5
4	20.6	5.2	21.4	21.0
5	24.2	8.8	44.4	33.9
6	19.7	7.5	43.7	25.5
7	26.2	10.0	32.8	32.3
8	19.0	8.3	26.6	20.7
9	30.1	10.1	57.3	43.6
10	24.9	8.2	35.0	35.8
11	39.1	16.3	53.1	43.0
12	51.8	17.2	80.4	76.7
Maximum values				
1	41.2	15.3	48.3	66.5
2	51.8	18.0	60.7	83.5
3	65.5	20.3	76.7	103.1
4	43.9	8.6	29.9	39.3
5	47.9	14.0	56.2	79.0
6	55.7	16.0	65.3	87.5
7	48.0	21.0	52.0	59.9
8	40.6	14.0	38.3	50.1
9	90.7	26.0	106.3	144.9
10	76.6	21.8	89.9	123.1
11	91.0	49.6	106.1	143.2
12	98.9	30.6	115.8	154.7
Minimum values				
1	4.6	8.1	24.7	2.5
2	6.6	4.6	41.3	6.1
3	3.3	1.1	12.3	2.9
4	4.4	1.1	7.2	5.2
5	3.2	1.6	21.0	2.6
6	4.2	1.2	15.0	4.7
7	3.6	4.9	12.0	2.2
8	3.7	4.6	15.6	2.5
9	4.4	1.1	12.6	5.4
10	3.9	1.9	6.6	3.3
11	3.3	1.2	9.4	1.5
12	4.6	1.4	32.7	4.1

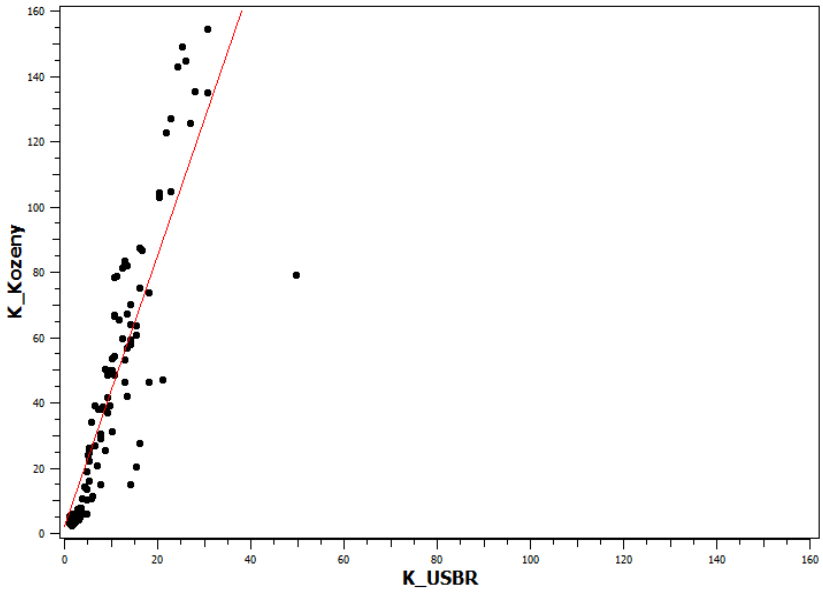

Figure A5.1: Scatter plot correlating K_g values obtained after Kozeny-Köhler with those obtained after USBR. The red line indicates the linear regression line. Source: *own.*

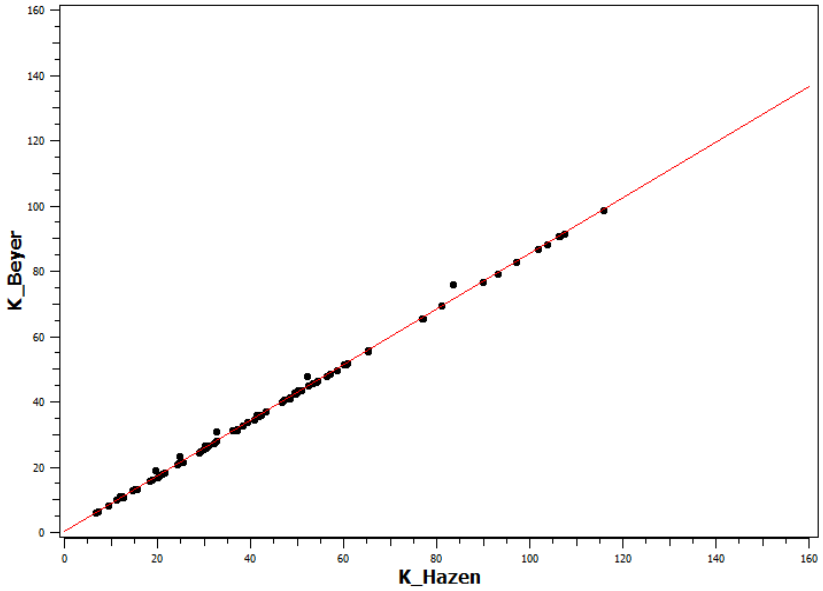

Figure A5.2: Scatter plot correlating K_g values obtained after Beyer with those obtained after Hazen. The red line indicates the linear regression line. Source: *own.*

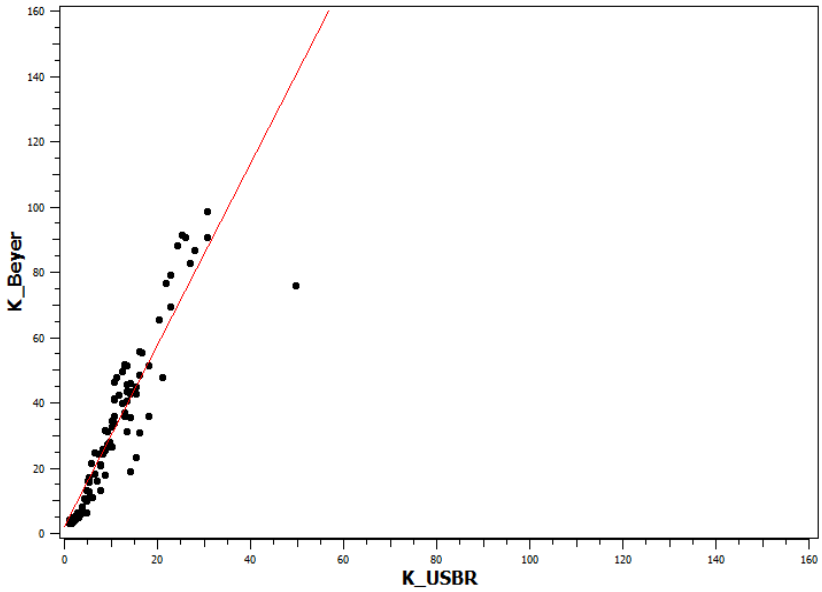

Figure A5.3: Scatter plot correlating K_g values obtained after Beyer with those obtained after USBR. The red line indicates the linear regression line. Source: *own.*

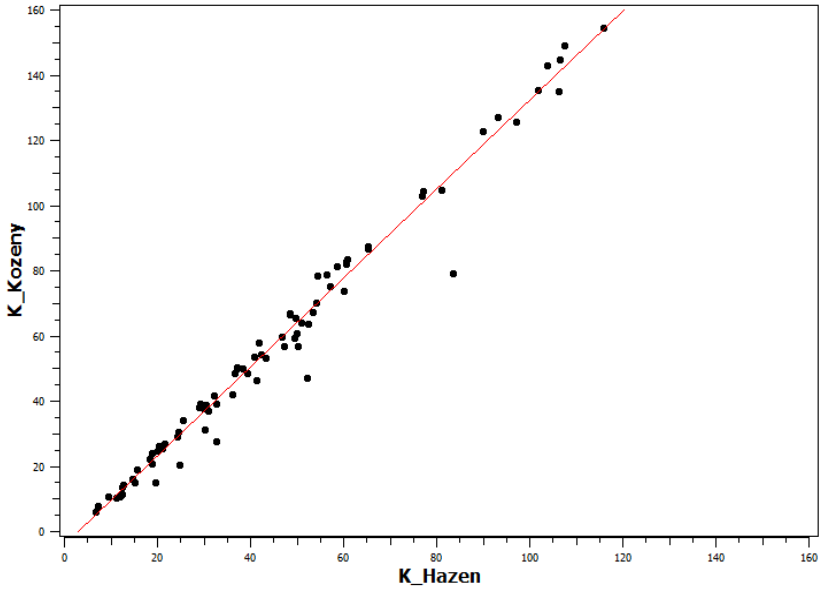

Figure A5.4: Scatter plot correlating K_g values obtained after Kozeny-Köhler with those obtained after Hazen. The red line indicates the linear regression line. Source: *own.*

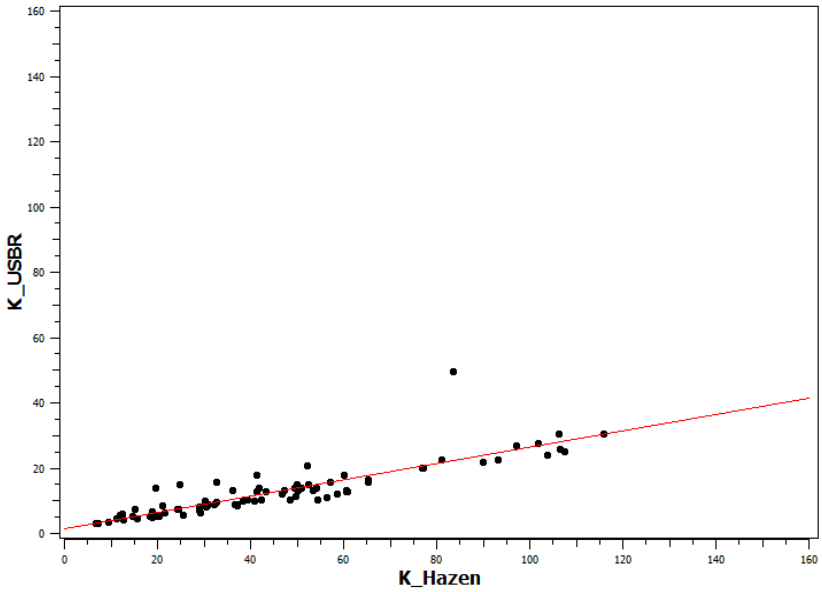

Figure A5.5: Scatter plot correlating K_g values obtained after USBR with those obtained after Hazen. The red line indicates the linear regression line. Source: *own.*

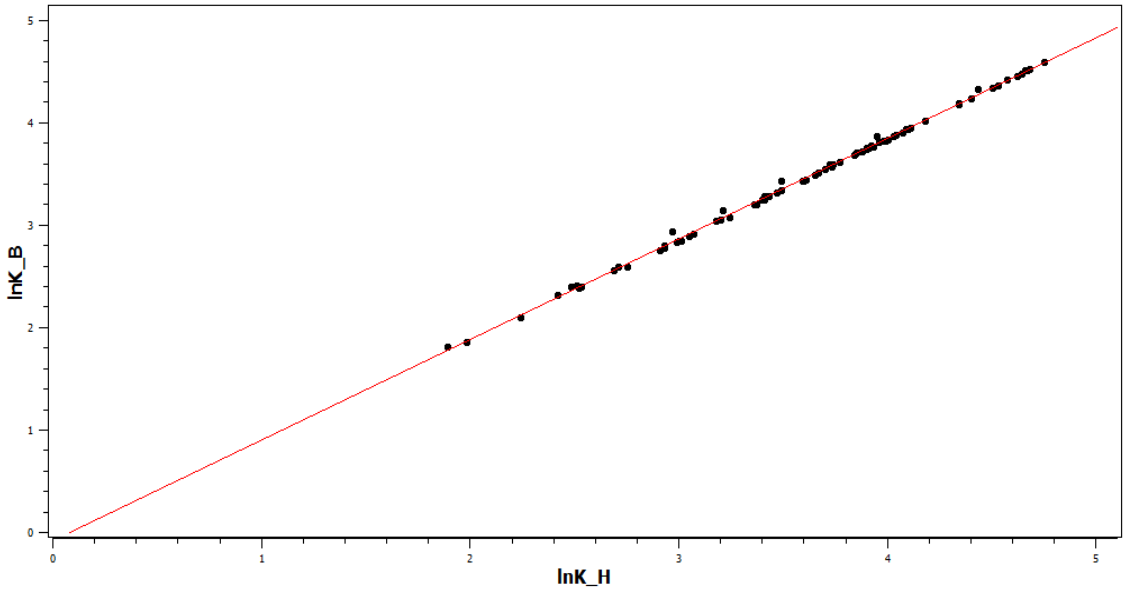

Figure A5.6: Scatter plot correlating ln (K_g) values obtained after Beyer with those obtained after Hazen. The red line indicates the linear regression line. Source: *own.*

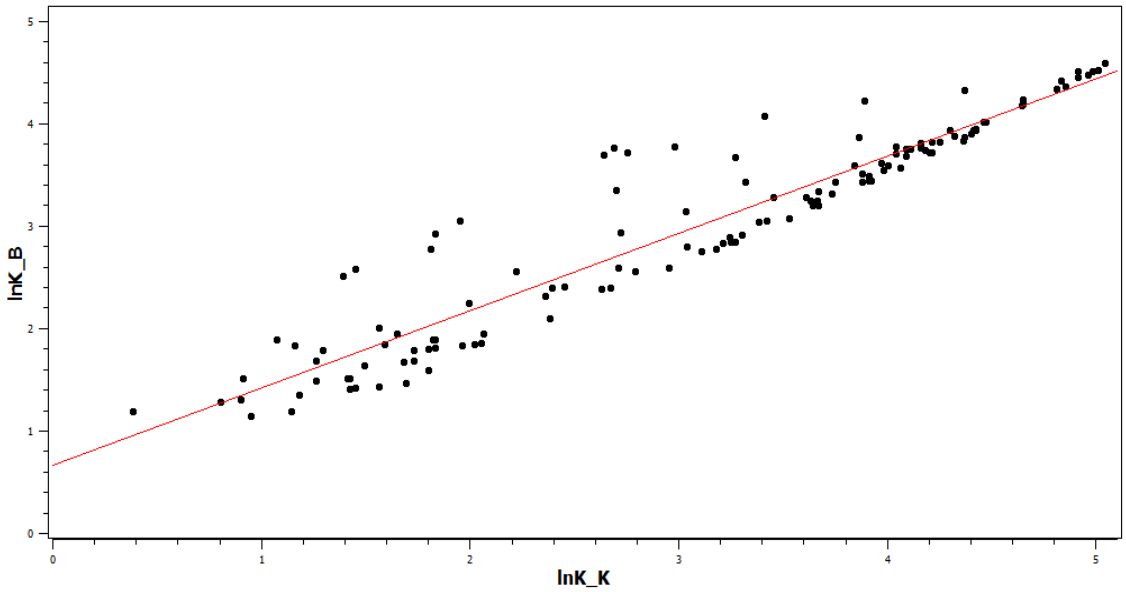

Figure A5.7: Scatter plot correlating ln (K_g) values obtained after Beyer with those obtained after Kozeny-Köhler. The red line indicates the linear regression line. Source: *own.*

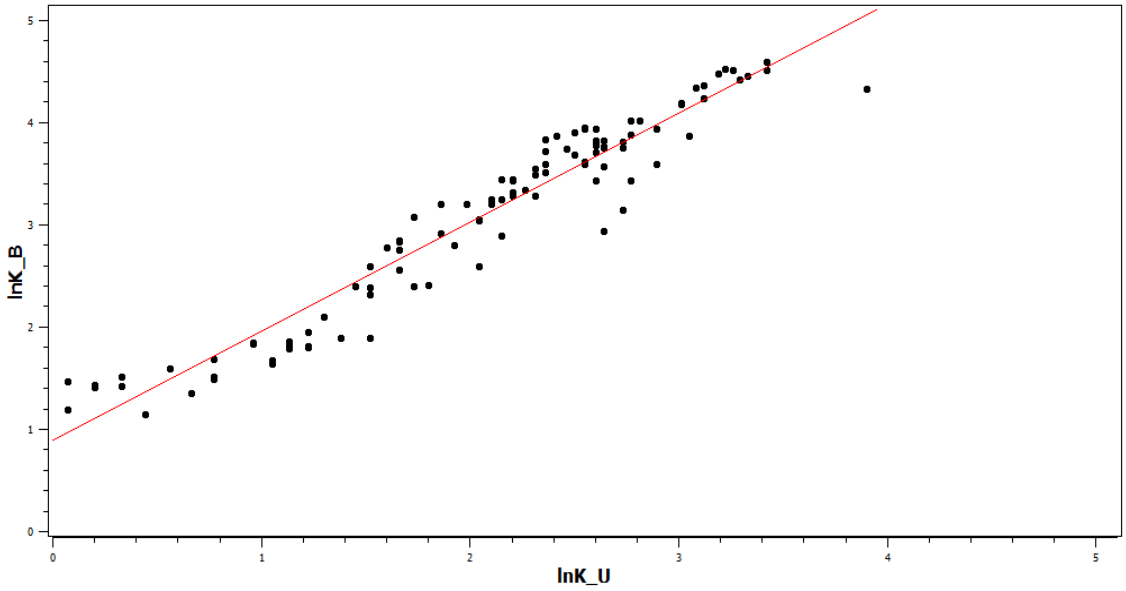

Figure A5.8: Scatter plot correlating ln (K_g) values obtained after Beyer with those obtained after USBR. The red line indicates the linear regression line. Source: *own.*

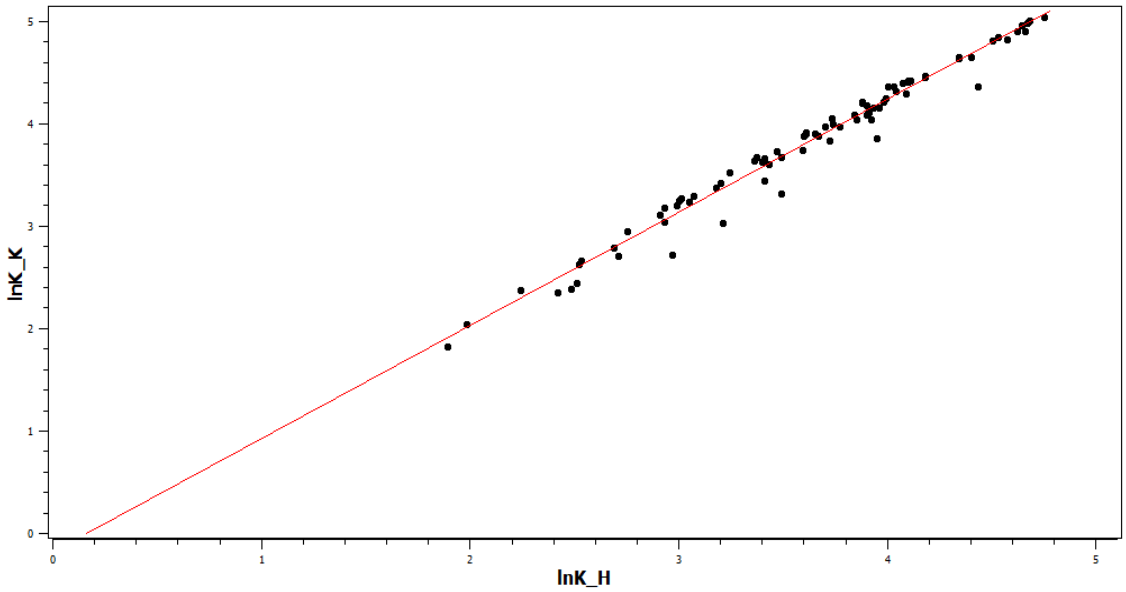

Figure A5.9: Scatter plot correlating ln (K_g) values obtained after Kozeny-Köhler with those obtained after Hazen. The red line indicates the linear regression line. Source: *own.*

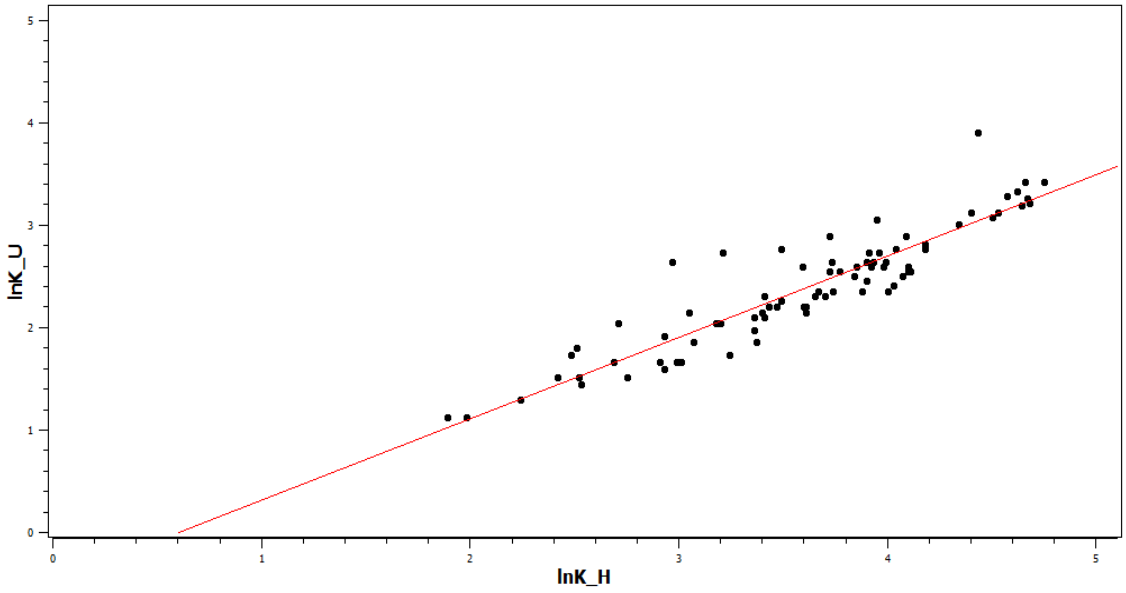

Figure A5.10: Scatter plot correlating ln (K_g) values obtained after USBR with those obtained after Hazen. The red line indicates the linear regression line. Source: *own.*

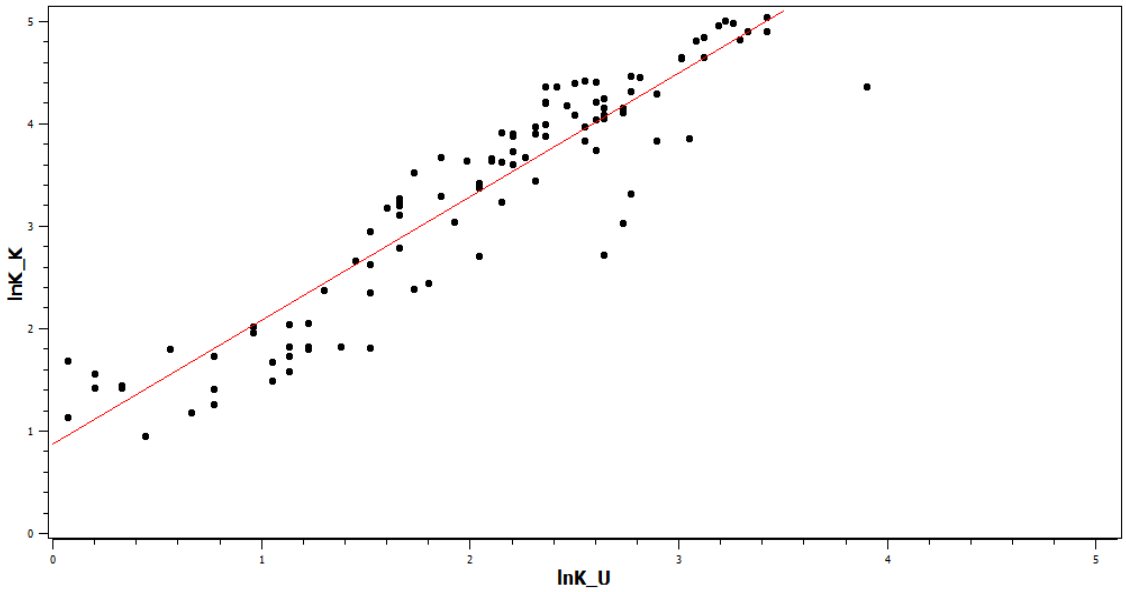

Figure A5.11: Scatter plot correlating ln (K_g) values obtained after Kozeny-Köhler with those obtained after USBR. The red line indicates the linear regression line. Source: *own.*

References

Abe, Y., R. Aravena, J. Zopfi, B. Parker, and D. Hunkeler (2009), Evaluating the fate of chlorinated ethenes in streambed sediments by combining stable isotope, geochemical and microbial methods, *J Contam Hydrol*, *107*(1-2), 10-21, doi: 10.1016/j.jconhyd.2009.03.002.

Acworth, R. I., and G. R. Dasey (2003), Mapping of the hyporheic zone around a tidal creek using a combination of borehole logging, borehole electrical tomography and cross-creek electrical imaging, New South Wales, Australia, *Hydrogeology Journal*, *11*(3), 368-377, doi: 10.1007/s10040-003-0258-4.

Adamson, D. T., and G. F. Parkin (2000), Impact of Mixtures of Chlorinated Aliphatic Hydrocarbons on a High-Rate, Tetrachloroethene-Dechlorinating Enrichment Culture, *Environ. Sci. Technol.*, *34*(10), 1959-1965, doi: 10.1021/es990809f.

Aeppli, C., T. B. Hofstetter, H. I. Amaral, R. Kipfer, R. P. Schwarzenbach, and M. Berg (2010), Quantifying in situ transformation rates of chlorinated ethenes by combining compound-specific stable isotope analysis, groundwater dating, and carbon isotope mass balances, *Environ Sci Technol*, *44*(10), 3705-3711, doi: 10.1021/es903895b.

Alexander, M. (1994), *Biodegradation and Bioremediation*, 302 pp., Academic Press, San Diego, CA.

Alexander, M. D., and D. Caissie (2003), Variability and comparison of hyporheic water temperatures and seepage fluxes in a small Atlantic salmon stream, *Ground Water*, *41*(1), 72-82.

Allen, D. J., W. G. Darling, D. C. Gooddy, D. J. Lapworth, A. J. Newell, A. T. Williams, D. Allen, and C. Abesser (2010), Interaction between groundwater, the hyporheic zone and a Chalk stream: a case study from the River Lambourn, UK, *Hydrogeology Journal*, *18*(5), 1125-1141, doi: 10.1007/s10040-010-0592-2.

Andersen, M. S., and R. I. Acworth (2009), Stream-aquifer interactions in the Maules Creek catchment, Namoi Valley, New South Wales, Australia, *Hydrogeology Journal*, *17*(8), 2005-2021, doi: 10.1007/s10040-009-0500-9.

Anderson, M. P. (2005), Heat as a ground water tracer, *Ground Water*, *43*(6), 951-968, doi: 10.1111/j.1745-6584.2005.00052.x.

Angermann, L., S. Krause, and J. Lewandowski (2012a), Application of heat pulse injections for investigating shallow hyporheic flow in a lowland river, *Water Resour. Res.*, *48*(12), W00P02, doi: 10.1029/2012wr012564.

Angermann, L., J. Lewandowski, J. H. Fleckenstein, and G. Nutzmann (2012b), A 3D analysis algorithm to improve interpretation of heat pulse sensor results for the determination of small-scale flow directions and velocities in the hyporheic zone, *J. Hydrol.*, *475*, 1-11, doi: 10.1016/j.jhydrol.2012.06.050.

Anibas, C., K. Buis, R. Verhoeven, P. Meire, and O. Batelaan (2011), A simple thermal mapping method for seasonal spatial patterns of groundwater–surface water interaction, *J. Hydrol.*, *397*(1-2), 93-104.

Anibas, C., U. Schneidewind, G. Vandersteen, I. Joris, P. Seuntjens, and O. Batelaan (2016), From streambed temperature measurements to spatial-temporal flux quantification: Using the LPML method to study groundwater-surface water interaction, *Hydrol. Process.*, *30*, 203-216, doi: 10.1002/hyp.10588.

Anibas, C., J. H. Fleckenstein, N. Volze, K. Buis, R. Verhoeven, P. Meire, and O. Batelaan (2009), Transient or steady-state? Using vertical temperature profiles to quantify groundwater-surface water exchange, *Hydrol. Process.*, *23*(15), 2165-2177, doi: 10.1002/Hyp.7289.

Anibas, C., B. Verbeiren, K. Buis, J. Chormanski, L. De Doncker, T. Okruszko, P. Meire, and O. Batelaan (2012), A hierarchical approach on groundwater-surface water interaction in wetlands along the upper Biebrza River, Poland, *Hydrology and Earth System Sciences*, *16*(7), 2329-2346, doi: 10.5194/hess-16-2329-2012.

Atashgahi, S., F. Maphosa, E. Dogan, H. Smidt, D. Springael, and W. Dejonghe (2013), Small-scale oxygen distribution determines the vinyl chloride biodegradation pathway in surficial sediments of riverbed hyporheic zones, *FEMS Microbiol Ecol*, *84*(1), 133-142, doi: 10.1111/1574-6941.12044.

Atashgahi, S., F. Maphosa, J. De Vrieze, P. J. Haest, N. Boon, H. Smidt, D. Springael, and W. Dejonghe (2014), Evaluation of solid polymeric organic materials for use in bioreactive sediment capping to stimulate the

degradation of chlorinated aliphatic hydrocarbons, *Appl Microbiol Biotechnol*, *98*(5), 2255-2266, doi: 10.1007/s00253-013-5138-9.

Aulenta, F., J. M. Gossett, M. P. Papini, S. Rossetti, and M. Majone (2005a), Comparative study of methanol, butyrate, and hydrogen as electron donors for long-term dechlorination of tetrachloroethene in mixed anerobic cultures, *Biotechnology and Bioengineering*, *91*(6), 743-753, doi: 10.1002/bit.20569.

Aulenta, F., A. Bianchi, M. Majone, M. Petrangeli Papini, M. Potalivo, and V. Tandoi (2005b), Assessment of natural or enhanced in situ bioremediation at a chlorinated solvent-contaminated aquifer in Italy: A microcosm study, *Environ. Int.*, *31*(2), 185-190, doi: 10.1016/j.envint.2004.09.014.

Azadpour-Keeley, A., H. H. Russel, and G. W. Sewell (1999), Microbial Processes Affecting Monitored Natural Attenuation of Contaminants in the Subsurface, 18 pp, EPA, Washington, DC.

Badin, A., G. Buttet, J. Maillard, C. Holliger, and D. Hunkeler (2014), Multiple Dual C-Cl Isotope Patterns Associated with Reductive Dechlorination of Tetrachloroethene, *Environ. Sci. Technol.*, *48*(16), 9179-9186, doi: 10.1021/es500822d.

Bakker, E., and M. Telting-Diaz (2002), Electrochemical sensors, *Anal Chem*, *74*(12), 2781-2800, doi: 10.1021/ac0202278.

Banzhaf, S., and T. Scheytt (2009), Effect of an artificial flood wave on the adjacent groundwater aquifer, *Grundwasser*, *14*(4), 265-275, doi: 10.1007/s00767-009-0109-x.

Bardini, L., F. Boano, M. B. Cardenas, R. Revelli, and L. Ridolfi (2012), Nutrient cycling in bedform induced hyporheic zones, *Geochimica Et Cosmochimica Acta*, *84*, 47-61, doi: 10.1016/j.gca.2012.01.025.

Bardini, L., F. Boano, M. B. Cardenas, A. H. Sawyer, R. Revelli, and L. Ridolfi (2013), Small-scale permeability heterogeneity has negligible effects on nutrient cycling in streambeds, *Geophysical Research Letters*, *40*(6), 1118-1122, doi: 10.1002/Grl.50224.

Barlow, J. R. B., and R. H. Coupe (2009), Use of heat to estimate streambed fluxes during extreme hydrologic events, *Water Resour. Res.*, *45*(1), W01403, doi: 10.1029/2007wr006121.

Barr, D. W. (2001), Turbulent flow through porous media, *Ground Water*, *39*(5), 646-650, doi: 10.1111/j.1745-6584.2001.tb02353.x.

Bartolino, J. R., and R. Niswonger (1999), Numerical simulations of vertical ground-water fluxes of the Rio Grande from ground-water temperature profiles, central New Mexico, *Water Resour. Invest. Rep. 99-4212*, 34 pp, U.S. Geological Survey.

Bartsch, S., S. Frei, M. Ruidisch, C. L. Shope, S. Peiffer, B. Kim, and J. H. Fleckenstein (2014), River-aquifer exchange fluxes under monsoonal climate conditions, *J. Hydrol.*, *509*, 601-614, doi: 10.1016/j.jhydrol.2013.12.005.

Battin, T. J., and D. Sengschmitt (1999), Linking Sediment Biofilms, Hydrodynamics, and River Bed Clogging: Evidence from a Large River, *Microbial ecology*, *37*(3), 185-196, doi: 10.1007/s002489900142.

Battin, T. J., L. A. Kaplan, J. Denis Newbold, and C. M. Hansen (2003), Contributions of microbial biofilms to ecosystem processes in stream mesocosms, *Nature*, *426*(6965), 439-442, doi: 10.1038/nature02152.

Bauer, S., M. Bayer-Raich, T. Holder, C. Kolesar, D. Muller, and T. Ptak (2004), Quantification of groundwater contamination in an urban area using integral pumping tests, *J Contam Hydrol*, *75*(3-4), 183-213, doi: 10.1016/j.jconhyd.2004.06.002.

Bear, J., and A. Cheng (2010), *Modeling Groundwater Flow and Contaminant Transport*, 834 pp., Springer, Dordrecht.

Bencala, K. E. (1993), A Perspective on Stream-Catchment Connections, *Journal of the North American Benthological Society*, *12*(1), 44-47, doi: 10.2307/1467684.

Bencala, K. E., and R. A. Walters (1983), Simulation of solute transport in a mountain pool-and-riffle stream: A transient storage model, *Water Resour. Res.*, *19*(3), 718-724, doi: 10.1029/WR019i003p00718.

Bencala, K. E., M. N. Gooseff, and B. A. Kimball (2011), Rethinking hyporheic flow and transient storage to advance understanding of stream-catchment connections, *Water Resour. Res.*, *47*, doi: 10.1029/2010wr010066.

Berryman, C. J. (2005), Tracer tests for investigating flow and transport in the hyporheic zone, *Science Report SC030155/8*, 41 pp, Environment Agency, Bristol.

Beven, K. (2001), How far can we go in distributed hydrological modelling?, *Hydrol. Earth Syst. Sci.*, *5*(1), 1-12.

Beven, K., and A. Binley (1992), The Future of Distributed Models - Model Calibration and Uncertainty Prediction, *Hydrol. Process.*, *6*(3), 279-298, doi: 10.1002/hyp.3360060305.

Beven, K., and P. Germann (2013), Macropores and water flow in soils revisited, *Water Resour. Res.*, *49*(6), 3071-3092, doi: 10.1002/Wrcr.20156.

Beven, K. J. (2000), Uniqueness of place and process representations in hydrological modelling, *Hydrology and Earth System Sciences*, *4*(2), 203-213.

Beyer, W. (1964), Zur Bestimmung der Wasserdurchlässigkeit von Kiesen und Sanden aus der Kornverteilung, *Wasserwirtschaft-Wassertechnik (WWT)*, *14*, 165-168.

Bianchin, M., L. Smith, and R. Beckie (2010), Quantifying hyporheic exchange in a tidal river using temperature time series, *Water Resour. Res.*, *46*, doi: 10.1029/2009wr008365.

Blenkinsopp, S. A., and M. A. Lock (1994), The Impact of Storm-Flow on River Biofilm Architecture, *Journal of Phycology*, *30*(5), 807-818, doi: 10.1111/j.0022-3646.1994.00807.x.

Blöschl, G. (2001), Scaling in hydrology, *Hydrol. Process.*, *15*(4), 709-711, doi: 10.1002/hyp.432.

Boano, F., R. Revelli, and L. Ridolfi (2007), Bedform-induced hyporheic exchange with unsteady flows, *Adv. Water Resour.*, *30*(1), 148-156, doi: 10.1016/j.advwatres.2006.03.004.

Boano, F., C. Camporeale, and R. Revelli (2010), A linear model for the coupled surface-subsurface flow in a meandering stream, *Water Resour. Res.*, *46*, doi: 10.1029/2009wr008317.

Boano, F., C. Camporeale, R. Revelli, and L. Ridolfi (2006), Sinuosity-driven hyporheic exchange in meandering rivers, *Geophysical Research Letters*, *33*(18), doi: 10.1029/2006gl027630.

Boano, F., J. W. Harvey, A. Marion, A. I. Packman, R. Revelli, L. Ridolfi, and A. Wörman (2014), Hyporheic flow and transport processes: Mechanisms, models, and biogeochemical implications, *Reviews of Geophysics*, *52*(4), 2012RG000417, doi: 10.1002/2012rg000417.

Böhlke, J. K., J. W. Harvey, and M. A. Voytek (2004), Reach-scale isotope tracer experiment to quantify denitrification and related processes in a nitrate-rich stream, midcontinent United States, *Limnology and Oceanography*, *49*(3), 821-838, doi: 10.4319/lo.2004.49.3.0821.

Bons, P. D., B. P. van Milligen, and P. Blum (2013), A general unified expression for solute and heat dispersion in homogeneous porous media, *Water Resour. Res.*, *49*(10), 6166-6178, doi: 10.1002/Wrcr.20488.

Botula, Y.-D., W. M. Cornelis, G. Baert, P. Mafuka, and E. Van Ranst (2013), Particle size distribution models for soils of the humid tropics, *J Soils Sediments*, *13*, 686-698, doi: 10.1007/s11368-012-0635-5.

Boulton, A. J., S. Findlay, P. Marmonier, E. H. Stanley, and H. M. Valett (1998), The functional significance of the hyporheic zone in streams and rivers, *Annual Review of Ecology and Systematics*, *29*, 59-81, doi: 10.1146/annurev.ecolsys.29.1.59.

Boulton, A. J., T. Datry, T. Kasahara, M. Mutz, and J. A. Stanford (2010), Ecology and management of the hyporheic zone: stream-groundwater interactions of running waters and their floodplains, *Journal of the North American Benthological Society*, *29*(1), 26-40, doi: 10.1899/08-017.1.

Bourg, A. C. M., C. Mouvet, and D. N. Lerner (1992), A Review of the Attenuation of Trichloroethylene in Soils and Aquifers, *Quarterly Journal of Engineering Geology*, *25*(4), 359-370, doi: 10.1144/Gsl.Qjeg.1992.025.04.10.

Bouwer, E. J. (1994), Bioremediation of chlorinated solvents using alternate electron acceptors, in *Hanbook of Bioremediation*, edited by R. D. Norris, R. E. Hinchee, R. Brown, P. L. McCarty, L. Semprini, J. T. Wilson, D. H. Kampbell, M. Reinhard, E. J. Bouwer, R. C. Borden, T. M. Vogel, J. M. Thomas and C. H. Ward, pp. 149-175, Lewis Publishers, Boca Raton, FL.

Bouwer, E. J., B. E. Rittmann, and P. L. McCarty (1981), Anaerobic degradation of halogenated 1- and 2-carbon organic compounds, *Environ Sci Technol*, *15*(5), 596-599, doi: 10.1021/es00087a012.

Bower, H., and R. C. Rice (1976), A slug test method for determining hydraulic conductivity of unconfined aquifers with completely or partially penetrating wells, *Water Resour. Res.*, *12*(3), 423-428.

Bradley, P. M., and F. H. Chapelle (1998), Micobial mineralization of VC and DCE under different terminal electron accepting conditions, *Anaerobe*, *4*, 81-87.

Bravo, H. R., F. Jiang, and R. J. Hunt (2002), Using groundwater temperature data to constrain parameter estimation in a groundwater flow model of a wetland system, *Water Resour. Res.*, *38*(8), doi: 10.1029/2000wr000172.

Bredehoeft, J. D., and I. S. Papadopulos (1965), Rates of vertical ground-water movement estimated from the Earth's thermal profile, *Water Resour. Res.*, *1*(2), 325-328.

Bridge, J. W. (2005), High resolution in-situ monitoring of hyporheic zone biogeochemistry, *Science Report SC030155/SR3*, 51 pp, Environment Agency, Bristol.

Briggs, M. A., L. K. Lautz, and D. K. Hare (2014), Residence time control on hot moments of net nitrate production and uptake in the hyporheic zone, *Hydrol. Process.*, *28*(11), 3741-3751, doi: 10.1002/Hyp.9921.

Briggs, M. A., L. K. Lautz, D. K. Hare, and R. González-Pinzón (2013), Relating hyporheic fluxes, residence times, and redox-sensitive biogeochemical processes upstream of beaver dams, *Freshwater Science*, *32*(2), 622-641, doi: 10.1899/12-110.1.

Briggs, M. A., L. K. Lautz, J. M. McKenzie, R. P. Gordon, and D. K. Hare (2012), Using high-resolution distributed temperature sensing to quantify spatial and temporal variability in vertical hyporheic flux, *Water Resour. Res.*, *48*, doi: 10.1029/2011wr011227.

Bronders, J., K. Touchant, I. Van der Keer, J. Patyn, and J. Provoost (2007), The characterization of contamination and the role of hydrogeology in the risk management of a mega Brownfield site., paper presented at IAH XXXV congress - Groundwater and ecosystems, Lisbon.

Brosten, T. R., J. H. Bradford, J. P. McNamara, M. N. Gooseff, J. P. Zarnetske, W. B. Bowden, and M. E. Johnston (2009), Multi-offset GPR methods for hyporheic zone investigations, *Near Surface Geophysics*, *7*(4), 247-257.

Brunke, M., and T. Gonser (1997), The ecological significance of exchange processes between rivers and groundwater, *Freshwater Biology*, *37*(1), 1-33, doi: 10.1046/j.1365-2427.1997.00143.x.

Brunner, P., P. G. Cook, and C. T. Simmons (2009), Hydrogeologic controls on disconnection between surface water and groundwater, *Water Resour. Res.*, *45*, doi: 10.1029/2008wr006953.

Brunner, P., C. T. Simmons, P. G. Cook, and R. Therrien (2010), Modeling Surface Water-Groundwater Interaction with MODFLOW: Some Considerations, *Ground Water*, *48*(2), 174-180, doi: 10.1111/j.1745-6584.2009.00644.x.

Buhmann, M. D. (2009), *Radial Basis Functions: Theory and Implementations*, 272 pp., Cambridge University Press.

Bukaveckas, P. A. (2007), Effects of channel restoration on water velocity, transient storage, and nutrient uptake in a channelized stream, *Environ Sci Technol*, *41*(5), 1570-1576, doi: 10.1021/es061618x.

Buss, S. R., M. O. Rivett, P. Morgan, and C. D. Bemment (2005), Attenuation of nitrate in the subsurface environment, *Science Report SC030155/SR2*, 108 pp, Environment Agency, Bristol.

Buss, S. R., Z. Cai, M. B. Cardenas, J. H. Fleckenstein, D. M. Hannah, K. Heppell, P. J. Hulme, T. Ibrahim, D. Kaeser, S. Krause, D. M. Lawler, D. N. Lerner, J. Mant, I. A. Malcolm, G. Old, G. Parkin, R. J. Pickup, G. Pinay, J. Porter, G. Rhodes, A. Richie, J. Riley, A. Robertson, D. Sear, B. Shields, J. W. S. Smith, J. H. Tellam, and P. Wood (2009), The Hyporheic Handbook - A handbook on the groundwater-surface water interface and hyporheic zone for environmental managers, *Science Report SC50070*, 280 pp, Environment Agency, Bristol.

Butler, E. C., and K. F. Hayes (1999), Kinetics of the transformation of trichloroethylene and tetrachloroethylene by iron sulfide, *Environ. Sci. Technol.*, *33*(12), 2021-2027, doi: 10.1021/Es9809455.

Butler, J. J. (1998), *The Design, Performance, and Analysis of Slug Tests*, 252 pp., Lewis Publishers, Boca Raton.

Butler, J. J., Jr. (2002), A simple correction for slug tests in small-diameter wells, *Ground Water*, *40*(3), 303-307, doi: 10.1111/j.1745-6584.2002.tb02658.x.

Butler, J. J., Jr., E. J. Garnett, and J. M. Healey (2003), Analysis of slug tests in formations of high hydraulic conductivity, *Ground Water*, *41*(5), 620-630, doi: 10.1111/j.1745-6584.2003.tb02400.x.

Cable, J. E., W. C. Burnett, J. P. Chanton, D. R. Corbett, and P. H. Cable (1997), Field evaluation of seepage meters in the coastal marine environment, *Estuarine Coastal and Shelf Science*, *45*(3), 367-375, doi: 10.1006/ecss.1996.0191.

Caers, J. (2011), *Modeling Uncertainty in the Earth Sciences*, 229 pp., Wiley-Blackwell, Chichester.

Calver, A. (2001), Riverbed permeabilities: information from pooled data, *Ground Water*, *39*(4), 546-553.

Cardenas, M. B. (2008a), The effect of river bend morphology on flow and timescales of surface water-groundwater exchange across pointbars, *J. Hydrol.*, *362*(1-2), 134-141, doi: 10.1016/j.jhydrol.2008.08.018.

Cardenas, M. B. (2008b), Surface water-groundwater interface geomorphology leads to scaling of residence times, *Geophysical Research Letters*, *35*(8), doi: 10.1029/2008gl033753.

Cardenas, M. B. (2010), Thermal skin effect of pipes in streambeds and its implications on groundwater flux estimation using diurnal temperature signals, *Water Resour. Res.*, *46*(3), W03536, doi: 10.1029/2009wr008528.

Cardenas, M. B., and V. A. Zlotnik (2003a), Three-dimensional model of modern channel bend deposits, *Water Resour. Res.*, *39*(6), 12, doi: 10.1029/2002wr001383.

Cardenas, M. B., and V. A. Zlotnik (2003b), A simple constant-head injection test for streambed hydraulic conductivity estimation, *Ground Water*, *41*(6), 867-871.

Cardenas, M. B., and J. L. Wilson (2006), The influence of ambient groundwater discharge on exchange zones induced by current-bedform interactions, *J. Hydrol.*, *331*(1-2), 103-109, doi: 10.1016/j.jhydrol.2006.05.012.

Cardenas, M. B., and J. L. Wilson (2007a), Hydrodynamics of coupled flow above and below a sediment-water interface with triangular bedforms, *Adv. Water Resour.*, *30*(3), 301-313, doi: 10.1016/j.advwatres.2006.06.009.

Cardenas, M. B., and J. L. Wilson (2007b), Effects of current-bed form induced fluid flow on the thermal regime of sediments, *Water Resour. Res.*, *43*(8), n/a-n/a, doi: 10.1029/2006wr005343.

Cardenas, M. B., and M. S. Markowski (2011), Geoelectrical imaging of hyporheic exchange and mixing of river water and groundwater in a large regulated river, *Environ Sci Technol*, *45*(4), 1407-1411, doi: 10.1021/es103438a.

Cardenas, M. B., J. L. Wilson, and V. A. Zlotnik (2004), Impact of heterogeneity, bed forms, and stream curvature on subchannel hyporheic exchange, *Water Resour. Res.*, *40*(8), doi: 10.1029/2004wr003008.

Cardenas, M. B., J. L. Wilson, and R. Haggerty (2008), Residence time of bedform-driven hyporheic exchange, *Adv. Water Resour.*, *31*(10), 1382-1386, doi: 10.1016/j.advwatres.2008.07.006.

Carrera, J., and S. P. Neuman (1986), Estimation of Aquifer Parameters under Transient and Steady-State Conditions .2. Uniqueness, Stability, and Solution Algorithms, *Water Resour. Res.*, *22*(2), 211-227, doi: 10.1029/Wr022i002p00211.

Chambon, J. C., P. L. Bjerg, C. Scheutz, J. Baelum, R. Jakobsen, and P. J. Binning (2013), Review of reactive kinetic models describing reductive dechlorination of chlorinated ethenes in soil and groundwater, *Biotechnol Bioeng*, *110*(1), 1-23, doi: 10.1002/bit.24714.

Chang, H. L., and L. Alvarez-Cohen (1996), Biodegradation of individual and multiple chlorinated aliphatic hydrocarbons by methane-oxidizing cultures, *Appl Environ Microbiol*, *62*(9), 3371-3377.

Chapelle, F. H., and P. M. Bradley (1998), Selecting remediation goals by assessing the natural attenuation capacity of groundwater systems, *Bioremediation Journal*, *2*(3-4), 227-238, doi: 10.1080/10889869809380381.

Chapman, S. W., B. L. Parker, J. A. Cherry, R. Aravena, and D. Hunkeler (2007), Groundwater-surface water interaction and its role on TCE groundwater plume attenuation, *J Contam Hydrol*, *91*(3-4), 203-232, doi: 10.1016/j.jconhyd.2006.10.006.

Chen, X., W. Dong, G. Ou, Z. Wang, and C. Liu (2013), Gaining and losing stream reaches have opposite hydraulic conductivity distribution patterns, *Hydrology and Earth System Sciences*, *17*(7), 2569-2579, doi: 10.5194/hess-17-2569-2013.

Chen, X. H. (2000), Measurement of streambed hydraulic conductivity and its anisotropy, *Environ. Geol.*, *39*(12), 1317-1324.

Cheng, C., J. X. Song, X. H. Chen, and D. M. Wang (2011), Statistical Distribution of Streambed Vertical Hydraulic Conductivity along the Platte River, Nebraska, *Water Resources Management*, *25*(1), 265-285, doi: 10.1007/s11269-010-9698-5.

Chiles, J. P., and P. Delfiner (2012), *Geostatistics: modeling spatial uncertainty*, 2nd ed., 734 pp., John Wiley and Sons, Hoboken, NJ.

Claret, C., and A. J. Boulton (2009), Integrating hydraulic conductivity with biogeochemical gradients and microbial activity along river-groundwater exchange zones in a subtropical stream, *Hydrogeology Journal*, *17*(1), 151-160, doi: 10.1007/s10040-008-0373-3.

Clement, T. P. (1997), RT3D - A Modular Computer Code for Simulating Reactive Multi-Species Transport in 3-Dimensional Groundwater Aquifers, 59 pp, Pacific Northwest National Laboratory, Richland, WA.

Clement, T. P. (2011), Complexities in hindcasting models-when should we say enough is enough?, *Ground Water*, *49*(5), 620-629, doi: 10.1111/j.1745-6584.2010.00765.x.

Coleman, N. V., T. E. Mattes, J. M. Gossett, and J. C. Spain (2002a), Biodegradation of cis-dichloroethene as the sole carbon source by a beta-proteobacterium, *Applied and Environmental Microbiology*, *68*(6), 2726-2730, doi: 10.1128/Aem.68.6.2726-2730.2002.

Coleman, N. V., T. E. Mattes, J. M. Gossett, and J. C. Spain (2002b), Phylogenetic and kinetic diversity of aerobic vinyl chloride-assimilating bacteria from contaminated sites, *Appl Environ Microbiol*, *68*(12), 6162-6171.

COMSOL-AB (2008), COMSOL Multiphysics Modeling Guide, 518 pp.

Conant, B., Jr. (2004), Delineating and quantifying ground water discharge zones using streambed temperatures, *Ground Water*, *42*(2), 243-257, doi: 10.1111/j.1745-6584.2004.tb02671.x.

Conant, B., Jr., J. A. Cherry, and R. W. Gillham (2004), A PCE groundwater plume discharging to a river: influence of the streambed and near-river zone on contaminant distributions, *J Contam Hydrol*, *73*(1-4), 249-279, doi: 10.1016/j.jconhyd.2004.04.001.

Constantz, J. (2008), Heat as a tracer to determine streambed water exchanges, *Water Resour. Res.*, *44*, doi: 10.1029/2008wr006996.

Constantz, J., D. Stonestrom, A. E. Stewart, R. Niswonger, and T. R. Smith (2001), Analysis of streambed temperatures in ephemeral channels to determine streamflow frequency and duration, *Water Resour. Res.*, *37*(2), 317-328, doi: 10.1029/2000wr900271.

Cote, J., and J. M. Konrad (2005), A generalized thermal conductivity model for soils and construction materials, *Can. Geotech. J.*, *42*(2), 443-458, doi: 10.1139/T04-106.

Côté, J., and J.-M. Konrad (2009), Assessment of structure effects on the thermal conductivity of two-phase porous geomaterials, *International Journal of Heat and Mass Transfer*, *52*(3–4), 796-804, doi: 10.1016/j.ijheatmasstransfer.2008.07.037.

Cox, M. H., G. W. Su, and J. Constantz (2007), Heat, Chloride, and Specific Conductance as Ground Water Tracers near Streams, *Ground Water*, *45*(2), 187-195.

Cranswick, R. H., P. G. Cook, M. Shanafield, and S. Lamontagne (2014), The vertical variability of hyporheic fluxes inferred from riverbed temperature data, *Water Resour. Res.*, *50*(5), 3994-4010, doi: 10.1002/2013wr014410.

Cressie, N. A. C. (1993), *Statistics for Spatial Data*, 900 pp., John Wiley & Sons Inc., New York.

Crossman, J., C. Bradley, A. Milner, and G. Pinay (2013), Influence of Environmental Instability of Groundwater-Fed Streams on Hyporheic Fauna, on a Glacial Floodplain, Denali National Park, Alaska, *River Research and Applications*, *29*(5), 548-559, doi: 10.1002/rra.1619.

Cuthbert, M. O., and R. Mackay (2013), Impacts of nonuniform flow on estimates of vertical streambed flux, *Water Resour. Res.*, *49*(1), 19-28, doi: 10.1029/2011wr011587.

Da Silva, M. L., and P. J. Alvarez (2008), Exploring the Correlation between Halorespirer Biomarker Concentrations and TCE Dechlorination Rates, *Journal of Environmental Engineering*, *134*(11), 895-901, doi: 10.1061/(asce)0733-9372(2008)134:11(895).

Dagan, G. (1986), Statistical-Theory of Groundwater-Flow and Transport - Pore to Laboratory, Laboratory to Formation, and Formation to Regional Scale, *Water Resour. Res.*, *22*(9), S120-S134, doi: 10.1029/Wr022i09sp0120s.

Dagan, G. (1989), *Flow and Transport in Porous Formations*, 465 pp., Springer, Heidelberg.

Dagan, G., and S. P. Neuman (2005), *Subsurface flow and transport: A stochastic approach*, 256 pp., Cambridge University Press.

Daniluk, T. L., L. K. Lautz, R. P. Gordon, and T. A. Endreny (2013), Surface water-groundwater interaction at restored streams and associated reference reaches, *Hydrol. Process.*, *27*(25), 3730-3746, doi: 10.1002/Hyp.9501.

Darcy, H. P. G. (1856), *Les fountaines publiques de la Ville de Dijon*, 647 pp., Victor Dalmont, Paris.

De Doncker, L. (2010), A Fundamental Study on Exchange Processes in River Ecosystems, PhD thesis, 475 pp, Universiteit Gent, Gent.

de Marsily, G. (1986), *Quantitative Hydrogeology: Groundwater Hydrology for Engineers*, 440 pp., Academic Press, Orlando, FL.

de Marsily, G., F. Delay, J. Goncalves, P. Renard, V. Teles, and S. Violette (2005), Dealing with spatial heterogeneity, *Hydrogeology Journal*, *13*(1), 161-183.

De Smedt, F. (2007), Analytical solution and analysis of solute transport in rivers affected by diffusive transfer in the hyporheic zone, *J. Hydrol.*, *339*(1-2), 29-38, doi: 10.1016/j.jhydrol.2007.02.002.

Deb, K., A. Pratap, S. Agarwal, and T. Meyarivan (2002), A fast and elitist multiobjective genetic algorithm: NSGA-II, *Evolutionary Computation, IEEE Transactions on*, *6*(2), 182-197, doi: 10.1109/4235.996017.

Derx, J., A. P. Blaschke, and G. Bloschl (2010), Three-dimensional flow patterns at the river-aquifer interface - a case study at the Danube, *Adv. Water Resour.*, *33*(11), 1375-1387, doi: 10.1016/j.advwatres.2010.04.013.

DHI (2009a), MIKE SHE Volume 1: User Guide, 230 pp.

DHI (2009b), MIKE SHE Volume 2: Reference Manual, 444 pp.

Diersch, H.-J. G. (2014), *FEFLOW - Finite Element Modeling of Flow, Mass and Heat Transport in Porous and Fractured Media*, 996 pp., Springer.

DIN (2013), DIN EN ISO 14688-1:2013-12 - Geotechnical investigation and testing - Identification and classification of soil - Part 1: Identification and description, edited by ISO.

Dodds, W. K., and J. Brock (1998), A portable flow chamber for in situ determination of benthic metabolism., *Freshwater Biology*, *39*(1), 49-59, doi: 10.1046/j.1365-2427.1998.00256.x.

Dong, W. H., X. H. Chen, Z. W. Wang, G. X. Ou, and C. Liu (2012), Comparison of vertical hydraulic conductivity in a streambed-point bar system of a gaining stream, *J. Hydrol.*, *450*, 9-16, doi: 10.1016/j.jhydrol.2012.05.037.

dov.vlaanderen.be Databank Ondergrond Vlaanderen, edited.

Duhamel, M., and E. A. Edwards (2007), Growth and yields of dechlorinators, acetogens, and methanogens during reductive dechlorination of chlorinated ethenes and dihaloelimination of 1,2-dichloroethane, *Environmental Science and Technology*, *41*(7), 2303-2310, doi: 10.1021/es062010r.

Duhamel, M., K. Mo, and E. A. Edwards (2004), Characterization of a highly enriched Dehalococcoides-containing culture that grows on vinyl chloride and trichloroethene, *Applied and Environmental Microbiology*, *70*(9), 5538-5545, doi: 10.1128/AEM.70.9.5538-5545.2004.

Dujardin, J., O. Batelaan, F. Canters, S. Boel, C. Anibas, and J. Bronders (2011), Improving surface-subsurface water budgeting using high resolution satellite imagery applied on a brownfield, *The Science of the total environment*, *409*(4), 800-809, doi: 10.1016/j.scitotenv.2010.10.055.

Dujardin, J., C. Anibas, J. Bronders, P. Jamin, K. Hamonts, W. Dejonghe, S. Brouyere, and O. Batelaan (2014), Combining flux estimation techniques to improve characterization of groundwater-surface-water interaction in the Zenne River, Belgium, *Hydrogeology Journal*, *22*(7), 1657-1668, doi: 10.1007/s10040-014-1159-4.

Ebel, B. A., and K. Loague (2006), Physics-based hydrologic-response simulation: Seeing through the fog of equifinality, *Hydrol. Process.*, *20*(13), 2887-2900, doi: 10.1002/Hyp.6388.

Ebrahim, G. Y., K. Hamonts, A. vanGriensven, A. Jonoski, W. Dejonghe, and A. Mynett (2013), Effect of temporal resolution of water level and temperature inputs on numerical simulation of groundwater-surface water flux exchange in a heavily modified urban river, *Hydrol. Process.*, *27*(11), 1634-1645, doi: 10.1002/Hyp.9310.

El Fantroussi, S., H. Naveau, and S. N. Agathos (1998), Anaerobic dechlorinating bacteria, *Biotechnology progress*, *14*(2), 167-188, doi: 10.1021/bp980011k.

Elfeki, A. M. M., G. Uffink, and S. Lebreton (2011), influence of temporal fluctuations and spatial heterogeneity on pollution transport in porous media, *Hydrogeology Journal*, *20*, 283-297.

Elliott, A. H., and N. H. Brooks (1997a), Transfer of nonsorbing solutes to a streambed with bed forms: Laboratory experiments, *Water Resour. Res.*, *33*(1), 137-151, doi: 10.1029/96WR02783.

Elliott, A. H., and N. H. Brooks (1997b), Transfer of nonsorbing solutes to a streambed with bed forms: Theory, *Water Resour. Res.*, *33*(1), 123-136, doi: 10.1029/96wr02784.

Ellis, P. A., and M. O. Rivett (2007), Assessing the impact of VOC-contaminated groundwater on surface water at the city scale, *J. Contam. Hydrol.*, *91*(1-2), 107-127, doi: 10.1016/j.jconhyd.2006.08.015.

Ellis, P. A., R. Mackay, and M. O. Rivett (2007), Quantifying urban river-aquifer fluid exchange processes: a multi-scale problem, *J Contam Hydrol*, *91*(1-2), 58-80, doi: 10.1016/j.jconhyd.2006.08.014.

Engdahl, N. B., and G. S. Weissmann (2010), Anisotropic transport rates in heterogeneous porous media, *Water Resour. Res.*, *46*, doi: 10.1029/2009wr007910.

Engdahl, N. B., E. T. Vogler, and G. S. Weissmann (2010), Evaluation of aquifer heterogeneity effects on river flow loss using a transition probability framework, *Water Resour. Res.*, *46*, doi: 10.1029/2009wr007903.

Engelhardt, I., H. Prommer, C. Moore, M. Schulz, C. Schuth, and T. A. Ternes (2013), Suitability of temperature, hydraulic heads, and acesulfame to quantify wastewater-related fluxes in the hyporheic and riparian zone, *Water Resour. Res.*, *49*(1), 426-440, doi: 10.1029/2012wr012604.

Engelhardt, I., M. Piepenbrink, N. Trauth, S. Stadler, C. Kludt, M. Schulz, C. Schuth, and T. A. Ternes (2011), Comparison of tracer methods to quantify hydrodynamic exchange within the hyporheic zone, *J. Hydrol.*, *400*(1-2), 255-266, doi: 10.1016/j.jhydrol.2011.01.033.

Essaid, H. I., C. M. Zamora, K. A. McCarthy, J. R. Vogel, and J. T. Wilson (2008), Using heat to characterize streambed water flux variability in four stream reaches, *Journal of environmental quality*, *37*(3), 1010-1023, doi: 10.2134/jeq2006.0448.

EU (2000), Directive 2000/60/EC of the European Parliament and of the Council establishing a framework for Community action in the field of water policy, edited, p. 82.

Evensen, G. (2003), The Ensemble Kalman Filter: theoretical formulation and practical implementation., *Ocean Dynamics 53*, 343-367.

Ewen, J., G. Parkin, and P. E. O'Connell (2000), Shetran: Distributed River Basin Flow and Transport Modeling System, *Journal of Hydrologic Engineering*, *5*(3), 250-258, doi: 10.1061/(Asce)1084-0699(2000)5:3(250).

Fairbanks, J., S. Panday, and P. S. Huyakorn (2001), Comparisons of linked and fully coupled approaches to simulating conjunctive surface/subsurface flow and their interactions. , paper presented at Proceedings of MODFLOW 2001 and Other Modelling Odysseys, Golden, CO, September 12-14, 2001.

Fanelli, R. M., and L. K. Lautz (2008), Patterns of water, heat, and solute flux through streambeds around small dams, *Ground Water*, *46*(5), 671-687, doi: 10.1111/j.1745-6584.2008.00461.x.

Fennell, D. E., and J. M. Gossett (1998), Modeling the production of and competition for hydrogen in a dechlorinating culture, *Environ. Sci. Technol.*, *32*(16), 2450-2460, doi: 10.1021/Es980136l.

Fennell, D. E., J. M. Gossett, and S. H. Zinder (1997), Comparison of butyric acid, ethanol, lactic acid, and propionic acid as hydrogen donors for the reductive dechlorination of tetrachloroethene, *Environ. Sci. Technol.*, *31*(3), 918-926, doi: 10.1021/Es960756r.

Ferguson, G., and V. Bense (2011), Uncertainty in 1D heat-flow analysis to estimate groundwater discharge to a stream, *Ground Water*, *49*(3), 336-347, doi: 10.1111/j.1745-6584.2010.00735.x.

Feris, K., P. Ramsey, C. Frazar, J. N. Moore, J. E. Gannon, and W. E. Holben (2003), Differences in hyporheic-zone microbial community structure along a heavy-metal contamination gradient, *Appl Environ Microbiol*, *69*(9), 5563-5573.

Feris, K. P., P. W. Ramsey, C. Frazar, M. Rillig, J. N. Moore, J. E. Gannon, and W. E. Holben (2004), Seasonal dynamics of shallow-hyporheic-zone microbial community structure along a heavy-metal contamination gradient, *Appl Environ Microbiol*, *70*(4), 2323-2331.

Fetter, C. W. (1999), *Contaminant hydrogeology*, 2nd ed., 500 pp., Prentice Hall, Upper Saddle River, NJ.

Fetter, C. W. (2001), *Applied hydrogeology*, 4th ed., 598 pp., Pearson Education, Upper Saddle River, NJ.

Findlay, S. (1995), Importance of Surface-Subsurface Exchange in Stream Ecosystems - the Hyporheic Zone, *Limnology and Oceanography*, *40*(1), 159-164.

Findlay, S., and R. L. Sinsabaugh (2006), Large-scale variation in subsurface stream biofilms: a crossregional comparison of metabolic function and community similarity, *Microb. Ecol.*, *52*(491-500).

Fischer, H., M. Pusch, and J. Schwoerbel (1996), Spatial distribution and respiration of bacteria in stream-bed sediments, *Archiv Fur Hydrobiologie*, *137*(3), 281-300.

Fleckenstein, J. H., R. G. Niswonger, and G. E. Fogg (2006), River-aquifer interactions, geologic heterogeneity, and low-flow management, *Ground Water*, *44*(6), 837-852, doi: 10.1111/j.1745-6584.2006.00190.x.

Fletcher, R. (1980), *Practical Methods of Optimization. Volume 1: Unconstrained Optimization*, 120 pp., John Wiley & Sons, New York, NY.

Fourier, J. B. J. (1822), *Theorie Analytique de la Chaleur*, F.Didot, Paris.

Freeze, R. A., and J. A. Cherry (1979), *Groundwater*, 604 pp., Prentice-Hall, Englewood Cliffs, NJ.

Frei, S., G. Lischeid, and J. H. Fleckenstein (2010), Effects of micro-topography on surface-subsurface exchange and runoff generation in a virtual riparian wetland - A modeling study, *Adv. Water Resour.*, *33*(11), 1388-1401, doi: 10.1016/j.advwatres.2010.07.006.

Freitas, J. G., M. O. Rivett, R. S. Roche, M. Durrant, C. Walker, and J. H. Tellam (2015), Heterogeneous hyporheic zone dechlorination of a TCE groundwater plume discharging to an urban river reach, *Science of The Total Environment*, *505*, 236-252, doi: 10.1016/j.scitotenv.2014.09.083.

Frissell, C. A., W. J. Liss, C. E. Warren, and M. D. Hurley (1986), A Hierarchical Framework for Stream Habitat Classification - Viewing Streams in a Watershed Context, *Environ. Manage.*, *10*(2), 199-214, doi: 10.1007/Bf01867358.

Fritz, B. G., D. P. Mendoza, and T. J. Gilmore (2009), Development of an electronic seepage chamber for extended use in a river, *Ground Water*, *47*(1), 136-140, doi: 10.1111/j.1745-6584.2008.00491.x.

Fry, V. A., J. D. Istok, L. Semprini, K. T. Oreilly, and T. E. Buscheck (1995), Retardation of Dissolved-Oxygen Due to a Trapped Gas-Phase in Porous-Media, *Ground Water*, *33*(3), 391-398, doi: 10.1111/j.1745-6584.1995.tb00295.x.

Fuller, C. C., and J. W. Harvey (2000), Reactive uptake of trace metals in the hyporheic zone of a mining-contaminated stream, Pinal Creek, Arizona, *Environ. Sci. Technol.*, *34*(7), 1150-1155, doi: 10.1021/Es990714d.

Furman, A. (2008), Modeling coupled surface-subsurface flow processes: A review, *Vadose Zone Journal*, *7*(2), 741-756, doi: 10.2136/Vzj2007.0065.

Gandy, C. J., J. W. Smith, and A. P. Jarvis (2007), Attenuation of mining-derived pollutants in the hyporheic zone: a review, *The Science of the total environment*, *373*(2-3), 435-446, doi: 10.1016/j.scitotenv.2006.11.004.

Garant, H., and L. Lynd (1998), Applicability of competitive and noncompetitive kinetics to the reductive dechlorination of chlorinated ethenes, *Biotechnol Bioeng*, *57*(6), 751-755.

Garbarini, D. R., and L. W. Lion (1985), Evaluation of sorptive partitioning of nonionic pollutants in closed systems by headspace analysis, *Environ Sci Technol*, *19*(11), 1122-1128, doi: 10.1021/es00141a018.

Gariglio, F. P., D. Tonina, and C. H. Luce (2013), Spatiotemporal variability of hyporheic exchange through a pool-riffle-pool sequence, *Water Resour. Res.*, *49*(11), 7185-7204, doi: 10.1002/wrcr.20419.

Garraway, M., L. Milford, D. Van Vliet, S. Bellamy, S. Murray, C. Gabriel, J. P. Jones, P. Delaney, Y. Qiao, and C. Neville (2011), Integrated Surface and Groundwater Model Review and Technical Guide, 116 pp.

Genereux, D. P., S. Leahy, H. Mitasova, C. D. Kennedy, and D. R. Corbett (2008), Spatial and temporal variability of streambed hydraulic conductivity in West Bear Creek, North Carolina, USA, *J. Hydrol.*, *358*(3-4), 332-353, doi: 10.1016/j.jhydrol.2008.06.017.

Gibert, J., J. A. Stanford, M.-J. Dole-Olivier, and J. V. Ward (1994), Basic attributes of groundwater ecosystems and prospects for research, in *Groundwater Ecology*, edited by J. Gibert, D. L. Danielopol and J. A. Stanford, pp. 7-40, Academic Press, London.

Gómez-Hernández, J. J., A. Sahuquillo, and J. E. Capilla (1997), Stochastic Simulation of Transmissivity Fields Conditional to Both Transmissivity and Piezometric Data - I. Theory, *J. Hydrol.*, *203*, 162-174.

Gomez, J. D., J. L. Wilson, and M. B. Cardenas (2012), Residence time distributions in sinuosity-driven hyporheic zones and their biogeochemical effects, *Water Resour. Res.*, *48*, doi: 10.1029/2012wr012180.

Gooseff, M. N., K. E. Bencala, D. T. Scott, R. L. Runkel, and D. M. McKnight (2005), Sensitivity analysis of conservative and reactive stream transient storage models applied to field data from multiple-reach experiments, *Adv. Water Resour.*, *28*(5), 479-492, doi: 10.1016/j.advwatres.2004.11.012.

Gooseff, M. N., J. K. Anderson, S. Wondzell, J. LaNier, and R. Haggerty (2006), A modeling study of hyporheic exchange pattern and the sequence, size, and spacing of stream bedforms in mountain stream networks, Oregon, USA, *Hydrol. Process.*, *20*(11), 2443–2457, doi: 10.1002/hyp.6349.

Goovaerts, P. (1997), *Geostatistics for natural resources evaluation*, 483 pp., Oxford University Press, New York, NY.

Gordon, R. P., L. K. Lautz, M. A. Briggs, and J. M. McKenzie (2012), Automated calculation of vertical pore-water flux from field temperature time series using the VFLUX method and computer program, *J. Hydrol.*, *420*, 142-158, doi: 10.1016/j.jhydrol.2011.11.053.

Goto, S., M. Yamano, and M. Kinoshita (2005), Thermal response of sediment with vertical fluid flow to periodic temperature variation at the surface, *J Geophys Res-Sol Ea*, *110*(B1), doi: 10.1029/2004jb003419.

Grimm, N. B., and S. G. Fisher (1984), Exchange between Interstitial and Surface-Water - Implications for Stream Metabolism and Nutrient Cycling, *Hydrobiologia*, *111*(3), 219-228, doi: 10.1007/Bf00007202.

Gupta, H. V., S. Sorooshian, and P. O. Yapo (1999), Towards improved calibration of hydrologic models: multiple and noncommensurable measures of information, *Water Resour. Res.*, *34*, 751-763.

Haario, H., E. Saksman, and J. Tamminen (2001), An adaptive Metropolis algorithm, *Bernoulli*, *7*(2), 223-242.

Haest, P. J., D. Springael, and E. Smolders (2010), Dechlorination kinetics of TCE at toxic TCE concentrations: Assessment of different models, *Water Res*, *44*(1), 331-339, doi: 10.1016/j.watres.2009.09.033.

Haldorson, H. H., and E. Damsleth (1990), Stochastic modeling, *Journal of Petroleum Technology*, *42*(4), 404-412.

Hamonts, K. (2009), Structure and pollutant-degrading activity of the microbial community in eutrophic river sediments impacted by discharging chlorinated aliphatic hydrocarbon-polluted groundwater., PhD thesis, 209 pp, Catholic University Leuven, Leuven.

Hamonts, K., A. Ryngaert, H. Smidt, D. Springael, and W. Dejonghe (2014), Determinants of the microbial community structure of eutrophic, hyporheic river sediments polluted with chlorinated aliphatic hydrocarbons, *FEMS Microbiol Ecol*, *87*(3), 715-732, doi: 10.1111/1574-6941.12260.

Hamonts, K., T. Kuhn, J. Vos, M. Maesen, H. Kalka, H. Smidt, D. Springael, R. U. Meckenstock, and W. Dejonghe (2012), Temporal variations in natural attenuation of chlorinated aliphatic hydrocarbons in eutrophic river sediments impacted by a contaminated groundwater plume, *Water Res*, *46*(6), 1873-1888, doi: 10.1016/j.watres.2012.01.001.

Hamonts, K., T. Kuhn, M. Maesen, J. Bronders, R. Lookman, H. Kalka, L. Diels, R. U. Meckenstock, D. Springael, and W. Dejonghe (2009), Factors Determining the Attenuation of Chlorinated Aliphatic Hydrocarbons in Eutrophic River Sediment Impacted by Discharging Polluted Groundwater, *Environ. Sci. Technol.*, *43*(14), 5270-5275, doi: 10.1021/Es8035994.

Hancock, P. J., A. J. Boulton, and W. F. Humphreys (2005), Aquifers and hyporheic zones: Towards an ecological understanding of groundwater, *Hydrogeology Journal*, *13*(1), 98-111, doi: 10.1007/s10040-004-0421-6.

Hannah, D. M., I. A. Malcolm, and C. Bradley (2009), Seasonal hyporheic temperature dynamics over riffle bedforms, *Hydrol. Process.*, *23*(15), 2178-2194, doi: 10.1002/Hyp.7256.

Hantush, M. M. (2005), Modeling stream-aquifer interactions with linear response functions, *J. Hydrol.*, *311*(1-4), 59-79, doi: 10.1016/j.jhydrol.2005.01.007.

Harbaugh, A. W. (2005), MODFLOW-2005, The U.S. Geological Survey modular ground-water model - the Ground-Water Flow Process, *Techniques and Methods - 6-A16*, 253 pp, U.S. Geological Survey, Reston, VA.

Harbaugh, A. W., E. R. Banta, M. C. Hill, and M. G. McDonald (2000), MODFLOW-2000, the U.S. Geological Survey modular ground-water model - User guide to modularization concepts and the Ground-Water Flow Process, *Open-File Report 00-92*, 121 pp, U.S. Geological Survey Reston, VA.

Harvey, F. E., D. R. Lee, D. L. Rudolph, and S. K. Frape (1997), Locating groundwater discharge in large lakes using bottom sediment electrical conductivity mapping, *Water Resour. Res.*, *33*(11), 2609-2615, doi: 10.1029/97wr01702.

Harvey, J. W., and B. J. Wagner (2000), Quantifying hydrologic interactions between streams and their subsurface hyporheic zones, in *Streams and ground waters*, edited by J. B. Jones and P. J. Mulholland, pp. 3-44, Academic Press, San Diego.

Harvey, J. W., B. J. Wagner, and K. E. Bencala (1996), Evaluating the reliability of the stream tracer approach to characterize stream-subsurface water exchange, *Water Resour. Res.*, *32*(8), 2441-2451, doi: 10.1029/96wr01268.

Harvey, J. W., J. K. Boehlke, M. A. Voytek, D. Scott, and C. R. Tobias (2013), Hyporheic zone denitrification: Controls on effective reaction depth and contribution to whole-stream mass balance, *Water Resour. Res.*, *49*(10), 6298-6316, doi: 10.1002/wrcr.20492.

Harvey, J. W., J. D. Drummond, R. L. Martin, L. E. McPhillips, A. I. Packman, D. J. Jerolmack, S. H. Stonedahl, A. F. Aubeneau, A. H. Sawyer, L. G. Larsen, and C. R. Tobias (2012), Hydrogeomorphology of the hyporheic zone: Stream solute and fine particle interactions with a dynamic streambed, *J. Geophys. Res.-Biogeosci.*, *117*, doi: 10.1029/2012jg002043.

Haston, Z. C., and P. L. McCarty (1999), Chlorinated ethene half-velocity coefficients (K-s) for reductive dehalogenation, *Environ. Sci. Technol.*, *33*(2), 223-226, doi: 10.1021/Es9805876.

Hatch, C. E., A. T. Fisher, C. R. Ruehl, and G. Stemler (2010), Spatial and temporal variations in streambed hydraulic conductivity quantified with time-series thermal methods, *J. Hydrol.*, *389*(3-4), 276-288, doi: 10.1016/j.jhydrol.2010.05.046.

Hatch, C. E., A. T. Fisher, J. S. Revenaugh, J. Constantz, and C. Ruehl (2006), Quantifying surface water-groundwater interactions using time series analysis of streambed thermal records: Method development, *Water Resour. Res.*, *42*(10), doi: 10.1029/2005wr004787.

Hazen, A. (1893), Some physical properties of sand and gravels, with special reference to their use in filtration, *Twenty Fourth Annual Report, State Board of Health of Massachusetts*, 541-566 pp.

He, J., Y. Sung, M. E. Dollhopf, B. Z. Fathepure, J. M. Tiedje, and F. E. Löffler (2002), Acetate versus hydrogen as direct electron donors to stimulate the microbial reductive dechlorination process at chloroethene-contaminated sites, *Environmental Science and Technology*, *36*(18), 3945-3952, doi: 10.1021/es025528d.

He, Y., C. Su, J. Wilson, R. Wilkin, C. Adair, T. Lee, P. Bradley, and M. Ferrey (2009), Identification and characterization methods for reactive minerals responisble for natural attenuation of chlorinated organic compounds in ground water, *600/R-09/115*, U.S. Environmental Protection Agency, Ada, OK.

Healy, R. W., and A. D. Ronan (1996), Documentation of computer program VS2DH for simulation of evergy transport in variably saturated porous media -- Modification of the U.S. Geological Survey's computer program VS2DT, 125 pp, U.S. Geological Survey.

Hendrickson, E. R., J. A. Payne, R. M. Young, M. G. Starr, M. P. Perry, S. Fahnestock, D. E. Ellis, and R. C. Ebersole (2002), Molecular analysis of Dehalococcoides 16S ribosomal DNA from chloroethene-contaminated sites throughout North America and Europe, *Appl Environ Microbiol*, *68*(2), 485-495.

Hespanha, J. P. (2009), *Linear Systems Theory*, 280 pp., Princeton University Press.

Hester, E. T., K. I. Young, and M. A. Widdowson (2013), Mixing of surface and groundwater induced by riverbed dunes: Implications for hyporheic zone definitions and pollutant reactions, *Water Resour. Res.*, *49*(9), 5221-5237, doi: 10.1002/wrcr.20399.

Higashino, M., and H. G. Stefan (2011), Non-linear effects on solute transfer between flowing water and a sediment bed, *Water Research*, *45*(18), 6074-6086, doi: 10.1016/j.watres.2011.09.004.

Hill, M. C., and C. R. Tiedeman (2007), *Effective groundwater model calibration: With analysis of data, sensitivities, predictions, and uncertainty*, 480 pp., Wiley.

Holliger, C., G. Wohlfarth, and G. Diekert (1999), Reductive dechlorination in the energy metabolism of anaerobic bacteria, *FEMS Microbiology Rev.*, *22*, 383-398.

Holzbecher, E. (2005), Inversion of temperature time series from near-surface porous sediments, *Journal of Geophysics and Engineering*, *2*(4), 343-348, doi: 10.1088/1742-2132/2/4/S07.

Hopmans, J. W., J. Simunek, and K. L. Bristow (2002), Indirect estimation of soil thermal properties and water flux using heat pulse probe measurements: Geometry and dispersion effects, *Water Resour. Res.*, *38*(1), 7-1 - 7-14, doi: 10.1029/2000wr000071.

Hornberger, G. M., J. P. Raffensberger, P. L. Wiberg, and K. N. Eshleman (1998), *Elements of Physical Hydrology*, 302 pp., The Johns Hopkins University Press, Baltimore.

Hsieh, P. A., W. Wingle, and R. W. Healy (2000), VS2DI-A graphical software package for simulating fluid flow and solute or energy transport in variably saturated porous media, *WRIR 99-4130*, 16 pp, U.S. Geological Survey.

Hunkeler, D., R. Aravena, K. Berry-Spark, and E. Cox (2005), Assessment of degradation pathways in an aquifer with mixed chlorinated hydrocarbon contamination using stable isotope analysis, *Environ. Sci. Technol.*, *39*(16), 5975-5981, doi: 10.1021/Es048464a.

Hunkeler, D., Y. Abe, M. M. Broholm, S. Jeannottat, C. Westergaard, C. S. Jacobsen, R. Aravena, and P. L. Bjerg (2011), Assessing chlorinated ethene degradation in a large scale contaminant plume by dual carbon-chlorine isotope analysis and quantitative PCR, *J. Contam. Hydrol.*, *119*(1-4), 69-79, doi: 10.1016/j.jconhyd.2010.09.009.

Hvorslev, M. J. (1951), Time lag and soil permeability in ground-water observations, 50 pp, US Army Corps of Engineers, Waterways Exper. Sta. Bull No. 36, Vicksburg, MS.

HydroGeoLogic (2000), MODHMS: A comprehensive MODFLOW-based hydrologic modelling system, Version 1.1 - Code Documentation and User's Guide, edited, HydroGeoLogic Incorporated, Herndon, VA.

Iribar, A., J. M. Sanchez-Perez, E. Lyautey, and F. Garabetian (2008), Differentiated free-living and sediment-attached bacterial community structure inside and outside denitrification hotspots in the river-groundwater interface, *Hydrobiologia*, *598*, 109-121, doi: 10.1007/s10750-007-9143-9.

Irvine, D. J., P. Brunner, H.-J. H. Franssen, and C. T. Simmons (2012), Heterogeneous or homogeneous? Implications of simplifying heterogeneous streambeds in models of losing streams, *J. Hydrol.*, *424-425*, 16-23, doi: 10.1016/j.jhydrol.2011.11.051.

Irvine, D. J., R. H. Cranswick, C. T. Simmons, M. A. Shanafield, and L. K. Lautz (2015a), The effect of streambed heterogeneity on groundwater-surface water exchange fluxes inferred from temperature time series, *Water Resour. Res.*, *51*(1), 198-212, doi: 10.1002/2014wr015769.

Irvine, D. J., L. K. Lautz, M. A. Briggs, R. P. Gordon, and J. M. McKenzie (2015b), Experimental evaluation of the applicability of phase, amplitude, and combined methods to determine water flux and thermal diffusivity from temperature time series using VFLUX 2, *J. Hydrol.*, *531*, 728-737, doi: 10.1016/j.jhydrol.2015.10.054.

Isaaks, E. H., and R. M. Srivastava (1989), *An Introduction to Applied Geostatistics*, 561 pp., Oxford University Press, New York.

Islam, A. M., E. A. Edwards, and R. Mahadevan (2010), Characterizing the metabolism of Dehalococcoides with a constraint-based model, *PLoS Comput. Biol. , 6*(8), doi: 10.1371/journal.pcbi.1000887.

Jensen, J. K., and P. Engesgaard (2011), Nonuniform Groundwater Discharge across a Streambed: Heat as a Tracer, *Vadose Zone Journal, 10*(1), 98-109, doi: 10.2136/Vzj2010.0005.

Jeong, H. Y., and K. F. Hayes (2007), Reductive dechlorination of tetrachloroethylene and trichloroethylene by mackinawite (FeS) in the presence of metals: reaction rates, *Environ Sci Technol, 41*(18), 6390-6396.

Jin, G., H. Tang, L. Li, and D. A. Barry (2011), Hyporheic flow under periodic bed forms influenced by low-density gradients, *Geophysical Research Letters, 38*(22), L22401, doi: 10.1029/2011GL049694.

Jin, G. Q., H. W. Tang, B. Gibbes, L. Li, and D. A. Barry (2010), Transport of nonsorbing solutes in a streambed with periodic bedforms, *Adv. Water Resour., 33*(11), 1402-1416, doi: 10.1016/j.advwatres.2010.09.003.

Jin, L., D. I. Siegel, L. K. Lautz, and M. H. Otz (2009), Transient storage and downstream solute transport in nested stream reaches affected by beaver dams, *Hydrol. Process., 23*(17), 2438-2449, doi: 10.1002/Hyp.7359.

Jones, J. B., and P. J. Mulholland, (ed.) (2000), *Streams and Ground Waters*, 425 pp., Academic Press, San Diego.

Jonsson, K., H. Johansson, and A. Worman (2003), Hyporheic exchange of reactive and conservative solutes in streams - tracer methodology and model interpretation, *J. Hydrol., 278*(1-4), 153-171, doi: 10.1016/S0022-1694(03)00140-9.

Journel, A. G., and E. K. Isaaks (1984), Conditional indicator simulation: application to a Saskatcheouan uranium deposit, *Mathematical Geology, 16*(7), 685-718.

Junk, W. J., P. B. Bayley, and R. E. Sparks (1989), The flood pulse concept in river-floodplain systems, *Can. Spec. Publ. Fish. Aquat. Sci., 106*, 110-127.

Kalbus, E., F. Reinstorf, and M. Schirmer (2006), Measuring methods for groundwater - surface water interactions: a review, *Hydrology and Earth System Sciences, 10*(6), 873-887.

Kalbus, E., C. Schmidt, F. Reinstorf, R. Krieg, and M. Schirmer (2008), How streambed temperatures can contribute to the determination of aquifer heterogeneity, *Grundwasser, 13*(2), 91-100, doi: 10.1007/s00767-008-0066-9.

Kalbus, E., C. Schmidt, J. W. Molson, F. Reinstorf, and M. Schirmer (2009), Influence of aquifer and streambed heterogeneity on the distribution of groundwater discharge, *Hydrology and Earth System Sciences, 13*(1), 69-77.

Kalbus, E., C. Schmidt, M. Bayer-Raich, S. Leschik, F. Reinstorf, G. U. Balcke, and M. Schirmer (2007), New methodology to investigate potential contaminant mass fluxes at the stream-aquifer interface by combining integral pumping tests and streambed temperatures, *Environmental Pollution, 148*(3), 808-816, doi: 10.1016/j.envpol.2007.01.042.

Kalman, R. E. (1960), A New Approach to Linear Filtering and Prediction Problems, *Journal of Fluids Engineering, 82*(1), 35-45, doi: 10.1115/1.3662552.

Karan, S., P. Engesgaard, and J. Rasmussen (2014a), Dynamic streambed fluxes during rainfall- runoff events, *Water Resour. Res., 50*(3), 2293-2311, doi: 10.1002/2013wr014155.

Karan, S., P. Engesgaard, M. C. Looms, T. Laier, and J. Kazmierczak (2013), Groundwater flow and mixing in a wetland-stream system: Field study and numerical modeling, *J. Hydrol., 488*, 73-83, doi: 10.1016/j.jhydrol.2013.02.030.

Karan, S., J. Kidmose, P. Engesgaard, B. Nilsson, M. Frandsen, D. A. O. Ommen, M. R. Flindt, F. O. Andersen, and O. Pedersen (2014b), Role of a groundwater-lake interface in controlling seepage of water and nitrate, *J. Hydrol., 517*, 791-802, doi: 10.1016/j.jhydrol.2014.06.011.

Kasahara, T., and S. M. Wondzell (2003), Geomorphic controls on hyporheic exchange flow in mountain streams, *Water Resour. Res., 39*(1), 1-14, doi: 10.1029/2002wr001386.

Kasenow, M. (2001), *Applied Ground-Water Hydrology and Well Hydraulics*, 2nd ed., 835 pp., Water Resources Publications LLC, Highlands Ranch, CO.

Käser, D. H., A. Binley, and A. L. Heathwaite (2013), On the Importance of Considering Channel Microforms in Groundwater Models of Hyporheic Exchange, *River Research and Applications*, *29*(4), 528-535, doi: 10.1002/rra.1618.

Käser, D. H., A. Binley, S. Krause, and A. L. Heathwaite (2014), Prospective modelling of 3D hyporheic exchange based on high-resolution topography and stream elevation, *Hydrol. Process.*, *28*(4), 2579-2594, doi: 10.1002/hyp.9758.

Kaufmann, F., G. Wohlfarth, and G. Diekert (1998), O-demethylase from Acetobacterium dehalogenans Substrate specificity and funtion of the participating proteins., *Eur. J. Biochem.*, *253*, 706-711.

Kaushal, S. S., P. M. Groffman, L. E. Band, E. M. Elliott, C. A. Shields, and C. Kendall (2011), Tracking Nonpoint Source Nitrogen Pollution in Human-Impacted Watersheds, *Environ. Sci. Technol.*, *45*(19), 8225-8232, doi: 10.1021/es200779e.

Kaviany, M. (1995), *Principles of Heat Transfer in Porous Media*, 2nd ed., 712 pp., Springer, New York.

Kazezyilmaz-Alhan, C. M. (2008), Analytical solutions for contaminant transport in streams, *J. Hydrol.*, *348*(3-4), 524-534, doi: 10.1016/j.jhydrol.2007.10.022.

Keery, J., and A. Binley (2007), Temperature measurements for determining groundwater-surface water fluxes, *Science Report SC030155/SR9*, 40 pp, Environment Agency, Bristol.

Keery, J., A. Binley, N. Crook, and J. W. N. Smith (2007), Temporal and spatial variability of groundwater-surface water fluxes: Development and application of an analytical method using temperature time series, *J. Hydrol.*, *336*(1-2), 1-16, doi: 10.1016/j.jhydrol.2006.12.003.

Kendall, M. (1975), *Rank Correlation Methods*, 4th ed., Charles Griffin, London.

Kennedy, C. D., D. P. Genereux, D. R. Corbett, and H. Mitasova (2009a), Relationships among groundwater age, denitrification, and the coupled groundwater and nitrogen fluxes through a streambed, *Water Resour. Res.*, *45*, doi: 10.1029/2008wr007400.

Kennedy, C. D., D. P. Genereux, D. R. Corbett, and H. Mitasova (2009b), Spatial and temporal dynamics of coupled groundwater and nitrogen fluxes through a streambed in an agricultural watershed, *Water Resour. Res.*, *45*, doi: 10.1029/2008wr007397.

Kennedy, C. D., D. P. Genereux, H. Mitasova, D. R. Corbett, and S. Leahy (2008), Effect of sampling density and design on estimation of streambed attributes, *J. Hydrol.*, *355*(1-4), 164-180, doi: 10.1016/j.jhydrol.2008.03.018.

Kennedy, J., R. C. Eberhardt, and Y. Shi (2001), *Swarm Intelligence*, 512 pp., Morgan Kaufmann, San Francisco.

Khan, F. I., T. Husain, and R. Hejazi (2004), An overview and analysis of site remediation technologies, *J Environ Manage*, *71*(2), 95-122, doi: 10.1016/j.jenvman.2004.02.003.

Kikuchi, C. P., T. P. A. Ferre, and J. M. Welker (2012), Spatially telescoping measurements for improved characterization of ground water-surface water interactions, *J. Hydrol.*, *446*, 1-12, doi: 10.1016/j.jhydrol.2012.04.002.

Kitanidis, P. K. (1997), *Introduction to geostatistics: Applications in Hydrogeology*, 272 pp., Cambridge University Press, New York, NY.

KMI (2014), Royal Meteorological Institute of Belgium. Klimatologisch overzicht van 2012 - Climate Overview of 2012, edited.

Koltermann, C. E., and S. M. Gorelick (1992), Paleoclimate signature in terrestrial flood deposits, *Science*, *256*, 1775-1782.

Koltermann, C. E., and S. M. Gorelick (1996), Heterogeneity in sedimentary deposits: A review of structure-imitating, process-imitating, and descriptive approaches, *Water Resour. Res.*, *32*(9), 2617-2658, doi: 10.1029/96wr00025.

Kozeny, J. (1953), *Hydraulik - Ihre Grundlagen und praktische Anwendung*, 588 pp., Springer, Wien.

Krause, S., and T. Blume (2013), Impact of seasonal variability and monitoring mode on the adequacy of fiber-optic distributed temperature sensing at aquifer- river interfaces, *Water Resour. Res.*, *49*(5), 2408-2423, doi: 10.1002/Wrcr.20232.

Krause, S., D. M. Hannah, and J. H. Fleckenstein (2009a), Hyporheic hydrology: interactions at the groundwater-surface water interface Preface, *Hydrol. Process.*, *23*(15), 2103-2107, doi: 10.1002/Hyp.7366.

Krause, S., D. M. Hannah, and T. Blume (2011), Interstitial pore-water temperature dynamics across a pool-riffle-pool sequence, *Ecohydrology*, *4*(4), 549-563, doi: 10.1002/Eco.199.

Krause, S., T. Blume, and N. J. Cassidy (2012), Investigating patterns and controls of groundwater up-welling in a lowland river by combining Fibre-optic Distributed Temperature Sensing with observations of vertical hydraulic gradients, *Hydrology and Earth System Sciences*, *16*(6), 1775-1792, doi: 10.5194/hess-16-1775-2012.

Krause, S., L. Heathwaite, A. Binley, and P. Keenan (2009b), Nitrate concentration changes at the groundwater-surface water interface of a small Cumbrian river, *Hydrol. Process.*, *23*(15), 2195-2211, doi: 10.1002/Hyp.7213.

Krause, S., C. Tecklenburg, M. Munz, and E. Naden (2013), Streambed nitrogen cycling beyond the hyporheic zone: Flow controls on horizontal patterns and depth distribution of nitrate and dissolved oxygen in the upwelling groundwater of a lowland river, *J. Geophys. Res.-Biogeosci.*, *118*(1), 54-67, doi: 10.1029/2012jg002122.

Krause, S., F. Boano, M. O. Cuthbert, J. H. Fleckenstein, and J. Lewandowski (2014), Understanding process dynamics at aquifer-surface water interfaces: An introduction to the special section on new modeling approaches and novel experimental technologies, *Water Resour. Res.*, *50*(2), 1847-1855, doi: 10.1002/2013wr014755.

Krauße, T., J. Cullmann, P. Saile, and G. H. Schmitz (2012), Robust multi-objective calibration strategies – possibilities for improving flood forecasting, *Hydrol. Earth Syst. Sci.*, *16*(10), 3579-3606, doi: 10.5194/hess-16-3579-2012.

Kuhn, T. K., K. Hamonts, J. A. Dijk, H. Kalka, W. Stichler, D. Springael, W. Dejonghe, and R. U. Meckenstock (2009), Assessment of the intrinsic bioremediation capacity of an eutrophic river sediment polluted by discharging chlorinated aliphatic hydrocarbons: a compound-specific isotope approach, *Environ Sci Technol*, *43*(14), 5263-5269, doi: 10.1021/es803600s.

Landon, M. K., D. L. Rus, and F. E. Harvey (2001), Comparison of instream methods for measuring hydraulic conductivity in sandy streambeds, *Ground Water*, *39*(6), 870-885.

Langston, G., M. Hayashi, and J. W. Roy (2013), Quantifying groundwater-surface water interactions in a proglacial moraine using heat and solute tracers, *Water Resour. Res.*, *49*(9), 5411-5426, doi: 10.1002/Wrcr.20372.

Lapham, W. W. (1989), Use of temperature profiles beneath streams to determine rates of vertical ground-water flow and vertical hydraulic conductivity, *Water Supply Paper 2337*, 44 pp, U.S. Geological Survey, Denver, CO.

LaSage, D. M., A. E. Fryar, A. Mukherjee, N. C. Sturchio, and L. J. Heraty (2008), Groundwater-derived contaminant fluxes along a channelized Coastal Plain stream, *J. Hydrol.*, *360*(1-4), 265-280, doi: 10.1016/j.jhydrol.2008.07.026.

Lautz, L. K. (2010), Impacts of nonideal field conditions on vertical water velocity estimates from streambed temperature time series, *Water Resour. Res.*, *46*, doi: 10.1029/2009wr007917.

Lautz, L. K. (2012), Observing temporal patterns of vertical flux through streambed sediments using time-series analysis of temperature records, *J. Hydrol.*, *464*, 199-215, doi: 10.1016/j.jhydrol.2012.07.006.

Lautz, L. K., and D. I. Siegel (2006), Modeling surface and ground water mixing in the hyporheic zone using MODFLOW and MT3D, *Adv. Water Resour.*, *29*(11), 1618-1633, doi: 10.1016/j.advwatres.2005.12.003.

Lautz, L. K., and R. M. Fanelli (2008), Seasonal biogeochemical hotspots in the streambed around restoration structures, *Biogeochemistry*, *91*(1), 85-104, doi: 10.1007/s10533-008-9235-2.

Lautz, L. K., and R. E. Ribaudo (2012), Scaling up point-in-space heat tracing of seepage flux using bed temperatures as a quantitative proxy, *Hydrogeology Journal*, *20*(7), 1223-1238, doi: 10.1007/s10040-012-0870-2.

Lautz, L. K., N. T. Kranes, and D. I. Siegel (2010), Heat tracing of heterogeneous hyporheic exchange adjacent to in-stream geomorphic features, *Hydrol. Process.*, *24*(21), 3074-3086, doi: 10.1002/Hyp.7723.

Lee, D. R. (1977), A device for seepage flux in lakes and estuaries *Limnology and Oceanography*, *22*(1), 140-147.

Lee, I. S., J. H. Bae, and P. L. McCarty (2007), Comparison between acetate and hydrogen as electron donors and implications for the reductive dehalogenation of PCE and TCE, *J. Contam. Hydrol.*, *94*(1-2), 76-85, doi: 10.1016/j.jconhyd.2007.05.003.

Lee, W., and B. Batchelor (2002), Abiotic reductive dechlorination of chlorinated ethylenes by iron-bearing soil minerals. 1. Pyrite and magnetite, *Environ. Sci. Technol.*, *36*, 5147-5154.

Lee, W., and B. Batchelor (2004), Abiotic reductive dechlorination of chlorinated ethylenes by iron-bearing phyllosilicates, *Chemosphere*, *56*(10), 999-1009, doi: 10.1016/j.chemosphere.2004.05.015.

Leek, R., J. Q. Wu, L. Wang, T. P. Hanrahan, M. E. Barbet, and H. X. Qiu (2009), Heterogeneous characteristics of streambed saturated hydraulic conductivity of the Touchet River, south eastern Washington, USA, *Hydrol. Process.*, *23*(8), 1236-1246, doi: 10.1002/Hyp.7258.

Leschik, S., A. Musolff, R. Krieg, M. Martienssen, M. Bayer-Raich, F. Reinstorf, G. Strauch, and M. Schirmer (2009), Application of integral pumping tests to investigate the influence of a losing stream on groundwater quality, *Hydrology and Earth System Sciences*, *13*(10), 1765-1774.

Levec, J., and R. G. Carbonell (1985), Longitudinal and lateral thermal dispersion in packed beds. Part I: Theory, *AIChE Journal*, *31*(4), 581-590, doi: 10.1002/aic.690310408.

Lewandowski, J., L. Angermann, G. Nutzmann, and J. H. Fleckenstein (2011a), A heat pulse technique for the determination of small-scale flow directions and flow velocities in the streambed of sand-bed streams, *Hydrol. Process.*, *25*(20), 3244-3255, doi: 10.1002/Hyp.8062.

Lewandowski, J., K. Meinikmann, G. Nützmann, and D. O. Rosenberry (2015), Groundwater – the disregarded component in lake water and nutrient budgets. 2. Effects of groundwater on nutrients, *Hydrol. Process.*, *29*(13), 2922-2955, doi: 10.1002/hyp.10384.

Lewandowski, J., A. Putschew, D. Schwesig, C. Neumann, and M. Radke (2011b), Fate of organic micropollutants in the hyporheic zone of a eutrophic lowland stream: results of a preliminary field study, *Science of the Total Environment*, *409*(10), 1824-1835, doi: 10.1016/j.scitotenv.2011.01.028.

Liu, C. X., and J. M. Zachara (2001), Uncertainties of Monod kinetic parameters nonlinearly estimated from batch experiments, *Environ. Sci. Technol.*, *35*(1), 133-141.

Lowry, C. S., J. F. Walker, R. J. Hunt, and M. P. Anderson (2007), Identifying spatial variability of groundwater discharge in a wetland stream using a distributed temperature sensor, *Water Resour. Res.*, *43*(10), doi: 10.1029/2007wr006145.

Lu, C. P., X. H. Chen, C. Cheng, G. X. Ou, and L. C. Shu (2012a), Horizontal hydraulic conductivity of shallow streambed sediments and comparison with the grain-size analysis results, *Hydrol. Process.*, *26*(3), 454-466, doi: 10.1002/Hyp.8143.

Lu, C. P., X. H. Chen, G. X. Ou, C. Cheng, L. C. Shu, D. H. Cheng, and E. K. Appiah-Adjei (2012b), Determination of the anisotropy of an upper streambed layer in east-central Nebraska, USA, *Hydrogeology Journal*, *20*(1), 93-101, doi: 10.1007/s10040-011-0792-4.

Luce, C. H., D. Tonina, F. Gariglio, and R. Applebee (2013), Solutions for the diurnally forced advection-diffusion equation to estimate bulk fluid velocity and diffusivity in streambeds from temperature time series, *Water Resour. Res.*, *49*(1), 488-506, doi: 10.1029/2012wr012380.

Mackay, D. M., and J. A. Cherry (1989), Groundwater Contamination - Pump-and-Treat Remediation .2., *Environ. Sci. Technol.*, *23*(6), 630-636, doi: 10.1021/Es00064a001.

Maier, H. R., Z. Kapelan, J. Kasprzyk, J. Kollat, L. S. Matott, M. C. Cunha, G. C. Dandy, M. S. Gibbs, E. Keedwell, A. Marchi, A. Ostfeld, D. Savic, D. P. Solomatine, J. A. Vrugt, A. C. Zecchin, B. S. Minsker, E. J. Barbour, G. Kuczera, F. Pasha, A. Castelletti, M. Giuliani, and P. M. Reed (2014), Evolutionary algorithms and other metaheuristics in water resources: Current status, research challenges and future directions, *Environmental Modelling & Software*, *62*(0), 271-299, doi: 10.1016/j.envsoft.2014.09.013.

Malard, F., D. Galassi, M. Lafont, S. Doledec, and J. V. Ward (2003), Longitudinal patterns of invertebrates in the hyporheic zone of a glacial river, *Freshwater Biology*, *48*(10), 1709-1725, doi: 10.1046/j.1365-2427.2003.01118.x.

Mann, H. B. (1945), Nonparametric Tests Against Trend, *Econometrica*, *13*(3), 163-171, doi: 10.2307/1907187.

Mantoglou, A., and J. L. Wilson (1982), The Turning Bands Method for Simulation of Random-Fields Using Line Generation by a Spectral Method, *Water Resour. Res.*, *18*(5), 1379-1394, doi: 10.1029/Wr018i005p01379.

Markstrom, S. L., R. G. Niswonger, R. S. Regan, D. E. Prudic, and P. M. Barlow (2008), GSFLOW-Coupled Ground-water and Surface-water FLOW model based on the integration of the Precipitation-Runoff Modelling System (PRMS) and the Modular Ground-Water Flow Model (MODFLOW-2005), *Techniques and Methods 6-D1*, 240 pp, U.S. Geological Survey.

Marzadri, A., D. Tonina, and A. Bellin (2013), Effects of stream morphodynamics on hyporheic zone thermal regime, *Water Resour. Res.*, *49*(4), 2287-2302, doi: 10.1002/wrcr.20199.

Marzadri, A., D. Tonina, A. Bellin, G. Vignoli, and M. Tubino (2010), Semianalytical analysis of hyporheic flow induced by alternate bars, *Water Resour. Res.*, *46*, doi: 10.1029/2009wr008285.

Matott, L. S., J. E. Babendreier, and S. T. Purucker (2009), Evaluating uncertainty in integrated environmental models: A review of concepts and tools, *Water Resour. Res.*, *45*(6), n/a-n/a, doi: 10.1029/2008WR007301.

Maxwell, R. M., S. J. Kollet, S. G. Smith, C. S. Woodward, R. D. Falgout, C. Baldwin, W. J. Bosl, R. Hornung, and S. Ashby (2009), PARFLOW User's Manual, v 1.3, edited, p. 127, Free Software Foundation, Inc.

Maymó-Gatell, X., Y.-t. Chien, J. M. Gossett, and S. H. Zinder (1997), Isolation of a Bacterium That Reductively Dechlorinates Tetrachloroethene to Ethene, *Science*, *276*(5318), 1568-1571, doi: 10.1126/science.276.5318.1568.

McCallum, A. M., M. S. Andersen, G. C. Rau, J. R. Larsen, and R. I. Acworth (2014), River- aquifer interactions in a semiarid environment investigated using point and reach measurements, *Water Resour. Res.*, *50*(4), 2815-2829, doi: 10.1002/2012wr012922.

McDonald, M. G., and A. W. Harbaugh (1988), A modular three-dimensional finite-difference ground-water flow model, *Techniques of Water-Resources Investigations - 6-A1*, 586 pp, U.S.Geological Survey, Reston, VA.

Miller, C. T., C. N. Dawson, M. W. Farthing, T. Y. Hou, J. Huang, C. E. Kees, C. T. Kelley, and H. P. Langtangen (2013), Numerical simulation of water resource problems: Models, methods, and trends, *Adv. Water Resour.*, *51*, 405-437.

Molina-Giraldo, N., P. Bayer, P. Blum, and O. A. Cirpka (2011), Propagation of seasonal temperature signals into an aquifer upon bank infiltration, *Ground Water*, *49*(4), 491-502, doi: 10.1111/j.1745-6584.2010.00745.x.

Molson, J. W., E. O. Frind, and C. D. Palmer (1992), Thermal energy storage in an unconfined aquifer: 2. Model development, validation, and application, *Water Resour. Res.*, *28*(10), 2857-2867, doi: 10.1029/92wr01472.

Morita, M., and B. C. Yen (2002), Modeling of conjunctive two-dimensional surface-three-dimensional subsurface flows, *J. Hydraul. Eng.-ASCE*, *128*(2), 184-200, doi: 10.1061/(Asce)0733-9429(2002)128:2(184).

Morris, M. D. (1991), Factorial sampling plans for preliminary computational experiments, *Technometrics*, *33*(2), 161-174.

Moser, D. P., J. K. Fredrickson, D. R. Geist, E. V. Arntzen, A. D. Peacock, S. M. Li, T. Spadoni, and J. P. McKinley (2003), Biogeochemical processes and microbial characteristics across groundwater-surface water boundaries of the Hanford Reach of the Columbia River, *Environ Sci Technol*, *37*(22), 5127-5134, doi: 10.1021/es034457v.

Mouvet, C., D. Barberis, and A. C. M. Bourg (1993), Adsorption isotherms of tri-and tetrachloroethylene by various natural solids, *J. Hydrol.*, *149*(1-4), 163-182.

Mulligan, C. N., and R. N. Yong (2004), Natural attenuation of contaminated soils, *Environ Int*, *30*(4), 587-601, doi: 10.1016/j.envint.2003.11.001.

Munz, M., S. Krause, C. Tecklenburg, and A. Binley (2011), Reducing monitoring gaps at the aquifer-river interface by modelling groundwater-surface water exchange flow patterns, *Hydrol. Process.*, *25*(23), 3547-3562, doi: 10.1002/Hyp.8080.

Mutua, S. M. (2013), Analysing the Influence of Groundwater-Surface Water Interaction on the Groundwater Balance in the Aa River, Master thesis, 69 pp, Vrije Universiteit Brussel, Brussels.

Naegeli, M. W., P. Huggenberger, and U. Uehlinger (1996), Ground penetrating radar for assessing sediment structures in the hyporheic zone of a prealpine river, *Journal of the North American Benthological Society*, *15*(3), 353-366, doi: 10.2307/1467282.

Naranjo, R. C., G. Pohll, R. G. Niswonger, M. Stone, and A. McKay (2013), Using heat as a tracer to estimate spatially distributed mean residence times in the hyporheic zone of a riffle-pool sequence, *Water Resour. Res.*, *49*(6), 3697-3711, doi: 10.1002/wrcr.20306.

Nash, J. E., and J. V. Sutcliffe (1970), River flow forecasting through conceptual models part I — A discussion of principles, *J. Hydrol.*, *10*(3), 282-290.

Newell, C. J., H. S. Rifai, J. T. Wilson, J. A. Connor, J. A. Aziz, and M. P. Suarez (2002), Calculation and Use of First-Order Rate Constants for Monitored Natural Attenuation Studies, 28 pp, EPA, Cincinnati, OH.

Nield, D. A. (2000), Modelling Fluid Flow and Heat Transfer in a Saturated Porous Medium, *Journal of Applied Mathematics & Decision Sciences*, *4*(2), 165-173.

Noorduijn, S. L., M. Shanafield, M. A. Trigg, G. A. Harrington, P. G. Cook, and L. Peeters (2014), Estimating seepage flux from ephemeral stream channels using surface water and groundwater level data, *Water Resour. Res.*, *50*(2), 1474-1489, doi: 10.1002/2012wr013424.

Nützmann, G., C. Levers, and J. Lewandowski (2014), Coupled groundwater flow and heat transport simulation for estimating transient aquifer-stream exchange at the lowland River Spree (Germany), *Hydrol. Process.*, *28*(13), 4078-4090, doi: 10.1002/hyp.9932.

Onderka, M., S. Banzhaf, T. Scheytt, and A. Krein (2013), Seepage velocities derived from thermal records using wavelet analysis, *J. Hydrol.*, *479*, 64-74, doi: 10.1016/j.jhydrol.2012.11.022.

Orghidan, T. (1959), Ein neuer Lebensraum des unterirdischen Wassers, der hyporheische Biotop., *Archiv für Hydrobiologie*, *55*, 392-414.

Packman, A., M. Salehin, and M. Zaramella (2004), Hyporheic exchange with gravel beds: Basic hydrodynamic interactions and bedform-induced advective flows, *J. Hydraul. Eng.-ASCE*, *130*(7), 647-656, doi: 10.1061/(Asce)0733-9429(2004)130:7(647).

Packman, A. I., and M. Salehin (2003), Relative roles of stream flow and sedimentary conditions in controlling hyporheic exchange, *Hydrobiologia*, *494*(1-3), 291-297, doi: 10.1023/a:1025403424063.

Painter, S., and M. S. Seth (2003), MULTIFLO User's Manual. MULTIFLO, Version 2.0: Two-Phase Nonisothermal Coupled Thermal-Hydrological-Chemical Flow Simulator., Center for Nuclear Waste Regulatory Analyses, San Antonio, TX.

Pankow, J. F., and J. A. Cherry (1996), *Dense Chlorinated Solvents and Other DNAPLs in Groundwater*, 522 pp., Waterloo Press, Portland, OR.

Pant, P., and S. Pant (2010), A review: advances in microbial remediation of trichloroethylene (TCE), *J Environ Sci (China)*, *22*(1), 116–126, doi: 10.1016/S1001-0742(09)60082-6.

Parkhurst, D. L., and C. A. J. Appelo (1999), USER'S GUIDE TO PHREEQC (VERSION 2) - A COMPUTER PROGRAM FOR SPECIATION, BATCH-REACTION, ONE DIMENSIONAL TRANSPORT, AND INVERSE GEOCHEMICAL CALCULATIONS, *Water-Resources Investigations Report 99-4259*, U.S. Geological Survey, Denver, CO.

Paulsen, R. J., C. F. Smith, D. O'Rourke, and T. F. Wong (2001), Development and evaluation of an ultrasonic ground water seepage meter, *Ground Water*, *39*(6), 904-911, doi: 10.1111/j.1745-6584.2001.tb02478.x.

Pintelon, R., and J. Schoukens (2012), *Systems Identification: A Frequency Domain Approach*, 2nd ed., 788 pp., IEEE Press, New York, NY.

Pintelon, R., J. Schoukens, and G. Vandersteen (1997), Model selection through a statistical analysis of the global minimum of a weighted non-linear least squares cost function, *IEEE Transactions on Signal Processing*, *45*(3), 686-693.

Pintelon, R., J. Schoukens, G. Vandersteen, and K. Barbe (2010a), Estimation of nonparametric noise and FRF models for multivariable systems-Part I: Theory, *Mechanical Systems and Signal Processing*, *24*(3), 573-595, doi: 10.1016/j.ymssp.2009.08.009.

Pintelon, R., J. Schoukens, G. Vandersteen, and K. Barbe (2010b), Estimation of nonparametric noise and FRF models for multivariable systems-Part II: Extensions, applications, *Mechanical Systems and Signal Processing*, *24*(3), 596-616, doi: 10.1016/j.ymssp.2009.08.010.

Pliakas, F., and C. Petalas (2011), Determination of Hydraulic Conductivity of Unconsolidated River Alluvium from Permeameter Tests, Empirical Formulas and Statistical Parameters Effect Analysis, *Water Resources Management*, *25*(11), 2877-2899, doi: 10.1007/s11269-011-9844-8.

Pollard, R. A. (1955), Measuring Seepage through Salmon Spawning Gravel, *J Fish Res Board Can*, *12*(5), 706-741.

Poole, G. C., S. J. O'Daniel, K. L. Jones, W. W. Woessner, E. S. Bernhardt, A. M. Helton, J. A. Stanford, B. R. Boer, and T. J. Beechie (2008), Hydrologic spiralling: The role of multiple interactive flow paths in stream ecosystems, *River Research and Applications*, *24*(7), 1018-1031, doi: 10.1002/Rra.1099.

Privett, B. J., J. H. Shin, and M. H. Schoenfisch (2008), Electrochemical sensors, *Anal Chem*, *80*(12), 4499-4517, doi: 10.1021/ac8007219.

Pruess, K., C. M. Oldenburg, and G. Moridis (1999), TOUGH2 user's guide, version 2.0, *LBNL-43134*, 198 pp, Lawrence Berkeley Natl. Lab., Berkeley, CA.

Ragas, A. M. J., J. L. M. Haans, and Leuven, R.S.W.E. (1997), Selecting water quality models for discharge permitting *European Water Pollution Control*, *7*(5), 59-67.

Rau, G. C., M. S. Andersen, and R. I. Acworth (2012a), Experimental investigation of the thermal time-series method for surface water-groundwater interactions, *Water Resour. Res.*, *48*, doi: 10.1029/2011wr011560.

Rau, G. C., M. S. Andersen, and R. I. Acworth (2012b), Experimental investigation of the thermal dispersivity term and its significance in the heat transport equation for flow in sediments, *Water Resour. Res.*, *48*, doi: 10.1029/2011wr011038.

Rau, G. C., M. S. Andersen, A. M. McCallum, and R. I. Acworth (2010), Analytical methods that use natural heat as a tracer to quantify surface water-groundwater exchange, evaluated using field temperature records, *Hydrogeology Journal*, *18*(5), 1093-1110, doi: 10.1007/s10040-010-0586-0.

Rau, G. C., M. S. Andersen, A. M. McCallum, H. Roshan, and R. I. Acworth (2014), Heat as a tracer to quantify water flow in near-surface sediments, *Earth-Science Reviews*, *129*, 40-58, doi: 10.1016/j.earscirev.2013.10.015.

Read, T., O. Bour, J. S. Selker, V. F. Bense, T. L. Borgne, R. Hochreutener, and N. Lavenant (2014), Active-distributed temperature sensing to continuously quantify vertical flow in boreholes, *Water Resour. Res.*, *50*(5), 3706-3713, doi: 10.1002/2014WR015273.

Refsgaard, J. C. (1996), Terminology, modelling protocol and classification of hydrological model codes, in *Distributed Hydrological Modelling*, edited by J. C. Refsgaard and M. B. Abbott, pp. 17-40, Kluwer.

Refsgaard, J. C., and B. Storm (1995), MIKE SHE, in *Computer models of watershed hydrology*, edited by V. J. Singh, pp. 809-846, Water Resources Publication, Littleton, CO.

Remy, N., A. Boucher, and J. Wu (2009), *Applied Geostatistics with SGeMS: A User's Guide*, 284 pp., Cambridge University Press.

Ren, J. H., and A. I. Packman (2004a), Stream-subsurface exchange of zinc in the presence of silica and kaolinite colloids, *Environ. Sci. Technol.*, *38*(24), 6571-6581, doi: 10.1021/es035090x.

Ren, J. H., and A. I. Packman (2004b), Modeling of simultaneous exchange of colloids and sorbing contaminants between streams and streambeds, *Environ. Sci. Technol.*, *38*(10), 2901-2911, doi: 10.1021/es0348521.

Ren, J. H., and A. I. Packman (2005), Coupled stream-subsurface exchange of colloidal hematite and dissolved zinc, copper, and phosphate, *Environ. Sci. Technol.*, *39*(17), 6387-6394, doi: 10.1021/es050168q.

Renard, P., and D. Allard (2013), Connectivity metrics for subsurface flow and transport, *Adv. Water Resour.*, *51*, 168-196, doi: 10.1016/j.advwatres.2011.12.001.

Riess, N. P. (2010), Nitrogen attenuation at the groundwater – surface water interface of a UK lowland river, PhD thesis, 210 pp, University of Sheffield, Sheffield.

Riser-Roberts, E. (1998), *Remediation of Petroleum Contaminated Soils*, 542 pp., Lewis Publishers, Boca Raton, FL.

Rivett, M. O., R. Ellis, R. B. Greswell, R. S. Ward, R. S. Roche, M. G. Cleverly, C. Walker, D. Conran, P. J. Fitzgerald, T. Willcox, and J. Dowle (2008), Cost-effective mini drive-point piezometers and multilevel samplers for monitoring the hyporheic zone, *Q. J. Eng. Geol. Hydrogeol.*, *41*, 49-60, doi: 10.1144/1470-9236/07-012.

Robinson, J. A., and J. M. Tiedje (1983), Non-linear estimation of Monod growth kinetic-parameters from a single substrate depletion curve, *Applied and Environmental Microbiology*, *45*(5), 1453-1458.

Rose, L., S. Krause, and N. J. Cassidy (2013), Capabilities and limitations of tracing spatial temperature patterns by fiber-optic distributed temperature sensing, *Water Resour. Res.*, *49*(3), 1741-1745, doi: 10.1002/wrcr.20144.

Rosenberry, D. O. (2008), A seepage meter designed for use in flowing water, *J. Hydrol.*, *359*(1-2), 118-130, doi: 10.1016/j.jhydrol.2008.06.029.

Rosenberry, D. O., and R. H. Morin (2004), Use of an electromagnetic seepage meter to investigate temporal variability in lake seepage, *Ground Water*, *42*(1), 68-77, doi: 10.1111/j.1745-6584.2004.tb02451.x.

Rosenberry, D. O., and J. W. LaBaugh (2008), Field techniques for estimating water fluxes between surface water and ground water, *U.S. Geological Survey Techniques and Methods 4-D2*, 128 pp, U.S. Geological Survey

Roshan, H., G. C. Rau, M. S. Andersen, and I. R. Acworth (2012), Use of heat as tracer to quantify vertical streambed flow in a two-dimensional flow field, *Water Resour. Res.*, *48*(W10508), doi: 10.1029/2012wr011918.

Roshan, H., M. O. Cuthbert, M. S. Andersen, and R. I. Acworth (2014), Local thermal non-equilibrium in sediments: Implications for temperature dynamics and the use of heat as a tracer, *Adv. Water Resour.*, *73*, 176-184, doi: 10.1016/j.advwatres.2014.08.002.

Rubin, Y. (2003), *Applied Stochastic Hydrogeology*, 391 pp., Oxford University Press, New York, NY.

Runkel, R. L. (1998), One-Dimensional Transport with Inflow and Storage (OTIS): A solute transport model for streams and rivers *Water Resour. Invest. Rep. 98-4018*, 73 pp, US Geological Survey, Denver, CO.

Runkel, R. L. (2010), One-dimensional transport with equilibrium chemistry (OTEQ) — A reactive transport model for streams and rivers, *U.S. Geological Survey Techniques and Methods Book 6, Chapter B6*, 101 pp.

Ryan, R. J., and M. C. Boufadel (2006), Influence of streambed hydraulic conductivity on solute exchange with the hyporheic zone, *Environ. Geol.*, *51*(2), 203-210, doi: 10.1007/s00254-006-0319-9.

Ryoo, D., H. Shim, K. Canada, P. Barbieri, and T. K. Wood (2000), Aerobic degradation of tetrachloroethene by toluene-o-xylene monooxygenase of Pseudomonas stutzeri OX1., *Nat. Biotechnol.*, *18*(775-778).

Salehin, M., A. I. Packman, and M. Paradis (2004), Hyporheic exchange with heterogeneous streambeds: Laboratory experiments and modeling, *Water Resour. Res.*, *40*(11), doi: 10.1029/2003wr002567.

Sawyer, A. H., and M. B. Cardenas (2009), Hyporheic flow and residence time distributions in heterogeneous cross-bedded sediment, *Water Resour. Res.*, *45*, doi: 10.1029/2008wr007632.

Sayde, C., J. B. Buelga, L. Rodriguez-Sinobas, L. El Khoury, M. English, N. van de Giesen, and J. S. Selker (2014), Mapping variability of soil water content and flux across 1–1000 m scales using the Actively Heated Fiber Optic method, *Water Resour. Res.*, *50*(9), 7302-7317, doi: 10.1002/2013WR014983.

Schaefer, C. E., C. W. Condee, S. Vainberg, and R. J. Steffan (2009), Bioaugmentation for chlorinated ethenes using Dehalococcoides sp.: comparison between batch and column experiments, *Chemosphere*, *75*(2), 141-148, doi: 10.1016/j.chemosphere.2008.12.041.

Schiedeck, T., P. Grathwohl, and G. Teutsch (1997), Literaturstudie zum natürlichen Rückhalt/Abbau von Schadstoffen im Grundwasser, *35/97*, Landesamt für Umweltschutz Baden-Württemberg, Karlsruhe, Germany.

Schmadel, N. M., B. T. Neilson, and T. Kasahara (2014), Deducing the spatial variability of exchange within a longitudinal channel water balance, *Hydrol. Process.*, *28*(7), 3088-3103, doi: 10.1002/hyp.9854.

Schmidt, C., M. Bayer-Raich, and M. Schirmer (2006), Characterization of spatial heterogeneity of groundwater-stream water interactions using multiple depth streambed temperature measurements at the reach scale, *Hydrology and Earth System Sciences*, *10*(6), 849-859.

Schmidt, C., M. Martienssen, and E. Kalbus (2011), Influence of water flux and redox conditions on chlorobenzene concentrations in a contaminated streambed, *Hydrol. Process.*, *25*(2), 234-245, doi: 10.1002/hyp.7839.

Schmidt, C., B. Conant, M. Bayer-Raich, and M. Schirmer (2007), Evaluation and field-scale application of an analytical method to quantify groundwater discharge using mapped streambed temperatures, *J. Hydrol.*, *347*(3-4), 292-307, doi: 10.1016/j.jhydrol.2007.08.022.

Schmidt, C., O. Buttner, A. Musolff, and J. H. Fleckenstein (2014), A method for automated, daily, temperature-based vertical streambed water-fluxes, *Fund Appl Limnol*, *184*(3), 173-181, doi: 10.1127/1863-9135/2014/0548.

Schmidt, C., E. Kalbus, R. Krieg, M. Bayer-Raich, S. Leschik, F. Reinstorf, M. Martienssen, and M. Schirmer (2008), Contaminant mass flow rates between groundwater, streambed sediments and surface water at the regionally contaminated site Bitterfeld, *Grundwasser*, *13*(3), 133-146, doi: 10.1007/s00767-008-0076-7.

Schneidewind, U., C. Anibas, G. Vandersteen, C. Schmidt, I. Joris, P. Seuntjens, and O. Batelaan (2013), Delineating Groundwater-Surface Water Interaction Using Temperature-Time Series Analysis Methods, paper presented at Proceedings of the 2nd European Symposium on Water Technology, VITO, Leuven, Belgium.

Schneidewind, U., P. J. Haest, S. Atashgahi, F. Maphosa, K. Hamonts, M. Maesen, M. Calderer, P. Seuntjens, H. Smidt, D. Springael, and W. Dejonghe (2014), Kinetics of dechlorination by Dehalococcoides mccartyi using different carbon sources, *J Contam Hydrol*, *157*, 25-36, doi: 10.1016/j.jconhyd.2013.10.006.

Schornberg, C., C. Schmidt, E. Kalbus, and J. H. Fleckenstein (2010), Simulating the effects of geologic heterogeneity and transient boundary conditions on streambed temperatures — Implications for temperature-based water flux calculations, *Adv. Water Resour.*, *33*(11), 1309-1319, doi: 10.1016/j.advwatres.2010.04.007.

Schwarzenbach, R. P., P. M. Gschwend, and D. M. Imboden (2003), *Environmental Organic Chemistry*, 2 ed., 1312 pp., John Wiley & Sons Inc., Hoboken, NJ.

Schwoerbel, J. (1961), Uber die Lebensbedingungen und die Besiedlung des hyporheischen Lebensraumes., *Archiv für Hydrobiologie Supplement*, *25*, 182-214.

Sear, D. A., L. B. Frostick, G. Rollinson, and T. E. Lisle (2008), The significance and mechanics of fine sediment infiltration and accumultaion in gravel spawning beds, in *Salmon Spawning Habitat in Rivers; Physical controls, biological responses and approaches to remediation.*, edited by D. A. Sear and P. DeVries, pp. 149-174, AFS, Bethesda, MD.

Sebok, E., C. Duque, P. Engesgaard, and E. Boegh (2015), Spatial variability in streambed hydraulic conductivity of contrasting stream morphologies: channel bend and straight channel, *Hydrol. Process.*, *29*(3), 458-472, doi: 10.1002/hyp.10170.

Sebok, E., C. Duque, J. Kazmierczak, P. Engesgaard, B. Nilsson, S. Karan, and M. Frandsen (2013), High-resolution distributed temperature sensing to detect seasonal groundwater discharge into Lake Væng, Denmark, *Water Resour. Res.*, *49*(9), 5355-5368, doi: 10.1002/wrcr.20436.

Selker, J. S., N. van de Giesen, M. Westhoff, W. Luxemburg, and M. B. Parlange (2006a), Fiber optics opens window on stream dynamics, *Geophysical Research Letters*, *33*(24), doi: 10.1029/2006gl027979.

Selker, J. S., L. Thevenaz, H. Huwald, A. Mallet, W. Luxemburg, N. V. de Giesen, M. Stejskal, J. Zeman, M. Westhoff, and M. B. Parlange (2006b), Distributed fiber-optic temperature sensing for hydrologic systems, *Water Resour. Res.*, *42*(12), doi: 10.1029/2006wr005326.

Semprini, L., M. E. Dolan, M. A. B. Mathias, G. D. Hopkins, and P. L. McCarty (2007), Laboratory, field, and modeling studies of bioaugmentation of butane-utilizing microorganisms for the in situ cometabolic treatment of 1,1-dichloroethene, 1,1-dichloroethane, and 1,1,1-trichloroethane, *Adv. Water Resour.*, *30*(6-7), 1528-1546, doi: 10.1016/j.advwatres.2006.05.017.

Shanafield, M., G. Pohll, and R. Susfalk (2010), Use of heat-based vertical fluxes to approximate total flux in simple channels, *Water Resour. Res.*, *46*, doi: 10.1029/2009wr007956.

Shanafield, M., C. Hatch, and G. Pohll (2011), Uncertainty in thermal time series analysis estimates of streambed water flux, *Water Resour. Res.*, *47*, doi: 10.1029/2010wr009574.

Shaw, R. D., and E. E. Prepas (1989), Anomalous, Short-Term Influx of Water into Seepage Meters, *Limnology and Oceanography*, *34*(7), 1343-1351.

Shope, C. L., J. E. Constantz, C. A. Cooper, D. M. Reeves, G. Pohll, and W. A. McKay (2012), Influence of a large fluvial island, streambed, and stream bank on surface water-groundwater fluxes and water table dynamics, *Water Resour. Res.*, *48*(6), W06512, doi: 10.1029/2011wr011564.

Šimůnek, J., M. , T. van Genuchten, and M. Šejna (2006), The HYDRUS Software Package for Simulating Two- and Three-Dimensional Movement of Water, Heat, and Multiple Solutes in Variably-Saturated Media, 241 pp, Prague, Czech Republic.

Slater, L. D., D. Ntarlagiannis, F. D. Day-Lewis, K. Mwakanyamale, R. J. Versteeg, A. Ward, C. Strickland, C. D. Johnson, and J. W. Lane (2010), Use of electrical imaging and distributed temperature sensing methods to characterize surface water-groundwater exchange regulating uranium transport at the Hanford 300 Area, Washington, *Water Resour. Res.*, *46*, doi: 10.1029/2010wr009110.

Smith, J. W. N. (2005), Groundwater-surface water interactions in the hyporheic zone, *Science Report SC030155/SR1*, 71 pp, Environment Agency, Bristol.

Smith, J. W. N., and D. N. Lerner (2007), A framework for rapidly assessing the pollutant retardation capacity of aquifers and sediments, *Q. J. Eng. Geol. Hydrogeol.*, *40*, 137-146, doi: 10.1144/1470-9236/06-032.

Smith, J. W. N., and D. N. Lerner (2008), Geomorphologic control on pollutant retardation at the groundwater-surface water interface, *Hydrol. Process.*, *22*(24), 4679-4694, doi: 10.1002/Hyp.7078.

Smith, J. W. N., B. W. J. Surridge, T. H. Haxton, and D. N. Lerner (2009), Pollutant attenuation at the groundwater-surface water interface: A classification scheme and statistical analysis using national-scale nitrate data, *J. Hydrol.*, *369*(3-4), 392-402, doi: 10.1016/j.jhydrol.2009.02.026.

Soetaert, K., V. deClippele, and P. Herman (2002), FEMME, a flexible environment for mathematically modelling the environment, *Ecological Modelling*, *151*(2-3), 177-193, doi: 10.1016/S0304-3800(01)00469-0.

Song, J. X., X. H. Chen, C. Cheng, S. Summerside, and F. J. Wen (2007), Effects of hyporheic processes on streambed vertical hydraulic conductivity in three rivers of Nebraska, *Geophysical Research Letters*, *34*(7), doi: 10.1029/2007gl029254.

Song, J. X., X. H. Chen, C. Cheng, D. M. Wang, S. Lackey, and Z. X. Xu (2009), Feasibility of grain-size analysis methods for determination of vertical hydraulic conductivity of streambeds, *J. Hydrol.*, *375*(3-4), 428-437, doi: 10.1016/j.jhydrol.2009.06.043.

Soto-Lopez, C. D., T. Meixner, and T. P. A. Ferre (2011), Effects of measurement resolution on the analysis of temperature time series for stream-aquifer flux estimation., *Water Resour. Res.*, *47*, WT2602.

Springer, R. K., and L. W. Gelhar (1991), Characterization of large-scale aquifer heterogeneity in glacial outwash by analysis of slug tests with oscillatory response, *Water Res. Invest. Rep.*, *91*(4034), 36-40.

Stallman, R. W. (1965), Steady one-dimensional fluid flow in a semi-infinite porous medium with sinusoidal surface temperature, *Journal of Geophysical Research*, *70*(12), 2821-2827.

Stanford, J. A., and A. R. Gaufin (1974), Hyporheic communities of two montana rivers, *Science*, *185*(4152), 700-702, doi: 10.1126/science.185.4152.700.

Stanford, J. A., and J. V. Ward (1988), The Hyporheic Habitat of River Ecosystems, *Nature*, *335*(6185), 64-66, doi: 10.1038/335064a0.

Stanford, J. A., and J. V. Ward (1993), An ecosystem perspective of alluvial rivers: connectivity and the hyporrheic corridor, *Journal of North American Benthological Society*, *12*, 48-60.

Staudinger, J., and P. V. Roberts (2001), A critical compilation of Henry's law constant temperature dependence relations for organic compounds in dilute aqueous solutions, *Chemosphere*, *44*(4), 561-576.

Stewart, W. J. (2009), *Probability, Markov Chains, Queues, and Simulation - The Mathematical Basis of Performance Modeling*, 758 pp., Princeton University Press, Princeton, NJ.

Stonedahl, S. H., J. W. Harvey, and A. I. Packman (2013), Interactions between hyporheic flow produced by stream meanders, bars, and dunes, *Water Resour. Res.*, *49*(9), 5450-5461, doi: 10.1002/Wrcr.20400.

Stonedahl, S. H., J. W. Harvey, A. Worman, M. Salehin, and A. I. Packman (2010), A multiscale model for integrating hyporheic exchange from ripples to meanders, *Water Resour. Res.*, *46*, doi: 10.1029/2009wr008865.

Stonedahl, S. H., J. W. Harvey, J. Detty, A. Aubeneau, and A. I. Packman (2012), Physical controls and predictability of stream hyporheic flow evaluated with a multiscale model, *Water Resour. Res.*, *48*, doi: 10.1029/2011wr011582.

Stonestrom, D. A., and K. W. Blasch (2003), Determining temperature and thermal properties for heat-based studies of surface-water ground-water interactions. , *Circular 1260*, 73-80 pp, USGS, Reston, VA.

Stonestrom, D. A., and J. Constantz (2003), Heat as a Tool for Studying the Movement of Ground Water Near Streams, *Circular 1260*, 105 pp, U.S. Geological Survey, Reston, VA.

Storey, R. G., R. R. Fulthorpe, and D. D. Williams (1999), Perspectives and predictions on the microbial ecology of the hyporheic zone, *Freshwater Biology*, *41*(1), 119-130, doi: 10.1046/j.1365-2427.1999.00377.x.

Storey, R. G., K. W. F. Howard, and D. D. Williams (2003), Factors controlling riffle-scale hyporheic exchange flows and their seasonal changes in a gaining stream: A three-dimensional groundwater flow model, *Water Resour. Res.*, *39*(2), doi: 10.1029/2002wr001367.

Storn, R., and K. Price (1997), Differential Evolution – A Simple and Efficient Heuristic for global Optimization over Continuous Spaces, *Journal of Global Optimization*, *11*(4), 341-359, doi: 10.1023/A:1008202821328.

Streetly, M., and M. G. Shepley (2005), East Shropshire Permo-Triassic Sandstone Groundwater Modelling Project - Final Report, 306 pp, Environmental Simulations International Ltd., Environment Agency, British Geological Survey.

Taniguchi, M., and Y. Fukuo (1993), Continuous Measurements of Groundwater Seepage Using an Automatic Seepage Meter, *Ground Water*, *31*(4), 675-679, doi: 10.1111/j.1745-6584.1993.tb00601.x.

Taniguchi, M., W. C. Burnett, C. F. Smith, R. J. Paulsen, D. O'Rourke, S. L. Krupa, and J. L. Christoff (2003), Spatial and temporal distributions of submarine groundwater discharge rates obtained from various types of seepage meters at a site in the Northeastern Gulf of Mexico, *Biogeochemistry*, *66*(1-2), 35-53, doi: 10.1023/B:Biog.0000006090.25949.8d.

Tarnawski, V. R., T. Momose, and W. H. Leong (2011), Thermal Conductivity of Standard Sands II. Saturated Conditions, *Int J Thermophys*, *32*(5), 984-1005, doi: 10.1007/s10765-011-0975-1.

Teles, V., J. P. Bravard, G. De Marsily, and E. Perrier (2001), Modelling of the construction of the Rhone alluvial plain since 15 000 years BP, *Sedimentology*, *48*(6), 1209-1224, doi: 10.1046/j.1365-3091.2001.00419.x.

Tercier-Waeber, M. L., and M. Taillefert (2008), Remote in situ voltammetric techniques to characterize the biogeochemical cycling of trace metals in aquatic systems, *Journal of environmental monitoring : JEM*, *10*(1), 30-54, doi: 10.1039/b714439n.

Therrien, R., R. G. McLaren, E. A. Sudicky, and S. M. Panday (2010), HydroGeoSphere A Three-dimensional Numerical Model Describing Fully-integrated Subsurface and Surface Flow and Solute Transport, 483 pp, Groundwater Simulations Group, University of Waterloo, Canada, Waterloo.

Tonina, D., and J. M. Buffington (2007), Hyporheic exchange in gravel bed rivers with pool-riffle morphology: Laboratory experiments and three-dimensional modeling, *Water Resour. Res.*, *43*(1), doi: 10.1029/2005wr004328.

Tonina, D., and J. Buffington (2009), Hyporheic exchange in mountain rivers. I: Mechanics and environmental effects, *Geography Compass*, *3*, 1063-1086, doi: 10.1111/j.1749-8198.2009.00226.x.

Toth, J. (1963), A Theoretical Analysis of Groundwater Flow in Small Drainage Basins, *Journal of Geophysical Research*, *68*(16), 4795-&, doi: 10.1029/Jz068i008p02354.

Triska, F. J., V. C. Kennedy, R. J. Avanzino, G. W. Zellweger, and K. E. Bencala (1989), Retention and Transport of Nutrients in a 3rd-Order Stream in Northwestern California - Hyporheic Processes, *Ecology*, *70*(6), 1893-1905, doi: 10.2307/1938120.

Tyler, S. W., J. S. Selker, M. B. Hausner, C. E. Hatch, T. Torgersen, C. E. Thodal, and S. G. Schladow (2009), Environmental temperature sensing using Raman spectra DTS fiber-optic methods, *Water Resour. Res.*, *45*, doi: 10.1029/2008wr007052.

UNESCO (2009), Water in a changing world, *The United Nations World Water Development Report 3*, 429 pp, UNESCO.

USEPA (1995), Contaminant specific fact sheets, Volatile organic chemicals, U.S. Environmental Protection Agency, Washington, DC.

van Berkel, M., G. Vandersteen, E. Geerardyn, R. Pintelon, H. J. Zwart, and M. R. de Baar (2014a), Frequency domain sample maximum likelihood estimation for spatially dependent parameter estimation in PDEs, *Automatica*, *50*(8), 2113-2119, doi: 10.1016/j.automatica.2014.05.027.

van Berkel, M., H. J. Zwart, G. M. D. Hogeweij, G. Vandersteen, H. van den Brand, M. R. de Baar, and the Asdex Upgrade Team (2014b), Estimation of the thermal diffusion coefficient in fusion plasmas taking frequency measurement uncertainties into account, *Plasma Physics and Controlled Fusion*, *56*(10), 105004 doi: 10.1088/0741-3335/56/10/105004.

Van Keer, I., J. Bronders, J. Verhack, J. Schwarzbauer, and R. Swennen (2011), Limitations in the use of compound-specific stable isotope analysis to understand the behaviour of a complex BTEX groundwater contamination near Brussels (Belgium), *Environ. Earth Sci.*, *66*(2), 457-470, doi: 10.1007/s12665-011-1254-y.

Vandenbohede, A., and L. Lebbe (2010), Parameter estimation based on vertical heat transport in the surficial zone, *Hydrogeology Journal*, *18*(4), 931-943, doi: 10.1007/s10040-009-0557-5.

Vandenbohede, A., A. Louwyck, and L. Lebbe (2009), Conservative Solute Versus Heat Transport in Porous Media During Push-pull Tests, *Transport in Porous Media*, *76*(2), 265-287, doi: 10.1007/s11242-008-9246-4.

Vandersteen, G., U. Schneidewind, C. Anibas, C. Schmidt, P. Seuntjens, and O. Batelaan (2015), Determining groundwater-surface water exchange from temperature-time series: Combining a local polynomial method with a maximum likelihood estimator, *Water Resour. Res.*, *51*(2), 922-939, doi: 10.1002/2014wr015994.

Vannote, R. L., G. W. Minshall, K. W. Cummins, J. R. Sedell, and C. E. Cushing (1980), The river continuum concept, *Can. J. Fish. Aquat. Sci.*, *37*, 130-137.

Verreydt, G., J. Bronders, I. Van Keer, L. Diels, and P. Vanderauwera (2010), Passive Samplers for Monitoring VOCs in Groundwater and the Prospects Related to Mass Flux Measurements, *Ground Water Monit. Remediat.*, *30*(2), 114-126, doi: 10.1111/j1745-6592.2010.001281.x.

Verreydt, G., M. D. Annable, S. Kaskassian, I. Van Keer, J. Bronders, L. Diels, and P. Vanderauwera (2013), Field demonstration and evaluation of the Passive Flux Meter on a CAH groundwater plume, *Environ Sci Pollut Res Int*, *20*(7), 4621-4634, doi: 10.1007/s11356-012-1417-8.

Vienken, T., and P. Dietrich (2011), Field evaluation of methods for determining hydraulic conductivity from grain size data, *J. Hydrol.*, *400*(1-2), 58-71, doi: 10.1016/j.jhydrol.2011.01.022.

Vieweg, M., N. Trauth, J. H. Fleckenstein, and C. Schmidt (2013), Robust Optode-Based Method for Measuring in Situ Oxygen Profiles in Gravelly Streambeds, *Environ. Sci. Technol.*, *47*(17), 9858-9865, doi: 10.1021/es401040w.

Vogt, T., P. Schneider, L. Hahn-Woernle, and O. A. Cirpka (2010), Estimation of seepage rates in a losing stream by means of fiber-optic high-resolution vertical temperature profiling, *J. Hydrol.*, *380*(1-2), 154-164, doi: 10.1016/j.jhydrol.2009.10.033.

Voss, C. I. (2011a), Editor's message: Groundwater modeling fantasies -part 1, adrift in the details, *Hydrogeology Journal*, *19*(7), 1281-1284, doi: 10.1007/s10040-011-0789-z.

Voss, C. I. (2011b), Editor's message: Groundwater modeling fantasies-part 2, down to earth, *Hydrogeology Journal*, *19*(8), 1455-1458, doi: 10.1007/s10040-011-0790-6.

Voss, C. I., and A. M. Provost (2008), SUTRA - a model for saturated-unsaturated variable-density ground water flow with solute or energy transport, *Technical report Water-resources Investigations Report 02-4231* 270 pp, U.S. Geological Survey, Reston VA.

Voytek, E. B., A. Drenkelfuss, F. D. Day-Lewis, R. Healy, J. W. Lane, Jr., and D. Werkema (2014), 1DTempPro: analyzing temperature profiles for groundwater/surface-water exchange, *Ground Water*, *52*(2), 298-302, doi: 10.1111/gwat.12051.

Vrana, B., G. A. Mills, I. J. Allan, E. Dominiak, K. Svensson, J. Knutsson, G. Morrison, and R. Greenwood (2005), Passive sampling techniques for monitoring pollutants in water, *Trac-Trends Anal. Chem.*, *24*(10), 845-868, doi: 10.1016/j.trac.2005.06.006.

Vrugt, J. (2005), AMALGAM: Ensemble Optimizer in which multiple different search strategies are run simultaneously, and learn from each other through information exchange using a common population of points, edited, Lecture notes - global_search.ppt.

Vrugt, J. A., and B. A. Robinson (2007), Improved evolutionary optimization from genetically adaptive multimethod search, *Proceedings of the National Academy of Sciences of the United States of America*, *104*(3), 708-711, doi: 10.1073/pnas.0610471104.

Vrugt, J. A., B. A. Robinson, and J. M. Hyman (2009), Self-Adaptive Multimethod Search for Global Optimization in Real-Parameter Spaces, *IEEE Transactions on Evolutionary Computation*, *13*(2), 243-259, doi: 10.1109/TEVC.2008.924428.

Vrugt, J. A., C. J. F. ter Braak, C. G. H. Diks, and G. Schoups (2013), Hydrologic data assimilation using particle Markov chain Monte Carlo simulation: Theory, concepts and applications, *Adv. Water Resour.*, *51*, 457-478, doi: 10.1016/j.advwatres.2012.04.002.

Vukovic, M., and A. Soro (1992), *Determination of Hydraulic Conductivity of Porous Media from Grains-Size Composition*, 54 pp., Water Resources Publications, LLC, Littleton.

Wagner, B. J., and J. W. Harvey (1997), Experimental design for estimating parameters of rate-limited mass transfer: Analysis of stream tracer studies, *Water Resour. Res.*, *33*(7), 1731-1741, doi: 10.1029/97wr01067.

Wang, X., H. Li, J. Yang, L. Wan, X. Wang, X. Jiang, and H. Guo (2014), Measuring in situ vertical hydraulic conductivity in tidal environments, *Adv. Water Resour.*, *70*, 118-130.

Ward, A. S., M. N. Gooseff, and K. Singha (2010), Characterizing hyporheic transport processes - Interpretation of electrical geophysical data in coupled stream-hyporheic zone systems during solute tracer studies, *Adv. Water Resour.*, *33*(11), 1320-1330, doi: 10.1016/j.advwatres.2010.05.008.

Ward, J. V., J. A. Stanford, and N. J. Voelz (1994), Spatial-Distribution Patterns of Crustacea in the Floodplain Aquifer of an Alluvial River, *Hydrobiologia*, *287*(1), 11-17, doi: 10.1007/Bf00006892.

Ward, J. V., C. T. Robinson, and K. Tockner (2002), Applicability of ecological theory to riverine ecosystems, *Int Ver Theor Angew*, *28*, 443-450.

Weatherill, J., S. Krause, K. Voyce, F. Drijfhout, A. Levy, and N. Cassidy (2014), Nested monitoring approaches to delineate groundwater trichloroethene discharge to a UK lowland stream at multiple spatial scales, *J Contam Hydrol*, *158*, 38-54, doi: 10.1016/j.jconhyd.2013.12.001.

Webb, R. H., and S. A. Leake (2006), Ground-water surface-water interactions and long-term change in riverine riparian vegetation in the southwestern United States, *J. Hydrol.*, *320*(3-4), 302-323, doi: 10.1016/j.jhydrol.2005.07.022.

Werisch, S., J. Grundmann, H. Al-Dhuhli, E. Algharibi, and F. Lennartz (2014), Multiobjective parameter estimation of hydraulic properties for a sandy soil in Oman, *Environ. Earth Sci.*, *72*, 4935-4956.

White, D. S. (1993), Perspectives of Defining and Delineating Hyporheic Zones, *Journal of North American Benthological Society*, *12*(1), 61-69.

Wiedemeier, T. H., M. A. Swanson, D. E. Moutoux, E. K. Gordon, J. T. Wilson, B. H. Wilson, D. H. Kampbell, P. E. Haas, R. N. Miller, J. E. Hansen, and F. H. Chapelle (1998), Technical Protocol for Evaluating Natural Attenuation of Chlorinated Solvents in Groundwater, *EPA/600/R-98/128*, 248 pp, EPA, Washington, DC.

Willems, P. (2000), Probabilistic modeling of the immission in receiving surface waters, PhD thesis, Catholic University of Leuven, Leuven, Belgium.

Willems, P. (2012), Model uncertainty analysis by variance decomposition, *Physics and Chemistry of the Earth*, *42-44*, 21-30, doi: 10.1016/j.pce.2011.07.003.

Williams, D. D. (1984), The hyporheic zone as a habitat for aquatic insects and associated arthopods, in *The ecology of aquatic insects*, edited by D. M. Rosenberg and V. H. Resh, pp. 430-455, Praeger, New York.

Wilson, J. T., J. W. Weaver, and D. H. Kampbell (1994), Intrinsic bio-remediation of TCE in ground water at an NPL site in St. Joseph, Michigan, paper presented at Proceedings of the EPA Symposium on Intrinsic Bioremediation of Ground Water, Denver, CO, August 30-September 1, 1994.

Winston, R. B. (2009), ModelMuse - A graphical user interface for MODFLOW-2005 and PHAST, *Techniques and Methods - 6-A29*, 52 pp, U.S. Geological Survey, Reston, VA.

Winter, T. C., J. W. Harvey, O. L. Franke, and W. M. Alley (1998), Ground Water and Surface Water A Single Resource, *1139*, 79 pp, U.S. Geological Survey, Denver, Co.

Woessner, W. W. (2000), Stream and fluvial plain ground water interactions: Rescaling hydrogeologic thought, *Ground Water*, *38*(3), 423-429, doi: 10.1111/j.1745-6584.2000.tb00228.x.

Wöhling, T., J. A. Vrugt, and G. F. Barkle (2008), Comparison of Three Multiobjective Optimization Algorithms for Inverse Modeling of Vadose Zone Hydraulic Properties, *Soil Sci Soc Am J*, *72*(2), 305-319, doi: 10.2136/sssaj2007.0176.

Wondzell, S. M., J. LaNier, and R. Haggerty (2009), Evaluation of alternative groundwater flow models for simulating hyporheic exchange in a small mountain stream, *J. Hydrol.*, *364*(1-2), 142-151, doi: DOI 10.1016/j.jhydrol.2008.10.011.

Wondzell, S. M., M. N. Gooseff, and B. L. McGlynn (2010), An analysis of alternative conceptual models relating hyporheic exchange flow to diel fluctuations in discharge during baseflow recession, *Hydrol. Process.*, *24*(6), 686-694, doi: 10.1002/hyp.7507.

Woodside, W., and J. H. Messmer (1961), Thermal Conductivity of Porous Media. I. Unconsolidated Sands, *Journal of Applied Physics*, *32*(9), 1688-1699.

Wörman, A., J. Riml, N. Schmadel, B. T. Neilson, A. Bottacin-Busolin, and J. E. Heavilin (2012), Spectral scaling of heat fluxes in streambed sediments, *Geophysical Research Letters*, *39*, doi: 10.1029/2012gl053922.

Wroblicky, G. J., M. E. Campana, H. M. Valett, and C. N. Dahm (1998), Seasonal variation in surface-subsurface water exchange and lateral hyporheic area of two stream-aquifer systems, *Water Resour. Res.*, *34*(3), 317-328, doi: 10.1029/97wr03385.

Yen, B. C., and C. W.-S. Tsai (2001), On noninertia wave versus diffusion wavein flood routing, *J. Hydrol.*, *244*(97-104).

Young, P. C., D. J. Pedregal, and W. Tych (1999), Dynamic harmonic regression, *Journal of Forecasting*, *18*(6), 369-394, doi: 10.1002/(sici)1099-131x(199911)18:6<369::aid-for748>3.0.co;2-k.

Younger, P. L., R. Mackay, and B. J. Connorton (1993), Streambed Sediment as a Barrier to Groundwater Pollution - Insights from Fieldwork and Modeling in the River Thames Basin, *J Inst Water Env Man*, *7*(6), 577-585.

Yu, S., and L. Semprini (2004), Kinetics and modeling of reductive dechlorination at high PCE and TCE concentrations, *Biotechnol Bioeng*, *88*(4), 451-464, doi: 10.1002/bit.20260.

Zheng, C., and P. P. Wang (1999), MT3DMS: A modular three-dimensional multispecies transport model for simulation of advection, dispersion, and chemical reactions of groundwater systems; documentation and user's guide., 280 pp, Vicksburg, MS.

Zheng, C., and G. D. Bennett (2002), *Applied Contaminant Transport Modeling*, 2nd ed., 621 pp., John Wiley and Sons Inc., New York.

Ziv-El, M., S. C. Popat, K. Cai, R. U. Halden, R. Krajmalnik-Brown, and B. E. Rittmann (2012), Managing methanogens and homoacetogens to promote reductive dechlorination of trichloroethene with direct delivery of H2 in a membrane biofilm reactor, *Biotechnology and Bioengineering*, *109*(9), 2200-2210, doi: 10.1002/bit.24487.

Zlotnik, V. (1994), Interpretation of Slug and Packer Tests in Anisotropic Aquifers, *Ground Water*, *32*(5), 761-766, doi: 10.1111/j.1745-6584.1994.tb00917.x.

Zlotnik, V. A., M. B. Cardenas, and D. Toundykov (2011), Effects of multiscale anisotropy on basin and hyporheic groundwater flow, *Ground Water*, *49*(4), 576-583, doi: 10.1111/j.1745-6584.2010.00775.x.

Scientific Curriculum Vitae

Education

PhD

10.2011 – present	Department of Soil Management, Ghent University, Gent, Belgium
Thesis Title:	Water Flow and Contaminant Transformation in the Hyporheic Zone of Lowland Rivers
Supervisors:	Prof. Dr. ir. Piet Seuntjens (Ghent University) Dr. ir. Ingeborg Joris (VITO) Prof. Dr Okke Batelann (Flinders University)
Funding:	36 months Marie Curie Fellowship – ESR within EU ITN FP7 project ADVOCATE (Advancing sustainable in situ remediation for contaminated land and groundwater – grant agreement 265063) affiliated to VITO – Flemish Institute for Technological Research 2 months PhD scholarship from Ghent University FWO travel grant for conference visit (EGU General Assembly 2015)

Courses followed:

- In –situ remediation of contaminated sites, September 4, 2014, CL:AIRE
- Sustainability evaluation, June 2-5, 2014, KU Leuven
- Career workshop, employment opportunities, developing an effective job search strategy, CVs and job applications, February 21, 2014, EAWAG
- Principles and application of flow and transport modeling in the subsurface, August 27-30, 2013, University of Liege
- Modeling transport and geochemical cycling processes in soil, March 25-28, 2013, UGent
- Spatial statistics, 2012/2013, UGent
- Interpretation and statistical analysis of environmental data, February 16-17, 2013, University of Liege
- Leadership foundation course, November 2012, UGent
- Conceptual model-building with Leapfrog, September 16, 2012, IAH (during conference)

- Assessment of contaminant source identification, natural processes and remediation performance using stable isotopes, June 21-22, 2012 Helmholtz Centre for Environmental Research – UFZ
- Application of innovative methods for site characterization, water & contaminant flux measurement in the subsurface, June 19-20, 2012, UFZ
- Assessment of contaminated sites - Established concepts and new methods, May 16, 2012, FH-DGG (during conference)
- Natural attenuation of pollution, May 2012, University of Sheffield
- Risk assessment in remediation, March 2012, University of Sheffield
- Advanced Academic English – Conference skills, 2012, UGent
- Project management – Academic and industry perspective, November 16-17, 2011, University of Sheffield

Secondment:

- March 29 – April 3, 2012 & October 14 – November 8, 2013 at University of Sheffield, Groundwater Protection and Remediation Group
  Supervisor: Dr. Steven Thornton

- *Topic:* Working on flow and transport data collected at the River Tern

MSc in Applied Environmental Geoscience

8.2006 – 9.2008	University of Tübingen, Tübingen, Germany
Thesis Title:	Determination of the Hydraulic Conductivity using Direct-Push Injection Logger
Supervisors:	Dr. Philipp Blum, Dr. Carsten Leuven, Dr. Peter Dietrich

BSc in Environmental and Resource Management

10.2002 – 7.2006	Brandenburg University of Technology (BTU), Cottbus, Germany
Thesis Title:	Geophysical Investigation of the Oil-Shale Bearing Structure “Erlenwiese” in the Vicinity of the World Heritage Site “Messel Pit Fossil Site”
Supervisors:	Prof. Dr. Rainer Herd, Prof. Dr. Hans-Jürgen Voigt

Teaching

- 2012-2014 Contaminant Transport in Soils - HYDRUS 1D Modelling exercises (Ghent University)
- 2012-2014 Soil Processes - HYDRUS 1D Modelling exercises (University of Antwerp)
- 2011 - Integrated Project – Assessment of Contaminant Remediation Options in HYDRUS 2D (Ghent University)

List of Publications as of June 2015

Articles published in international peer-reviewed scientific journals

1 Lessoff, S.C., **Schneidewind, U**., Leven, C., Blum, P., Dietrich, P., Dagan, G. (2010): Spatial Characterization of the Hydraulic Conductivity Using Direct-Push Injection Logging. *Water Resources Research, 46 (12), W12502, doi:10.1029/2009WR008949.*

2 **Schneidewind, U.***, Haest, P.J.*, Atashgahi, S.*, Maphosa, F., Hamonts, K., Maesen, M., Calderer, M., Seuntjens, P., Smidt, H., Springael, D., Dejonghe, W. (2014): Kinetics of dechlorination by *Dehalococcoides mccartyi* using different carbon sources. *Journal of Contaminant Hydrology, 157, 25-36, doi: 10.1016/j.jconhyd.2013.10.006.*

3 Vandersteen, G.*, **Schneidewind, U.***, Anibas, C.*, Schmidt, C., Seuntjens, P., Batelaan, O. (2015), Determining groundwater-surface water exchange from temperature time series: Combining a local polynomial method with a maximum likelihood estimator. *Water Resources Research, 51(2), 922-939, doi: 10.1002/2014WR015994.*

4 Anibas, C.*****, **Schneidewind, U.***, Vandersteen, G., Joris, I., Seuntjens, P., Batelaan, O. (2016): From streambed temperature measurements to spatial-temporal flux quantification: Using the LPML method to study groundwater-surface water interaction. *Hydrological Processes, 30, 203-216, doi: 10.1002/hyp.10588.*

*refers to equal contribution

Peer-reviewed conference proceedings

1 **Schneidewind, U.,** Anibas, C., Vandersteen, G., Schmidt, C., Joris, I., Seuntjens, P., Batelaan, O. (2013): Delineating Groundwater-Surface Water Interaction Using Temperature-Time Series Analysis Methods. *Proceedings of the 2nd European Symposium on Water Technology, Leuven, 20.-21.11.2013, p. 219-225, ISBN 9789058570109.*

2 Atashgahi, S., Haest, P.J., Carpentier, C., Maphosa, F., Eisenmann, H., **Schneidewind, U.,** Slobodník, J., Seuntjens, P., Smidt, H., Springael, D., Dejonghe, W. (2013): Development of rehabilitation technologies to decrease pollutant influx between groundwater and surface water near river banks – AQUAREHAB WP3. *Proceedings of the 2nd European Symposium on Water Technology, Leuven, 20.-21.11.2013, p. 241-246, ISBN 9789058570109.*

Other peer-reviewed articles

1 **Schneidewind, U.,** Anibas, C., Joris, I., Seuntjens, P. (2015): Delineating Groundwater-Surface Water Interaction. *ADVOCATE Bulletin 9, 9 pages, DOI: 10.13140/RG.2.1.2730.6405.*

Peer-reviewed conference abstracts with oral or poster presentation

1 Macis, L., Margagliotti, M., **Schneidewind, U.**, Cicci, G., Salerno, A., Leven, C. (2009): Comparison of Different Pumping Techniques for Depth-Discrete Groundwater Sampling. *Novel Methods for Subsurface Characterization and Monitoring: From Theory to Practice, Leipzig, 13.-16.05.2009.*

2 **Schneidewind, U.**, Lessoff, S.C., Blum, P., Leven, C., Dietrich, P. (2009): Determination of the Hydraulic Conductivity Using the Direct-Push Injection Logger. *Novel Methods for Subsurface Characterization and Monitoring: From Theory to Practice, Leipzig, 13.-16.05.2009.*

3 Dietrich, P., Lamert, H., Schütze, C., **Schneidewind, U**., Werban, U. (2009): Combination of different methods for the detection and monitoring of CO2 degassing at the near surface, *Eos Trans. AGU, 90* (52), Fall Meet. Suppl., Abstract H21E-0897.

4 Bohling, G., Liu, G., Butler, J.J., Reboulet, E.C., Vienken, T., **Schneidewind, U.** (2009): Geostatistical Simulation of Centimeter-Scale Hydraulic Conductivity Estimates from Direct-Push Logging at the MADE Site, *Eos Trans. AGU, 90* (52), Fall Meet. Suppl., Abstract H43C-1038.

5 Schütze, C., Lamert, H., Vienken, T., **Schneidewind, U**., Zschornack, L., Werban, U., Dietrich, P. (2010): Kombinierter Einsatz geophysikalischer und gasgeochemischer Methoden zur Erkundung tektonischer Störungszonen. (Combined use of geophysical and geochemical methods for the exploration of tectonic faults.) *70. Jahrestagung der Deutschen Geophysikalischen Gesellschaft (DGG), Bochum, 15.-18.03.2010.*

6 Lamert, H., Schütze, C., Werban, U., **Schneidewind, U**., Dietrich, P. (2010): Risikobewertung von CO_2-Leckagen – Monitoringkonzept mit hierarchischem Ansatz. (Risk assessment of CO_2 leakage – A monitoring concept with a hierarchical approach.) *70. Jahrestagung der Deutschen Geophysikalischen Gesellschaft (DGG), Bochum, 15.-18.03.2010.*

7 **Schneidewind, U.**, Lessoff, S.C., Leven, C., Blum, P., Dietrich, P., Dagan, G. (2010): Spatial Characterization of Hydraulic Conductivity with Direct-Push Injection Logging. *Grundwasser für die Zukunft, SDGG 67, p. 109, Meeting of the German Hydrogeological Society (FH-DGG), Tübingen, 12.-16.05.2010.*

8 Schuetze, C., Lamert, H.**, Schneidewind, U.**, Werban, U.**,** Dietrich, P. (2010): A hierarchic approach for the characterization of CO_2 permeable pathways using geophysical and geochemical methods. *Near Surface 2010 - 16th European Meeting of Environmental and Engineering Geophysics, Zurich, 06.-08.09.2010.*

9 Dagan, G., **Schneidewind, U.**, Dietrich, P., Leven, C., Blum, P., Lessoff, S.C. (2010): Stochastic characterization of hydraulic conductivity of Lauswiesen aquifer by direct-push injection logging. *IAHR International Groundwater Symposium, Valencia, 22.-24.09.2010.*

10 Dietrich, P., Lamert, H., **Schneidewind, U.**, Leven, C. (2011): Heat tracer test as an efficient tool for the investigation of connectivity in heterogeneous aquifers. *Novel Methods for Subsurface Characterization and Monitoring: From Theory to Practice, Cape Cod, 09.-11.05.2011.*

11 **Schneidewind, U.**, Li, T., Leven, C., Dietrich, P., Bayer, P., Blum, P. (2011): Monitoring heat flow in groundwater. *In-Situ Environmental Monitoring and Policy – The Application of Sensors and Passive Samplers, Gent, 26.-27.05.2011.*

12 **Schneidewind, U.**, Verbeiren, B., De Becker, P., De Bie, E., Batelaan, O. (2011): Hydrological modelling as a tool for the management and regeneration of an open heath-land ecosystem. *ModelCare 2011 – Models- Repositories of Knowledge, Leipzig, 18.-22.09.2011.*

13 Dietrich, P., Lamert, H., **Schneidewind, U.**, Leven, C. (2011): The combination of Direct-Push injection logging and heat tracer test for the investigation of connectivity in heterogeneous aquifers. *Geological Society of America – Annual Meeting, Minneapolis, 09.-12.10.2011.*

14 **Schneidewind, U**., Joris, I., Batelaan, O., Schirmer, M., Seuntjens, P. (2012): Assessing Heterogeneity in Flow and Transport Processes at the Groundwater-Surface Interface and Their Role in the Degradation of Organic Contaminants. *Geophysical Research Abstracts 14, EGU2012-10106. EGU General Assembly 2012, Vienna, 22.-27.04.2012.*

15 **Schneidewind, U.**, El-Rawy, M. De Becker,P., Batelaan, O. (2012): Analysis and Rehabilitation of a Groundwater-Dependent Ecosystem in Belgium. *Geophysical Research Abstracts 14, EGU2012-3721. EGU General Assembly 2012, Vienna, 22.-27.04.2012.*

16 Anibas, C., **Schneidewind, U.**, Vandersteen, G., Batelaan, O. (2012): Die Lokal-polynomiale Methode zur Bestimmung von Grundwasser-Oberflächenwasseraustauschraten: Theorie und Praxis. (The local polynomial method for determining groundwater-surface water exchange rates: Theory and practice.) *Grundwasserschutz und Grundwassernutzung. SDGG 78, p. 83, Meeting of the German Hydrogeological Society (FH-DGG), Dresden, 16.-20.05.2012.*

17 **Schneidewind, U.**, El-Rawy, M., Bashir, I., Abdollahi, K., De Becker, P., Zijl, W., Batelaan, O. (2012): Groundwater Modeling and Ecosystem Management – The Case of Houthalen-Helchteren Military Domain. *Grundwasserschutz und Grundwassernutzung. SDGG 78, p. 152, Meeting of the German Hydrogeological Society (FH-DGG), Dresden, 16.-20.05.2012.*

18 Batelaan, O., El-Rawy, M., **Schneidewind, U.**, Dams, J., De Becker, P. (2012): Role of groundwater flow systems in the ecology of wetlands. *39th IAH congress, Niagara Falls, 16.-21.09.2012.*

19 **Schneidewind, U.**, Haest, P.J., Hamonts, K., Atashgahi, S., Dejonghe, W., Seuntjens, P. (2012): Investigating natural attenuation of chlorinated ethenes at a contaminated site in Belgium. *39th IAH congress, Niagara Falls, 16.-21.09.2012.*

20 **Schneidewind, U.**, Haest, P.J., Hamonts, K., Atashgahi, S., Dejonghe, W., Seuntjens, P. (2012): Modeling reductive dechlorination of a CAH containing plume entering the Zenne river. *Remediation Technologies and their Integration in Water Management, Barcelona, 25.-26.09.2012.*

21 Batelaan, O., El-Rawy, M., **Schneidewind, U**., De Becker, P. (2013): Scenario modelling of drainage impact of a groundwater-dependent heath ecosystem, Belgium. *Geophysical Research Abstracts 15, EGU2013-6710. EGU General Assembly 2013, Vienna, 07.-12.04.2013.*

22 Batelaan, O., El-Rawy, M., **Schneidewind, U.,** Dams, J., De Becker, P., (2013): Regional Groundwater Flow and Ecohydrology. *International Symposium on Regional Groundwater Flow: Theory, Applications and Future Development. 21-23 June 2013, Xi'an, China. China Geological Survey, Commission on Regional Groundwater Flow, IAH. p. 4.*

23 Anibas, C., **Schneidewind, U.**, Vandersteen, G., Huysmans, M., Joris, I., Batelaan, O. (2013): The Local Polynomial Method: A novel processing tool to quantify surface-subsurface exchange flows using temperature time series and their frequency response. *Knowledge for the Future. IAHS Joint Assembly, Gothenburg, 22.-26.07.2013.*

24 Anibas, C., Huysmans, M., **Schneidewind, U**., Joris, I., Vandersteen, G., Batelaan, O. (2013): The Local Polynomial Method for characterization of spatial and temporal variability of groundwater-surface water interaction. *Solving the Groundwater Challenges for the 21st Century. 40th IAH congress, Perth, 15.-20.09.2013.*

25 **Schneidewind, U.**, Anibas, C., Vanderstenn, G., Batelaan, O., Joris, I., Seuntjens, P., Voloshchenko, O. (2013): Determining Vertical Groundwater-Surface Water Exchange Using a New Approach to Solve the 1D Heat Transport Equation. *Abstract H33F-1455, AGU Fall Meeting 2013, San Francisco, 09.-13.12.2013.*

26 **Schneidewind, U**., Anibas, C., Vandersteen, G., Joris, I., Seuntjens, P., Batelaan, O. (2014): Determining Groundwater-Surface Water Exchange Fluxes and Their Spatial Variability Using the Local Polynomial Method LPML. *Geophysical Research Abstracts 16, EGU2014-10258. EGU General Assembly 2014, Vienna, 27.04.-02.05.2014.*

27 **Schneidewind, U.**, Anibas, C., Vandersteen, G., Joris, I., Batelaan, O., Schmidt, C. (2014): Bestimmung von vertikalen Grundwasser-Oberflächenwasseraustauschraten mittels Temperaturzeitreihenanalyse am Beispiel des Slootbeek. *Grundwasser trifft Boden und Energie. Bayreuther Forum Ökologie 2014, Vol.118, Abstract O6.13 Meeting of the German Hydrogeological Society (FH-DGG), Bayreuth, 28.-31.05.2014.*

28 **Schneidewind, U.,** Joris, I., Seuntjens, P., Thornton, S. (2014): Investigating the Impact of Heterogeneity in Streambed Sediments on Flow, Transport and Biodegradation Processes in the Hyporheic Zone. *In Situ Remediation 2014 Conference, London, 02.-04.09.2014.*

29 **Schneidewind, U.,** van Berkel, M., Anibas, C., Vandersteen, G., Joris, I., Seuntjens, P., Batelaan, O. (2015): LPMLE3: A New Analytical Approach to Determine Vertical Groundwater-Surface Water Exchange Flux under Uncertainty and Heterogeneity. *Geophysical Research Abstracts 17, EGU2015-5107. EGU General Assembly 2015, Vienna, 12.04.-17.04.2015.*

30 **Schneidewind, U.,** Thornton, S., Van De Vijver, E., Joris, I., Seuntjens, P. (2015): Spatial Variability of Streambed Hydraulic Conductivity of a Lowland River. *Geophysical Research Abstracts 17, EGU2015-5363. EGU General Assembly 2015, Vienna, 12.04.-17.04.2015.*

31 Anibas, C., **Schneidewind, U.,** Vandersteen, G., Huysmans, M., Batelaan, O. (2015): Studying temporal and spatial variations of groundwater-surface water exchange flux for the Slootbeek (Belgium) using the LPML method. *Geophysical Research Abstracts 17, EGU2015-9531. EGU General Assembly 2015, Vienna, 12.04.-17.04.2015.*

Reports

1 Dagan, G., Lessoff, S., Dietrich, P., Vienken, T., **Schneidewind, U.**, Leven, C. (2010): Development of new methods for aquifer characterization. *German-Israeli cooperation in water technology research, 11th Status Seminar, Darmstadt/Germany,11.-13.10.2010,* 11 pages.

2 Batelaan, O., El-Rawy, M., **Schneidewind, U.**, De Becker, P., Herr, C. (2012): Doorrekenen van maatregelen voor herstel van vochtige heidevegetaties op het Schietveld van Houthalen-Helchteren via grondwatermodellering. (Scenario analysis and groundwater modeling for the rehabilitation of wet heathlands at Houthalen-Helchteren military domain.). *Client: Agentschap voor Natuur en Bos (Nature and Forest Authority). Project number: LNE/ANB/LIM-2010/10.* 250 pages.

3 **Schneidewind, U.** (2013): Contaminant transport and attenuation in the hyporheic zone of streams. *State of science report for ADVOCATE project. Grant agreement no. 265063.* 83 pages.

4 **Schneidewind, U.**, Joris, I. (2013): Modeling contaminant transport and attenuation in the hyporheic zone of streams – model guidance document. *Deliverable for ADVOCATE project. Grant agreement no. 265063.* 43 pages.

Theses

1 Geophysical Investigation of the Oil-Shale Bearing Structure "Erlenwiese" in the Vicinity of the World Heritage Site "Messel Pit Fossil Site". *Thesis for Bachelor of Science (BSc), Brandenburg University of Technology, Cottbus, Germany. 26 July 2006.* 90 pages.

2 Determination of the Hydraulic Conductivity using Direct-Push Injection Logger. *Thesis for Master of Science (MSc), University of Tübingen, Tübingen, Germany. September 2008.* 175 pages.